2023-08-01

Electrochemical Approaches To Life-Support Resources In Space Missions And Nuclear Technologies: Hydrogen Peroxide And Uranium Films

Armando Manuel Pena-Duarte
University of Texas at El Paso

ELECTROCHEMICAL APPROACHES TO LIFE-SUPPORT RESOURCES IN SPACE MISSIONS AND NUCLEAR TECHNOLOGIES: HYDROGEN PEROXIDE AND URANIUM FILMS

ARMANDO MANUEL PEÑA-DUARTE

Doctoral Program in Chemistry

APPROVED:

Carlos R. Cabrera, Ph.D., Chair

Stella A. Quiñones, Ph.D.

Dino Villagrán, Ph.D.

Jorge Gardea-Torresdey, Ph.D.

Stephen L. Crites, Jr., Ph.D.
Dean of the Graduate School

To:

Julia – *The Grandmother*

Lorinda – *The Mother*

Anibal – *The Brother*

Andreina – *The Sister*

Aranza – *The Niece*

Lemuel – *The Husband*

ELECTROCHEMICAL APPROACHES TO LIFE-SUPPORT RESOURCES IN SPACE MISSIONS AND NUCLEAR TECHNOLOGIES: HYDROGEN PEROXIDE AND URANIUM FILMS

by

ARMANDO MANUEL PEÑA-DUARTE

DISSERTATION

Presented to the Faculty of the Graduate School of
The University of Texas at El Paso
in Partial Fulfillment
of the Requirements
for the Degree of

DOCTOR OF PHYLOSOPHY

Department of Chemistry and Biochemistry
THE UNIVERSITY OF TEXAS AT EL PASO

August 2023

Acknowledgements:

I truly want to thank to:

God Who has been my driving force during my whole life.

The University of Texas at El Paso, especially to the Department of Chemistry and Biochemistry, for promoting knowledge and cutting-edge research—ensuring a successful future for El Paso, Texas, and USA.

The University of Puerto Rico at Rio Piedras, where I began my PhD, especially to the NASA Fellowship Puerto Rico Space Grant Consortium Grant No. NNX15AI11H for funding my space-electrochemical research.

My mentor, Dr. Carlos R Cabrera, for all his advice and mentorship in a professional and personal level. I am truly grateful for his dedication to scientific research, mentoring, and education.

The UTEP Chemistry Graduate Advisor Team for the help and guidance that I have received before and after moving to UTEP.

Dr. Stella A Quiñones, Dr. Dino Villagrán, and Dr. Jorge Gardea-torresdey, for their time and for being part of my UTEP PhD Dissertation committee.

Dr. Ramonita Diaz-Ayala (UPRRP) for her mentorship during our XPS and instrumentation work in the Molecular Science and Research Center in Puerto Rico.

Dr. Brenda Torres (UTEP) for her guidance during my years as Teaching Assistant at UTEP.

My friends and colleagues Dr. Nadja Solis (UPRRP) and Dr. Myreisa Morales (UPRRP), for sharing science, life, and coffee—coloring and befriending our PhD pathway.

My new colleague and friend, Dr. Yermary Morales Lozada (UTEP), for all her advice in a professional and personal level.

My colleagues, protagonists of exciting scientific discussions in our lab, Dr. Joesene Soto (UPRRP), Dr. Juan Corchado (UPRRP), Dr. Carlos Velez (UPRRP), Dr. Luis Betancourt (UPRRP), and Alexis J Acevedo-Gonzalez (UPRRP).

The fundamental pillars of my data, my undergrads, Aminda Cheney-Irgens (NSF-REU), Kathleen L. Hayes (NSF-REU), Jose Luis Lasso (UTEP), Sarah Leon (UTEP), Alan Murguia (UTEP).

The NASA Fellowship from NASA Puerto Rico Space Grant Consortium No. NNX15AI11H at the UPR, and the NASA Phase II SBIR Contract NNX16CA43P trough Faraday Technology Inc.

The National Science Foundation NSF-PREM: Center for interfacial Electrochemistry of Energy Materials (CiE^2M) grant number DMR-1827622, NSF REU PR-CLIMB Grant No. 1757365, NASA Phase II SBIR Contract NNX16CA43P, and Center for Alkaline Based Energy Solutions (CABES), an Energy Frontier Research Center funded by the U.S. Department of Energy, Office of Science, Basic Energy Sciences under award number DE-SC0019445.

The Department of Energy-National Nuclear Security Administration-Minority Serving Institution Partnership Program (MSIPP) Scholarly Partnership in Nuclear Security (SPINS) Consortium, grant number DE-NA0003980, and the National Science Foundation Major Research Instrumentation (NSF-MRI) program with the award number 1828729 for the XPS instrument located at Alabama A&M University.

Table of Contents

Figures

Tables

I. Introduction, The Problem, and The Proposal

Space missions represent a huge spectrum of possibilities where we can get in as scientists. Space race has developed several technological advances delivering mission success in the aerospace timeline,[1, 2] and the number is still growing—demanding new materials and developments for extreme performing applications of fuel cells, batteries, supercapacitors, and safe sources of nuclear sources.[1-10]

If we think about people living in space, they work, have food, take showers, generate waste, produce bacteria and viruses, and required novel sources of energy. In this sense, space missions need: life-support solutions, auto-sustainable closed-loop living environments, cleaning and sanitizing solutions against bacteria and viruses, and safe nuclear-based resources of energy—with fissile materials with well-controlled dimensions within the core fuel elements—.[3, 7, 8, 11, 12] Likewise, to guarantee safety conditions, reduce costs, and facilitate operational logistic, space missions must reduce their dependence on terrestrial resources and suitable nuclear fuel systems—,[3, 7, 8, 12] developing *in-situ* technologies or at least finding safe ways to transport resources from Earth.

In this sense, secure-cleaned environments and nuclear-based energy sources systems represent ones of the several technological challenges faced by human closed-loop living systems during space missions.[3, 13 14, 15] Herein—H_2O_2 and U-based materials emerge as sterilization solution and nuclear source of energy, respectively—I proposed the design and development of electrochemical strategies for life support system in space missions—evaluating electrocatalytic developments for *in-situ* H_2O_2 production and producing stable U-based films as a first strategic approximation of fissile transportable films.

Hydrogen peroxide represents a clean oxidant that just produce H_2O and O_2 after its decomposition, is safe for direct skin contact at concentrations below 5% w/w,[13] and has exhibited sterilization capability.[16] H_2O_2 is demanded in several fields of application such as manufacturing, chemistry, medicine, and cleaning and sanitizing solutions against exposures to bacteria and viruses, such as the COVID-19.[11, 17] [11, 18] However, H_2O_2 production needs innovative, more efficient, and sustainable methods, due to the low efficient and unsafe industrial procedures that are currently implemented.[19]

Cleaning requirements for space missions need to become auto-sustainable, allowing closed-loop living systems to be less dependent on earth resources. Innovative methods are emerging to develop an electrochemical direct production of H_2O_2, by controlling the oxygen reduction reaction (ORR)[20] via two-electrons pathway.[21] [11, 13] [22] [23] In aqueous systems, the ORR could occur either via two-electrons (Equation i.1) or via four-electrons (Equation i.2) pathways.[24]

$$\boldsymbol{O_2 + 2H^+ + 2e^- \rightarrow H_2O_2} \; ; \; E^0 = 0.6700\, V \qquad \text{(i.1)}$$

$$\boldsymbol{O_2 + 4H^+ + 4e^- \rightarrow 2H_2O} \; ; \; E^0 = 1.229\, V \qquad \text{(i.2)}$$

Controlling the ORR via two-electrons pathway for *in-situ* electrochemical syntheses of H_2O_2, represents an alternative to the current industrial production of peroxide, avoiding unsafe and expensive transport procedures from Earth to space, preventing stockpiles of toxic precursors, just needing water supply onboard the spacecraft.[3, 13]

Likewise, uranium-based technologies under atmospheric environments remain incomplete and require novel insights and experimental improvements. Uranium composites formation, with homogenous and stable composition is particularly useful for several applications under different atmospheric conditions.[25-28] Stabilization of uranium compounds need solutions against non-inert environments to: (1) improve safety; (2) produce cost-effective processes; and (3) generate environmentally friendly systems for extraction, recycling and recovery, transportation and storage, and fuel

development.[29-39] Lately, diverse techniques to control the uranium oxidation have been developed.[40] Uranium oxides are used in catalysts,[41, 42] semiconducting approaches,[43, 44] nuclear technologies,[45] and neutron sensors based on fission-tagging neutron capture.[46-48]

Specifically for space applications, the used of HEU supported in aerogels for core fission fragment rocket engine, as advance propulsion solutions for interplanetary mission, has currently resumed for study.[14, 15] U235 is one of the most practical fissile material due to uranium fission release more than 81% as kinetic energy.[49] The idea is that fission fragments escape from the core of a nuclear reactor.[50] The fuel elements in the core can consist of several parallel of fuel (uranium) plates.[6, 51-53] Plate thickness affects the core power density generated due to it determine the ratio of fuel-volume to fuel-element surface area accessible for elimination of heat.[5] Variations in plate thicknesses produce changes in peak power locations and magnitude increments of the peak power.[54] In this sense, more homogeneous fuel element films with well-controlled thickness are needed to improve the efficiency of reactor reactors.

References

(1) NASA. *Human Spaceflight, in: https://www.nasa.gov/specials/60counting/spaceflight.html*. (accessed May 23, 2023).

(2) Aerospace. *Aerospace 60th Anniversary Timeline, in: https://aerospace.org/timeline#event-aerospace-60th-anniversary-timeline*. (accessed May 23, 2023).

(3) Nelson, G. J.; Vijapur, S. H.; Hall, T. D.; Brown, B. R.; Peña-Duarte, A.; Cabrera, C. R. Electrochemistry for Space Life Support. *Electrochemical Society Interface* **2020**, *29* (1), 47-52. DOI: 10.1149/2.f06201if.

(4) Winter, M.; Brodd, R. J. What Are Batteries, Fuel Cells, and Supercapacitors? *Chemical Reviews* **2004**, *104* (10), 4245-4270. DOI: 10.1021/cr020730k.

(5) Lin, C.-S.; Youinou, G. Design and Analysis of a 250 MW Plate-fuel Reactor for Nuclear Thermal Propulsion. *Nuclear and Emerging Technologies for Space* **2020**, 95-99.

(6) Yuan, Q.; Zhao, J.; Mok, D. H.; Zheng, Z.; Ye, Y.; Liang, C.; Zhou, L.; Back, S.; Jiang, K. Electrochemical Hydrogen Peroxide Synthesis from Selective Oxygen Reduction over Metal Selenide Catalysts. *Nano Letters* **2021**. DOI: 10.1021/acs.nanolett.1c04420.

(7) Harvey, S.; Communication, I. O. o. P. I. a. *Ensuring Safety on Earth from Nuclear Sources in Space, https://www.iaea.org/newscenter/news/ensuring-safety-on-earth-from-nuclear-sources-in-space*. 2020. (accessed May 21, 2023).

(8) Vogel, S. C.; Monreal, M. J.; Shivprasad, A. P. Materials for Small Nuclear Reactors and Micro Reactors, Including Space Reactors. *JOM* **2021**, *73* (11), 3497-3498. DOI: 10.1007/s11837-021-04897-3.

(9) Aerospace. *A Brief History of Space Exploration, in: https://aerospace.org/article/brief-history-space-exploration*. (accessed May 23, 2023).

(10) Aerospace. *Delivering Mission Success Across The Space Enterprise, in: https://aerospace.org/what-we-do/deliver-solutions-space*. (accessed May 23, 2023).
(11) Peña-Duarte, A.; Vijapur, S. H.; Hall, T. D.; Hayes, K. L.; Larios-Rodríguez, E.; Pilar-Albaladejo, J. D.; Santiago, M. E. B.; Snyder, S.; Taylor, J.; Cabrera, C. R. Iron Quantum Dots Electro-Assembling on Vulcan XC-72R: Hydrogen Peroxide Generation for Space Applications. *ACS Applied Materials & Interfaces* **2021**. DOI: 10.1021/acsami.1c05649.
(12) Fulton, J.; Laboratories, S. N. *Space Nuclear Launch Safety, https://energy.sandia.gov/programs/nuclear-energy/launch-safety-for-space-nuclear-missions/*. (accessed May 21, 2023).
(13) Vijapur, S. H.; Hall, T. D.; Taylor, E.; Wang, D.; Snyder, S.; Skinn, B.; Peña-Duarte, A.; Cabrera, C. R.; Sweterlitsch, J. *In- Situ* Resource Utilization for Electrochemical Generation of Hydrogen Peroxide for Disinfection. *ICES: International Conference on Environmental Systems* **2019**, *38*, 14 pages.
(14) Weed, R. *Aerogel Core Fission Fragment Rocket Engine, NIAC 2023 Phase I and Phase II Selections, https://www.nasa.gov/directorates/spacetech/niac/2023/*. 2023. (accessed 2023 May 21).
(15) Weed, R.; Horsley, M.; Chapline, G. Aerogel Supported Fission Fragment Rocket Engine Core. *Nuclear and Emerging Technologies for Space (NETS-2022), Proceedings* **2022**.
(16) Rutala, W. A.; Weber, D. J.; Healthcare, T.; (HICPAC)., I. C. P. A. C. Guideline for Disinfection and Sterilization in Healthcare Facilities. United States Centers for Disease Control and Prevention, http://www.cdc.gov/hicpac/pdf/guidelines/Disinfection_Nov_2008.pdf.
(17) Campos-Martin, J. M.; Blanco-Brieva, G.; Fierro, J. L. G. Hydrogen Peroxide Synthesis: An Outlook beyond the Anthraquinone Process. *Angewandte Chemie International Edition* **2006**, *45* (42), 6962-6984, https://doi.org/10.1002/anie.200503779. DOI: https://doi.org/10.1002/anie.200503779 (acccessed 2022/08/28).
(18) Strukul, G. *Catalytic oxidations with hydrogen peroxide as oxidant*; Springer Science & Business Media, 2013.
(19) de Frutos Escrig, P.; Garriga Meco, Á.; Padilla Polo, A. Improved Procedure for Hydrogen Peroxide Production by Oxidation of Secondary Alcohols and Oxygenated Cosolvents. *Industrial & Engineering Chemistry Research* **2008**, *47* (21), 8025-8031. DOI: 10.1021/ie800159u.
(20) Sánchez-Sánchez, C. M.; Rodríguez-López, J.; Bard, A. J. Scanning Electrochemical Microscopy. 60. Quantitative Calibration of the SECM Substrate Generation/Tip Collection Mode and Its Use for the Study of the Oxygen Reduction Mechanism. *Analytical Chemistry* **2008**, *80* (9), 3254-3260. DOI: 10.1021/ac702453n.
(21) Xia, C.; Xia, Y.; Zhu, P.; Fan, L.; Wang, H. Direct electrosynthesis of pure aqueous H₂O₂ solutions up to 20% by weight using a solid electrolyte. *Science* **2019**, *366* (6462), 226. DOI: 10.1126/science.aay1844.
(22) Chen, S.; Chen, Z.; Siahrostami, S.; Kim, T. R.; Nordlund, D.; Sokaras, D.; Nowak, S.; To, J. W. F.; Higgins, D.; Sinclair, R.; et al. Defective Carbon-Based Materials for the Electrochemical Synthesis of Hydrogen Peroxide. *ACS Sustainable Chemistry & Engineering* **2018**, *6* (1), 311-317. DOI: 10.1021/acssuschemeng.7b02517.
(23) Lu, Z.; Chen, G.; Siahrostami, S.; Chen, Z.; Liu, K.; Xie, J.; Liao, L.; Wu, T.; Lin, D.; Liu, Y.; et al. High-efficiency oxygen reduction to hydrogen peroxide catalysed by oxidized carbon materials. *Nature Catalysis* **2018**, *1* (2), 156-162. DOI: 10.1038/s41929-017-0017-x.
(24) Yeager, E. Electrocatalysts for O2 reduction. *Electrochimica Acta* **1984**, *29* (11), 1527-1537. DOI: https://doi.org/10.1016/0013-4686(84)85006-9.
(25) Jamal, G. E.; Gouder, T.; Eloirdi, R.; Jonsson, M. Monitoring the gradual change in oxidation state during surface oxidation or reduction of uranium oxides by photoemission spectroscopy of the 5f states. *Journal of Nuclear Materials* **2022**, *560*, 153504. DOI: https://doi.org/10.1016/j.jnucmat.2021.153504.
(26) Salvato, D.; Vigier, J. F.; Dieste Blanco, O.; Martel, L.; Luzzi, L.; Somers, J.; Tyrpekl, V. Innovative preparation route for uranium carbide using citric acid as a carbon source. *Ceramics International* **2016**, *42* (15), 16710-16717. DOI: https://doi.org/10.1016/j.ceramint.2016.07.138.

(27) Lammers, L. N.; Rasmussen, H.; Adilman, D.; deLemos, J. L.; Zeeb, P.; Larson, D. G.; Quicksall, A. N. Groundwater uranium stabilization by a metastable hydroxyapatite. *Applied Geochemistry* **2017**, *84*, 105-113. DOI: https://doi.org/10.1016/j.apgeochem.2017.06.001.
(28) Gouder, T.; Eloirdi, R.; Caciuffo, R. Direct observation of pure pentavalent uranium in U2O5 thin films by high resolution photoemission spectroscopy. *Scientific Reports* **2018**, *8* (1), 8306. DOI: 10.1038/s41598-018-26594-z.
(29) Maslakov, K. I.; Teterin, Y. A.; Popel, A. J.; Teterin, A. Y.; Ivanov, K. E.; Kalmykov, S. N.; Petrov, V. G.; Springell, R.; Scott, T. B.; Farnan, I. XPS study of the surface chemistry of UO2 (111) single crystal film. *Applied Surface Science* **2018**, *433*, 582-588. DOI: https://doi.org/10.1016/j.apsusc.2017.10.019.
(30) Ulrich, K.-U.; Ilton, E. S.; Veeramani, H.; Sharp, J. O.; Bernier-Latmani, R.; Schofield, E. J.; Bargar, J. R.; Giammar, D. E. Comparative dissolution kinetics of biogenic and chemogenic uraninite under oxidizing conditions in the presence of carbonate. *Geochimica et Cosmochimica Acta* **2009**, *73* (20), 6065-6083. DOI: https://doi.org/10.1016/j.gca.2009.07.012.
(31) Matzke, H. Radiation damage-enhanced dissolution of UO2 in water. *Journal of Nuclear Materials* **1992**, *190*, 101-106. DOI: https://doi.org/10.1016/0022-3115(92)90080-5.
(32) He, H.; Qin, Z.; Shoesmith, D. W. Characterizing the relationship between hyperstoichiometry, defect structure and local corrosion kinetics of uranium dioxide. *Electrochimica Acta* **2010**, *56* (1), 53-60. DOI: https://doi.org/10.1016/j.electacta.2010.09.064.
(33) Smirnov, A. L.; Rychkov, V. N.; Umanskii, A. B.; Galyanina, E. A.; Klyushnikov, A. M. Kinetic features of underground uranium leaching from ores of hydrogenous uranium deposits. *Radiochemistry* **2009**, *51* (1), 61-64. DOI: 10.1134/S1066362209010147.
(34) He, H.; Zhu, R. K.; Qin, Z.; Keech, P.; Ding, Z.; Shoesmith, D. W. Determination of Local Corrosion Kinetics on Hyper-Stoichiometric UO[sub 2+x] by Scanning Electrochemical Microscopy. *Journal of The Electrochemical Society* **2009**, *156* (3), C87. DOI: 10.1149/1.3046112.
(35) Shoesmith, D. W.; Sunder, S. The prediction of nuclear fuel (UO2) dissolution rates under waste disposal conditions. *Journal of Nuclear Materials* **1992**, *190*, 20-35. DOI: https://doi.org/10.1016/0022-3115(92)90072-S.
(36) Glazoff, M.; Van Rooyen, I.; Coryell, B.; Parga, C. *Comparison of Nuclear Fuels for TREAT: UO2 vs U3O8*; 2016.
(37) Delegard, C. H.; Schmidt, A. J. *Uranium Metal Reaction Behavior in Water, Sludge, and Grout Matrices*; PNNL--17815; United States, 2008. http://inis.iaea.org/search/search.aspx?orig_q=RN:40057505.
(38) Energy, U. D. o. *US Department of Energy Strategic Plan, at: https://www.energy.gov/downloads/us-department-energy-strategic-plan-0*. 2020. (accessed.
(39) Harris, W. E.; Kolthoff, I. M. The Polarography of Uranium. III. Polarography in Very Weakly Acid, Neutral or Basic Solution1. *Journal of the American Chemical Society* **1947**, *69* (2), 446-451. DOI: 10.1021/ja01194a073.
(40) Burrell, A. K.; McCleskey, T. M.; Shukla, P.; Wang, H.; Durakiewicz, T.; Moore, D. P.; Olson, C. G.; Joyce, J. J.; Jia, Q. Controlling Oxidation States in Uranium Oxides through Epitaxial Stabilization. *Advanced Materials* **2007**, *19* (21), 3559-3563, https://doi.org/10.1002/adma.200701157. DOI: https://doi.org/10.1002/adma.200701157 (acccessed 2022/04/06).
(41) Walker, G. S.; Lapszewicz, J. A.; Foulds, G. A. Partial oxidation of methane to methanol-comparison of heterogeneous catalyst and homogeneous gas phase reactions. *Catalysis Today* **1994**, *21* (2), 519-526. DOI: https://doi.org/10.1016/0920-5861(94)80175-4.
(42) Lazareva, S.; Ismagilov, Z.; Kuznetsov, V.; Shikina, N.; Kerzhentsev, M. Uranium oxide catalysts: environmental applications for treatment of chlorinated organic waste from nuclear industry. *Environmental Technology* **2019**, *40* (14), 1881-1889. DOI: 10.1080/09593330.2018.1432696.
(43) Craig, A. K.; Sanjoy, M.; David, S.; Thomas, M.; Brandon, S.; Taylor, C.; Jerrad Philip, A. Semiconductor neutron detectors using depleted uranium oxide. In *Proc.SPIE*, 2014; Vol. 9213. DOI: 10.1117/12.2063501.

(44) Young, C.; Petrosky, J.; Mann, J. M.; Hunt, E. M.; Turner, D.; Kelly, T. The work function of hydrothermally synthesized UO2 and the implications for semiconductor device fabrication. *physica status solidi (RRL) – Rapid Research Letters* **2016**, *10* (9), 687-690, https://doi.org/10.1002/pssr.201600203. DOI: https://doi.org/10.1002/pssr.201600203 (acccessed 2022/04/06).
(45) Enriquez, E.; Wang, G.; Sharma, Y.; Sarpkaya, I.; Wang, Q.; Chen, D.; Winner, N.; Guo, X.; Dunwoody, J.; White, J.; et al. Structural and Optical Properties of Phase-Pure UO2, α-U3O8, and α-UO3 Epitaxial Thin Films Grown by Pulsed Laser Deposition. *ACS Applied Materials & Interfaces* **2020**, *12* (31), 35232-35241. DOI: 10.1021/acsami.0c08635.
(46) Bacak, M.; Aïche, M.; Bélier, G.; Berthoumieux, E.; Diakaki, M.; Dupont, E.; Gunsing, F.; Heyse, J.; Kopecky, S.; Laurent, B.; et al. A compact fission detector for fission-tagging neutron capture experiments with radioactive fissile isotopes. *Nuclear Instruments and Methods in Physics Research Section A: Accelerators, Spectrometers, Detectors and Associated Equipment* **2020**, *969*, 163981. DOI: https://doi.org/10.1016/j.nima.2020.163981.
(47) Reichenberger, M. A.; Unruh, T. C.; Ugorowski, P. B.; Ito, T.; Roberts, J. A.; Stevenson, S. R.; Nichols, D. M.; McGregor, D. S. Micro-Pocket Fission Detectors (MPFDs) for in-core neutron detection. *Annals of Nuclear Energy* **2016**, *87*, 318-323. DOI: https://doi.org/10.1016/j.anucene.2015.08.022.
(48) Unruh, T.; Reichenberger, M.; Stevenson, S.; McGregor, D.; Tsai, K. *Enhanced Micro-Pocket Fission Detector for High Temperature Reactors - FY17 FInal Project Report* . U.S. Department of Energy - Office of Scientific and Technical Information, United States, 2017. https://doi.org/10.2172/1468579DOI: doi:10.2172/1468579.
(49) Clark, R.; Sheldon, R. Dusty Plasma Based Fission Fragment Nuclear Reactor. In *41st AIAA/ASME/SAE/ASEE Joint Propulsion Conference & Exhibit*, Joint Propulsion Conferences, American Institute of Aeronautics and Astronautics, 2005.
(50) Chapline, G. Fission fragment rocket concept. *Nuclear Instruments and Methods in Physics Research Section A: Accelerators, Spectrometers, Detectors and Associated Equipment* **1988**, *271* (1), 207-208. DOI: https://doi.org/10.1016/0168-9002(88)91148-5.
(51) Technology, M. I. o. *Nuclear Reactor Laboratory, Core Description, https://nrl.mit.edu/reactor/core-description*. 2023. (accessed May 21, 2023).
(52) Newswire, A. N. S.-N. *Inside MIT's Nuclear Reactor - ANS Nuclear Cafe Friday Matinee, https://www.ans.org/news/article-2060/inside-mits-nuclear-reactor-ans-nuclear-cafe-friday-matinee/*. 2018. (accessed May 21, 2023).
(53) Mark, D. D.; Sebastian, S.; Vincent, M. L. Nuclear Thermal Propulsion. In *Nuclear Reactors*, Chad, L. P. Ed.; IntechOpen, 2022; p Ch. 1.
(54) DeHart, M. D.; Karriem, Z.; Pope, M. A.; Johnson, M. P. Fuel element design and analysis for potential LEU conversion of the Advanced Test Reactor. *Progress in Nuclear Energy* **2018**, *104*, 117-135. DOI: https://doi.org/10.1016/j.pnucene.2017.09.007.

II. Hypotheses, Goals, and Specific Aims

This dissertation comprehends the design, creation, and implementation of novel electrochemical approaches—for life support systems in space and nuclear applications. We hypothesized that *(i)* the introduction of sustainable elements—iron and nitrogen—in a carbonaceous matrix would create anchoring functional groups which would control the ORR via two-electrons pathway, producing *in-situ* H_2O_2 in low conductivity water; *(ii)* a chronoamperometric electroplating in aqueous media—in a region with high competition of hydrogen evolution—would create homogenous and stable thin films of uranium-based materials free of voids or big particles of uranium precursor.

Our hypotheses were investigated and tested by pursuing the following main goals:

1. To design a novel non-precious metal catalyst, via the RoDSE method, to produce *in-situ* H_2O_2 in low conductivity water.
2. To thermally synthesize a novel metal-free catalyst to produce *in-situ* H_2O_2 in low conductivity water.
3. To create a chronoamperometric method to produce stable and transportable uranium-based thin films.

In order to achieve our main goals, we pursued the following specific aims which were divided in four different projects.

1. To design, built, and evaluate the performance-function our *eml-II* under terrestrial conditions (Project 1).
2. To determine the optimal conditions of operation of our *eml-II* under terrestrial conditions (Project 1).
3. To take the parabolic flight and evaluate the performance-function of our *eml-II* under μ-*g* conditions (Project 1).

4. To study iron electrochemistry and iron electroplating in 0.1 M $KClO_4$ by using a cyclic voltammetry study (Project 2).
5. To synthesize iron quantum dots onto Vulcan by using the RoDSE technique (Project 2).
6. To prepare N-and C-based material by using thermal treatments (Project 3).
7. To evaluate the H_2O_2 production on the Fe-, N-, and C-based catalysts by using the RDE and RRDE analyses (Project 2, Project 3).
8. To evaluate the *in-situ* H_2O_2 production on the Fe-, N-, and C-based catalysts inside the *eml-II* (Project 2, Project 3).
9. To design a chronoamperometric setup to create uranium-based films (Project 4).
10. To synthesize uranium-based films through the designed chronoamperometric setup (Project 4).
11. To evaluate reproducibility of the uranium-electroplating method by using XPS analysis (Project 4).
12. To determine the chemical and physical properties of the novel material synthesized (Project 2, Project 3, Project 4).

CHAPTER 1. Electrochemistry on 1-g & μ-g: Fundamentals and In-Situ H_2O_2 Production

1.1 Introduction

In a collaborative work with the National Aeronautics and Space Administration (NASA) and Faraday Technology, Inc. (FTI), and under the NASA Phase II SBIR Contract NNX16CA43P, we developed an electrochemical microgravity laboratory to produce *in-situ* hydrogen peroxide for space applications. NASA required to produce *in-situ* H_2O_2 under the water resource—with a conductivity of 2–3 μS/cm, a pH of 5.5–6.7, and a total organic carbon (TOC) content between 0.18 and 2.5 mg/L—available onboard the International Space Station (ISS). FTI proposed the use of the U.S. patent number 6,254,762, for low conductivity water stream, a concept of our collaborator De Nora Technology, Inc.

In this Chapter we describe the electrochemical fundamentals that we took in consideration to solve the problems related to bubbles formation and low conductivity stream on Earth and under microgravity conditions, in order to achieve our aim focused on designing, building, and evaluating the performance-function of a pilot prototype for *in-situ* H_2O_2 generation.

1.1.1 Electrochemistry under one-atmosphere (*1-g*) environments

Electrochemistry, as a surface science require—for a properly microscopic understanding of electrochemical reactions and the electron relocation associated—an in-depth study and control of the place where the electron transfer occur, the solid/liquid interface.[55] Like in a movie, following current densities, we can monitor numerous electrochemical phenomena that occur in the solid/liquid interface. However, if the solid/liquid interface is blocked electron transfer is avoided, avoiding the redox process.

For example, bubbles formed during an electrochemical process—that involve evolution of gases—reduce mass transfer on the vicinity of the electrode.[56] Size and rate of formation of bubbles are determined by several factors such as potential applied, current density generated, electrode material and surface, pH, and electrolyte affect the gas bubble size distribution.[11, 57] Nucleation, growth, and detachment—the gas evolution phases—occur as follow: gas molecules nucleate on the electrode surface producing tiny bubbles, a posterior growing occurs by coalescency and diffusion of more molecules of gas, the formed bigger bubbles detach from the electrode when buoyancy overcome the surface tension force, or when external forces remove the bubbles.[57]

To promote electron transfer in the vicinity of the catalytic active size, a water electrolysis reactor needs: water as fuel, conductive media (electrolyte), a gas diffusion layer as electron conduction pathway, a cationic exchange membrane as a proton conduction pathway, and a catalyst as an active electroactive site. However, bubbles formation and low conductivity restrictions for μ-*g* applications need to be solved to assure high efficiency of the reactor. If we have in consideration the strategies used in electrochemical reactors to improve the mass transport rate—forced electrolyte flow with external pumps, a mechanical movement of the electrode within the cell, or a use of three-dimensional electrodes like porous carbon cloths—they can facilitate or help with the bubbles issues by increasing the bubble-flux and producing small bubble sizes. In addition, to solve the low conductivity of the water resource onboard the ISS, FTI proposed the use of the De Nora low conductivity water stream U.S. patent number 6,254,762, filling the gap between anode and cathode with beads of a proton-exchange-based material. More details are discussed in section 1.2.3.

1.1.2 Electrochemistry under microgravity (μ-g) environments

Now, having understood how we can control bubbles and low conductivity stream on Earth, we need to considerate how μ-g influences electrochemical energy conversion phenomena that involves gases and bubbles.[58] Bubbles represent a huge obstacle for electrochemical reactions under reduced gravity due to current density decreases with the formation of bubbles in μ-g.[59] Several experiments have studied bubbles behavior under μ-g environments. Ammonia oxidation currents, on platinum-base catalysts, decreases to 63% under μ-g in comparison to experiments at *1-g*.[58, 60-62] The detachment of N_2 from the platinum nanoparticles at microgravity conditions may be occurring between 5 to 10 seconds, whereas on ground bubbles detach in about 2 seconds.[63-65] Thermo-mechanically, the migration of a bubble under microgravity can be generated by a thermal gradient on the system.[66] Geometry and dimensions affect bubbles interaction with the surface of the electrode, the higher the active geometrical area, the strongest anchoring of the bubble to the surface, making detachment more difficult.[67]

Evaluating the mass transfer phenomena[68] in a μ-g environment, convection disappears when buoyant force is cero and migration turns inappreciable by using an inert electrolyte, leaving diffusion to govern the movement of redox molecules away from the electrode surface. In summary, microgravity is a buoyancy free environment that promotes motionless in the components within a liquid. Surface tension is the driving force for the bubble detachment in the absence of gravity,[69] but at higher electrical fields better detachment of the bubbles can be obtained.[70]

1.1.3 The μ-g systems

Several systems allow the development of experiments under microgravity conditions. Table 1.1 shows a comparative approach of some platforms. Satellites offer high accuracy in results due to a constant level of microgravity for long periods of time

(years), although satellite missions are highly expensive, require complicate logistics, and experiments cannot return to earth. ISS and Foton capsule offer reduced disturbances in the microgravity conditions during several days of microgravity, however experiments must be miniaturized and confined to reduced volume and missions have human spaceflight restrictions. Sounding rockets offer intermediate costs and minutes of microgravity, but human restrictions and motor vibrations can affect the experiments. Drop towers offer high repeatability, but short loops of microgravity and volume and mass of experiments allowed are small. Even though parabolic flights also have short periods of microgravity (~20 s), allow high mass and volume to design the experiments, and the most important, offer a laboratory-like environment.[71] Based on the exposed above and on our experience developing experiments in parabolic flights, we decide to use the parabolic flights as the system to reproduce microgravity environments.

Table 1.1. Comparison of different microgravity systems. [71]

System	t	a_{res} (g_o)	m_{max} (kg)	V_{max} (m^3)	a_{max} (g_o)	Observation
Satellite	5-10 years	$\leq 10^{-7}$	>> 1000	180	10	High costs
ISS	30 d	$\leq 10^{-6}$	704	1.2	10	Human spaceflight restrictions
Foton capsule	12-18 d	$\leq 10^{-5}$	650	1.6	10	High costs
Sounding rocket	750 s	$\leq 10^{-5}$	800	4.9	13	Intermediate costs
Drop tower	9.3 s	$\approx 10^{-6}$	161.5	1.54	18	High repeatability
Parabollic flights	20 s	$\leq 10^{-3}$	>> 1000	>> 250	2.5	Laboratory-like environment

1.2 The Cabrera's Lab – NASA – FTI collaborative work

Here, we present a descriptive work developed during my internships in collaboration with the research team at FTI. We needed to design and select appropriate parts for the *eml-II* to optimize performance in terms of peroxide production efficiency, operating current density, and stability. After several online meetings with FTI, working from Cabrera's Lab and traveling to FTI, we developed the following contributions to the final configuration of the *eml-II* system. To protect the confidentiality of the project, just part of the results that has been published are presented in this Chapter.

1.2.1 The Electrochemical Microgravity Laboratory II (*eml-II*) Setup – A descriptive approach

We sent our electrochemical microgravity laboratory (*eml*) to Faraday Technology Inc, in Dayton Ohio, and I was traveling for about three years to redesign and reassemble the double contained Makrolon™ box previously developed in Cabrera's Lab following the NASA guidelines for parabolic flights.[60-62] The NASA approved Electrochemical Microgravity Laboratory (*eml*) was disassembled, cleaned, and redesigned internally to adapt it to the new configuration for H_2O_2 sensing in microgravity conditions, see in Figure 1.1.

Figure 1.1. First containment configuration of the NASA approved Electrochemical Microgravity Laboratory (*eml*): disassembled, cleaned and redesigned to adapt the new configuration for *in-situ* H_2O_2 production.

A custom-made triple containment configuration was modified for the *μ-g* experiment. The first containment barrier for the liquid is shaped by the reactor and water lines, see Appendix 1.1. All the devices were in three different safety second containments with dimensions of 14" x 10" x 9" made of polycarbonate as is shown in Figure 1.1. These three second containments were framed in a third polycarbonate containment of 47" x 14" x 12". All boxes were bolted to an aluminum base plate with dimensions of 50" x 22" x ½" that will be bolted to the aircraft through AN-6 Steel Bolts (3/8" diam.).

Aluminum and stainless-steel supports, rails and braces were designed, cut, and ended to belt each device and artefact, like pumps, oxygen gas cylinder, RO water reservoir, fuel cell, UV detector, etc. Subsequently, these were assembled over aluminum blocks as can be observed in Figure 1.2.

Figure 1.2. Designed, cut, and ended aluminum and stainless-steel supports, rails, and braces to belt devices and artefacts within the eml-II.

Each device and artefact, assembled over aluminum blocks, were mounted inside devices were in three different safety second containments with dimensions of 14″ x 10″ x 9″ made of polycarbonate as shown as can be observed below, see Figure 1.3.

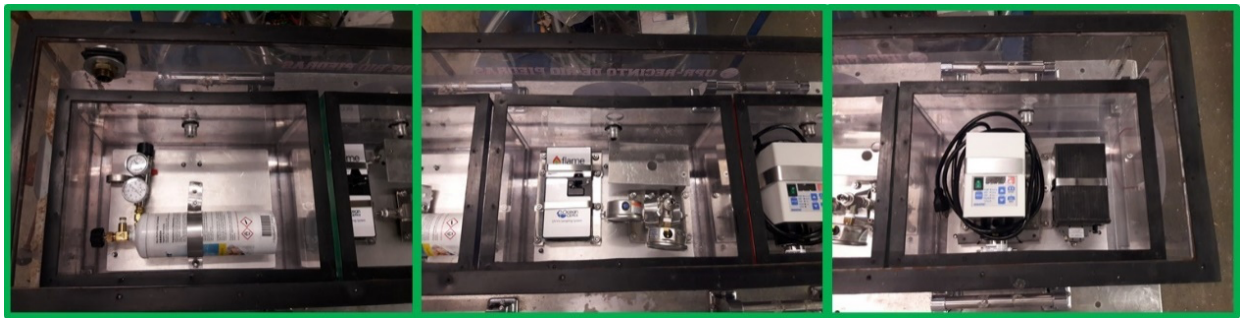

Figure 1.3. Devices without electrical connections inside of three different safety second containments with dimensions of 14″ x 10″ x 9″ made of polycarbonate.

The three second containments were mounted inside the third polycarbonate containment. All boxes were fastened to an aluminum base plate. The main base was disposed with six AN-6 Steel Bolts and 3/8″ of diameter to bolt it to the aircraft through, see Figure 1.4.

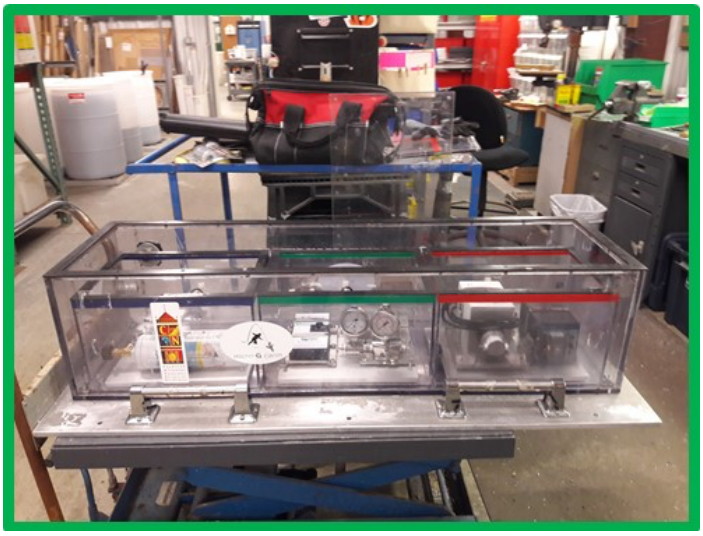

Figure 1.4. Final configuration without electrical connections of the new Electrochemical Microgravity Laboratory II (*eml-II*).

As shows Figure 4, after incorporating the peroxide generation system within the *eml-II*, pressure regulator and oxygen cylinder were placed in the containment on the left, the central containment hold the PGU, UV-Vis, and back pressure system, and the pumps were placed in the containment on the left.

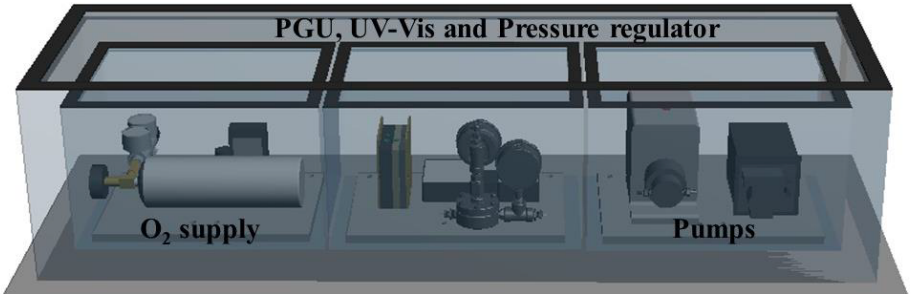

Figure 1.5. Schematic representation of the *eml-II* final configuration without electrical connections.[72]

Internal electrical installations and oxygen and water connections were developed inside the *eml-II* as shown in figure 1.6. Diagram of electrical load and components arrangement is shown in figure 1.7.

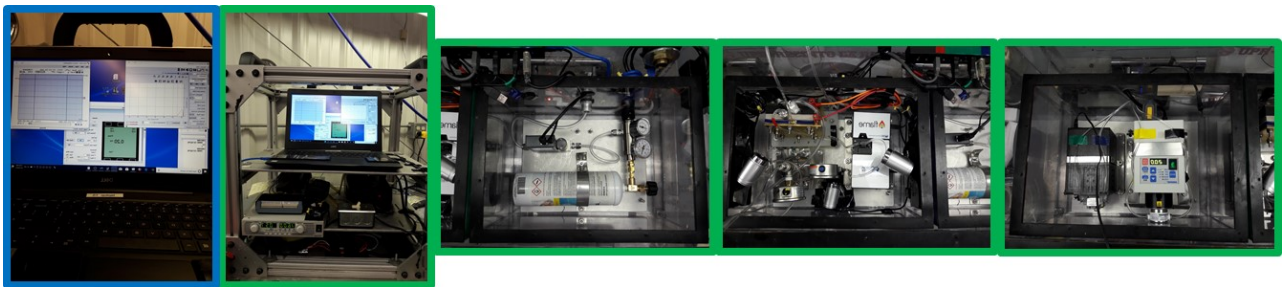

Figure 1.6. Final configuration of the *eml-II* with electrical connections and control software.

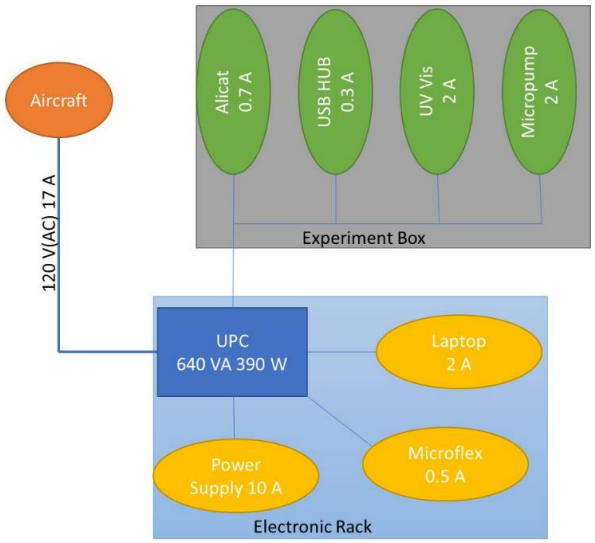

Figure 1.7. Diagram of electrical load and components arrangement of the *eml-II* (Standard Safety and Operating Procedures at FTI).

1.2.2 The reactor parts – A brief description

The gas diffusion electrode (GDE): After an exhaustive evaluation of several carbon cloth gas diffusion electrodes (GDEs) with microporous layer (MPL)—and based on its best performance within the PGU in terms of wettability, GDL/MPL structure, and catalytic activity for hydrogen peroxide production—the CeTech carbon cloth GDE MPL was selected as our GDE to stablish the base-line of our experiments.[13] Furthermore, we developed and evaluated a range of catalysts that will be presented in next Chapters.

Proton conductive beads: After testing ionic conduction pathways, ion exchange capacity, and packing densities of several acidic cation exchange resins,[13] AmberLite™ IR120 H, with an ion exchange capacity of 1.8 meq/mL by wetted bed volume, was

selected as our solid electrolyte to facilitate electrolyte ionic conductivity in low conductivity water feed streams.

Back-pressure regulator: The back pressure on the catholyte was balanced using the Equilibar LF Series Precision Back Pressure Regulator N^0 LF2SNN12-NSMP10T100F5VVB. This regulator equilibrates pressure with the same source of oxygen used for the ORR, avoiding that the RO water diffuses—across the hydrophobic GDE—from the cathode chamber into the oxygen compartment.

The micropumps: Geared micropumps were selected—among other tested pumps––and used to control the flow in the catholyte chamber and in the anode. This kind of micropumps prevent oscillator pressure waves in the catholyte chamber, and therefore facilitates the back pressure balancing across the GDE, reducing formation of bubbles inside the catholyte chamber.

The Anode: A mixed metal oxide (MMO) coated Ti mesh, assembled to a Ti based plate, was used as anode to reduce weight and improved electrical performance. Based on a collaboration with DeNora, the MMO anode titanium plate was designed, machined, and assembled to the titanium plate. Previously, graphite and stainless steel 316 (SS316) blocks were tested as anode, however, high cell overpotential produce damages in the flow field area of the blocks.

Polymer-electrolyte membrane (PEM): NAFION 117 was used as PEM and was assembled to the MMO anode as shown in Figure 1.8. Initial trials were done using NAFION 115, NAFION117, Sustainion™, and Selemion™, coated with 3 mg/cm^2 of $IrRuO_x$, however, these coated membranes presented insufficient support, folding, and losing electrical contact with other components during operation.

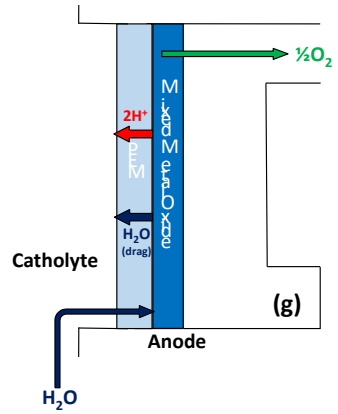

Figure 1.8. Polymer-electrolyte membrane (PEM) and mixed metal oxide (MMO) anode configuration in the PGU.[13]

The detector: The Faraday Technology Inc UV absorption-based in-line detector (FTI-UV) was used for a continuous determination of the hydrogen peroxide that is formed in the reactor. The H_2O_2 quantification was done applying the Beer-Lambert Law, see equation 1.1,

$$A = \log(I_o/I) = \varepsilon bc, \qquad \text{Equation 1.1}$$

where: A is absorbance, I_o is the initial light intensity, I is the light intensity, ε is the molar extinction coefficient of H_2O_2 which is 43.6/M.cm at 240 nm,[73, 74] b the path length of 0.01 cm, and c is the molar concentration. A transportable FLAME-CHEM UV-Vis Spectrometer Systems from Ocean Optics Inc. was assembled to the PGU. Quartz cuvettes from Starna Cells, see Figure 1.9, were used to reduce the pressure changes in the catholyte chamber.

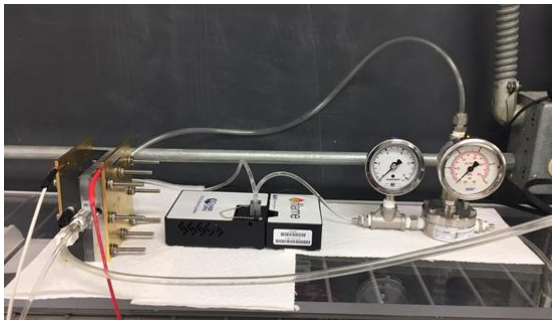

Figure 1.9. UV-Vis spectrometer and back pressure regulator assembled to the PGU.[13]

A calibration curve—set measuring absorption at 240 nm of H_2O_2 standards, prepared with commercial 3% w/w hydrogen peroxide—was used to determinate the *in-situ* H_2O_2 formation. Concentration profile is shown in Figure 1.10.

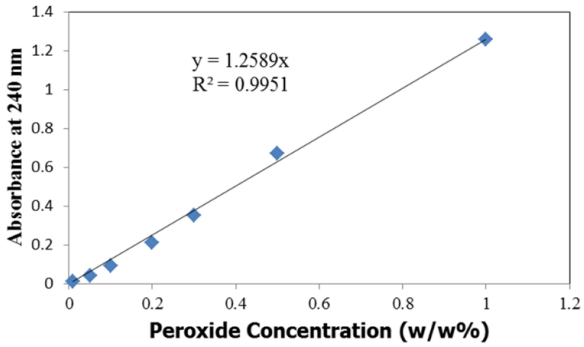

Figure 1.10. Calibration curve of hydrogen peroxide based on UV absorption spectra, with molar extinction coefficient of H_2O_2 which is 43.6/M.cm at 240 nm.[13]

The oxygen source: A 14L oxygen cylinder and a digital Alicat pressure regulator were used as source of oxygen and as gas regulator, respectively.

The recording process: We install tree webcams in the *eml-II* central compartment to follow the performance of the experiment and the stability of the setup.

The control center: an external rack with all the electronics components was used to remotely control all the devices inside the *eml-II*. A power supply, controlled by computer software and external shutdown signals from a programmable logic controller, was used to manage the PGU, micropumps, oxygen pressure, video cams, and the UV detector during the *eml-II* operation under 1-g and μ-g environments.

The catholyte chamber: A polyether ether ketone (PEEK) block was used as the container for the catholyte chamber due to its durability and less brittleness. The catholyte chamber—a constant 2.5 cm x 2.5 cm working area and controlled electrode to PEM gap of ⅜" with total volume of 4.7 mL. Other chambers with different sizes were built and tested with acrylic, plexiglass, polycarbonate; however, all these materials shown brittleness and lack of flatness, cracking and leaking the catholyte. This final configuration requires 42.3 mL/min as flowrate to achieve 3 catholyte volume turnovers

in a twenty-seconds-loop at μ-g—used was. Flowrates was determined without AmberLite™ IR120 H. The beads were retained within the catholyte chamber settling the chamber with a 500 μm filter cloth as shows Figure 1.11.[13]

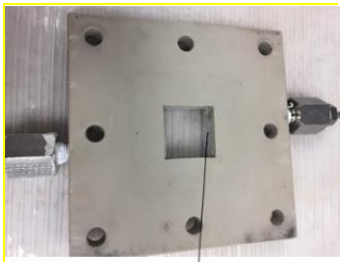

Figure 1.11. Catholyte chamber with < 500 μm filter cloth for AmberLite™ IR120 H beads retention.[13]

1.2.3 The Prototype Generation Unit (PGU) – The Fundamentals

To implement the requirements established by NASA—using the ISS water—FTI proposed the use of the U.S. patent number 6,254,762 of De Nora Technology for peroxide generation from low conductivity electrolytes utilizing ion-exchange resin particles, see Appendix 1.2. A schematic representation of the Peroxide Generation Unit (PGU) is shown in Figure 1.12. The PGU involves a cathode-anode configuration which is split by a catholyte chamber, filled with beads of a proton-exchange polymer. In the cathode, back-pressured oxygen goes through a gas diffusion electrode, controlling the rection $O_2 + H_2O + 2e^- \rightarrow HO_2^- + OH^-$. Whereas a mixed metal oxide pressed against the cation electrolyte membrane works as anode, where protons are produce following the reaction $H_2O \rightarrow \frac{1}{2} O_2 + 2H^+ + 2e^-$, with the general reaction $\frac{1}{2} O_2 + H_2O \rightarrow H_2O_2$. The ionomer beads in the catholyte chamber enables the transfer of H^+ crossways the water stream—from anode to cathode.[3, 11, 13, 72]

Briefly, RO water goes in the catholyte chamber, diffusing across the proton exchange membrane (PEM) to the interface between the mixed metal oxide (MMO) catalyst and the PEM at the anode. Once at the anode, water is split to O_2 and H^+ protons by applying a direct electrical potential (DC) to the PGU. Then, protons cross the membrane, moving out from the anode-PEM interface, reaching the GDE at the cathode

through the conductive beads. Protons react with oxygen to form peroxide at the cathode. Finally, catholyte, oxygen, and hydrogen peroxide are transported to the UV-detector and stored in the collector container. The resulting flux of protons is generated by the attraction of protons to the negative charge at the cathode, dragging them by diffusion across the PEM from the anode to the catholyte, and across the conductive beads to the GDL at the cathode.

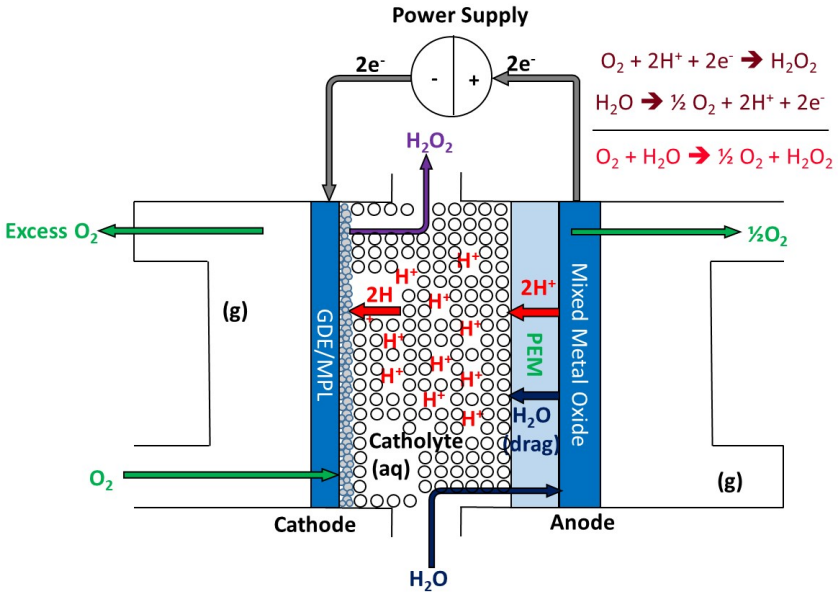

Figure 1.12. Schematic representation of the Peroxide Generation Unit (PGU).[11, 13, 72]

1.2.4 The proposed catholyte chamber designs

I proposed—to the FTI team—two new catholyte chamber designs. The first one, an expanded input-output catholyte chamber (EIOCC), was taught to reduce stationary electrolyte zones, avoid bubbles accumulation inside the chamber, and improve the liquid flow inside the chamber, reducing sudden contractions and expansions in the joints between the chamber and the input and output channels. FTI builds the EIOCC as shows Figure 1.13. In fluid mechanics, joints with sudden changes in diameter are responsible of energy balances with irreversible pressure drops. The increased area of flow in the joints between the chamber and input and output channels at the EIOCC,

improves pressure distribution inside the PGU, and prevents the earlier observed water leaking from the catholyte chamber to the oxygen compartment.

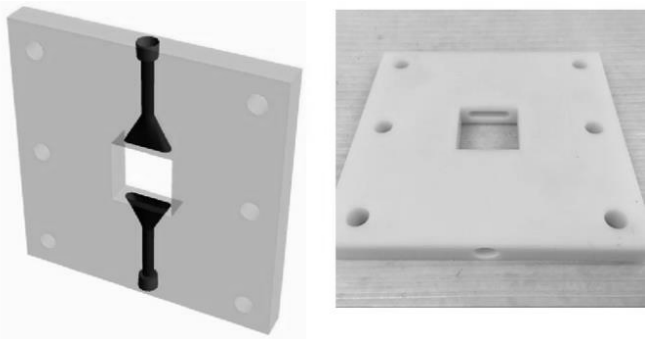

Figure 1.13. Catholyte plate with lofted channels for flow improvement. [72]

FTI used COMSOL to investigate fluid mechanic parameters in the packed bed EIOCC as is shown in Figure 1.14. FTI's model indicates that the entry length must be at least equivalent to the width of the active area to prevent stationary electrolyte zones inside the PGU. Currently, FTI is using the EIOCC for the new *Alpha-Scale-PGU* prototype which will be used for industrial *in-situ* H_2O_2 production in hospital and health centers.[72]

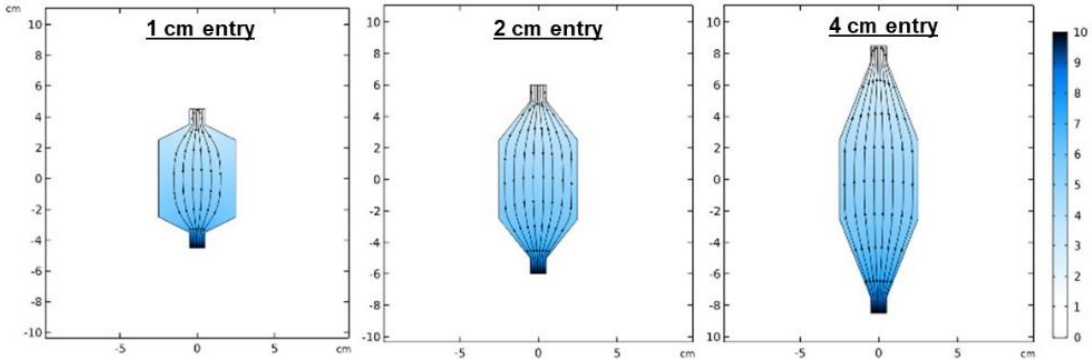

Figure 1.14. COMSOL flow designs developed by FTI to determine target entry path length and slope to improve flow uniformity through reactor working area.

Secondly, I designed and proposed a flow field catholyte chamber (FFCC) to increase the retention time of the RO water, and to reduce the ohmic resistance of the cell. FTI fabricated a CCFF with ⅜" channels, as shows Figure 1.15. This model has been used by FTI in upgrades of the PGU for other for space applications.[75]

Figure 1.15. Catholyte plate with incorporated flow fields for retention time improvement.[75]

1.3 The *1-g* tests

1.3.1 Single-pass configuration

FTI started the polarization and H_2O_2 production tests with RO water and other electrolytes under a continuous flow with a *single-pass* configuration through the PGU, The control parameters studied and controlled under the single-pass configuration—catalysts, GDE MPLs, conductive beads, flow rate, applied potential, cell alignment, DC vs pulse operation, catholyte plate thickness, and flow field—proved that the PGU was highly efficient to produce H_2O_2.[13] We also, characterized new ORR catalysts and results will be described in Chapters 2 and 3. Briefly, as an example, we used the following configuration to characterize the CeTech carbon cloth GDE MPL in a single-pass configuration, see Appendix 1.3. The optimized single-pass parameters were used to test the PGU under a recycled continuous flow as explained in next section.

1.3.2 Multi-pass configuration

Our principal aim in this Chapter was to prepare the Electrochemical Microgravity Laboratory II (*eml-II*), shown in Figure 1.6, for the parabolic flights. For this, we assembled, tested the final *eml-II* conformation, and determined the optimal operation conditions under a continuous flow with a *multi-pass* configuration—recirculating the electrolyte into the PGU until reach the H_2O_2 concentration needed.

We evaluated reversibility of polarization parameters inside the *eml-II*, going back and forward on applied potential and the anode flow, see Figure 1.16. AmberLite™ IR120 H was utilized as the ion exchange electrolyte, CeTech carbon cloth GDE MPL was used as gas diffusion layer (GDE), a total of 100 ml was recirculated at 10 ml/min through catholyte chamber, and pressure was balanced at 0.2 psi. Figure 1.16 confirm the reversibility of the *eml-II*, after switching the anode water circulation ratio between 0 and 3 ml/min, and potentials between 2 to 8 volts. These experiments showed that we can modify potential and anode flow rate in the anode, keeping reversibility in output current within the *eml-II*.

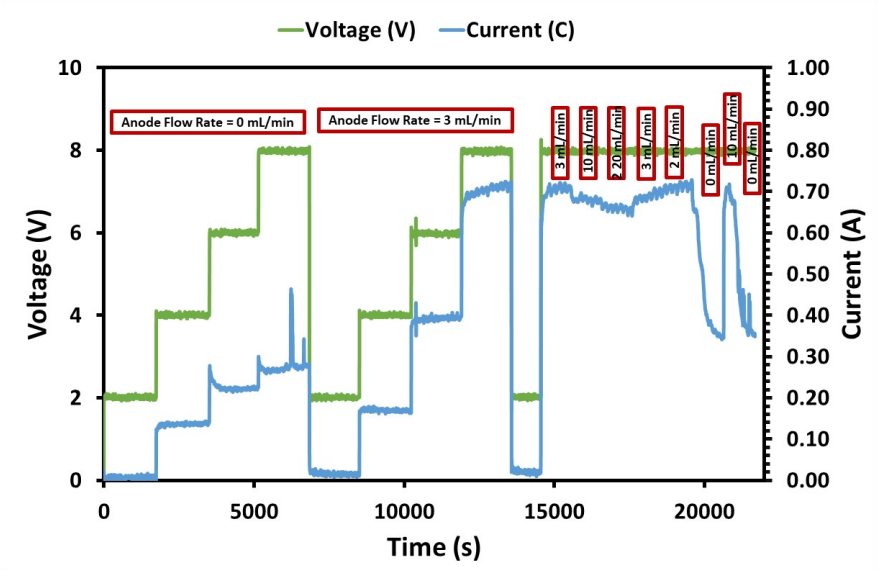

Figure 1.16. Reversibility of polarization parameters inside the *eml-II*, going back and forward on applied potential and the anode flow. AmberLite™ IR120 H was utilized as the ion exchange electrolyte, CeTech carbon cloth GDE MPL was used as gas diffusion layer (GDE), a total of 100 ml was recirculated at 10 ml/min through catholyte chamber, and pressure was balanced at 0.2 psi.

RO Water flow rate inside the whole assembled system was extremely variable in the beginning of the filling procedure. Oscillations in the oxygen balance pressure produced high resistance to water movement through the system, slowing down the RO water filling process. In this sense, and due to an input pressure of 1 psi prevent the complete filling of tubing and connections with RO water, we progressively increased

the balance pressure from 0.05 to 0.1 to 0.2 psi to avoid excess of oxygen at the cathode line. All these pressure changes determined that running 10mL/min of RO Water during 3 min were enough for a complete fill of the tubes, catholyte chamber, UV-visible cell, and back pressure system. Similarly, using a RO flow ratio of 30mL/min, 2 min were required for a complete filling of internal compartments. After controlling the flow and balance pressure, additional PGUs were assembled to test leaks, bubbles absence at the cathode water line, and stability at balance pressure higher than 0.2 psi.

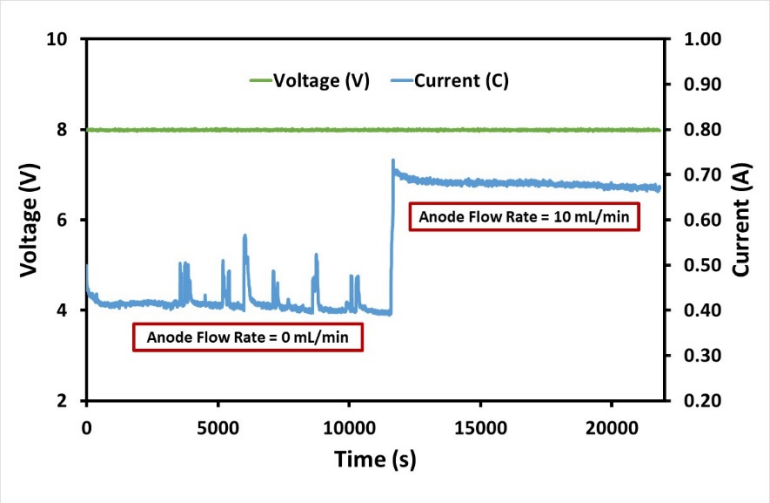

Figure 1.17. Stability of the *eml-II* under a multi-pass configuration, controlling the anode water circulation ratio at 0 (left) and 10 (right) ml/min. AmberLite™ IR120 H was utilized as the ion exchange electrolyte, CeTech carbon cloth GDE MPL was used as gas diffusion layer (GDE), a total of 100 ml was recirculated at 10 ml/min through catholyte chamber, and pressure was balanced at 0.2 psi.

Similarly, we evaluated how the anode water flow influences current, pressure and bubbles formation at 8 V. After 11500 s without water at the anode (0 mL/min), flow rate was increased to 10 mL/min. Figure 1.17 shows that the PGU produces 0.48 A at 0 mL/min, noticing absence of bubbles at the RO water cathode line. Passing RO water through the anode at 10 ml/min, we observed an instantaneous increment in current to 0.67 A. Also, gas bubbles were sporadically produced at the cathode line, possibly due to the increment of the water splitting ratio, forming more oxygen. Figure 1.18 shows, after running RO in the anode at a flow rate of 10 ml/min, a slight variation in the slope of

hydrogen peroxide concentration as a function of time. After 6 hours running this multi-pass test, we achieved 0.47 w/w% of hydrogen peroxide.

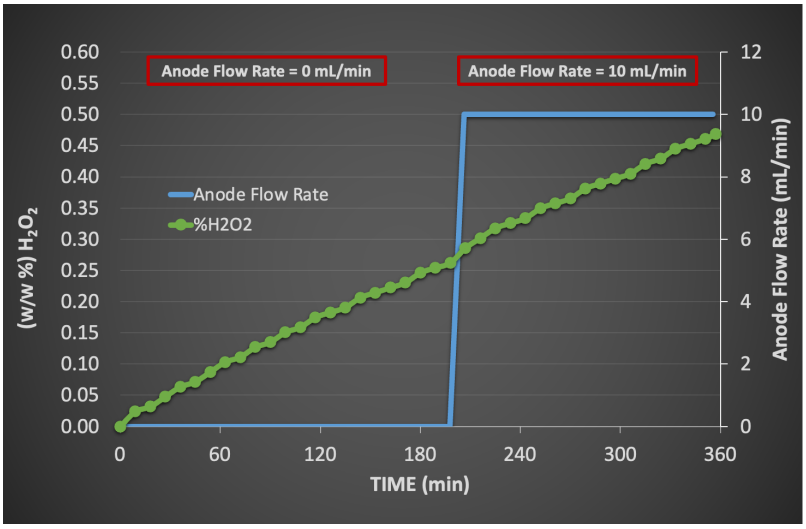

Figure 1.18. Hydrogen peroxide production in the *eml-II* under a multi-pass configuration, controlling the anode water circulation ratio at 0 (left) and 10 (right) ml/min. AmberLite™ IR120 H was utilized as the ion exchange electrolyte, CeTech carbon cloth GDE MPL was used as gas diffusion layer (GDE), a total of 100 ml was recirculated at 10 ml/min through catholyte chamber, and pressure was balanced at 0.2 psi.

We evaluated the peroxide generation performance under more extreme conditions within the *eml-II*, increasing the time of polarization treatments and the voltage to 16 V. AmberLite™ IR120 H was utilized as the ion exchange electrolyte, CeTech carbon cloth GDE MPL was used as gas diffusion layer (GDE), a total of 100 ml was recirculated at 20 ml/min through catholyte chamber, and pressure was balanced at 0.2 psi. Figures 1.19a) and 1.19b) confirm the stability of the PGU controlling the anode water circulation ratio at 5 and 10 ml/min, respectively.

Figure 1.20 shows a comparison of H_2O_2 production with anode water circulation flow rates at 5 and 10 mL/min at 16 V. After 100 min of operation, RO water flowing through the anode at 5 and 10mL/min allowed 0.10 w/w% of hydrogen peroxide. After this time, a slight increment in the of H_2O_2 production was achieved at 5 ml/min. However, at 10 ml/min production of hydrogen peroxide was more stable, reaching a pseudo-plateau after 300 min. The increased and unstable production of peroxide at 5

ml/min can be due to slower the flow higher the H^+ transfer ratio from the anode to the membrane. The rate of production of H^+ is higher than the rate of reposition of molecules of water close to the other side of the membrane, therefore in some point membrane is deficient on numbers of molecules of water needed to produce H^+. This is solved increasing the flow rate to 10 ml/min which equilibrate or reposed faster the molecules of water consumed in the anode.

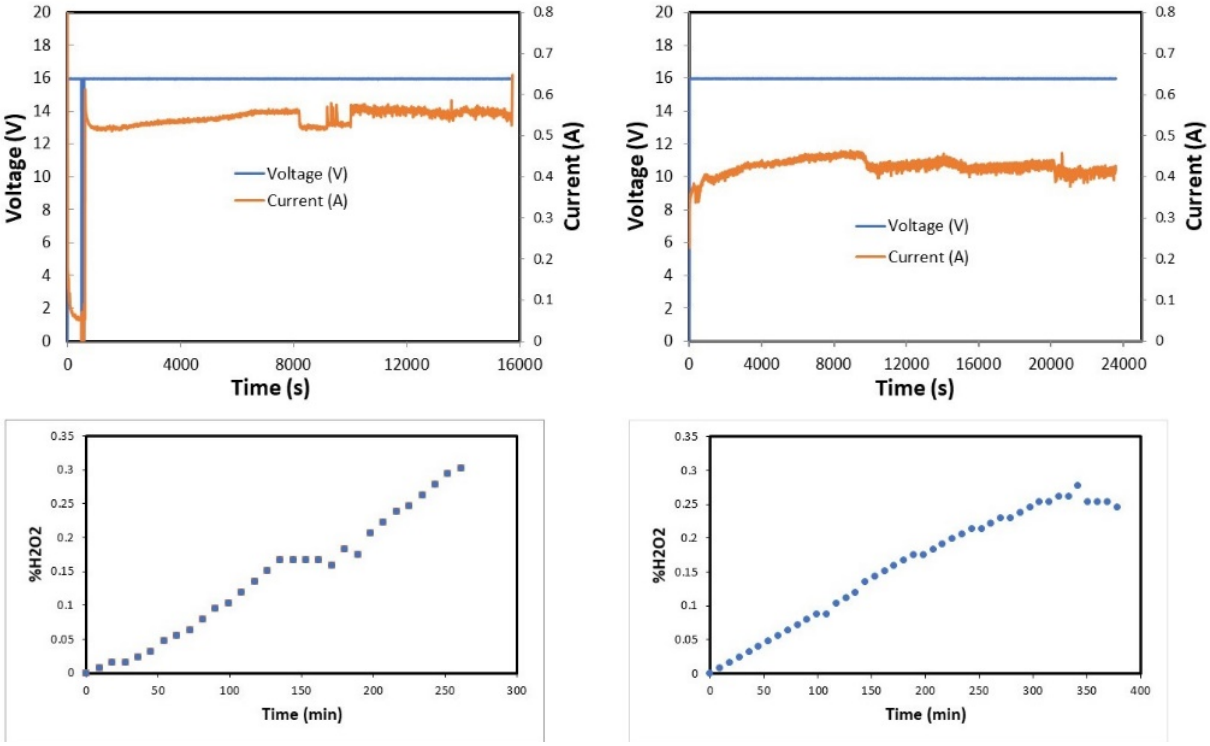

Figure 1.19. Stability of the eml-II under a multi-pass configuration, controlling the anode water circulation ratio at 5 (left) and 10 (right) ml/min. AmberLiteTM IR120 H was utilized as the ion exchange electrolyte, CeTech carbon cloth GDE MPL was used as gas diffusion layer (GDE), a total of 100 ml was recirculated at 20 ml/min through catholyte chamber, and pressure was balanced at 0.2 psi.

A comparison of variables evaluated in the last three tests are reported in Table 1.2. These variables were studied as part of a preliminary performance-function evaluation of our *eml-II*. Multi-pass constant polarization trials shown successful operation of internal electrical installations, and oxygen and water connections. These results represent a starting point to set our system in such a way that reproducible and repeatable data can generated.

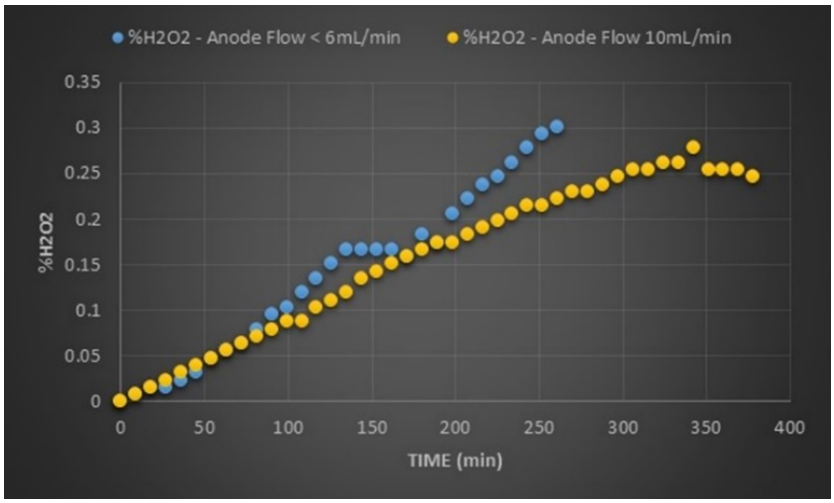

Figure 1.20. Comparison of H_2O_2 production with anode water circulation flow rates at 5 and 10 mL/min. AmberLite™ IR120 H was utilized as the ion exchange electrolyte, CeTech carbon cloth GDE MPL was used as gas diffusion layer (GDE), a total of 100 ml was recirculated at 20 ml/min through catholyte chamber, and pressure was balanced at 0.2 psi.

Table 1.2. Comparison of variables evaluated in at 8 and 16 V.

Test	Voltage (V)	Cathode Flow Rate (mL/min)	Anode Flow Rate (mL/min)	Current (A)	Total Time (min)	%H_2O_2
1	8	10	0	0.48	~ 198	0.26
		10	10	0.67	~ 357	0.47
2	16	20	5	0.55	~ 260	0.30
3	16	20	10	0.42	~ 380	0.25

It is necessary to denote, once system was fully filled, water flow and gas pressure were stabilized. A parallel measurement of cathodic RO Water flow rate was made using a graduate cylinder and chronometer to evaluate that the flow rate value on the top of pump was accurate: 10mL/min.

Due to water was observed in the oxygen compartment, we increase the balance pressure to maintain a catholyte flow in the chamber that allows us to produce enough peroxide concentration in a fully enclosed system without any water reservoir during the flight test. We reduced the RO water volume connecting, in closed-loop configuration, a long tube that worked as reservoir. The total volume of RO water in the closed loop system, needed to concentrate an adequate quantity of H_2O_2, was 50 mL. After testing different combination of RO water flow rates and balance pressures, the optimal

conditions founded—to allow the RO water filling process without water flooding in the oxygen compartment—were 15 mL/min and 1psi, respectively. The anode flow was kept at 10 mL/min, see Figure 1.21.

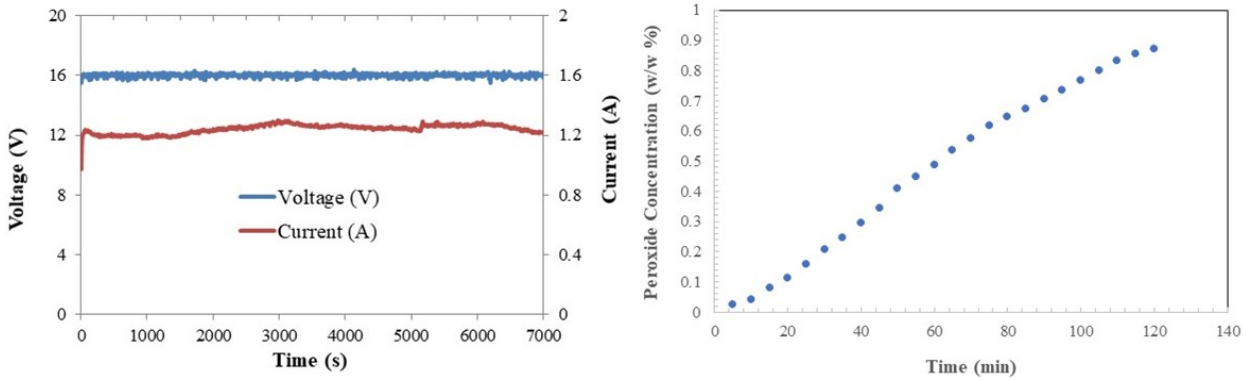

Figure 1.21. Performance of the *eml-II* under a multi-pass configuration, controlling the anode water circulation ratio at 10 mL/min. AmberLite™ IR120 H was utilized as the ion exchange electrolyte, CeTech carbon cloth GDE MPL was used as gas diffusion layer (GDE), a total of 50 ml was recirculated at 15 ml/min through catholyte chamber, and pressure was balanced at 1 psi. This configuration produced 1 w/w% H2O2 was after 2 hours of experiment.

After running several experiments under a multi-pass configuration setup in the *eml-II*, we were able to identify the following operation parameters: balance pressure progressively increases at 16V hence we need a lower operation potential, a catholyte flow rate of 20mL/min will generate measurable peroxide concentration during the 3h zero-gravity flight test, and a total RO water volume of 35 mL will promote a faster accumulation of peroxide. For a catholyte volume of 35 mL flowing at 20 mL/min we have 2.5 passes per 17 sec zero-g, every two minutes a full volume pass, and the system has a volume of 10 mL between the PGU exit and UV-Visible cell, needing 30 seconds to go through the whole channel. We expect a current of 0.2 A which needs an applied voltage between 12 to 14 V. In this sense, we evaluated performance of the *eml-II* under a multi-pass configuration at 12 V, recirculating a total volume of 35 ml, at 20 ml/min through catholyte chamber, balancing pressure at 1 psi, and controlling the anode water circulation ratio at 0 and 10 mL/min, see Figure 1.22. This arrangement, producing 0.33

w/w% H_2O_2 after 1 hour of operation, was established as the optimal setup configuration to be used under *μ-g* conditions.

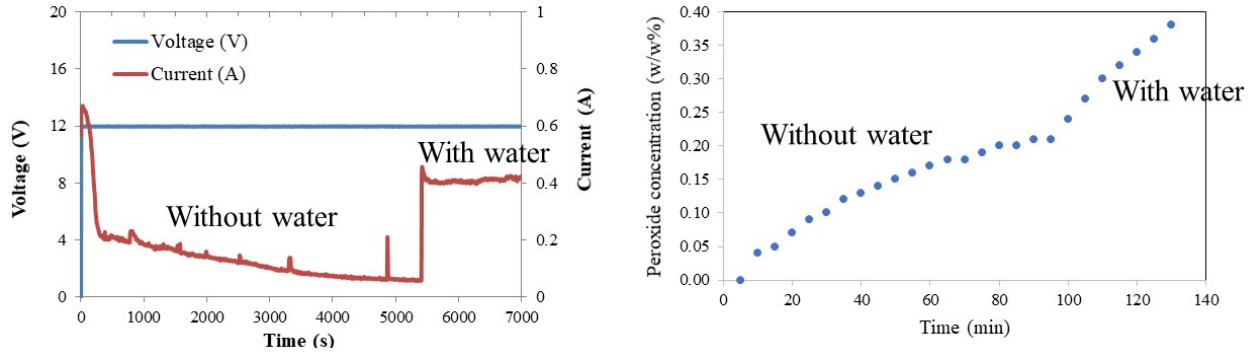

Figure 1.22. Performance of the *eml-II* under a multi-pass configuration, controlling the anode water circulation ratio at 0 and 10 mL/min. AmberLite™ IR120 H was utilized as the ion exchange electrolyte, CeTech carbon cloth GDE MPL was used as gas diffusion layer (GDE), a total of 35 ml was recirculated at 20 ml/min through catholyte chamber, and pressure was balanced at 1 psi. This configuration produced 0.33 w/w% H_2O_2 was after 2 hours of experiment.

1.4 The *μ-g* tests

The compulsory protocols and documentation to address safety conditions in the parabolic flight were completed, submitted, and approved by Zero-G Corporation and the Federal Aviation Administration (FAA), which certify the *eml-II* for the parabolic flight. It is necessary to emphasize that the parabolic flight was delayed during several months due to aircraft repair procedures, FAA approvals, and storms in the Caribbean and Florida areas.

1.4.1 The parabolic flight

The parabolic flights were developed in Sanford, Florida. We received the parabolic flight trainings in the facilities of Zero-G Corporation. The aerobatic maneuvers know as parabolas, see Figure 1.23, were carried out aboard a modified Boeing 727, the G-Force One. Before starting a parabola, specially trained pilots controlled the G-Force One in parallel to the horizon level at an altitude of 24,000 feet, pulling up to gradually increase the angle of the aircraft to 45° to the horizon, and reaching an altitude of 32,000

feet. During this pull-up, the system experienced a hypergravity of about *2-g*. Then, pilots pushed over the G-Force One, promoting the microgravity segment of the parabola, flying a larger arc over the top of the parabola, during approximately 20 seconds, keeping everything weightless inside the airplane. Finally, a pull-out is retaken, re-experiencing *2-g* hypergravity, and allowing a progressive recovery of *1-g*. Parabolas were repeated 35 times—reproducing 2 parabolas with lunar gravity (one sixth your weight), and 3 parabolas with Martian gravity (one third your weight), and 30 parabolas with *μ-g* –each taking about ten miles of airspace to be done.[76-79]

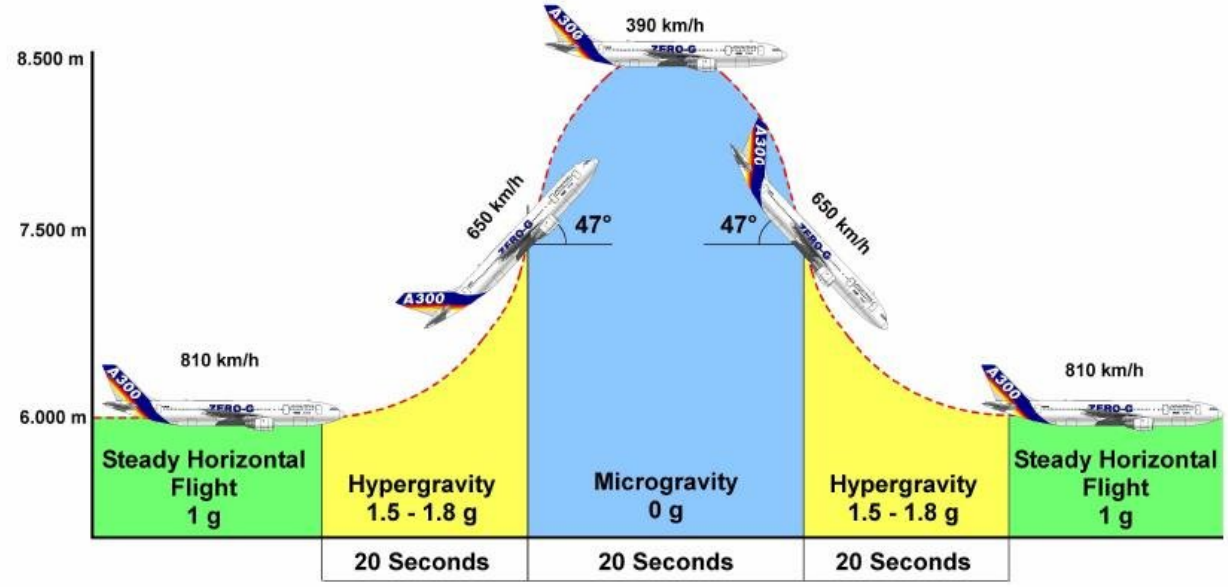

Figure 1.23. Schematic maneuver of the parabolic flight.[76, 77]

1.4.2 The *μ-g* results

Optimized conditions from ground-based performance data, reported in section 1.3.2, were implemented during the parabolic flight test to evaluate the production of H_2O_2 in a *μ-g* environment. Figure 1.24 shows the accelerometer data acquired during parabolic flight test: 2 Martian, 3 Lunar and 25 zero-gravity parabolas, each having a mean of 20 s under *μ-g*.[72]

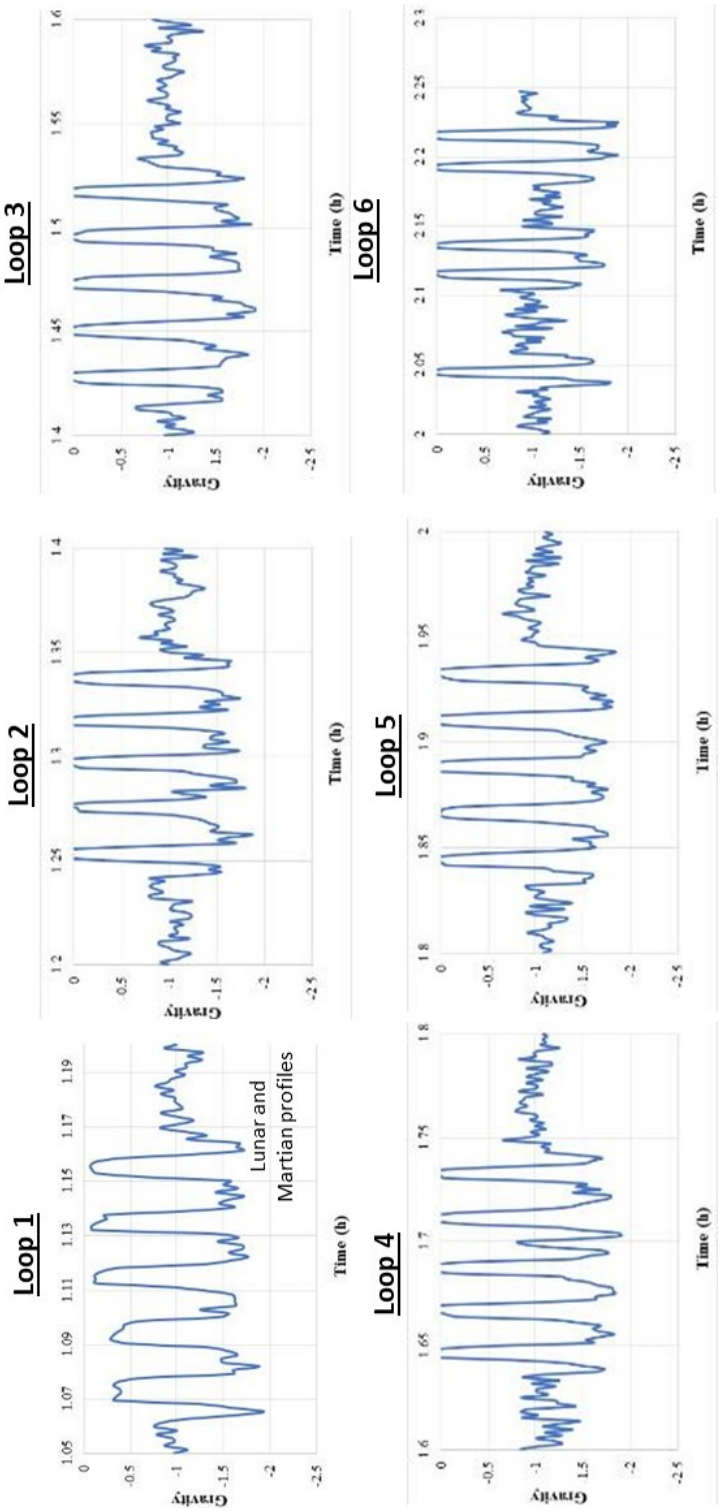

Figure 1.24. The parabolic flight accelerometer data, showing Martian and Lunar profiles in loop 1 and μ-g profiles in loops 2 through 6.[72]

In-situ peroxide experiment in the parabolic flight test was conducted circulating water under a closed-loop configuration in both cathode and anode. Even though optimized conditions, determined in section 1.3.2, were applied during the parabolic flight test, new strategic actions were adapted to obtain significant information during the flight test: pressure buildup was observed (Figure 1.25 and Appendix 1.4) which led us to increase the back pressure to 3 psi; low current was observed at the desired 12 V operation without water in anode, therefore, a higher potential of 16 V was applied during the flight; pressure buildup was observed at 16 V with water circulation in anode, thus, we decreased the potential to 8 V during the *μ-g* test. Finally, the parabolic flight test was achieved with following managing conditions: a multi-pass configuration, AmberLite™ IR120 H as ion exchange beads, 35 mL RO water as electrolyte with a flow rate of 20 mL/min, a catholyte plate thickness of 0.37", a pressure balance of 3 psi, a CeTech W1S 1005 as gas diffusion electrode in the cathode, 3 mL of catholyte volume with beads, 16 V without water in anode and 8 V with water in anode.[72]

After finishing the parabolic tests, the *eml-II* achieved 0.08 w/w % of *in-situ* H_2O_2, demonstrating the viability of generating hydrogen peroxide under *μ-g* conditions. The flight test showed that there are no adverse effects of *μ-g* environments on the performance of *eml-II* system in comparison with terrestrial conditions.[72]

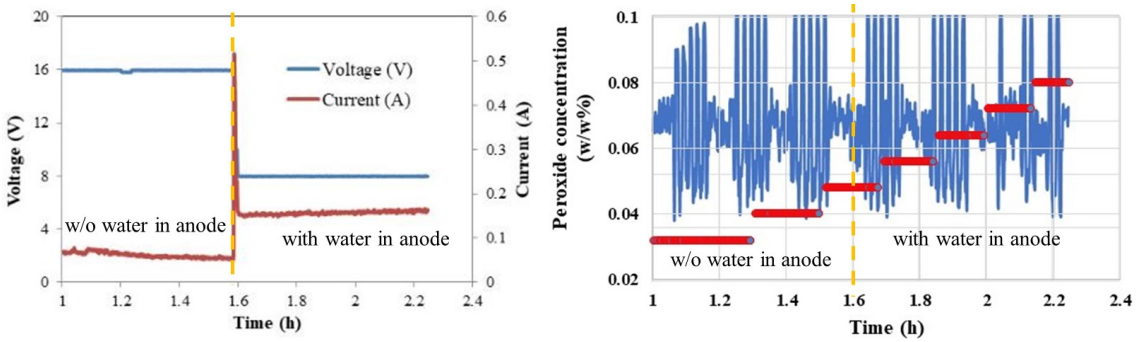

Figure 1.25. The *eml-II* performance function during the parabolic flight. On the left, *μ-g* polarization curves with water and without water in the anode. On the right, peroxide concentration generated (red dots) and accelerometer profile (blue line) as a function of time.[72]

1.5 Conclusions

We were able to disassemble, clean, and redesign the NASA approved Electrochemical Microgravity Laboratory (*eml*) to design, build, and evaluate the new Electrochemical Microgravity Laboratory II (*eml-II*), that was configurated for *in-situ* hydrogen peroxide production under microgravity conditions. The *eml-II* accomplishes the NASA requirements of producing *in-situ* H_2O_2 under the water resource available onboard the ISS—with a conductivity of 2–3 μS/cm, a pH of 5.5–6.7, and a total organic carbon (TOC) content between 0.18 and 2.5 mg/L—using the U.S. patent number 6,254,762, for low conductivity water stream. Also, the nucleation, growth, and detachment of bubble, preventing super bubbles formation, was facilitated controlling the mass transport rate with forced electrolyte flow with external micropumps and using three-dimensional GDLs as electrodes.

The performance-function of the *eml-II* system was tested at *1-g*—under a multi-pass configuration, at 12 V, a CeTech W1S 1005 as gas diffusion electrode, with AmberLite™ IR120 H as ion exchange beads, recirculating a total volume of 35 ml at 20 ml/min through catholyte chamber with thickness of 0.37", balancing pressure at 1 psi, and controlling the anode water circulation ratio at 0 and 10 mL/min—producing 0.33 w/w% H_2O_2 after 2 hours of operation. These experimental conditions were established as the optimal setup configuration to be used under *μ-g* conditions.

The parabolic flight was successfully carried out aboard a modified Boeing 727, the G-Force One from Zero-G Corporation. The *eml-II* at *μ-g* achieved—under a multi-pass configuration, AmberLite™ IR120 H as ion exchange beads, 35 mL RO water as electrolyte with a flow rate of 20 mL/min, a catholyte plate thickness of 0.37", a CeTech W1S 1005 as gas diffusion electrode in the cathode, 3 mL of catholyte volume with beads, a pressure balance of 3 psi, 16 V without water in anode and 8 V with water in anode—0.08 w/w % of *in-situ* H_2O_2, demonstrating the viability of generating hydrogen peroxide under *μ-g* conditions. The flight test showed that there are no adverse effects of *μ-g*

environments on the performance of *eml-II* system in comparison with terrestrial conditions.

The successful performance of the *eml-II* during the parabolic flight evidence that it can be used to produce *in-situ* hydrogen peroxide as life support system in future space missions.

1.6 Acknowledgments

The authors express their gratitude of both NASA Fellowship from NASA Puerto Rico Space Grant Consortium No. NNX15AI11H at the UPR, and the NASA Phase II SBIR Contract NNX16CA43P trough Faraday Technology Inc.

1.7 References

(1) Bentley, C. L.; Kang, M.; Unwin, P. R. Nanoscale Surface Structure–Activity in Electrochemistry and Electrocatalysis. *Journal of the American Chemical Society* **2019**, *141* (6), 2179-2193. DOI: 10.1021/jacs.8b09828.
(2) Albuquerque, I. L. T.; Cavalcanti, E. B.; Vilar, E. O. Mass transfer study of electrochemical processes with gas production. *Chemical Engineering and Processing: Process Intensification* **2009**, *48* (9), 1432-1436. DOI: https://doi.org/10.1016/j.cep.2009.08.006.
(3) Khosla, N. K.; Venkatachalam, S.; Somasundaran, P. Pulsed electrogeneration of bubbles for electroflotation. *Journal of Applied Electrochemistry* **1991**, *21* (11), 986-990. DOI: 10.1007/BF01077584.
(4) Peña-Duarte, A.; Vijapur, S. H.; Hall, T. D.; Hayes, K. L.; Larios-Rodríguez, E.; Pilar-Albaladejo, J. D.; Santiago, M. E. B.; Snyder, S.; Taylor, J.; Cabrera, C. R. Iron Quantum Dots Electro-Assembling on Vulcan XC-72R: Hydrogen Peroxide Generation for Space Applications. *ACS Applied Materials & Interfaces* **2021**. DOI: 10.1021/acsami.1c05649.
(5) Brinkert, K.; Mandin, P. Fundamentals and future applications of electrochemical energy conversion in space. *npj Microgravity* **2022**, *8* (1), 52. DOI: 10.1038/s41526-022-00242-3.
(6) Kaneko, H.; Tanaka, K.; Iwasaki, A.; Abe, Y.; Negishi, A.; Kamimoto, M. Water electrolysis under microgravity condition by parabolic flight. *Electrochimica Acta* **1993**, *38* (5), 729-733. DOI: https://doi.org/10.1016/0013-4686(93)80245-U.
(7) Acevedo, R.; Poventud-Estrada, C. M.; Morales-Navas, C.; Martínez-Rodríguez, R. A.; Ortiz-Quiles, E.; Vidal-Iglesias, F. J.; Sollá-Gullón, J.; Nicolau, E.; Feliu, J. M.; Echegoyen, L.; et al. Chronoamperometric Study of Ammonia Oxidation in a Direct Ammonia Alkaline Fuel Cell under the Influence of Microgravity. *Microgravity Science and Technology* **2017**, *29* (4), 253-261. DOI: 10.1007/s12217-017-9543-z.
(8) Poventud-Estrada, C. M.; Acevedo, R.; Morales, C.; Betancourt, L.; Diaz, D. C.; Rodriguez, M. A.; Larios, E.; José-Yacaman, M.; Nicolau, E.; Flynn, M.; et al. Microgravity Effects on Chronoamperometric Ammonia Oxidation Reaction at Platinum Nanoparticles on Modified Mesoporous Carbon Supports. *Microgravity Science and Technology* **2017**, *29* (5), 381-389. DOI: 10.1007/s12217-017-9558-5.

(9) Nicolau, E.; Poventud-Estrada, C. M.; Arroyo, L.; Fonseca, J.; Flynn, M.; Cabrera, C. R. Microgravity effects on the electrochemical oxidation of ammonia: A parabolic flight experiment. *Electrochimica Acta* **2012**, *75*, 88-93. DOI: https://doi.org/10.1016/j.electacta.2012.04.079.
(10) Yang, X.; Karnbach, F.; Uhlemann, M.; Odenbach, S.; Eckert, K. Dynamics of Single Hydrogen Bubbles at a Platinum Microelectrode. *Langmuir* **2015**, *31* (29), 8184-8193. DOI: 10.1021/acs.langmuir.5b01825.
(11) Chen, Q.; Wiedenroth, H. S.; German, S. R.; White, H. S. Electrochemical Nucleation of Stable N2 Nanobubbles at Pt Nanoelectrodes. *Journal of the American Chemical Society* **2015**, *137* (37), 12064-12069. DOI: 10.1021/jacs.5b07147.
(12) Fernández, D.; Maurer, P.; Martine, M.; Coey, J. M. D.; Möbius, M. E. Bubble Formation at a Gas-Evolving Microelectrode. *Langmuir* **2014**, *30* (43), 13065-13074. DOI: 10.1021/la500234r.
(13) Balasubramaniam, R.; Lacy, C. E.; Woniak, G.; Subramanian, R. S. Thermocapillary migration of bubbles and drops at moderate values of the Marangoni number in reduced gravity. *Physics of Fluids* **1996**, *8* (4), 872-880. DOI: 10.1063/1.868868 (acccessed 5/23/2023).
(14) Carrera, J.; Parthasarathy, R. N.; Gollahalli, S. R. Bubble formation from a free-standing tube in microgravity. *Chemical Engineering Science* **2006**, *61* (21), 7007-7018. DOI: https://doi.org/10.1016/j.ces.2006.07.021.
(15) Polcaro, A.; Mascia, M.; Palmas, S.; Vacca, A. Electrochemical Oxidation of Phenolic and Other Organic Compounds at Boron Doped Diamond Electrodes for Wastewater Treatment: Effect Of Mass Transfer. *Annali di chimica* **2004**, *93*, 967-976.
(16) Thompson, R. L.; DeWitt, K. J.; Labus, T. L. MARANGONI BUBBLE MOTION PHENOMENON IN ZERO GRAVITY. *Chemical Engineering Communications* **1980**, *5* (5-6), 299-314. DOI: 10.1080/00986448008935971.
(17) Herman, C.; Iacona, E.; Földes, I. B.; Suner, G.; Milburn, C. Experimental visualization of bubble formation from an orifice in microgravity in the presence of electric fields. *Experiments in Fluids* **2002**, *32* (3), 396-412. DOI: 10.1007/s003480100366.
(18) Grosse, J. Thermal and Mechanical Design and Simulation for the first high precision Quantum Optics Experiment on a Sounding Rocket. 2016.
(19) Vijapur, S. H.; Hall, T. D.; Taylor, E. J.; Wang, D.; Snyder, S.; Skinn, B.; Peña-Duarte, A.; Cabrera, C. R. *In- Situ* Resource Utilization for Electrochemical Generation of Hydrogen Peroxide for Disinfection. . *ICES: International Conference on Environmental Systems* **2021**, 12 pages.
(20) Vijapur, S. H.; Hall, T. D.; Taylor, E.; Wang, D.; Snyder, S.; Skinn, B.; Peña-Duarte, A.; Cabrera, C. R.; Sweterlitsch, J. *In- Situ* Resource Utilization for Electrochemical Generation of Hydrogen Peroxide for Disinfection. *ICES: International Conference on Environmental Systems* **2019**, *38*, 14 pages.
(21) Noble, R. W.; Gibson, Q. H. The Reaction of Ferrous Horseradish Peroxidase with Hydrogen Peroxide. *Journal of Biological Chemistry* **1970**, *245* (9), 2409-2413. DOI: https://doi.org/10.1016/S0021-9258(18)63167-9.
(22) Hsu, C.-C.; Lo, Y.-R.; Lin, Y.-C.; Shi, Y.-C.; Li, P.-L. A Spectrometric Method for Hydrogen Peroxide Concentration Measurement with a Reusable and Cost-Efficient Sensor. In *Sensors*, 2015; Vol. 15, pp 25716.
(23) Nelson, G. J.; Vijapur, S. H.; Hall, T. D.; Brown, B. R.; Peña-Duarte, A.; Cabrera, C. R. Electrochemistry for Space Life Support. *Electrochemical Society Interface* **2020**, *29* (1), 47-52. DOI: 10.1149/2.f06201if.
(24) Vijapur, S. H.; Hall, T. D.; Taylor, E.; More, S. R.; Sweterlitsch, J. J.; Ewert, M. K.; Castro-Wallace, S. L.; Byrne, V.; Dunbar, B. J.; Nguyen, H. N.; et al. In-Situ Electrochemical Generation and Utilization of Hydrogen Peroxide for Disinfection. *ICES: International Conference on Environmental Systems* **2022**, 11.
(25) Pletser, V.; Frischauf, N.; Laufer, R.; Cohen, D. *Parabolic Flights with Gliders as an Innovative Low-Cost Platform for Microgravity and Hypergravity Research*; 2017.
(26) European Space Agency (ESA), Copyright 2005.
(27) *ESA: https://www.esa.int/Education/Fly_Your_Thesis/Parabolic_manoeuvres. (accessed May 22, 2023).*
(28) Glushchuk, A.; Buffone, C.; Chikov, S.; Queeckers, P.; Dubois, F. *Condensation on single finger-like fin under various gravity conditions*; 2013.

CHAPTER 2. Non-Precious Metal Catalysts for In-Situ Hydrogen Peroxide Production

2.1 Introduction

Previously, we have developed the peroxide generation unit (PGU), a technology for *in-situ* H_2O_2 production under terrestrial and zero-gravity environtments.[3, 13] Parabolic flights demonstrated the comparable high performance of our PGU on Earth and under microgravity conditions. Even though, the success of the PGU and projecting a scalable *in-situ* production of H_2O_2 on space missions, the design of novel catalysts is needed. Accordingly, precursors materials for these catalysts have to be accessible, cheap, abundant in terrestrial or extraterrestrial locations, and catalyze the ORR via two-electrons pathway. As precursors materials, we propose carbon and iron compounds which are involved in several physical and chemical processes on earth and space.[80] Besides, the use of carbon and iron-based compounds allows reliable, clean, and affordable energy science-driven technologies required in the US DOE Strategic Plan.[38]

Iron-based materials prevent degradation in fuel cells, contributing to extended lifetimes.[81] Iron oxides have been synthesized via coprecipitation and subsequent thermal treatments,[82] however, the Fe_3O_4 and α-Fe_2O_3 products often have shown particles in bulk sizes and poor electrical conductivity. A good electrical performance is a crucial feature in the electrode-electrolyte interface for fuel cells, batteries, and supercapacitors.[4] Several works have been focused on creating metal oxide on highly conductive nanocarbon composites to improve the redox reactions performance and the electrical characteristics of the catalysts.[83, 84] Thermal syntheses have been used to produce composites of iron and carbon but with low yields for large scale applications.[83] Likewise, nanostructured iron- and carbon-based materials, oriented to energetic applications, have been synthesized via chemical vapor deposition (CVD); however, this method produces

inactivated iron nanoparticles that are covered with carbon nanotubes and aerogels.[85] Besides of materials with good electrical properties, nanosized dimensions are desired to improve the catalytic activity in different chemical systems.[84] Controlling experimental conditions allows the synthesis of nano-dimensional structures with different morphologies such as quantum dots (QDs).[86] A QD is any solid in which all dimensions decrease to a few nanometers.[87]

The challenge to overcome is the bulk production of highly dispersed iron QDs onto powdered carbon substrates (Fe/Vulcan), assuring a continuous electron pathway in the interface iron-carbon. A successful electrochemical method, known as the rotating disk slurry electrodeposition technique (RoDSE),[88] have been largely used for bulk production of catalytic powders, growing metallic nanoparticles onto diverse supports and preventing aggregation.[84, 88, 89] In RoDSE, the working electrode is rotated, generating a constant flux that continuously replaces the concentration of precursors in the diffusion layer, where the electrodeposition has place.[89]

In this Chapter, we present a novel RoDSE electro-assembling—without high temperatures nor hazardous compounds—of iron-based QDs onto Vulcan XC-72R. The physicochemical characterization revealed 4 nm Fe-based QDs, highly dispersed on the surface of Vulcan. The Fe/Vulcan ORR catalysis control was shown by the Koutecky-Levich (K-L) analysis, the rotating ring-disk electrode (RRDE) technique, and *in-situ* H_2O_2 generation experiments in the PGU. Overall, our findings confirm the electrosynthesis of Fe QDs with a continuous electron pathway in the interface iron-carbon, tunable oxidation states, and a control of the ORR via two-electrons pathway.

2.2 Experimental setup

2.2.1 Electrochemical techniques

Cyclic voltammetry (CV) experiments were done on clean glassy carbon electrode immersed in a 5 mM $FeCl_3$ / 0.1 M $KClO_4$ solution bubbled with nitrogen during 15 min and stored in a capped three-way cell. Reversible hydrogen electrode (RHE) and Pt wire were used as refence and counter electrodes, respectively. A total of 49 cycles were scanned between 0.5 V to -0.9 V vs. RHE at 10 mV/s. A Biologic SP200s Potentiostat/Galvanostat Electrochemical Workstation was used for the CV experiments.

Iron nanoparticles were electrodeposited on Vulcan XC-72R by using the RoDSE technique,[88] at the potential selected from CV studies: -855 mV vs. RHE. A glassy carbon rotating disk electrode (RDE) with geometric area of 0.20 cm^2 was used for the RoDSE synthesis. RDE was previously polished in an eight-pattern movement on felt pads with 1.0, 0.3, and 0.05 μm aluminum oxide (Buehler Micropolish); rinsed with DI water; and sonicated during 10 min in ethanol. RHE and Pt-mesh were used as reference and counter electrodes, respectively. 20 mg of Vulcan XC-72R in 20mL of 0.1 M $KClO_4$ solution were ultrasonicated for 1 hour to prepare the precursor slurry suspension. This slurry suspension was transferred to the centered compartment of the three-electrode RoDSE cell, whereas the other two cells were filled with 20 mL of 0.1 M $KClO_4$. The total volume in each compartment was brought to 25 mL with 0.1 M $KClO_4$. Then, 2 mL of 5.0 mM $FeCl_3$ solution were added into the carbon slurry and bubbled vigorously with ultrahigh purity nitrogen for 15 min. Afterwards, the RDE was rotated at 2400rpm and polarized at -855 mV vs. RHE for 1 hour. This rotating-polarization step was repeated with three additional aliquots of 2 mL each. Finally, the slurry was filtered through a 0.22 mm Nylon membrane, washed with 1L of DI water and 20 mL ethanol, and dried in a desiccator for 24 hours.

Inks were prepared by sonicating for 1 hour 1 mg of catalyst with 50 mL of DI water, 50 ◎L of isopropanol, 150 ◎L of ethanol and 20 ◎L of Nafion® solution (5% perfluorinated resin in ethanol from Aldrich). Afterward, 3 μL of the prepared ink were dropped cast on a cleaned glassy carbon electrode and dried at room temperature for 15 min. CVs were done in 0.1 M KOH solution at a window potential between -0.4 and 1.2 V vs. RHE. The oxygen reduction reaction (ORR) kinetic and the Koutechy-Levich (K-L)[90] analysis were studied on a glassy carbon rotating disk electrode (RDE), in a O_2-saturated 0.1 M KOH solution, scanning the potential from 1.0 V to -0.3 V vs. RHE at 10 mV/s and rotation speeds between 400 and 2400 rpm. The hydrodynamic rotating ring disk electrode (RRDE) study was done on a glassy carbon disk and a Pt ring electrode, immersed in 0.1 M KOH and 1600 rpm of rotation speed. The disk potential was swept between 1.0 to -0.4 V vs. RHE at a scan rate of 10 mV/s, and the ring potential was fixed at 1.20 V vs. RHE.

2.2.2 Structural and chemical-physical properties

Metal loading in the catalysts was determined by using Induced Coupled Plasma-Optical Emission Spectroscopy (ICP-OES), with triplicate-quantitative analyses in an Optima 8000 Perkin Elmer ICP-OES. 10 mg of sample were digested in 10 mL of a nitric acid and hydrochloric acid solution at a 1:3 molar ratio. Solution was reduced until a volume of 1 mL, filtered through a Whatman glass microfiber filter (GF/F grade), and diluted with 2% HNO_3.

Samples were placed onto a carbon-coated copper grid and analyzed by Transmission electron microscopy (TEM), transmission scanning electron microscopy (STEM), and the high-angle annular dark-field scanning transmission electron microscopy (HAADF-STEM, Contrast-Z). Micrographs were obtained at 200 KV in a FEI

Tecnai F20 G2, with and X-ray fluorescence-energy dispersive spectrometry (EDS) system and an Oxford X-Max detector.

Iron-based catalyst synthesized were characterized by X-ray diffraction (XRD) using a RIGAKU SmartLab X-ray diffractometer with a high-speed ID detector D/teX Ultra. Experiments were done in reflectance Bragg-Brentano geometry, with a Cu Kα radiation source of λ=1.5406 Å, current was set at 44 mA and voltage at 40 kV.

Raman spectroscopy was done at room temperature in a Thermo Scientific DXR Raman Microscope with a laser wavelength of 532 nm and a power of 5.0 mW, scanning wavelengths between 100 and 3000 cm^{-1} with an error of ± 2 cm^{-1}.

Surface analysis by X-ray photoelectron spectroscopy (XPS). was used to determine the surface chemical composition of samples. Measurements were done in a PHI 5600ci spectrometer, with an Al Kα polychromatic X-ray source of 350 W at 45°, and a hemispherical electron energy analyzer. Pressure in the ultrahigh vacuum analysis chamber was below $9x10^{-9}$ mbar and spot aperture was 500 μm. Carbon tape was used to fix and hold the samples. Survey and high-resolution spectra, at the Fe 2p, C 1s, and O 1s XPS binding energy regions, were recorded. Curve fitting analysis was carried out using Multipack Physical Electronics software, correcting binding energies with the C 1s peak at 284.5 eV.

X-ray absorption spectroscopy (XAS) experiments were done in the beamline for materials measurements (BMM) 6-BM in the National Synchrotron Light Source II (NSLS II) at Brookhaven National Laboratory. The sample was grinded and spread on a Kapton tape until achieving a uniform film. The energy of the absorption spectra was calibrated using an iron metal foil. The Fe K-edge absorption spectra was obtained in transmission mode and analyzed using the DEMENTER program package.[91] The scattering paths during generated in the extended X-ray absorption fine structure (EXAFS) analysis were calculated with the crystal information files PDF 01-072-6226 for hematite and PDF 01-080-6402 for magnetite, obtained from the ICDD PDF4+.

2.2.3 *In-situ* electrochemical H_2O_2 production

For the *in-situ* electrochemical hydrogen peroxide generation samples were dispersed in an ethanol:isopropanol:water (1:1:2) mixture with a total solution volume of 750μL and 60μL of Nafion solution 5% in ethanol. Each dispersion was painted onto a CeTech carbon cloth gas diffusion electrode microporous layer (GDE-MPL). The electrolyte, a mixture of Nafion NR 50 Beads and POWDion-Insoluble 40-60 mesh, was activated at 80°C in successive steps as follow: 3% H_2O_2 for 1 hour, DI water for 2 hours and 1 M H_2SO_4, and stored in DI water. Reverse osmosis (RO) water was flowing through the 0.37" thick catholyte plate at a flow rate of 2 mL/min and pressure balance was held at 1 psi. The system was configurated in a single-pass arrangement to determine the differential polarization plots, output current, and the H_2O_2 w/w% of Fe/Vulcan and the GDE-MPL at 4V, 6V, 8V, 10V, 12V, and 14V.

2.3 Results and Discussion

2.3.1 The iron nucleation – a cyclic voltammetry (CV) study

Figure 2.1 shows the cyclic voltammetry study, of a glassy carbon electrode in a nitrogen-purged 5 mM $FeCl_3$ and 0.1 M $KClO_4$ solution, developed at 10 mV/s between 0.5 V to -0.9 V vs. RHE. CV was started at 0.5 V vs. RHE to assure that Fe^{3+} and Fe^{2+} were present at the beginning of the analysis, in the bulk solution and on the near surface of the electrode, respectively.

The CV in Figure 2.1a) shows some characteristic peaks of Fe-based bulk materials studied in different electrolytes.[92, 93] The current crossovers between cathodic and anodic signals is associated to reversible systems which involve undissolved species, such as nucleation and growth of metallic iron; the presence of a crossover in a CV evidences nuclei formation on the electrode.[94, 95] Even though---the pH of the 5 mM $FeCl_3$ in 0.1 M

$KClO_4$ solution was 4.07±0.01, which implies that aqueous iron species exist as ferrous and ferric ions rather than forming complexes with anionic electrolytes[96]---the Ic and IIc cathodic peaks, shown in Figure 2.1, suggest presence of iron hydroxide species.[93] In the literature, the Ic and IIc current peaks have been ambiguously assigned to Fe^{3+} to Fe^0 and Fe^{3+} to Fe^{2+} to Fe^0 reduction processes and, as well as, to $Fe(OH)_x$ to Fe^0 reduction;[93, 96, 97] the IIIc peak is related to the Fe^{2+} to Fe^0 reduction process.[98] Also, peaks Ic and IIc can correspond to the reduction of FeOOH to $Fe(OH)_2$.[98] The simultaneous presence of Fe^{2+} and Fe^{3+} species is probable at the electrode interface: based on the iron/chloride Pourbaix E-pH diagram at 25 ^{0}C, the iron complexes containing both iron species, will be formed near the electrode under our experimental conditions.[99] The resulting iron complexes, with positive formal charge, are balanced with ClO_4^- and Cl^- species in the outer-sphere complex.[100]

In the anodic region of Figure 2.1a), the Ia current peak is related with oxidation processes of adsorbed hydrogen.[98] Peak IIa is generated the oxidation of Fe^0. Finally, peak IIIa is produced whether as oxidation of an early ferrous hydroxide layer, or by direct iron oxides aggregation under the presence of Fe^{2+} and Fe^{3+} cations.[93, 96, 97] Even though an in-depth analysis is required to characterize all the iron species involved in the redox processes at the selected potential window, this CV analysis was focused on define the electrodeposition potential of iron to produce Fe- and C-based catalysts.

As shown in Figure 2.2, a total of 49 CVs were done between 0.5 V and -0.9 V vs. RHE at 10 mV/s; the cathodic and anodic current peaks growth as the number of cycles increases. The peaks of current, characteristic for iron, show changes in current and shape due to the growth on the electrodeposited iron. In the first cycle, the oxidation peaks Ia, IIa, and IIIa were analogous to those exhibited in Figure 2.1. In the second cycle, peaks Ia and IIa disappear, but IIIa peak current intensity growths until the third cycle when start decreasing. Peak intensity of IIIc decrease as the iron concentration is spent over time, and its slow decreasing indicate that Fe electrodeposition is a limiting step on this CV .

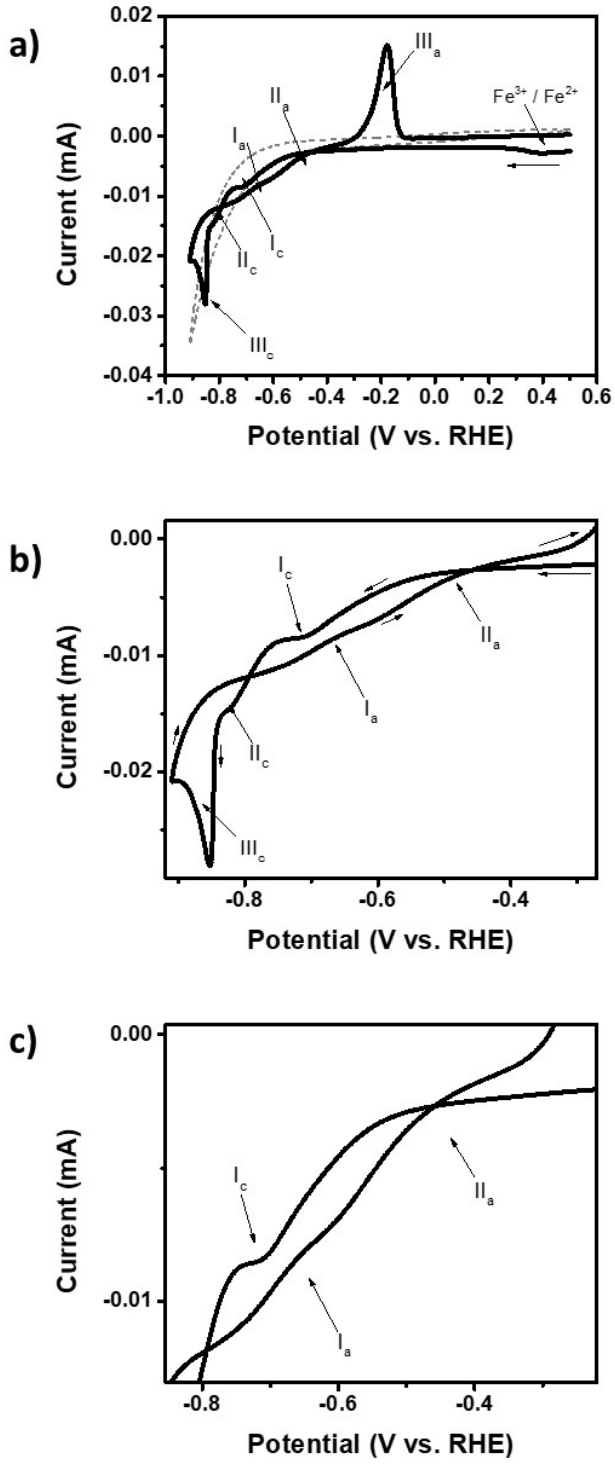

Figure 2.1. Cyclic voltammetry of Fe^{3+} at a GCE, at a scan rate of 10 mV/s and at room temperature. The first cyclic voltammogram (a) in 0.1 M $KClO_4$ (dashed gray line) and in a 5 mM $FeCl_3$/0.1 M $KClO_4$ solution (solid black line). Enlarged views of the potential windows (b) between -0.9V and -0.3V vs. RHE oxidation and (c) and between -0.85V and -0.2V vs RHE are shown below.

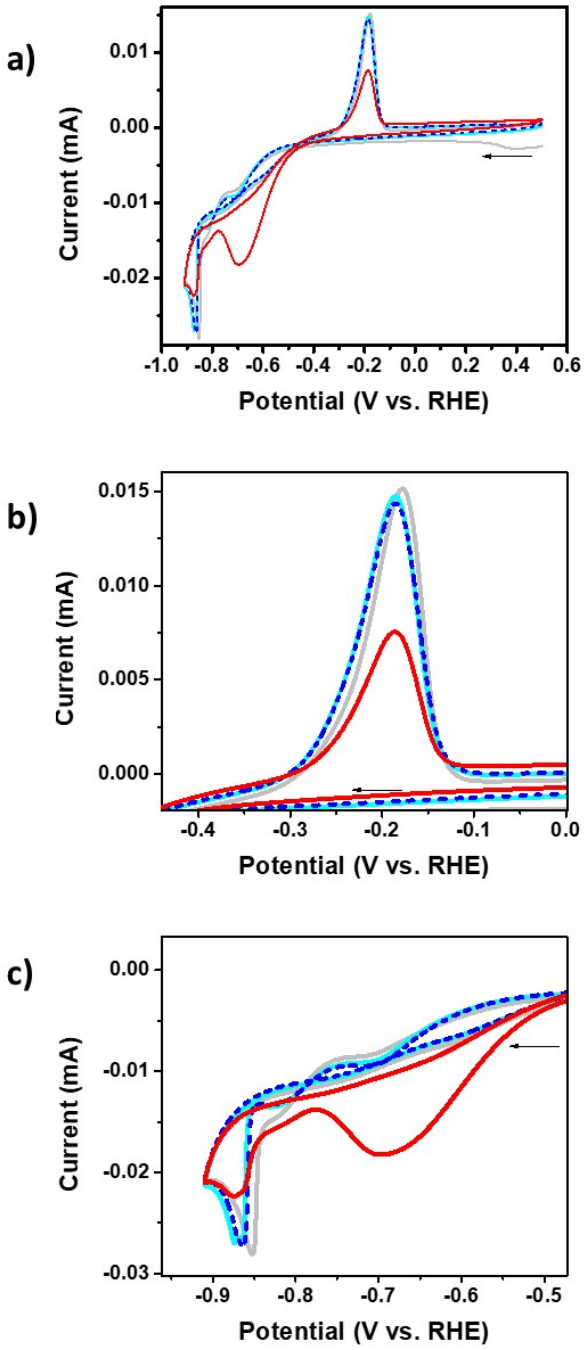

Figure 2.2. (a) Cyclic voltammetry profiles vs. RHE, at a scan rate of 10 mV/s and at room temperature, of a glassy carbon electrode immersed in a 5 mM $FeCl_3$ / 0.1 M $KClO_4$ solution. The deviation of the first cycle (solid gray line), from the successive 2 (solid light blue line), 3 (dashed dark blue line) and 49 cycles (solid red line), is observed in both reduction and oxidation peaks. The potential is swept in the cathodic direction starting at 0.5 V and ending at -0.9 V. Enlarged views of the (b) oxidation and (c) reduction peaks are shown below.

A slow and gradual deposition of iron in 0.1M $KClO_4$ electrolyte allows the growth of very small nanostructures which can explain the current changes---in intensity, potential shifts, and behavior---from the second cycle onward: an iron film or iron clusters can be created onto the glassy carbon electrode during the first cycle; the following iron depositions can occur whether on vacancies of the GC surface, or on the active iron-based sites formed on the electrode surface during the first CV.

In the next section, we explain the Fe deposition on Vulcan XC-72R carbon support through the RoDSE technique at -855 mV vs. RHE. Even though, Figure 2.1 shows that -855 mV vs. RHE is the redox potential to transform Fe^{2+} to Fe^0, carbon flakes in the slurry suspension can generate metal depolarization during the RoDSE process.[84, 89]

2.3.2 The RoDSE technique and the iron electrodeposition

Figure 2.3 shows the RoDSE chronoamperometry profile obtained when -855 mV vs. RHE were applied to the glassy carbon electrode immersed in 5 mM $FeCl_3$ + 0.1 M $KClO_4$ + Vulcan XC-72R slurry. Current profiles of the four successive 2.00 mL aliquots of 5 mM $FeCl_3$ are shown in Figure 2.3.

In Figure 2.3, profiles of each added aliquot revealed the characteristic current-time plots, in which the current is decreasing as a function of electrodeposition time, until a quasi-plateau is reached, due to a reduction of Fe concentration in solution.[84, 89] This current vs. time curve performance is comparable to a characteristic instantaneous nucleation growth.[84] Initially, for all the aliquots, a small current peak was observed in the cathodic current at ca. 20 s, corresponding to an initiation period of iron nucleation on the glassy carbon electrode or on the Vulcan. Then, an exponential increment in current is observed until about 200 s, that can be produced by the Fe nucleation on Vulcan or on the GC electrode, the mass transfer rate around the particles, and the hydrogen evolution. Finally, a current quasi-plateau is reached due to the Fe^{3+} concentration

decreases in solution. Current associated with hydrogen evolution influences the profile behavior of each aliquot, creating the random patterns of current observed in Figure 2.3.[93] The use of potassium perchlorate as electrolyte prevents the creation of new functionalities on Vulcan and promotes stable Fe-complexes instead of precipitated species.

The hydrodynamic flow generated by the RDE draws all the precursors to an infinitesimal distance to the GC surface, producing a laminar, stable, and continuous flow in the radial vicinity of the electrode, where the electrochemical reduction occurs. At these microscopic dimensions, iron electroreduction might occur in three different ways: (*i*) on the surface of the glassy carbon electrode; (*ii*) in solution and drifting the formed iron QDs into the slurry; and (*iii*) directly on Vulcan, forming the expected Fe/C catalyst. In Figure 2.3, the behavior of the current-time profile is determined by the following factors: Fe-catalyst and electrode interaction, Fe-Vulcan shape and size, Fe QDs concentration, reactants diffusion coefficient in the slurry, RDE surface conditions, nanoparticle residence time on the electrode, and applied potential.[101] The potential of reduction at -855 mV, needed for iron electrodeposition (see Figure 2.1) add two additional variable: water reduction and hydrogen evolution process occur simultaneously.

Figure 2.3 shows chronoamperometric profiles with sharp current spikes which can be due to iron nanostructures, drifting free or assembled onto Vulcan, hitting the RDE glassy carbon surface. In addition, these current spikes are signs that solid iron aggregates have been grown: iron nanoparticles are corroded once they are in contact with water, then, the electrochemical reduction of iron oxides is produced, when they hit the RDE surface.[102]

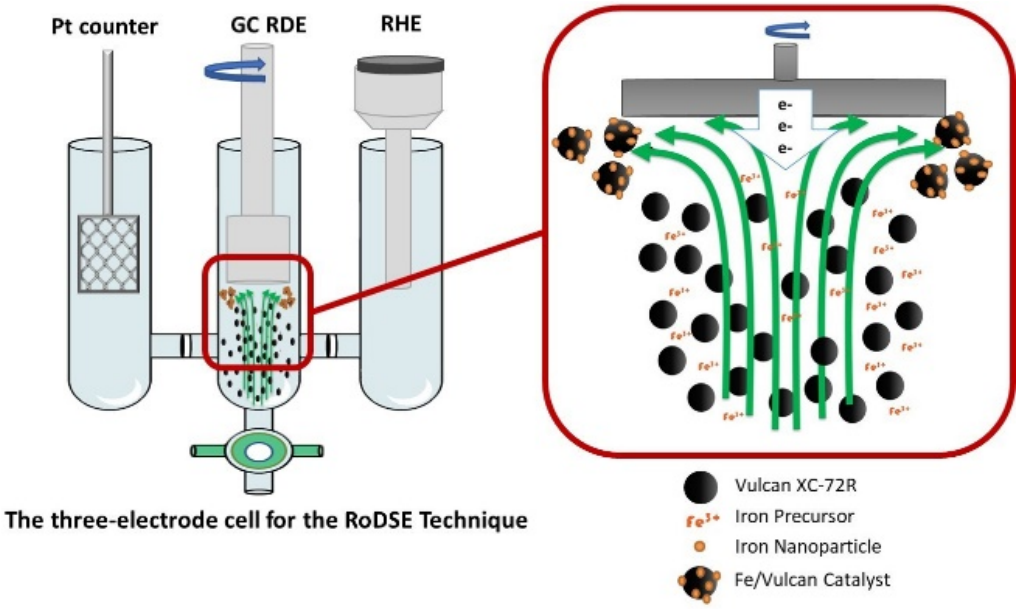

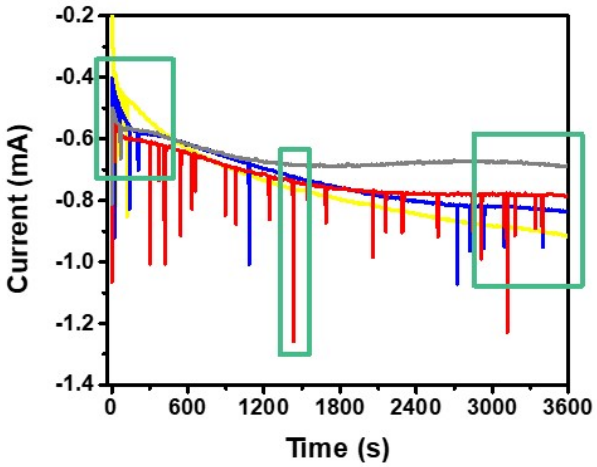

Figure 2.3. *Up:* Schematic of the RoDSE synthesis setup of the Fe/Vulcan in 0.1M KOH at -855mV. The three-compartment electrode cell diagram corresponds from right to left to a reversible hydrogen reference electrode, glassy carbon rotating disk working electrode, and Pt auxiliary electrode. *Down:* Chronoamperometry RoDSE profile for the iron electrodeposition onto Vulcan XC-72R. Current profiles for the FeQDs/C catalyst were obtained in 20.0 mg of carbonaceous matrix in 20.0 mL of 0.1M $KClO_4$ slurry. A glassy carbon RDE, at a rotating speed of 1900 rpm and an applied potential of -0.855 V vs RHE, were used. The chronoamperometric process was repeated three additional times with the addition of 2.00 mL aliquots of 5 mM $FeCl_3$ in each repetition: aliquot 1 (yellow line), aliquot 2 (blue line), aliquot 3 (red line), and aliquot 4 (gray line).

In the hydrodynamic RoDSE method, where the diffusion layer is forced by convection, an infinitesimal temporal resolution regime governs both: the electron transfer and the electrochemical determination of transitional charged species are. The

characteristic timescale $t_{characteristic}$ is calculated by means of the expression $t_{characteristic}=Ad^2D^{-1}$, where A is a proportionality parameter that depends on the technique, D is the diffusion coefficient, and d is the size of a stationary diffusion layer which is controlled by each technique.[103] The transient currents generated in the chronoamperogram (Figure 2.3) can be studied comparing them with methods such as steady-state micro- and nano-electrodes and scanning electrochemical microscopy, methods in which the electrochemical measurements are independent of the double layer charging currents. [103, 104] Forced convection generated in the RoDSE technique increases the collision incidence considerably,[105] however, experiments carried out under controlled flow conditions allow to determine the collision transient currents.[106]

Three processes can be responsible for transient current spikes present in the chronoamperometry: catalytic current provoked by new Fe QDs growing on previously formed Fe-Vulcan particles, electrocatalytic amplification (ECA) induced by the H_2O/H^+ reduction on Fe-Vulcan particles in contact with the RDE, and direct electroreduction of oxidized Fe QDs. QDs may be oxidized on Vulcan surface and can form iron/iron-oxides core-shell structures in aqueous solutions.[101, 107] In stochastic electrochemical techniques signals are amplified in presence of iron.[104, 108] negative values of enthalpy, Gibbs energies of formation, and standard entropy associates with the iron corrosion process in aqueous solution, as well as, the surface energy associate with the small-particle-size of the iron QDs, promote iron oxidation under our experimental conditions. During the first seconds of each aliquot, current peaks are produced by a higher concentration of Fe around the electrode;[84, 88, 89, 109] adding the subsequent aliquots, the frequency and intensity of spikes are determined by Fe QDs generation, as well as, by chloride concentration increment which prevents hydrogen evolution. As summary, electron transfer occur very fast during the particle-electrode impacts,[110] and hydrogen is co-produced on the iron-base quantum dots surface producing transient current peaks.[111]

2.3.3 A cyclic voltammetry study of the Fe-based catalyst

Figure 2.4 shows a cyclic voltammetry study of the electrochemically synthesized Fe-Vulcan. Presence of iron oxides and hydroxides are confirmed by the Fe^{3+}/Fe^{2+} currrent peaks. A current profile comparison between Figure 2.4 and Figure 2.1 shows differences regarding intensity and shape of peaks; these differences are produced by: nanoscopic distribution of a determined material onto another different solid, electrolyte, pH, and surface textural properties. A convolution[112] of current peaks is suggested by peak asymmetry and small current bumps observed in Figure 2.4, e.g. a contribution different iron-based electrochemical routes[92, 93, 96-98] can take place simultaneously at the potential window used. For future Fe applications, we recommend an in-depth cyclic voltammetry study, as well as a current curve-fitting to determine peaks associated with specific electrochemical modifications.[112]

Exposing the Fe QDs to hydroxide ions, or to the atmosphere during post-synthesis manipulation, promote simultaneous presence of ferrous and ferric species in our catalyst. Iron electrochemistry[93, 96-98] and CVs of bulk iron structures[92, 93] allow us to associate regions Ic, IIc, IIIc, IVc, Ia, IIa, IIIa, and IVa (see Figure 2.4), with iron species that can be formed during the potential sweep. Regions Ic and IIc may correspond to the reduction processes of Fe^{3+} to Fe^0, Fe^{3+} to Fe^{2+} to Fe^0, and FeOOH to $Fe(OH)_2$. At region IIIc occur the Fe^{2+} to Fe^0 reduction. Region IVc could be associated with the reduction of corrosion compounds,[113] produced by the OH^- in the electrolyte. The Fe QDs corrosion is promoted by particle size effect.

In the anodic backward potential sweep, the region Ia related to the oxidation of absorbed hydrogen[98, 114] is barely noticeable. In region IIa occur the oxidation of Fe^0 to Fe^{2+}. Finally, electrooxidation of $Fe(OH)_2$ to Fe^{3+} species such as iron (III) oxides and oxyhydroxides are promoted in region IIIa.[98] At the region IVa, inner iron (II) oxide might be oxidized to iron (III) oxide.[92]

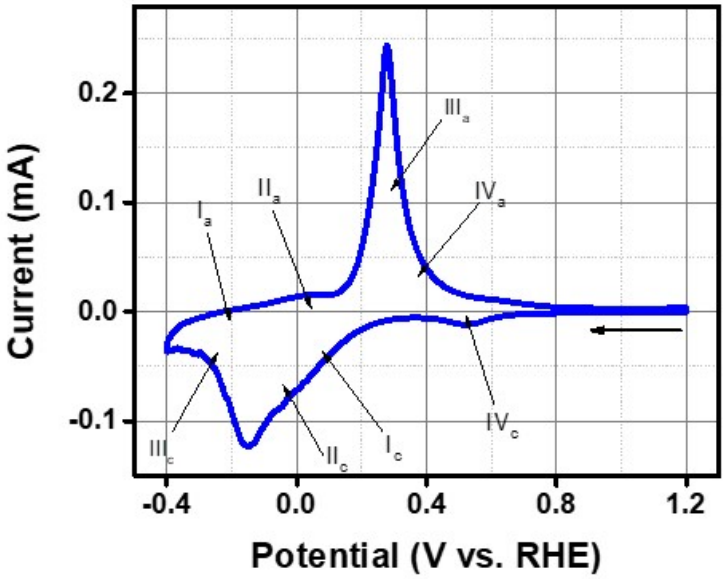

Figure 2.4. First cycle of the cyclic voltammetry analysis of the electrochemically synthesized iron-based catalyst supported on Vulcan XC-72R, via the RoDSE technique. CV analysis was done in a nitrogen-purged 0.1 M KOH solution. Characteristic cathodic and anodic peaks of Fe species are displayed in the voltammogram. Potential scan rate was 10 mV/s.

Appendix 2.1 shows a second cycle recorded immediately after the CV presented in Figure 2.4. In the first cycle, electrolyte diffusion through the catalyst is reached, allowing a second CV with increment in current intensity, that suggest that redox reactions move forward as the surface modifications go on into the porosity of the catalyst. We consider that more ordered structures of iron oxides and hydroxides can be generated after consecutive cycles. Comparing the CVs of our Fe-Vulcan with bulk iron systems,[92, 93] we consider that QDs confinement effect and the conductive carbonaceous substrate produce peaks with more definition and sharpness. The interpretation of Figure 2.4 and Appendix 2.2 is based on the iron electrochemistry previously reported in the literature[93, 96-98] Even though, we used this CV analysis to determine the iron presence on the catalyst, an in-depth iron CV study is required to describe all iron species involved.

2.3.4 Structural and chemical-physical properties

Induced Coupled Plasma-Optical Emission Spectroscopy (ICP-OES) allow us to determine iron loading and the efficiency of the RoDSE technique to electrodeposit iron. Appendix 2.3 shows that 15.54% of iron by mass was deposited onto of Vulcan, with an electrodeposition efficiency of 62.16% per mass, in comparison with the 25.00% of iron by mass loaded as precursor. ICP-OES results validate the RoDSE technique to electrodeposit iron with loading higher than sixty percent, which is an outstanding amount, having in consideration the competition between three simultaneous reactions: iron nucleation, water/protons reduction, and the constant evolution of hydrogen.

Figure 2.5. shows transmission electron microscopy (TEM), scanning transmission electron microscopy (STEM), and high-angle annular dark-field scanning transmission electron microscopy (HAADF-STEM) studies, with structural details of the electrodeposited Fe-Vulcan. Figure 2.5a (TEM) and Figure 2.5b (HRTEM), show carbon particles with diameters between 30 and 50 nm and branched-nanochains and structure cabbage-like which works as anchoring support for metal nanoparticles. In Figure 2.5d (TEM) and Figure 2.5e (HRTEM) show metal-based nanoparticles as dark spots supported on a lighter background of carbon. Iron presence is confirmed by the energy dispersive X-ray spectroscopy (EDS) analysis shown in Figure 2.5g. Figure 2.5d and Figure 2.5e show well-dispersed Fe QDs with a narrow nanoparticle size distribution between 2 and 6 nm, and a mean of 4 nm (see Figure 2.5h). The electron diffraction pattern in Appendix 2.4 confirms the presence iron-oxide compounds. Electron microscopy results confirm that the synthesized catalyst consists of iron-based QDs onto Vulcan XC-72R. Due to the narrow size distribution (below 10 nm) of the Fe QDs, as well as the semiconductor properties iron oxides, with small band gap values,[115] we named our iron particles as quantum dots.[86, 87]

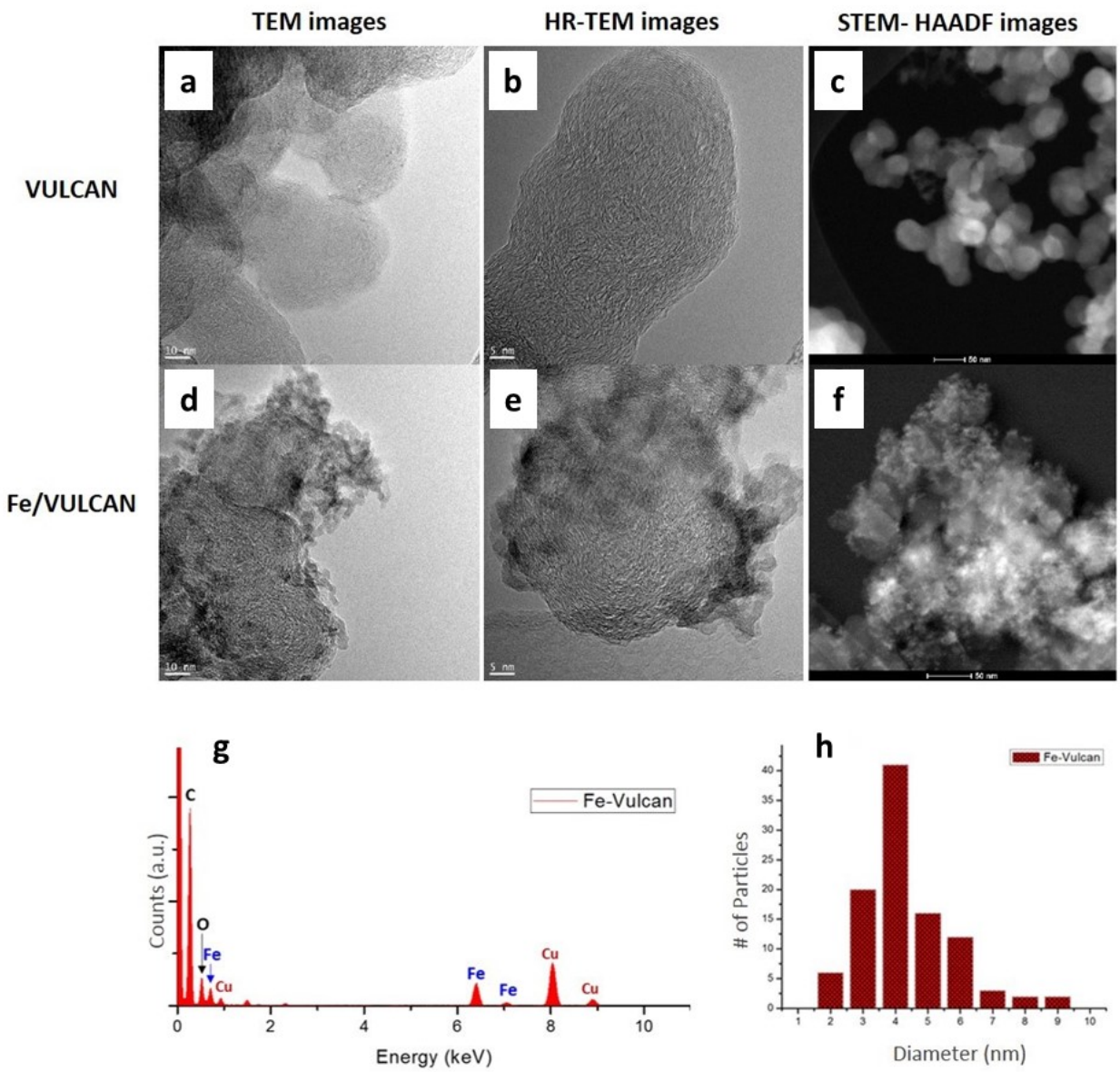

Figure 2.5. Transmission electron microscopy (TEM) (a,d), high resolution transmission electron microscopy (HR-TEM) (b,e), and high-angle annular dark-field scanning transmission electron microscopy (HAADF-STEM) (Contrast-Z) (c,f), of Vulcan and the Fe/Vulcan catalyst electrodeposited by the RoDSE technique. The energy dispersive X-Ray spectroscopy (EDS) analysis evidences the presence of iron (g). The particle size histogram shows a narrow size distribution about 4 nm of Fe-based QDs onto Vulcan (h).

Appendix 2.5 shows the diffractograms of the iron-based nanostructures and carbon support, with broad and ill-defined peaks are typical of nanostructures.[116]. The characteristic α-Fe diffraction peak appears at a 2θ of 46.1°, corresponding to the facet (110) (JCPDS card No. 06-0696). Iron facets (200) and (211) are indistinguishable due to

the low intensity of iron signals, in comparison the Vulcan peaks. Two intense and broad peaks at 2θ equal to 24.4° and 43.3°, coincide with the diffraction planes (002) and (101), respectively (JCPDS card No. 41-1487), characteristic for carbon materials. In Vulcan XC-72R, the interlayer scattering produces the reflection (002) line, whereas the intralayer scattering generates the (101) line. Peak intensity and shape of carbon faces changed after the RoDSE treatment, indicating electrodeposition iron. Due to its high surface area and greater availability of surface reactive sites, the iron QDs obtained by the RoDSE technique are corrode faster than bulk metallic iron,[117, 118] which is evidence by presence of peaks associated with diffraction patterns of magnetite (Fe_3O_4), maghemite (g-Fe_2O_3), hematite (a-Fe_2O_3), goethite (a-FeOOH) or lepidocrocite (g-FeOOH). At room temperature and air-based environments, geometry and size of nanoparticles will determine the velocity of oxidation through a cation diffusion mechanism during short periods of time.[118] Based on that, we hypothesize that our iron QDs are a product of oxidative transformations from Fe^0 to $Fe^{2+/3+}$ to Fe^{3+}; the oxidation gradient are determined by variables such as: particle size, storage conditions, longevity, and sample manipulation during the synthesis and characterization protocols. These iron oxidation processes, couple with broad diffraction peaks, heterogeneous composition of the catalyst, the Fe/C ratio of peak intensities, preclude to calculate the average particle size using Scherrer's equation.

Raman spectroscopy was used to determine iron and carbon species presents in the Fe/Vulcan catalyst. Figure 2.6 shows the Raman spectra of the Vulcan and Fe/Vulcan, with subtle-peak at 1050-1100 cm-1 related to an sp^3 rich phase in carbon configurations;[119] intensity and width of peaks decrease after iron electrodeposition. Vulcan and Fe/Vulcan show the G-band corresponding to the E_{2g} symmetry is localized around 1580cm^{-1}. Likewise, both samples present the D-band located at 1350 cm^{-1} and that correspond the diamond C−C single bonds between sp^3 hybridized carbon atoms. The sp^3-rich phase appears at 1180 cm^{-1}.[84] Vulcan show a small protuberance about 1600-

1650 cm^{-1} that broad the G-band.[84, 89] A broad and small peak at 850 cm^{-1} corresponds to hydrogen-free carbon arrangements; after iron deposition process, this peak increase in intensity indicating: that Vulcan was reduced during the RoDSE treatment, or that iron oxides like hematite were formed.[120] Presence of hematite is proved the peaks at 212 and 280 cm^{-1}. The peak at 398 cm^{-1} corresponds to goethite. Peaks at 477 and 590 cm^{-1} belong to maghemite, and the peak at 698 cm^{-1} to magnetite.[121] The degree of graphitization, I^D/I^G ratio, is used to quantify the number of defects generated on the samples after of the RoDSE process. The Fe/Vulcan shows a lower area for the graphitic and sp^2-rich peak in Figure 2.6, increasing its I^D/I^G ratio. The higher I^D/I^G, in comparison with the value for pristine Vulcan, is attributed to the Fe QDs electrodeposited.

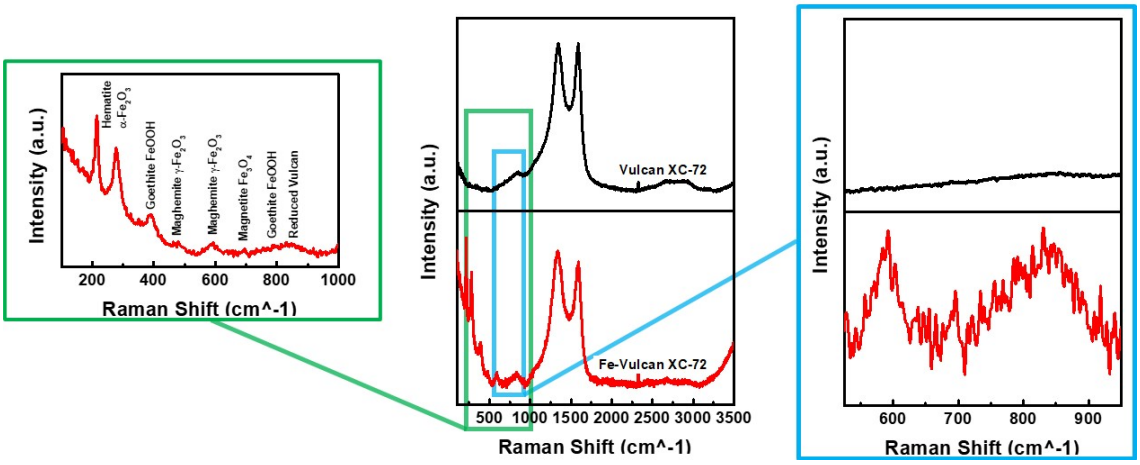

Figure 2.6. Raman spectra of the Vulcan XC-72R before and after the iron electrodeposition (Fe/Vulcan) by the RoDSE technique. Enlarged views of the characteristic regions of iron compounds are shown in both sides of the main Raman figure.

X-ray photoelectron spectroscopy (XPS) spectra, used to determine the oxidation states of our iron-based catalysts, are shown in Figure 2.7a), with a Voigt[122] curve fitting analysis of the XPS $Fe2p_{3/2}$, C1s, and O1s binding energy regions, see Table 2.1.[84] After a Shirley background subtraction, peaks were curve fitted into Gaussian-Lorentzian components with similar FWHM and χ^2 values lower than 6 units. Binding energies were corrected by the C 1s peak at 284.5 eV, see Appendix 2.7.

Figure 2.7b) and Table 2.1 show the curve fitted C1s spectrum of Fe/Vulcan, [84, 89] with the following functionalities: graphitic sp^2 carbon (284.8 eV), C-OH/C-O-C sp^3 (286.5 eV), carbonyl species (288.1 eV), COOH/COOR groups (289.6 eV), and p-p* transitions (290.9 eV). The sp^2 carbon hybridization state, or unfunctionalized carbon, is the main C1s constituent in Vulcan, with at 71% of contribution at 284.8 eV. Peaks located between 286.1 eV and 288.6 eV are related to carbon atoms linked to oxygen in molecular species such as hydroxyl, carboxyl, or carboxylic groups. This oxygen-based molecules confer hydrophilicity to Vulcan, making its structure more accessible to the aqueous iron precursors and electrolyte, and facilitating the access to oxygen-based sites that act as anchoring-nucleation sites during the electrodeposition.

The O 1s[123] curve fitting analysis is reported in Figure 2.7b) and Table1, with a distribution of peaks located at 529.6 eV, 531.4 eV, 533.1 eV, 534.8 eV, and 537.0 eV, which are associated with Fe^{3+} ($FeOOH/Fe_2O_3$), Fe^{2+}(FeO) and $Fe^{2+/3+}$(Fe_3O_4), C-O, C=O/O-C=O, and water molecules on the iron oxide surface[124], respectively. The curve fitted XPS O1s reflects that a 44% of the O1s signals come from iron oxide species .[123] The oxygen-based functionalities on Vulcan reach a 26% which can act as partial-oxidation-sites for the Fe-QDs at the Vulcan support.

The small size of our Fe QDs, their dispersion on Vulcan, and the exceptional interaction of Fe atoms with X-ray, determine intensity of peaks in the XPS Fe 2p spectrum reported in Figure 2.7d and Appendix 2.6. Vulcan XC-72R support may block the XPS Fe 2p signal for metallic iron and oxidized species.[84, 89] The broadness of the XPS Fe 2p peaks is generated by electrostatic interactions, crystal field exchanges, and the spin-orbit coupling between the 2p core-holes and the unpaired 3d electrons of photoionized iron (II/III).[125, 126] The Fe $2p_{3/2}$ and Fe $2p_{1/2}$ binding energy peak assignments are 712.1 and 725.8 eV, respectively. These binding energies and the ΔE=13.7 eV between both peaks are typical values for iron compounds. Table 2.1 summarizes the contribution of each component obtained from the curve fitting analysis of the XPS Fe $2p_{3/2}$ peak.[123]

Transition metals and compounds with high-spin must consider multiplet contribution in their fitting processes---high-spin Fe(II) and Fe(III) contain unpaired d-electrons and accordingly reveal multiplet splitting structures.[123, 125, 126] Only the XPS Fe $2p_{3/2}$ signal[123] was analyzed due to curve fitting analysis, into the spin-orbit split multiplet components, of the whole Fe 2p is overextended and can generate inaccurate results.

Table 2.1. XPS oxidation state contribution (%) of the C 1s, O 1s and Fe $2p_{3/2}$ binding energy components for the Fe/Vulcan XC–72R catalyst synthesized by the RoDSE technique.

Binding energy region	Interaction assignments	Binding energy (eV)	Ratio contribution (%)
C 1s	graphitic sp^2	284.8	71.16
	C-OH/C-O-C sp^3	286.5	17.95
	carbonyl species	288.1	5.37
	COOH/COOR groups	289.6	2.49
	p-p*	290.9	3.03
O 1s	Fe^{3+} ($FeOOH/Fe_2O_3$)	529.6	10.88
	Fe^{2+}(FeO) & $Fe^{2+/3+}$(Fe_3O_4)	531.4	32.74
	C-O	533.1	36.05
	C=O/O-C=O	534.8	16.31
	H_2O on iron oxide	537.0	4.03
Fe $2p_{3/2}$	Fe^{2+} "pre-peak"	708.1	5.58
	Fe^{2+} Multiplet Peak (1 of 3)	710.4	41.74
	Fe^{2+} Multiplet Peak (2 of 3)	712.0	27.47
	Fe^{2+} Multiplet Peak (3 of 3)	713.0	17.18
	Fe^{2+} Satellite Peak	714.6	8.03

Our Fe QDs reveals oxidation states previously described for bulk compunds.[123, 126] The triplet splitting in Figure 2.7d) implies the presence of iron (II) compounds. Likewise, oxides with oxidation state Fe (III) must be present due to the fast oxidation activation by the nanosized dimensions of our samples; however, the low signal in the Fe 2p region makes the curve fitting analysis challenging to evaluate Fe(III) quadruplets.[123] Iron-based core/shell-like structures can be formed, with metallic iron inside covered by oxygen-based compounds.[127]

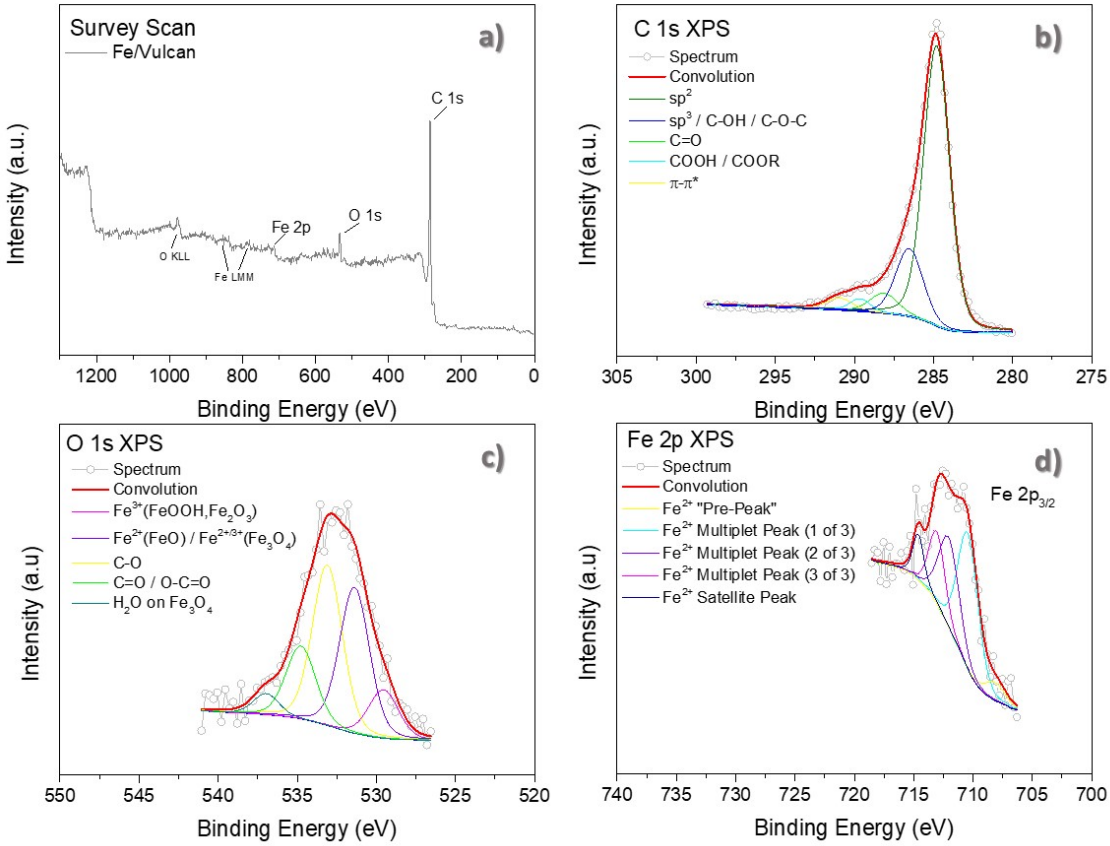

Figure 2.7. X-ray photoelectron spectroscopy survey scan (a), and the Voigt deconvolution analysis of the C $1s_{1/2}$ (b), O $1s_{1/2}$ (c), and Fe $2p_{3/2}$ (d) binding energy regions for the iron-based QDs onto Vulcan XC-72R electrodeposited by the RoDSE technique.

Figure 2.8a) shows the X-ray absorption near edge structure (XANES) spectra of Fe/Vulcan and metallic iron as reference. The Fe/Vulcan edge shows an energy shift towards higher energies compared to the iron metal foil. Fe/Vulcan shows an increment in the intensity of its white line relative the iron reference. Both results suggest presence oxidized Fe-based compounds. Figure 2.8b) shows the Fourier transformed extended X-ray absorption fine structure (EXAFS) signals taken at Fe K-edge for Fe/Vulcan. The single scattering path of a Fe-O bond in the hematite (Fe_2O_3) crystal structure[127] is observed as strongest scattering contribution in the first coordination shelf at 1.44 Å. Nevertheless, the asymmetry of the peak in Fe/Vulcan suggests a contribution of an Fe-O bond in magnetite (Fe_3O_4). Appendix 2.8 shows XAFS data at the Fe edge for Fe/Vulcan

catalyst and the Fe foil. The Fe K absorption edge exhibits higher sensitivity to both Fe (II,III) oxidation states, as well as differences in structure:[91] suggesting that Fe/Vulcan has a mixture of hematite and magnetite, and confirming the mixture of iron compounds reported by XRD, TEM, Raman, and XPS.

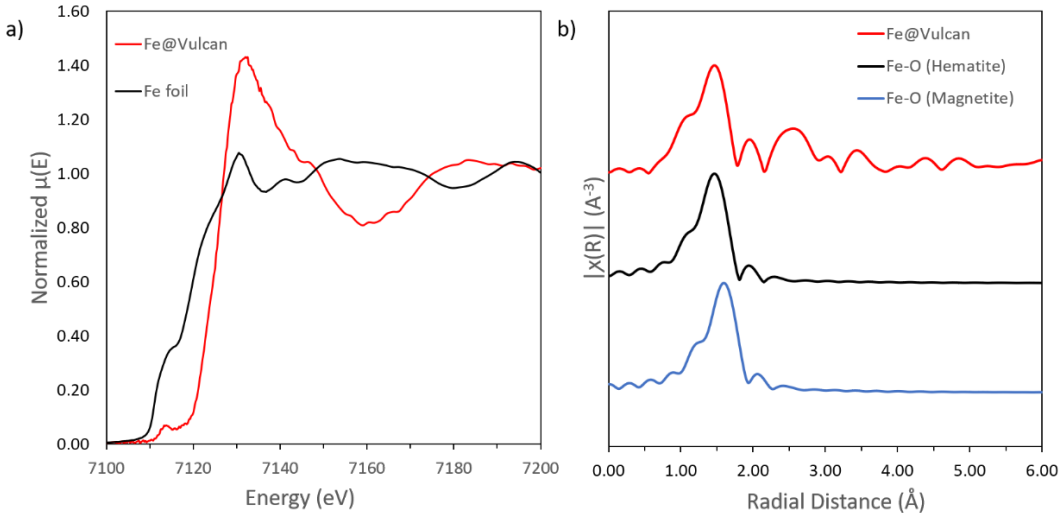

Figure 2.8. Comparison of X-ray absorption near edge structure (XANES) spectra (a) of Fe/Vulcan (red) and Fe metal foil (black). Comparison the Fourier transformed extended X-ray absorption fine structure (EXAFS) radial distribution signals taken at Fe K-edge for Fe/Vulcan (b), with k weight of 2, with the calculated single scattering paths contributions of hematite (black) and magnetite (blue).

2.3.4 Electrochemical oxygen reduction reaction (ORR) kinetics by the Koutechy-Levich (K-L) analysis

Hydrodynamic linear swept voltammetry experiments were used to study the ORR in the triple-compartment cell system detailed in the experimental setup; the RDE was immersed in an O_2-saturated 0.1 M KOH solution, rotated at speeds between 400 and 2400 rpm, and the potential scanned at 10 mV/s. As shows Appendix 2.10, there is a proportional correlation between the rotation speed and the current density produced, a typical behavior in a steady-stay polarization regime. Appendix 2.11 shows that the iron reduction signal vanishes after the first CV, indicating complete reduction iron species to Fe^0. Even though our Fe QDs have a mixture of iron oxides, they are electrochemically controlled and reduced to iron Fe^0 though a tuning-treatment.

A Koutechy-Levich (K-L) analysis[90] of the RDE data was done to evaluate the ORR kinetics and determine the transferred electron number (*n*-value), by using Equation 2.1:

$$\frac{1}{j} = \frac{1}{j_k} + \frac{1}{j_d} = \frac{1}{nFkC^0} + \frac{1}{0.62nFD_{O_2}^{2/3}\nu^{-1/6}C^0\omega^{1/2}} \qquad \text{Equation 2.1}$$

where j is the current density at a given potential, j_k and j_d are the kinetic and diffusion limited current densities, k is the rate constant for O_2 reduction, n is the number of electrons involved in the ORR, F is the Faraday constant (96485 C mol^{-1}), w is the rotation rate (rad s^{-1}), C^0 is the saturation concentration of O_2 in 0.1 M KOH at 1 atm O_2 pressure, D_O is the O_2 diffusion coefficient and v is the solution kinematic viscosity.

As is shown in Appendix 2.10, Fe/Vulcan shows a higher limited diffusion current in comparison with Vulcan. Appendix 2.9 indicates that the *n*-value of Fe/Vulcan is 2.6, suggesting Fe/Vulcan catalyst favored the ORR via two-electron pathway, whereas Vulcan XC-72R reveals an *n*-value of 1.6 in alkaline media. Appendix 2.10a), Appendix 2.10b), and Appendix 2.9 show that the onset potentials (E_{onset}) were 0.566, 0.642, and 0.876 V vs. RHE for Fe/Vulcan, Vulcan XC-72R, and Pt(20%)/C, respectively Likewise, the half-wave potential ($E_{1/2}$) were 0.467, 0.573, and 0.785 V vs. RHE for the Fe/Vulcan, Vulcan XC-72R, and Pt(20%)/C, respectively. For Fe/Vulcan, the E_{onset} and $E_{1/2}$ parameters are shifted toward more negative values, which can be consequences of Vulcan modifications at the RoDSE synthesis.[89] Even though the E_{onset} and $E_{1/2}$ obtained after electrodepositing iron, the diffusion limited current density (j_D) and the n_{e^-} transfer capacity growth, showing an improvement in the catalytic global activity---Fe promote the j_D needed for an efficient ORR.

Fe/Vulcan control the ORR kinetics via two-electrons pathway to produce H_2O_2 as a function of the applied potential. The RoDSE technique tailors the electronic structure of the Fe- and C-based catalyst: incorporating Fe QDs and modifying the surface of Vulcan. This further suggests that the ORR is strongly dependent on the nature of the

active sites present on the surface of both Fe and C. An in-depth H_2O_2 study is shown in the next two sections.

2.3.5 Rotating Ring-Disk Electrode (RRDE) for H_2O_2 Analysis

Figure 2.9 shows the Fe/Vulcan steady-state linear sweep voltammetry, obtained though the Rotating Ring Disk Electrode (RRDE) technique at a rotation speed of 1600 rpm. Experiments were done at 10 mV/s in an O_2-saturated 0.1M KOH solution and a potential window between -400 and 500 mV vs. RHE for the glassy carbon disk, while the Pt ring was maintained at 1.2V vs. RHE. Reproducibility was tested after 3 different inked-electrode trials. The cathodic blue line shows that current growth as a function of the applied potential, confirming diffusion and controlled ORR at the Fe/Vulcan catalyst. The ORR E_{onset} is located at 570 mV, reaching diffusion limited performance between -400 and 150 mV vs. RHE. As the potential becomes more negative, the Fe/Vulcan decreases its current in the diffusion limited region between -400 and -200 mV vs. RHE, suggesting that the *n*-value is increasing in this region.

The top-red line in Figure 2.9a) shows the ring-current associated with the process of formation-degradation of hydrogen peroxide. This data was simultaneously recorded with potential scan at the glassy carbon disk. The H_2O_2 selectivity ($\%H_2O_2$) and the electron transfer number, *n*, were calculated using Equation 2.2 and Equation 2.3:[20]

$$\%H2O2 = 200\left(\frac{IRing/N}{IDisk+IRing/N}\right) \qquad \text{Equation 2.2}$$

$$n = \left(\frac{4IDisk}{IDisk+\frac{IRing}{N}}\right) \qquad \text{Equation 2.3}$$

Where I_{Ring} is the ring current, I_{Disk} is the disk current, and N is the collection efficiency. Figure 2.9b) and Figure 2.9c) evidenced that Fe/Vulcan transfers 2.5 e^-, that represent a production of 75% of H_2O_2 at a potential window between 350 and 450 mV.

A detailed evaluation of the ring current (red-line), shown in Figure 2.9a), allows us to follow the typical stages, previously reported by Hasche *et al.*,[128] related to the H_2O_2 lifetime in the RRDE analysis. At potentials above 600 mV vs. RHE, stage I, H_2O_2 is undetectable. Ring current increases at potentials between 350 and 600 mV vs. RHE, stage II, indicating production of hydrogen peroxide. The highest values of current are observed in stage III, between 250 and 350 mV vs. RHE. The H_2O_2 concentration start decreasing between 300 to 0 mV, stage IV, where the rate of peroxide consumed by the ring is higher than the peroxide formed on the disk. In stage V, between 0 and -400 mV, the hydrogen peroxide formation is weak but constant a broad potential window. ide ions.

Figure 2.9c) shows that at potentials more negative than 150 mV, the number of electrons (*n*) transferred is 4. Even though the Fe/Vulcan onset potential is shifted toward more negative potentials, in comparison with the commercial Pt/Carbon catalyst, Fe/Vulcan is a candidate to be redesigned and improved to control the ORR via four-electron pathway. As shown in Figure 2.9a), the highest concentration peroxide was observed between 300 and 500 mV vs. RHE. At potentials more negative than -200mV vs. RHE, current decreases which can be attributed to the cathodic reduction of H_2O_2 forming hydroxide.

The RRDE analysis reflects that the Fe/Vulcan catalyst produces 75% of H_2O_2 at potentials more positives than 300 mV vs. RHE, that is a typical potential region where cathode operates in fuel cells.[129] The reduction of hydrophilic functional groups, generated on Vulcan during the RoDSE process, will prevent water flooding in the cathode. The RoDSE technique produces an iron-carbon composite with three-phase contact points for oxygen, electrolyte, and catalyst,[23] which promote our Fe/Vulcan as catalyst for the *in-situ* H_2O_2 production.

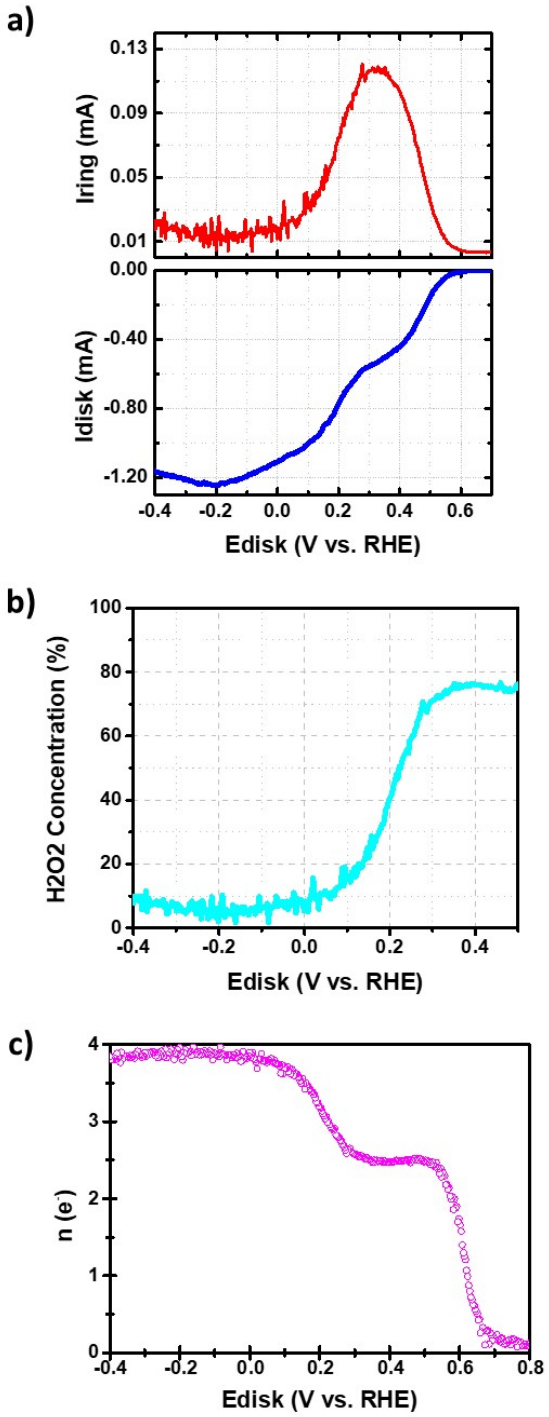

Figure 2.9. Data collected during the hydrodynamic RRDE study of Fe/Vulcan for the ORR as a function of potential vs. RHE. a) Plot of the disk current, I_{disk}, (dark blue line) and ring current, I_{ring} (red line). b) Concentration of hydrogen peroxide (% H_2O_2: light blue line) vs. E_{disk} vs. NHE. c) Number of electrons (*n*) involved in the oxygen reduction reaction. The RRDE analysis was completed by testing Fe/Vulcan ink on glassy carbon disk and Pt ring in KOH 0.1 M. The Fe/Vulcan/GC disk electrode potential was swept at a scan rate of 10 mV/s, the Pt ring potential was fixed at 1.20 V vs. RHE, and the RRDE rotation speed was 1600 rpm.

2.3.6 *In-situ* electrochemical H_2O_2 production

The 75% of H_2O_2 determined with the RRDE analysis encouraged us to go a step further, testing the Fe/Vulcan in the *in-situ* peroxide generation unit (PGU) developed by in Chapter 1.[3] The PGU was ran under simulated drinking water resources available in the International Space Station (ISS): pH between 5.5 and 6.7, conductivity between 2 and 3 mS/cm, and total organic carbon (TOC) from 0.18 to 2.5m/L.[13] The catholyte flow was streamed in a single-pass configuration to determine the optimal configuration of the PGU under terrestrial conditions, developing the on-Earth baseline for future experiments under Zero-G environments. The operation of the PGU was widely described in Chapter 1. Figure 2.10 shows the single-pass polarization plots at 4V, 6V, 8V, and 10V, using the commercial GDE-MPL and the Fe/Vulcan catalyst. The output currents at 12V and 14V were discarded due to their instability and formation of bubbles inside the chamber.

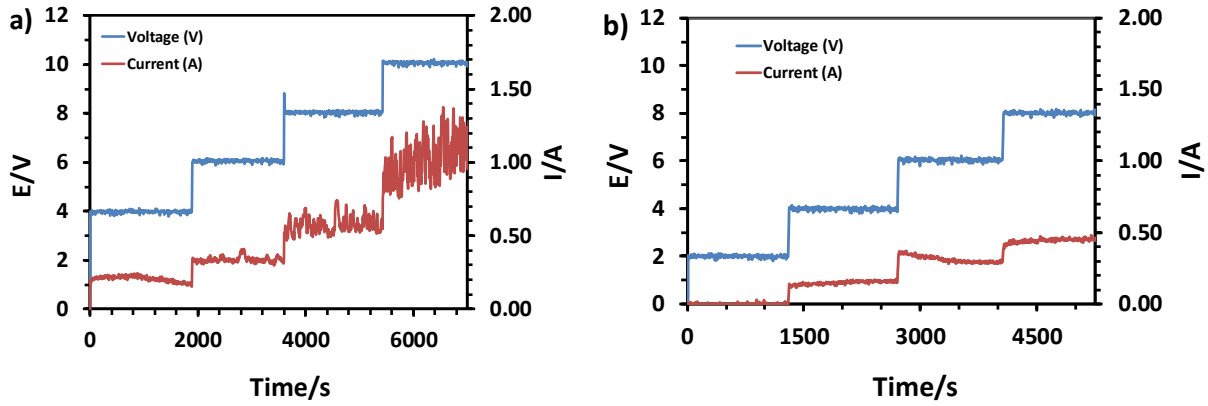

Figure 2.10. Polarization curves for the *in-situ* hydrogen peroxide generation on the Fe/Vulcan (a) and the GDE (b). Polarization curves of Fe/Vulcan and the GDE-MPL were done in RO water at different potentials.

Appendix 2.12 and Table 2.2 compare the *in-situ* H_2O_2 production, and the output currents produced by the GDE-MPL and the Fe/Vulcan catalyst RO water at 4V, 6V, and 8V. At 6V, Fe/Vulcan and GDE-MPL produce 0.056 (560 ppm) and 0.030 (330 ppm) w/w% H_2O_2, respectively. In addition, Fe/Vulcan generates 0.35 amps of output current, while the GDE-MPL yields 0.28 amps. Comparing both catalysts in RO water, Fe/Vulcan

produces 87% more of hydrogen peroxide and a 25 % extra of output current than the commercial GDE-MPL.

Table 2.2. *In-situ* H_2O_2 generation and output current produced by the GDE-Fe/Vulcan and GDE-MLP catalysts at an applied voltage of 4V, 6V, and 8V.

E	**Fe/Vulcan**		**GDE-MPL**	
	H_2O_2	**I**	**H_2O_2**	**I**
(V)	(w/w %)	(A)	(w/w %)	(A)
4	0.024	0.17	0.006	0.16
6	0.056	0.35	0.030	0.28
8	0.032	0.55	0.050	0.44

The high ORR selectivity, toward a two-electron pathway shown by the Fe/Vulcan at 6V---and having in consideration that the low conductivity (2-3 mS/cm) of RO water is unfavorable for all electrochemical reaction---represents a promising result for the *in-situ* H_2O_2 production. The Fe/Vulcan catalyst can be used at low potentials, 4 and 6 V, promoting a longer lifetime for the catalyst and the PGU components, preventing water-splitting process, and decreasing formation of bubbles.

Additionally, Fe/Vulcan is more stable than the commercial GDL-MPL. Appendix 2.13 shows an exponential decay behavior of the GDE-MPL output current as a function of time the at 6 V, which occur in seconds from 0.315 amps at 3120 sec, to 0.281 amps at 3840 sec. This decrease in current can indicate decomposition of the GDE-MPL, with a resulting cathode water flooding. After opening the PGU tested with the GDL-MPL, we observed water penetration and flooding in the cathode. However, the Fe/Vulcan current remains stable at the same time window, cathode continued dry after the PGU test. In future studies, in order to stockpile and increase the concentration of H_2O_2, PGU experiments will be done in a recycle loop orientation. Besides, we strongly suggest experiments in the PGU with extended operation periods to test the Fe/Vulcan stability. As well as, we propose to test the Fe/Vulcan material under the microgravity conditions evaluated in Chapter 1.

2.4 Conclusions

We have designed and controlled an electrodeposition synthesis, via the RoDSE technique, to produce iron quantum dots onto a solid carbonaceous support. The structural and physicochemical characterization exposes that our well-dispersed 4nm Fe QDs are an arrangement of different oxidations states of iron: Fe^{0}, $Fe^{2+/3+}$, and Fe^{3+}. Even though, under atmospheric conditions our Fe QDs presented a gradient of oxidation---determined by the particle size, synthesis and storage conditions, longevity, and sample manipulation during the characterization protocols---their tunability as a function of potential was shown by reducing them to Fe^{0} before each ORR kinetics.

The RDE, RRDE, and PGU results revealed that the Fe/Vulcan catalyzes the ORR, controlling the mechanism via two-electron pathway. Comparing the performance of both catalysts inside the PGU, Fe/Vulcan produces 87% more hydrogen peroxide and 25 % more current than the commercial GDE-MPL. This *in-situ* H_2O_2 production---under compatibility conditions of the drinking water resources available in the ISS---triggers up our Fe/C catalyst for sanitizing solutions in space missions. Additionally, the electrodeposited Fe/Vulcan is a promising material to be used in the PGU at low potentials: 4 and 6 V.

Vulcan---with its anchoring-nucleation sites---has proven to be a good support for iron electrodeposition, preventing the Fe QDs agglomeration, and providing a conductive framework for an enhanced ORR.

Current transients produced in the RoDSE synthesis are associated with an amplification of signals of current, generated by the electrocatalytic interaction of the Fe/Vulcan-H_2O/H^{+} couple. These transients of current open a new line of research focused on the study of amplified signals in electrochemical reactions---inside of a fluidized bed reactor-like, where the electrocatalyst can be used as a label to obtain higher

electrocatalytic yields in large-scale production of H_2 and O_2, gases highly demanded for energy and human activities on Earth and space---which represents a fascinating investigation field.

We achieved the parameters established by the US DoE Strategic Plan, using iron and carbon as precursors---that are abundant on Earth and space, have shown low toxicity, and are highly stable---to synthesize the Fe/Vulcan.

2.5 Acknowledgments

The authors express their gratitude of both NASA Fellowship from NASA Puerto Rico Space Grant Consortium No. NNX15AI11H at the UPR, and the NASA Phase II SBIR Contract NNX16CA43P trough Faraday Technology Inc. This work was supported by the National Science Foundation NSF-PREM: Center for Interfacial Electrochemistry of Energy Materials (CiE2M) grant number DMR-1827622. The use of the Cornell Center for Materials Research Shared Facilities, which are supported through the NSF MRSEC grant number DMR-1719875, are greatly appreciated. Also, the authors expose their gratitude for NSF REU PR-CLIMB Grant: 1560278. This research used resources of beamline (BMM) 6-BM of the National Synchrotron Light Source II in Brookhaven National Laboratory; a U.S. Department of Energy (DOE) Office of Science User Facility operated for the DOE Office of Science by Brookhaven National Laboratory under Contract DE-SC0012704. The RoDSE setup schematic was done in collaboration with Dra. Myreisa Morales and Mr. Jeriel Dumeng. Also, authors thank Mr. Jeriel Dumeng for his participation in the iron tuning-treatment for the RDE study for the ORR.

2.6 References

(1) Vijapur, S. H.; Hall, T. D.; Taylor, E.; Wang, D.; Snyder, S.; Skinn, B.; Peña-Duarte, A.; Cabrera, C. R.; Sweterlitsch, J. *In- Situ* Resource Utilization for Electrochemical Generation of Hydrogen Peroxide for Disinfection. *ICES: International Conference on Environmental Systems* **2019**, *38*, 14 pages.

(2) Nelson, G. J.; Vijapur, S. H.; Hall, T. D.; Brown, B. R.; Peña-Duarte, A.; Cabrera, C. R. Electrochemistry for Space Life Support. *Electrochemical Society Interface* **2020**, *29* (1), 47-52. DOI: 10.1149/2.f06201if.

(3) Caruana, D. J.; Holt, K. B. Astroelectrochemistry: the role of redox reactions in cosmic dust chemistry. *Physical Chemistry Chemical Physics* **2010**, *12* (13), 3072-3079, 10.1039/B917817A. DOI: 10.1039/B917817A.
(4) Energy, U. D. o. *US Department of Energy Strategic Plan, at: https://www.energy.gov/downloads/us-department-energy-strategic-plan-0*. 2020. (accessed.
(5) Shimizu, K.; Sepunaru, L.; Compton, R. G. Innovative catalyst design for the oxygen reduction reaction for fuel cells. *Chemical Science* **2016**, *7* (5), 3364-3369, 10.1039/C6SC00139D. DOI: 10.1039/C6SC00139D.
(6) Singh, B. P.; Kumar, A.; Duarte, A. P.; Rojas, S. J.; Crespo-Medina, M.; Areizaga-Martinez, H. I.; Vega-Olivencia, C. A.; Tomar, M. S. Synthesis, characterization, and electrochemical response of iron oxide nanoparticles for sensing acetaminophen. *Materials Research Express* **2016**, *3* (10), 106105. DOI: 10.1088/2053-1591/3/10/106105.
(7) Winter, M.; Brodd, R. J. What Are Batteries, Fuel Cells, and Supercapacitors? *Chemical Reviews* **2004**, *104* (10), 4245-4270. DOI: 10.1021/cr020730k.
(8) Li, Y.; Zhang, H.; Wang, S.; Lin, Y.; Chen, Y.; Shi, Z.; Li, N.; Wang, W.; Guo, Z. Facile low-temperature synthesis of hematite quantum dots anchored on a three-dimensional ultra-porous graphene-like framework as advanced anode materials for asymmetric supercapacitors. *Journal of Materials Chemistry A* **2016**, *4* (29), 11247-11255, 10.1039/C6TA02927B. DOI: 10.1039/C6TA02927B.
(9) Betancourt, L. E.; Ortiz-Rodríguez, Á. M.; Corchado-García, J.; Cabrera, C. R. RoDSE Synthesized Fine Tailored Au Nanoparticles from Au(X)4– (X = Cl–, Br–, and OH–) on Unsupported Vulcan XC-72R for Ethanol Oxidation Reaction in Alkaline Media. *ACS Applied Energy Materials* **2019**, *2* (1), 287-297. DOI: 10.1021/acsaem.8b01284.
(10) Peña, A.; Puerta, J.; Guerrero, A.; Cañizales, E.; Brito, J. L. Catalytic Chemical Vapor Deposition Synthesis of Carbon Aerogels of High-Surface Area and Porosity. *Journal of Nanotechnology* **2012**, *2012*, 5 pages. DOI: https://doi.org/10.1155/2012/708626.
(11) Lindberg, V.; Hellsing, B. Metallic quantum dots. *Journal of Physics: Condensed Matter* **2005**, *17* (13), S1075-S1094. DOI: 10.1088/0953-8984/17/13/004.
(12) Parak, W. J.; Manna, L.; Nann, T. Fundamental Principles of Quantum Dots. In *Nanotechnology. Volume 1: Principles and Fundamentals.*, Schmid, G. Ed.; Nanotechnology (VCH), WILEY-VCH Verlag GmbH & Co. KGaA, Weinheim, 2008.
(13) Santiago, D.; Rodríguez-Calero, G. G.; Rivera, H.; Tryk, D. A.; Scibioh, M. A.; Cabrera, C. R. Platinum Electrodeposition at High Surface Area Carbon Vulcan-XC-72R Material Using a Rotating Disk-Slurry Electrode Technique. *Journal of The Electrochemical Society* **2010**, *157* (12), F189. DOI: 10.1149/1.3489948.
(14) Vélez, C. A.; Corchado-García, J.; Rojas-Pérez, A.; Serrano-Alejandro, E. J.; Santos-Homs, C.; Soto-Pérez, J. J.; Cabrera, C. R. Manufacture of Pd/Carbon Vulcan XC-72R Nanoflakes Catalysts for Ethanol Oxidation Reaction in Alkaline Media by RoDSE Method. *Journal of The Electrochemical Society* **2017**, *164* (14), D1015-D1021. DOI: 10.1149/2.1041714jes.
(15) Koutetskii, Y.; Levich, V. G. The use of a rotating disc electrode for studying kinetic and catalytic processes in electrochemistry. *Dokl. Akad. Nauk SSSR.* **1957**, *117* (3), 441-444.
(16) Koningsberger, D. C.; Prins, R. *X-ray absorption : principles, applications, techniques of EXAFS, SEXAFS, and XANES*; New York : Wiley, 1988.
(17) Haupt, S.; Strehblow, H. H. Corrosion, layer formation, and oxide reduction of passive iron in alkaline solution: a combined electrochemical and surface analytical study. *Langmuir* **1987**, *3* (6), 873-885. DOI: 10.1021/la00078a003.
(18) Grujicic, D.; Pesic, B. Iron nucleation mechanisms on vitreous carbon during electrodeposition from sulfate and chloride solutions. *Electrochimica Acta* **2005**, *50* (22), 4405-4418. DOI: https://doi.org/10.1016/j.electacta.2005.02.013.
(19) Mallik, A.; Ray, B. C. Evolution of Principle and Practice of Electrodeposited Thin Film: A Review on Effect of Temperature and Sonication. *International Journal of Electrochemistry* **2011**, *2011*, 568023. DOI: 10.4061/2011/568023.

(20) Grujicic, D.; Pesic, B. Electrodeposition of copper: the nucleation mechanisms. *Electrochimica Acta* **2002**, *47* (18), 2901-2912. DOI: https://doi.org/10.1016/S0013-4686(02)00161-5.
(21) Lee, J.; Kim, S.; Shinb, D. Electrodeposition of Iron in HNO3 Solution Containing IronDissolved from Copper Slag. *Journal of The Electrochemical Society* **2014**, *161* (14), D719-D724. DOI: 10.1149/2.0341414jes.
(22) Zhang, H. Rotating Ring-Disk Electrode and Spectroelectrochemical Studies on the Oxidation of Iron in Alkaline Solutions. *Journal of The Electrochemical Society* **1994**, *141* (3), 718. DOI: 10.1149/1.2054798.
(23) Duschek, K.; Uhlemann, M.; Schlörb, H.; Nielsch, K.; Leistner, K. Electrochemical and in situ magnetic study of iron/iron oxide films oxidized and reduced in KOH solution for magneto-ionic switching. *Electrochemistry Communications* **2016**, *72*, 153-156. DOI: https://doi.org/10.1016/j.elecom.2016.09.018.
(24) Beverskog, B.; Puigdomenech, I. Revised pourbaix diagrams for iron at 25–300 °C. *Corrosion Science* **1996**, *38* (12), 2121-2135. DOI: https://doi.org/10.1016/S0010-938X(96)00067-4.
(25) Cornell, R. M.; Schwertmann, U. *The Iron Oxides : Structure, Properties, Reactions, Occurences and Uses*; 2003. DOI: 10.1002/3527602097.
(26) Bard, A. J.; Zhou, H.; Kwon, S. J. Electrochemistry of Single Nanoparticles via Electrocatalytic Amplification. *Israel Journal of Chemistry* **2010**, *50* (3), 267-276. DOI: 10.1002/ijch.201000014 (acccessed 2020/04/10).
(27) Shimizu, K.; Tschulik, K.; Compton, R. G. Exploring the mineral–water interface: reduction and reaction kinetics of single hematite (α-Fe2O3) nanoparticles. *Chemical Science* **2016**, *7* (2), 1408-1414, 10.1039/C5SC03678J. DOI: 10.1039/C5SC03678J.
(28) Zhou, X. S.; Mao, B. W.; Amatore, C.; Compton, R. G.; Marignier, J. L.; Mostafavi, M.; Nierengarten, J. F.; Maisonhaute, E. Transient electrochemistry: beyond simply temporal resolution. *Chemical Communications* **2016**, *52* (2), 251-263, 10.1039/C5CC07953E. DOI: 10.1039/C5CC07953E.
(29) Kwon, S. J.; Bard, A. J. Analysis of Diffusion-Controlled Stochastic Events of Iridium Oxide Single Nanoparticle Collisions by Scanning Electrochemical Microscopy. *Journal of the American Chemical Society* **2012**, *134* (16), 7102-7108. DOI: 10.1021/ja300894f.
(30) Jiang, J.; Huang, X.; Wang, L. Effect of forced convection on the collision and interaction between nanoparticles and ultramicroelectrode. *Journal of Colloid and Interface Science* **2016**, *467*, 158-164. DOI: https://doi.org/10.1016/j.jcis.2016.01.009.
(31) Alligrant, T. M.; Anderson, M. J.; Dasari, R.; Stevenson, K. J.; Crooks, R. M. Single Nanoparticle Collisions at Microfluidic Microband Electrodes: The Effect of Electrode Material and Mass Transfer. *Langmuir* **2014**, *30* (44), 13462-13469. DOI: 10.1021/la503628h.
(32) Zhang, H.; Sepunaru, L.; Sokolov, S. V.; Laborda, E.; Batchelor-McAuley, C.; Compton, R. G. Electrochemistry of single droplets of inverse (water-in-oil) emulsions. *Physical Chemistry Chemical Physics* **2017**, *19* (24), 15662-15666, 10.1039/C7CP03300A. DOI: 10.1039/C7CP03300A.
(33) Dick, J. E.; Bard, A. J. Toward the Digital Electrochemical Recognition of Cobalt, Iridium, Nickel, and Iron Ion Collisions by Catalytic Amplification. *Journal of the American Chemical Society* **2016**, *138* (27), 8446-8452. DOI: 10.1021/jacs.6b03202.
(34) Kim, B.-K.; Boika, A.; Kim, J.; Dick, J. E.; Bard, A. J. Characterizing Emulsions by Observation of Single Droplet Collisions—Attoliter Electrochemical Reactors. *Journal of the American Chemical Society* **2014**, *136* (13), 4849-4852. DOI: 10.1021/ja500713w.
(35) Rees, N. V.; Banks, C. E.; Compton, R. G. Ultrafast Chronoamperometry of Acoustically Agitated Solid Particulate Suspensions: Nonfaradaic and Faradaic Processes at a Polycrystalline Gold Electrode. *The Journal of Physical Chemistry B* **2004**, *108* (48), 18391-18394. DOI: 10.1021/jp040602v.
(36) Klapper, H. S.; Zajec, B.; Heyn, A.; Legat, A. Elucidating Nucleation Stages of Transgranular Stress Corrosion Cracking in Austenitic Stainless Steel by In Situ Electrochemical and Optical Methods. *Journal of The Electrochemical Society* **2019**, *166* (11), C3326-C3335. DOI: 10.1149/2.0411911jes.

(37) Caballero-Briones, F.; Artés, J. M.; Díez-Pérez, I.; Gorostiza, P.; Sanz, F. Direct Observation of the Valence Band Edge by in Situ ECSTM-ECTS in p-Type Cu2O Layers Prepared by Copper Anodization. *The Journal of Physical Chemistry C* **2009**, *113* (3), 1028-1036. DOI: 10.1021/jp805915a.
(38) Albu, C.; Van Damme, S.; Abodi, L. C.; Demeter, A. S.; Deconinck, J.; Topa, V. Influence of the applied potential and pH on the steady-state behavior of the iron oxide. *Electrochimica Acta* **2012**, *67*, 119-126. DOI: https://doi.org/10.1016/j.electacta.2012.02.008.
(39) Khaselev, O.; Sykes, J. M. In-situ electrochemical scanning tunneling microscopy studies on the oxidation of iron in alkaline solution. *Electrochimica Acta* **1997**, *42* (15), 2333-2337. DOI: https://doi.org/10.1016/S0013-4686(96)00416-1.
(40) Tamirat, A. G.; Rick, J.; Dubale, A. A.; Su, W.-N.; Hwang, B.-J. Using hematite for photoelectrochemical water splitting: a review of current progress and challenges. *Nanoscale Horizons* **2016**, *1* (4), 243-267, 10.1039/C5NH00098J. DOI: 10.1039/C5NH00098J.
(41) Miller, H. A.; Bellini, M.; Oberhauser, W.; Deng, X.; Chen, H.; He, Q.; Passaponti, M.; Innocenti, M.; Yang, R.; Sun, F.; et al. Heat treated carbon supported iron(ii)phthalocyanine oxygen reduction catalysts: elucidation of the structure–activity relationship using X-ray absorption spectroscopy. *Physical Chemistry Chemical Physics* **2016**, *18* (48), 33142-33151, 10.1039/C6CP06798K. DOI: 10.1039/C6CP06798K.
(42) Pullin, H.; Springell, R.; Parry, S.; Scott, T. The effect of aqueous corrosion on the structure and reactivity of zero-valent iron nanoparticles. *Chemical Engineering Journal* **2017**, *308*, 568-577. DOI: https://doi.org/10.1016/j.cej.2016.09.088.
(43) Wang, C. M.; Baer, D. R.; Thomas, L. E.; Amonette, J. E.; Antony, J.; Qiang, Y.; Duscher, G. Void formation during early stages of passivation: Initial oxidation of iron nanoparticles at room temperature. *Journal of Applied Physics* **2005**, *98* (9), 094308. DOI: 10.1063/1.2130890 (acccessed 2020/04/18).
(44) Schwan, J.; Ulrich, S.; Batori, V.; Ehrhardt, H.; Silva, S. R. P. Raman spectroscopy on amorphous carbon films. *Journal of Applied Physics* **1996**, *80* (1), 440-447. DOI: 10.1063/1.362745 (acccessed 2020/04/19).
(45) Hanesch, M. Raman spectroscopy of iron oxides and (oxy)hydroxides at low laser power and possible applications in environmental magnetic studies. *Geophysical Journal International* **2009**, *177* (3), 941-948. DOI: 10.1111/j.1365-246X.2009.04122.x (acccessed 4/20/2020).
(46) Kwon, J. H.; Wilson, L. D.; Sammynaiken, R. Synthesis and characterization of magnetite and activated carbon binary composites. *Synthetic Metals* **2014**, *197*, 8-17. DOI: https://doi.org/10.1016/j.synthmet.2014.08.010.
(47) Jain, V.; Biesinger, M. C.; Linford, M. R. The Gaussian-Lorentzian Sum, Product, and Convolution (Voigt) functions in the context of peak fitting X-ray photoelectron spectroscopy (XPS) narrow scans. *Applied Surface Science* **2018**, *447*, 548-553. DOI: https://doi.org/10.1016/j.apsusc.2018.03.190.
(48) Biesinger, M. C.; Payne, B. P.; Grosvenor, A. P.; Lau, L. W. M.; Gerson, A. R.; Smart, R. S. C. Resolving surface chemical states in XPS analysis of first row transition metals, oxides and hydroxides: Cr, Mn, Fe, Co and Ni. *Applied Surface Science* **2011**, *257* (7), 2717-2730. DOI: https://doi.org/10.1016/j.apsusc.2010.10.051.
(49) Meier, M.; Hulva, J.; Jakub, Z.; Pavelec, J.; Setvin, M.; Bliem, R.; Schmid, M.; Diebold, U.; Franchini, C.; Parkinson, G. S. Water agglomerates on Fe₃O₄(001). *Proceedings of the National Academy of Sciences* **2018**, *115* (25), E5642. DOI: 10.1073/pnas.1801661115.
(50) Gupta, R. P.; Sen, S. K. Calculation of multiplet structure of core p -vacancy levels. II. *Physical Review B* **1975**, *12* (1), 15-19. DOI: 10.1103/PhysRevB.12.15.
(51) Grosvenor, A. P.; Kobe, B. A.; Biesinger, M. C.; McIntyre, N. S. Investigation of multiplet splitting of Fe 2p XPS spectra and bonding in iron compounds. *Surface and Interface Analysis* **2004**, *36* (12), 1564-1574. DOI: 10.1002/sia.1984 (acccessed 2020/03/31).
(52) Signorini, L.; Pasquini, L.; Savini, L.; Carboni, R.; Boscherini, F.; Bonetti, E.; Giglia, A.; Pedio, M.; Mahne, N.; Nannarone, S. Size-dependent oxidation in iron/iron oxide core-shell nanoparticles. *Physical Review B* **2003**, *68* (19), 195423. DOI: 10.1103/PhysRevB.68.195423.

(53) Sánchez-Sánchez, C. M.; Rodríguez-López, J.; Bard, A. J. Scanning Electrochemical Microscopy. 60. Quantitative Calibration of the SECM Substrate Generation/Tip Collection Mode and Its Use for the Study of the Oxygen Reduction Mechanism. *Analytical Chemistry* **2008**, *80* (9), 3254-3260. DOI: 10.1021/ac702453n.
(54) Hasché, F.; Oezaslan, M.; Strasser, P.; Fellinger, T.-P. Electrocatalytic hydrogen peroxide formation on mesoporous non-metal nitrogen-doped carbon catalyst. *Journal of Energy Chemistry* **2016**, *25* (2), 251-257. DOI: https://doi.org/10.1016/j.jechem.2016.01.024.
(55) Dembinska, B.; Brzozowska, K.; Szwed, A.; Miecznikowski, K.; Negro, E.; Di Noto, V.; Kulesza, P. J. Electrocatalytic Oxygen Reduction in Alkaline Medium at Graphene-Supported Silver-Iron Carbon Nitride Sites Generated During Thermal Decomposition of Silver Hexacyanoferrate. *Electrocatalysis* **2019**, *10* (1), 112-124. DOI: 10.1007/s12678-018-0501-3.
(56) Lu, Z.; Chen, G.; Siahrostami, S.; Chen, Z.; Liu, K.; Xie, J.; Liao, L.; Wu, T.; Lin, D.; Liu, Y.; et al. High-efficiency oxygen reduction to hydrogen peroxide catalysed by oxidized carbon materials. *Nature Catalysis* **2018**, *1* (2), 156-162. DOI: 10.1038/s41929-017-0017-x.

CHAPTER 3. Metal-Free Nitrogen-Doped Nanocarbons for In-Situ H_2O_2 Production

3.1 Introduction

We have developed electrochemical method for *in-situ* hydrogen peroxide production under terrestrial and zero-gravity flight experiments.[3, 13] Similarly, we have synthesized and successfully tested iron- and carbon-based catalysts to produce *in-situ* hydrogen peroxide with an electrochemical approach.[11]

Currently, we are aiming our research to produce metal-free catalysts to prevent metal leaching during the production of hydrogen peroxide. However, a metal-free electrocatalyst need a conductive support, with capacitive energy storage, and stability during long periods of time. The capacitive energy storage can be enhanced by preparing highly porous structures with larger surface area, and by increasing the polarizabilities at the electrochemical interface.[130] [131] Due to their structural and physicochemical properties, [132] [133] carbon nano-onions (CNOs) seem as candidates to be modified in order to improve their conductivity, stability, and energy storage capacity.

We can improve electrical[134] and catalytic properties[135] of carbonaceous materials by introducing nitrogen-active[136] anchoring sites through nitrogen-doping treatments. Heating CNOs between 700 to 800 Celsius degrees, the detachment of functional groups causes formation of swinging bonds on carbon atoms,[137] which can form N-C bonds if in presence of dicyandiamide (2-cyanoguanidine). Heating dicyandiamide to 700 Celsius degrees results in generation of nitrogen and cyano fragments, that act as precursors for nitrogen groups.[138] N-doping can be done by condensation of dicyandiamide to produce mesoporous N-doped materials with high local order,[139] with just NH_3 and HCN as decomposition products.[140]

In this Chapter, we reveled a N-doping method using dicyandiamide as nitrogen source and carbon nano-onions (CNOs) and Vulcan XC-72R as carbonaceous precursors. Electrochemical properties and H_2O_2 production in 0.1 M KOH were proved by the Koutecký-Levich (K-L) kinetics analysis, the rotating ring-disk electrode (RRDE) technique, and *in-situ* H_2O_2 generation in the Peroxide Generation Unit (PGU) develop by our team.[13] [11] Results show that the nitrogen-based catalyst synthesized---the nitrogen-doped carbon nano-onions (NCNOs) and the nitrogen-doped Vulcan (NVulcan)---are efficient for the *in-situ* H_2O_2 production under the compatibility conditions of the drinking water resources available in the International Space Station (ISS): 2-3 mS/cm of conductivity, a pH window between 5.5 and 6.7, and total organic carbon (TOC) concentration range <0.18 to 2.5m/L. [141] Having in consideration that RO water is electrochemically unfavorable, in comparison with a strong electrolyte such as a 0.1 M KOH solution, we consider that our results are promising for the *in-situ* hydrogen peroxide production. The method presented here, catalyzed by nitrogen-doped nanocarbons, represents an alternative to the existing industrial method used for H_2O_2 production changing hazardous and costly techniques, and switching them toward, sustainable, ecological, heavy-duty, and low-cost nitrogen-based systems.

3.2 Experimental Setup

3.2.1 Materials and Electrochemical Methods

Synthesized carbon nano-onions (CNOs)[133] and commercial Vulcan XC-72R were used as carbon-based substrates, and dicyandiamide (2-cyanoguanidine) was used as nitrogen source. The nitrogen-doping process of the carbon-based substrates was done at 700 Celsius degrees, during 1 hour under argon atmosphere. System was previously purged with argon and heated with a temperature increasing rate of 3 Celsius degrees

per minute until reach 700 Celsius degrees. After finishing the thermal treatment, system was cold down at 5 Celsius degrees per min.

3.2.2 Physicochemical Characterization

The metal presence in Vulcan and CNOs was determined by using Induced Coupled Plasma–Optical Emission Spectroscopy (ICP–OES). Concentrations of Fe, Co, Mn, Pd and Pt were obtained with an Optima 8000 Perkin Elmer ICP – OES, with standard plasma parameters as shown in Table SI1b and SI1c. Metal extraction was done digesting 10 mg of each sample with a 10 mL aqua regia solution, refluxing them until 1 mL remained. An extra aliquot of 5 mL of aqua regia was added to all samples and heated until a paste was produced. The solutions were filtered through Whatman glass microfiber filters (GF / F grade) and volume was completed to 25 mL with 2% HNO_3 solution.

Chemical functionalities of the pristine CNOs and Vulcan, and the nitrogen-based catalysts were evaluated with Raman Spectroscopy. Raman spectra were obtained with a Thermo Scientific DXR Raman Microscope with a laser wavelength of 532 mm at room temperature. Measurements were done in a wavelength window between 100 and 3000 cm^{-1}, with an error of ±2 cm^{-1}, and 5.0 mW pf laser power.

Surface chemical compositions of nitrogen-based catalysts were obtained with X-ray Photoelectron Spectroscopy (XPS). A PHI 5600ci spectrometer, with an Al Kα polychromatic X-ray source of 350 W settled at 45° and a hemispherical electron energy analyzer and 500 μm X-ray spot aperture, was used to obtain the XPS spectra. Pressure was kept bellow 9×10^{-9} mbar inside the ultrahigh vacuum analysis chamber. Samples were fixed ana analyzed on carbon tape. Survey spectra and high-resolution spectra for Fe 2p, C 1s, and O 1s XPS binding energy regions were fitted and analyzed using

Multipack Physical Electronics curve-fitting software. The binding energy was corrected by the C 1s peak at 284.5 eV.

Electron microscopy was done with a 200 kV JEOL ARM 2200 at the Instituto de Investigación de Materiales of the Universidad Nacional Autónoma de México. The study was performed with spherical aberration-corrected scanning transmission electron microscopy (Cs-STEM), operated in STEM mode at accelerating voltage of 80 or 200 kV, and coupled with energy dispersive X-ray spectrometer (EDS). Micrographs were studied with Gatan Microscopy Suite (DigitalMicrogragh).

3.2.3 Electrochemical Characterization

Inks of NCNOs, CNOs, NVulcan, and Vulcan were prepared mixing, and sonicating for 1 h, 1 mg of catalyst with 50 mL of DI water, 50 μL of isopropanol, 150 μL of ethanol, and 20 μL of 5% Nafion solution. Subsequently, 3 μL of the prepared ink were dropped cast on a cleaned glassy carbon surface, and dried at room temperature for 15 min. ORR activity was measured on a glassy carbon rotating disk electrode (RDE) at a potential window from 0.9V to −0.2V vs RHE. The Koutecký-Levich (K–L) analysis[90] was completed in O_2-saturated 0.1 M KOH solution, at 10 mV/s, and rotation speeds between 400 and 2400 rpm. Similarly, the rotating ring disk electrode (RRDE) analysis was completed by testing the modified glassy carbon disk and its respective Pt ring, fixed at 1.20 V, in 0.1 M KOH and 1600 rpm. The potential was scanned at 10 mV/s between 0.9V and 0V vs RHE.

For the *In-situ* H_2O_2 generation process, electrolyzer output currents and the H_2O_2 percentage weight/weight concentration (H_2O_2 w/w%) in aqueous solution were obtained as a function of the discrete potentials 2, 4, 6, 8, and 10 V. Samples were sonicated during 1 h in a 1:1:2 ethanol:isopropanol:water and 60 μL of 5% Nafion ethanol-based solution. Inks were brushed onto new CeTech carbon cloth gas diffusion electrodes

(GDEs). 2 mL/min of reverse osmosis (RO) water constantly run through the 0.37" thickness catholyte plate. The balance pressure was held at 1 psi. A mixture of Nafion NR 50 Beads and POWDion-Insoluble, 40–60 mesh, was used as electrolyte. The Nafion-based electrolyte was activated at 80 °C in sequential phases as follow: 3% H_2O_2 for 1 h, DI water for 2 h, 1 M H_2SO_4, and stored in DI water. A single pass configuration was used to obtain the polarization curves and determine the concentration hydrogen peroxide produced.

3.3 Results

3.3.1 Raman Spectroscopy

Carbon species on the pristine substrates and on the synthesized nitrogen-doped catalyst were studied by Raman spectroscopy. Figure 3.1 shows Raman spectra of the undoped and N-doped CNOs and Vulcan XC-72R species. All samples show a broad band at 850 cm-1 which remains constant after thermal treatment, and that corresponds to hydrogen-free carbon structures.[119] Likewise, another peak appears at 1000-1200 cm^{-1} on each spectra, this peak is attributed to a sp^3 rich phase in the carbon configuration.[119] Breathing modes of C−C single bonds, which requires a defect for its activation, are shown in the D band at 1350 cm^{-1}; whereas the G peak at 1580 cm^{-1} corresponds to graphitic E_{2g} phonon at G.[142] The CNOs D and G signals emerge at 1340 and 1570 cm^{-1}. Even though the D band of the NCNOs catalyst appears at the same 1340 cm^{-1}, the G band shifts 10 cm^{-1} to 1580 cm^{-1}, decreasing its intensity when compared with CNOs. Similarly, Vulcan shown D and G peaks at 1340 and 1590 cm^{-1}, respectively; NVulcan displays them at 1351 and 1583 cm^{-1}.

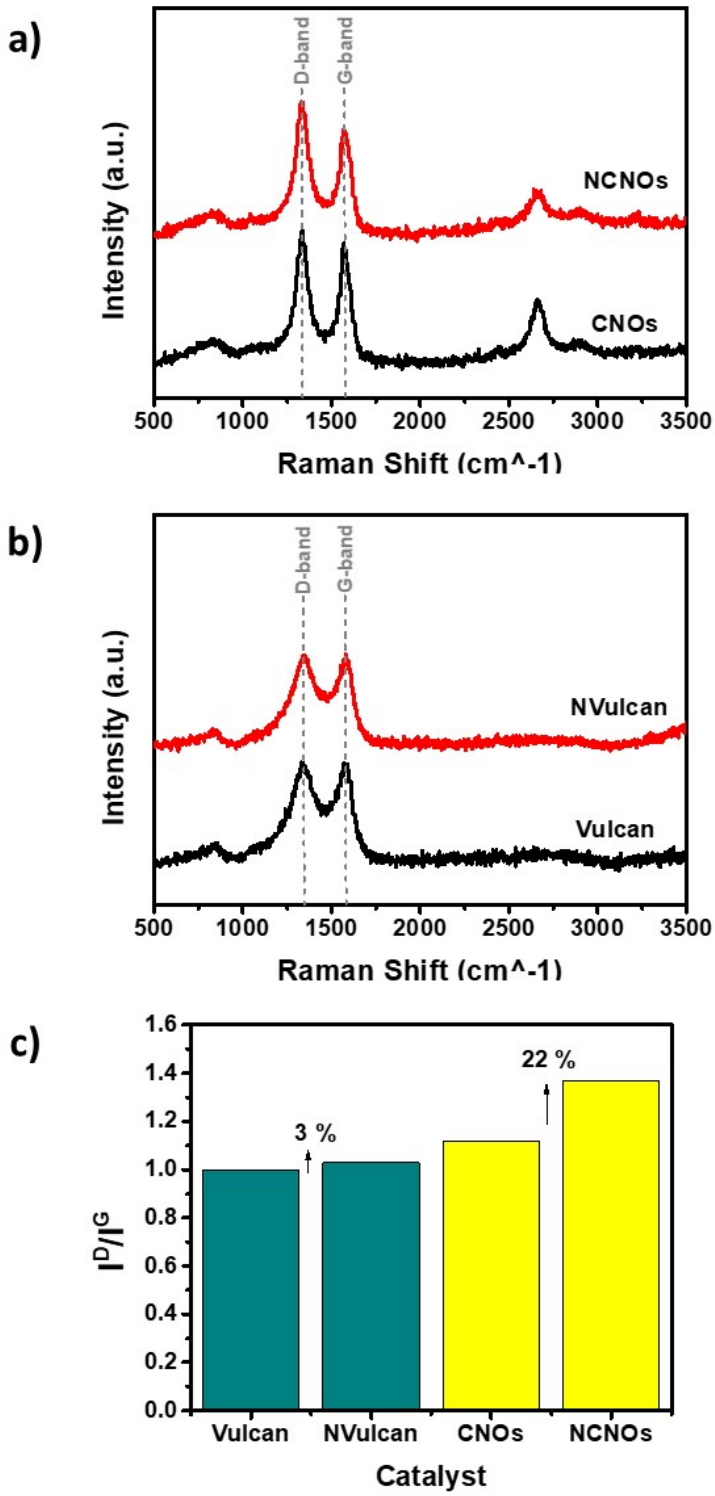

Figure 3.1. Characteristic regions of carbon structures are shown in the Raman spectra of the CNOs and Vulcan XC-72R before and after nitrogen doping process: (a) CNOs and NCNOs, (b) Vulcan and NVulcan, and (c) the degree of graphitization, ID/IG ratio, of each carbonaceous material.

The number of defects in the carbon structures are quantified by the degree of graphitization (I^D/I^G ratio) in Table 3.1. The NCNOs spectrum shows a lower area for the graphitic and sp^2-rich peak, see Figure 3.1a), resulting in an I^D/I^G ratio of 1.37. The higher I^D/I^G ratio, in comparison with the pristine CNOs value, I^D/I^G=1.12, can be attributed to structural changes after nitrogen integration into the CNOs. NVulcan shows an I^D/I^G=1.03 and the pristine Vulcan an I^D/I^G=1.00, see Figure 3.1b). A partial decreasing of sp^3 structures could occur in CNOs and Vulcan after N-doping treatment which produce more internal alterations in CNOs than in Vulcan, as shown in Figure 3.1c): the I^D/I^G shows a 22% of increment after N-doping of CNOs, whereas it was just 3 % after Vulcan doping.

Table 3.1. The degree of graphitization, I^D/I^G ratio, of the CNOs and Vulcan XC-72R before and after the nitrogen-doping treatment.

Pristine Material	**I^D/I^G (± 0.01)**		**Increment (± 0,01%)**
	Undoped	N-Doped	
Vulcan	1.00	1.03	3.00
CNOs	1.12	1.37	22.30

Figure 3.1a) shows the NCNOs and CNOs second-order Raman peaks between 2300 and 3050 cm^{-1}. Three Raman bands appears at 2440, 2660 cm^{-1}, and 2890 cm^{-1} for CNOs; and at 2430, 2670 and 2910 cm^{-1} in the NCNOs spectrum. The highest band at 2600-2700 cm^{-1} belongs to the overtone of the Raman first order at 1350 cm^{-1}.[143] The peak around 2850-2950 cm^{-1} could fit to a mixture from strong Raman modes at 1350 and 1620 cm^{-1}.[144] The peak at 2600-2700 cm-1 is could be a combination of bands at 2719, 2687 and 2684 cm^{-1}. Even though the highly oriented pyrolytic graphite (HOPG) peak at 2684 cm^{-1} and the nanotube peak at 2687 cm^{-1} could be interconnected, nanotube peak has been ambiguously assigned in the literature.[144] As shown Figure 3.1b), the three bands corresponding to the second-order Raman were absent in the Vulcan spectra: high sp^3 configurations in the carbon amorphous structures do not show overtones in the Raman

second region.[142] Amorphous carbon produce broad first-order peaks with low intensity, reducing the signal intensity to the overtone of the Raman second order region.

3.3.2 Transmission Electron Microscopy (TEM)

Figure 3.2 shows TEM micrographs at two different magnifications for CNOs (a and b), NCNOs (c and d), Vulcan (d and e), and NVulcan (g and h). Onion-like structures,[131, 137, 145] with graphitic concentric shells, are presented in CNOs and NCNOs micrographs. Even though Raman analysis show a 22% of variation in the I^D/I^G after N-doping in CNOs, TEM experiments show no morphological differences between NCNOs and CNOs. A high-resolution TEM (HR-TEM) study is highly suggested to determine probable changes in the onion-like carbon shells. For his part, NVulcan and Vulcan micrographs evidence structural changes after the N-doping treatment; NVulcan seem more contracted, compacted, and aggregated than its precursor, Vulcan.

3.3.3 Induced Coupled Plasma-Optical Emission Spectroscopy (ICP-OES)

Iron, platinum, palladium, cobalt, and manganese content were determined through ICP-OES. As shown Appendix 3.1a), in CNOs the iron and cobalt concentrations by mass are below (0.003±0.001)% and (0.0004 ± 0.0001)%, respectively. Whereas, manganese, palladium and platinum are below detection limit (BDL), see Appendix 3.1b) and Appendix 3.1c). Comparing these values with Vulcan XC-72R, the concentration by mass of iron and cobalt are below (0.009±0.001)% and (0.0006 ± 0.0002)%, respectively. Palladium and platinum are below BDL, and Manganese is below quantification limit (BQL). ICP-OES results certify that, in terms of catalytic developments, CNOs and Vulcan XC-72R are metal-free materials, allowing the study of the influence of nitrogen in the ORR kinetics after N-doping treatment.

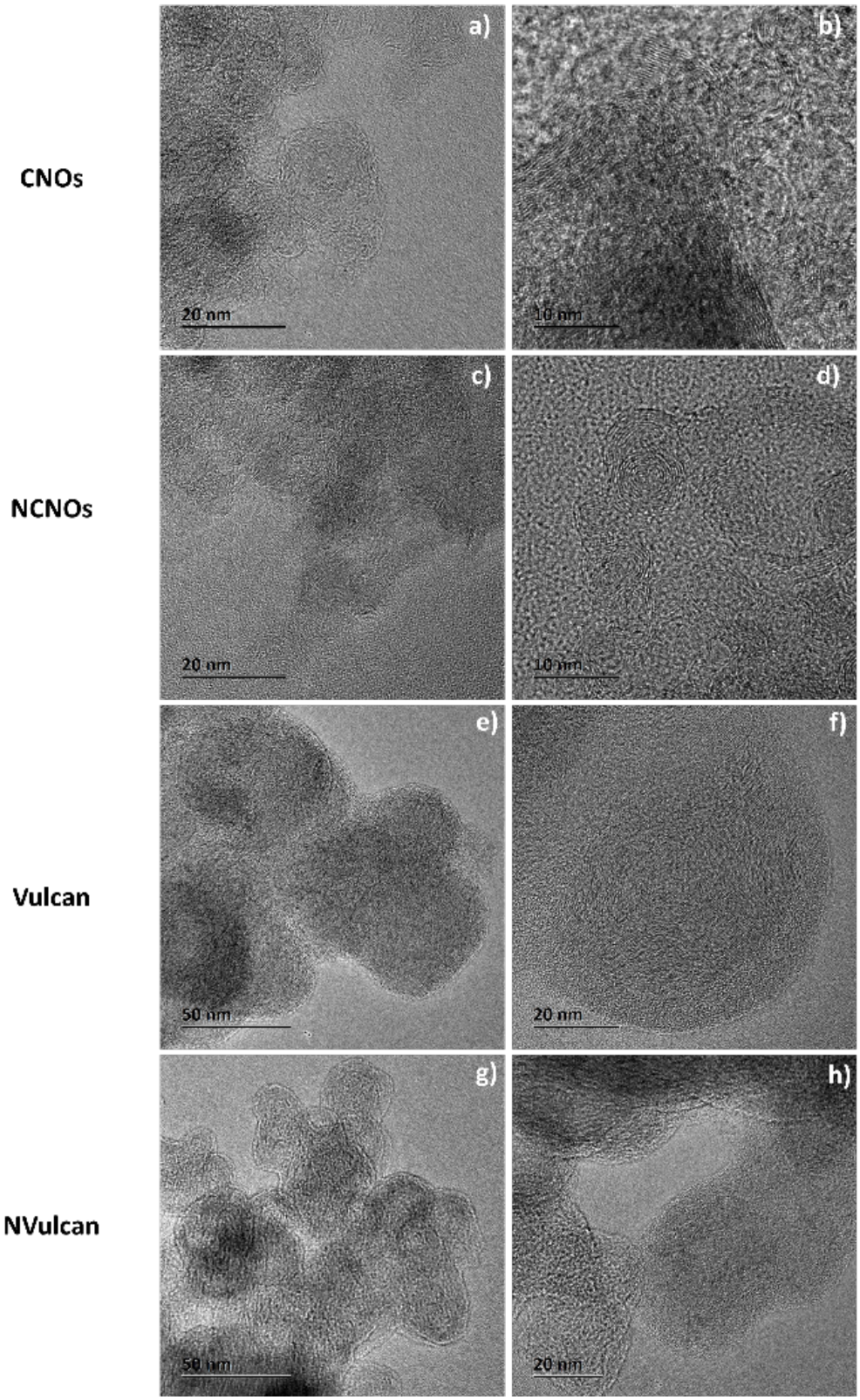

Figure 3.2. Transmission Electron Microscopy (TEM) micrographs at the pristine CNOs (a and b), NCNOs after N-Doping process (c and d), pristine Vulcan (d and e), and NVulcan after doping process (g and h).

3.3.4 Rotating Disk Electrode Analysis – The Koutecký-Levich (K-L) Study

The ORR catalytic activity, of the N-doped samples and the pristine CNOs and NVulcan, was tested in an O_2 saturated 0.1 M KOH solution, see Figure 3.3a). The steady-state polarization was analyzed at a potential scan rate of 10 mV/s and rotating speeds from 400 to 2400 rpm (Appendix 3.2). As classically expected in a steady-state polarization curve, current density growth as the rotation speed increases, revealing a proportional correlation between them. The Koutecký-Levich (K-L) analysis[90, 146, 147] was done by applying Equation 3.1,

$$\frac{1}{j} = \frac{1}{j_k} + \frac{1}{j_d} = \frac{1}{nFkC^0} + \frac{1}{0.62nFD_{O_2}^{2/3}\nu^{-1/6}C^0\omega^{1/2}} \quad (3.1)$$

where j is the measured current density at a given potential, j_k and j_d are the kinetic and diffusion limited current densities, k is the O_2 reduction rate constant, n is the number of electrons involved in the oxygen reduction reaction, F is the Faraday constant (96485 C mol^{-1}), ω is the rotation rate (rad s^{-1}), C^0 is the O_2 saturation concentration in 0.1 M KOH at 1 atm O_2 pressure, D_O is the diffusion coefficient of O_2, and ν is the kinematic viscosity of the solution. Appendix 3.2 shows the disk current vs. rotation speed curves at given potentials, where the slopes and intercepts vary as a function of the applied potential. RDE experiments reveled the number of transferred electrons (n-value), that is related to the mechanism of redox processes during the ORR kinetics. Table 3.2 summarizes the Koutecký-Levich (K-L) [90, 146, 147] analysis results.

The NCNOs and NVulcan evidence a growth in the diffusion-limited current density (j_D), in comparison with CNOs and Vulcan, exhibiting a linear relationship between the rotation speed and the limiting current density, Appendix 3.2. As shown Table 3.2, N-doped samples shift their ORR half-wave potential ($E_{1/2}$) to more positive values: 0.604, 0.298, 0.556, 0.555 vs. RHE to the NCNOs, CNOs, NVulcan, and Vulcan XC-72R, respectively. The onset potential (E_{onset}) result in 0.717, 0.535, 0.634, 0.634 V vs. RHE to the NCNOs, CNOs, NVulcan, and Vulcan XC-72R, respectively.

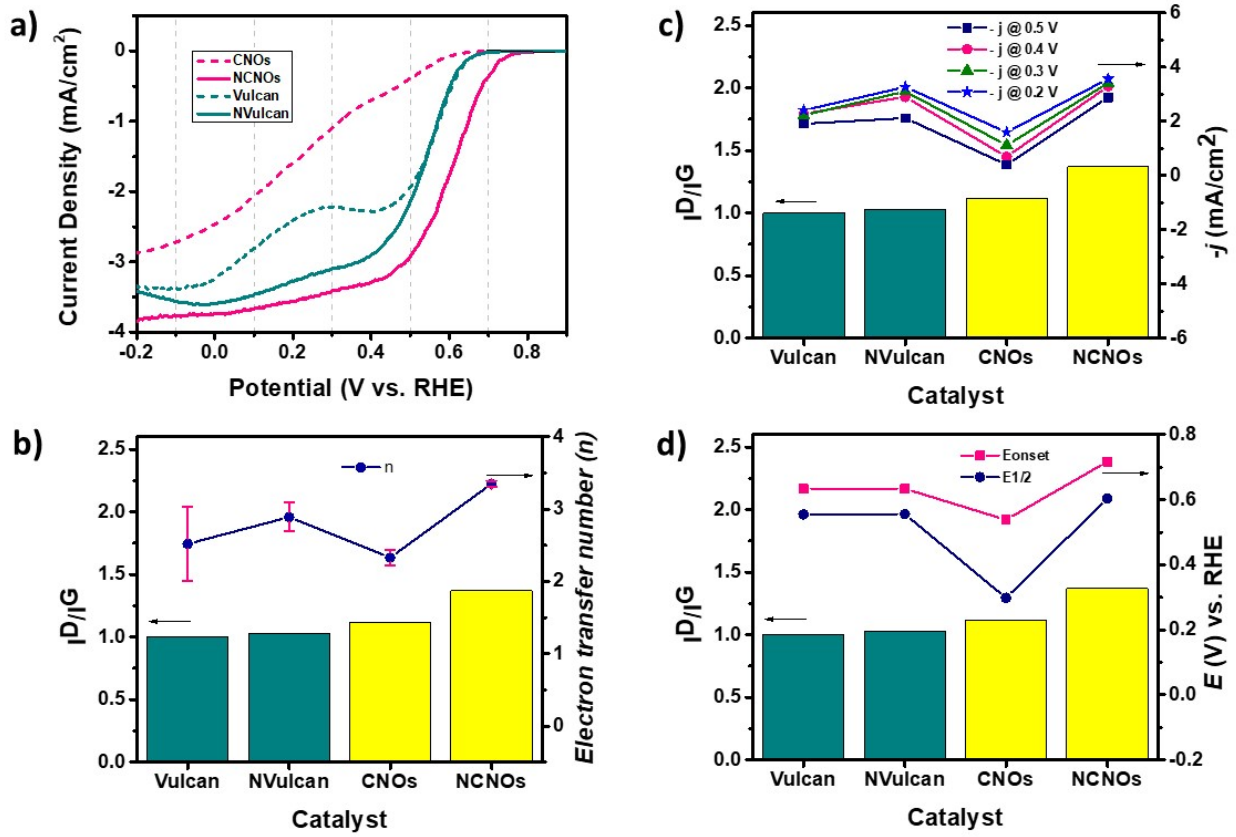

Figure 3.3. Quantitative ORR kinetics the parameters determined in O_2 saturated 0.1M KOH for the CNOs and Vulcan XC-72R before and after the N-doping treatment: polarization plot (a), I^D/I^G ratios and electron number transfer as a function of catalyst (b), I^D/I^G ratios and current density at different potentials as a function of catalyst (c), and I^D/I^G ratios and onset potential (E_{onset}) and half-wave potential ($E_{1/2}$) as a function of catalyst (d).

The NCNOs electron transfer number is 3.35±0.04 e^-, see Table 3.2, suggesting a four-electron pathway in the oxygen reduction process in 0.1M KOH solution. The CNOs K-L analysis revealed a n=2.3±0.1 e^- in alkaline media. Likewise, NVulcan reached a n=2.9±0.2 e^-, suggesting that the NVulcan produces a mixture between two- and four-electron pathway during the ORR. Vulcan XC-72R reveals an n of 2.5±0.5 e^- in alkaline media. Although the Vulcan E_{onset}=0.634 V vs. RHE remains constant after the N-doping process, the growing in the diffusion-limited current density indicates an increment in global catalytic activity, see Figure 3.3c). Figures 3.3b), 3.3c), and 3.3d), confirm

correspondences between the increment of I^D/I^G ratios---22% for CNOS and 3 % for Vulcan---and the growth of the *n*, *j*, E_{onset}, and $E_{1/2}$ values, respectively.

As shown Figure 3.3, electrochemical properties are enhanced by increasing the disorder grade (I^D/I^G) after the N-doping process. The N-thermal treatment produces structural changes, creating conductive N-C bonds, catalytic nitrogen functional groups, new porosity and surface area, and an enriched chemical-physical environment that boost the ORR catalytic properties. Even though, porosity and surface area analysis will be ideal, these analyses are out of the scope of our research. After doping process, the internal structure inside NCNOs and NVulcan will have a mean micropore size wide enough to allow electrolyte and analytes go inside the pores,[148] promoting the diffusion and migration of species inside of the catalysts during the ORR kinetics. [89] ORR E_{onset} and $E_{1/2}$ values for the NCNOs increase as compared with CNOs, showing that ORR catalytic activity improves in terms of diffusion current density and dependents on the nature of the nitrogen-based sites generated after the N-doping process. The aggregated N-based functional groups can change hydrophilicity/hydrophilic ratio, facilitating that analytes and electrolyte penetrate the catalysts during the electrochemical process.

NVulcan show and improved ORR activity in comparison with Vulcan, promoting a combination of the two- and four-electron pathway mechanisms. Even though, in comparison with Vulcan, NVulcan keeps constant its onset potential, it improves its diffusion current density. Nitrogen-doped samples reach the necessary current (j_D) to catalyze the ORR. The NVulcan develops a synergy in the H_2O_2 kinetic---H_2O and H_2O_2 production is a proportional function of the applied potential. NCNOs and NVulcan reach a limiting current density plateau indicating improved diffusion[149] in comparison with their respective precursors which lack of the needed limiting current to reach the ORR. To understand mechanism of the H_2O_2 formation onto our N-catalysts, an in-depth rotating ring-disk electrode (RRDE) analysis is presented in the next section.

Table 3.2. The K-L quantitative ORR kinetics the parameters determined in 0.1M KOH for the CNOs and Vulcan XC-72R before and after the N-doping treatment.

Catalyst	E_{onset} (± 0.001 V vs RHE)	$E_{1/2}$ (± 0.001 V vs RHE)	n (# of e-)	± σ (# of e-)
NCNOs	0.717	0.604	3.35	0.04
CNOs	0.535	0.298	2.3	0.1
NVulcan	0.634	0.556	2.9	0.2
Vulcan	0.634	0.555	2.5	0.5

3.3.5 The Rotating Ring-Disk Electrode Analysis – The Hydrogen Peroxide Production

The NCNOs and NVulcan polarization curves, obtained via the Rotating Ring Disk Electrode (RRDE) Technique, are shown in Figure 3.4. We scan the potential between 850 and 0 mV vs. RHE in a O_2-saturated 0.1M KOH solution, at a scan rate of 10mV/s, and a rotation speed of 1600 rpm. The solid green and pink lines in Figure 3.4a) represent the disk cathodic current (I_D) for the NVulcan and NCNOs, respectively. The ORR is catalyzed between 500 and 600 mV_{RHE} on NVulcan, and between 550 and 700 mV_{RHE} on NCNOs. Diffusion and controlled ORR on the catalyst's surface is confirmed the I_D growing as a function of potential scans. The ORR on NVulcan starts at E_{onset} of 600 mV_{RHE} and reach diffusion limited behavior between 300 and 0 mV_{RHE}. Similarly, the NCNOs E_{onset} is 700 mV_{RHE}, and its diffusion limited behavior is reached between 400 and 0 mV_{RHE}.

RRDE experiments are focused on the H_2O_2 production during the hydrodynamic catalytic analysis at a fixed voltage of 1.2 V which simultaneously oxidizes the peroxide that is formed on the inked disk. H_2O_2 oxidation generate the ring anodic current (I_R) signal. Dotted green and pink lines in Figure 3.4a) correspond to the I_R for the NVulcan and NCNOs, respectively. The H_2O_2 selectivity ($\%H_2O_2$), Equation 3.2, and the electron transfer number (n), Equation 3.3, were calculated was as follow:[20, 150, 151]

$$\%H2O2 = 200\left(\frac{IRing/N}{IDisk+IRing/N}\right) \tag{3.2}$$

$$n = \left(\frac{4IDisk}{IDisk+\frac{IRing}{N}}\right) \tag{3.3}$$

Where I_{Ring} is the ring current, I_{Disk} is the disk current, and N is the collection efficiency.

As shown Figure 3.4b), NVulcan produces an of 3.2 electrons in O_2 saturated 0.1 M KOH, between 550 and 600 mV_{RHE}, with a production of (45-55)% of H_2O_2, see Figure 3.4c). The most stable and lowest detectable formation rates of peroxide is produced between 0 to 300 mV, with an n value of 3.3 and 30 to 35 % of H_2O_2. Likewise, between 550 and 600 mV_{RHE}, NCNOs transfers 3.4-3.5 electrons and generates (45-50)% of H_2O_2. NCNOs catalyst have an n value of 3.6-3.7 and produces about 20 % of H_2O_2, at the window potential between 0 to 300 mV. The RRDE analysis reflects that the NVulcan catalyst produces 15% more H_2O_2 when compared with NCNOs.

The dotted pink line in Figure 3.4a) shows five characteristic states of current associated with the H_2O_2 formation rate as a function of the voltage applied on the NCNOs- and NVulcan-inked disk.[11, 128] Higher potentials than 750 mV vs. RHE, stage I, shows absence of hydrogen peroxide. Between 600 to 750 mV vs. RHE, stage II, the increasing current denotes production of peroxide. Stage III, between 500 to 600 mV, the constant peroxide formation-decomposition rate is evidenced by the pseudo-plateau of higher values of current. At potentials between 300 to 500 mV, stage IV, peroxide formed on the disk is lower that peroxide consumed on the ring. Lastly, at potentials between 0 and 300 mV, stage V, peroxide production is low but constant due to disk current density is higher at less positive potentials, reducing the current efficiency for hydrogen peroxide formation.

The RRDE analysis shows that NVulcan and NCNOs are catalytically equivalent in terms of hydrogen peroxide generation, with 50% of production between 550 and 600 mV_{RHE}. At potentials below 300 mV, in a region characteristic of the cathode operation in a fuel cell,[129] NCNOs catalyze the ORR via four electrons (n = 3.7) with a production of 20% of hydrogen peroxide. With the N-doping process, the pristine CNOs and Vulcan gained a conductive network and nitrogen anchoring sites where ORR occurs. Also,

nitrogen doping produces N-functional groups that can promote hydrophilic structures, improving electrolyte and analyte transport during the ORR kinetics. The improved conductivity, the enhanced current density obtained, and the increased E_{onset} and $E_{1/2}$, that characteristics that distinguish or NCNOs and NVulcan catalysts and from their pristine precursors.

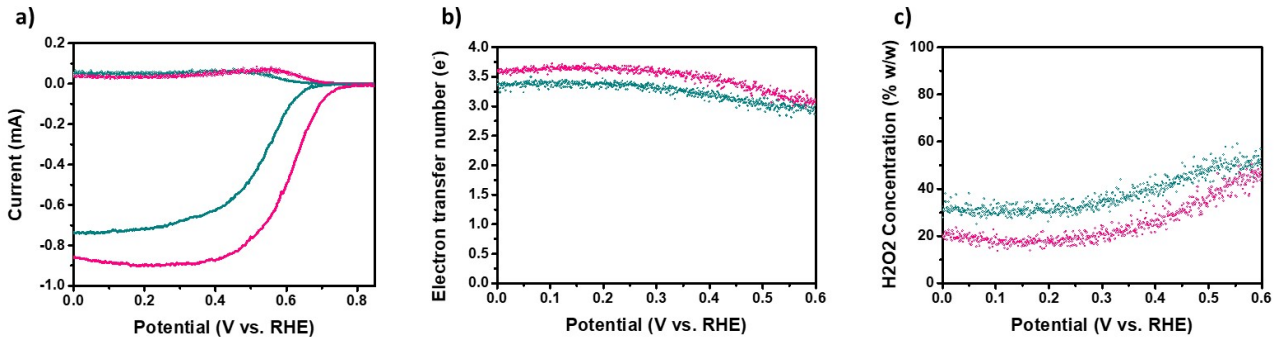

Figure 3.4. Data collected during the hydrodynamic RRDE study of the ORR as a potential function vs. RHE for NCNOs (pink line) and NVulcan (green line) in oxygen saturated 0.1M KOH: (a) disk and current profiles, (b) number of electrons involved in the oxygen reduction reaction, and (c) concentration of hydrogen peroxide. The RRDE analysis was completed by running the catalysts inks onto a glassy carbon disk with a Pt ring at 1600 rpm. The Pt disk potential was swept at a scan rate of 10 mV/s, whereas the ring potential was fixed at 1.20 V vs. RHE.

RDE and RRDE results shown efficient catalysts with controlled ORR process via two- and four-electron pathways. The ORR electron transfer pathway will be controlled and directed through an appropriate modification of the chemical structures on the catalyst surface, adding stable nitrogen and oxygen functional groups, and improving electrical properties of the materials.[148, 152]

3.3.6 Surface analysis by X-ray photoelectron spectroscopy (XPS)

XPS was used to determine the surface chemical composition of NCNOs and NVulcan. Appendix 3.5.a and Appendix 3.5b show the XPS spectra of the N 1s binding energy region of CNOs and Vulcan, respectively; evidencing absence on N in the pristine carbon supports. Figure 3.5 shows the N 1s, O 1s, and C 1s XPS spectra with their respective curve fitting analysis and contribution rate comparison. Before the Voigt

profile analysis[122] used for the curve fitting analysis, into Gaussian-Lorentzian components with similar FWHM, a Shirley background was subtracted. c^2 was below 3 units for all the samples. C 1s peak at 284.5 eV corrected shifts of the binding energies.[153] Appendix 3.3 shows the specific binding energies for the main nitrogen groups in nitrogen doped nanocarbons: pyridinic (398.1-398.9 eV), pyridonic (399.6-399.9),[154] pyrrolic (400.1-400.8), graphitic (401.0-401.6 eV), and N-oxides (402.0-405.0) eV.[134, 155-158]

Figure 3.5a) and 3.5d) show the N 1s region curve fitting analysis for NCNOs and NVulcan, respectively. The relative distribution for each nitrogen-based group and their respective binding energy are summarized in Table 3.3. Nitrogen species in NCNOs are distributed as follow: pyridinic (31.42%), pyridonic (17.59%), pyrrolic (31.58%), quaternary (12.59%), and oxides (6.82%). Though for NVulcan, pyridinic (24.41%), pyridonic (39.21%), pyrrolic (12.57%), quaternary (21.43%), and oxides (2.38%)---Pyridinic and pyrrolic groups lead the nitrogen species at NCNOS; N-pyridonic is the principal N-based group at NVulcan---The initial oxidation degree on the precursors could be the responsible for the final composition of the functional groups in NCNOS and NVulcan.[155] We speculate that the stability of the pristine carbon substrate and its amorphousness-degree determine the nitrogen-based functional group distribution. The N 1s XPS results evidence that the thermal treatment successfully doped with nitrogen both CNOs and NVulcan.

A nitrogen atom bonded to two carbon atoms, a N-pyridinic group, donate one π-electron to aromatic analogous π-systems present in the carbonaceous network of NCNOs and NVulcan. Similarly, a nitrogen atom connected to two carbon atoms in a five-membered heterocycle, a pyrrolic nitrogen group, donates a pair of π-electrons to π-systems that could be inside the NCNOs and NVulcan structures. Pyridinic and pyrrolic functionalities donate free electrons, improving capacitance and electrical properties, and promoting the ORR catalysis.[157, 158]

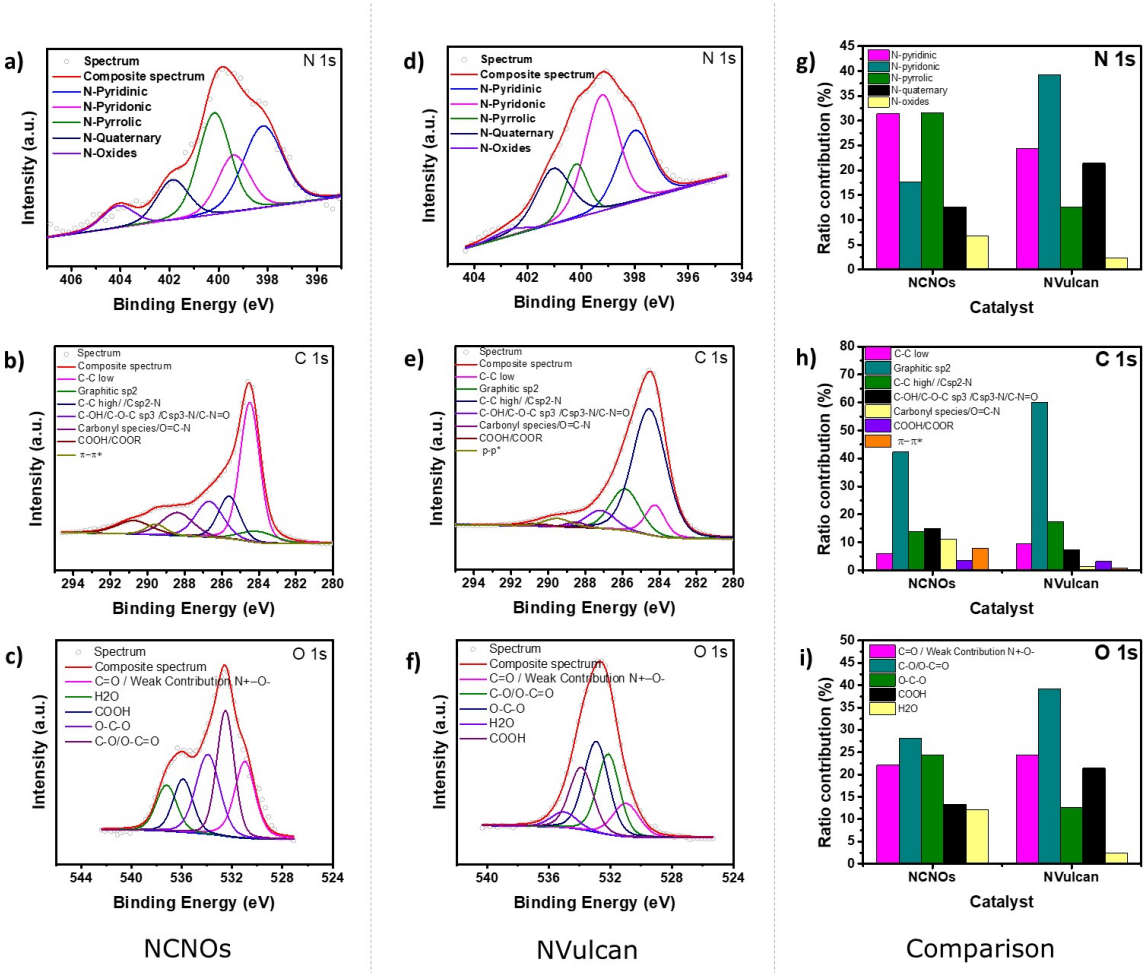

Figure 3.5. X-ray photoelectron spectroscopy (XPS) Voigt deconvolution analysis of the N 1s, C 1s, and O1s binding energy regions for the NCNOs (a, b, and c) and NVulcan (d, e, and f) catalysts analyses. Comparison plot of the percentual ratio contribution by nitrogen, carbon, and oxygen species for the NCNOs and NVulcan catalysts (g, h, and i).

During a doping process, a quaternary nitrogen substitute carbon atoms in the graphene layer, bonding to three carbon atoms into the CNOs and Vulcan frameworks. Graphitic nitrogen lacks free electrons to share, however N-inclusions in the graphitic frame might generate structural modifications.[156] Oxidic nitrogen (oxidized N-pyridinic) is formed by a nitrogen atom connected to two carbon and one oxygen atoms. Interaction of graphitic nitrogen with other atoms in the NCNOs and NVulcan, can produce the N-oxides peak in the XPS spectra. Also, atomic configuration with extremely closed nitrogen atoms can generate signals at higher binding energies. Furthermore, the peak about 401-

402 eV can be correlated to graphitic nitrogen which has shown binding energies between 401 and 403, even in the absence of oxidized nitrogen.[157, 159]

Table 3.3. X-ray photoelectron spectroscopy oxidation state contribution (%) of the N 1s binding energy components, shown in Figure 3.5, for the NCNOs and NVulcan catalysts.

Sample	N 1s Interaction assignments	Binding energy (± 0.01 eV)	Contribution (± 0.1 %)
NCNOs	N-pyridinic	398.20	31.4
	N-pyridonic	399.38	17.6
	N-pyrrolic	400.17	31.6
	N-quaternary	401.88	12.6
	N-oxides	404.08	6.8
NVulcan	N-pyridinic	398.00	24.4
	N-pyridonic	399.22	39.2
	N-pyrrolic	400.20	12.6
	N-quaternary	401.04	21.4
	N-oxides	402.67	2.4

Figures 3.5b, 3.5e, and 3.5h show the XPS C 1s binding energy spectra of NCNOs, NVulcan and the peak contribution analysis, respectively.[84, 89, 153] Appendix 3.4 shows the curve fitting study of the NCNOs spectrum with the surface functional groups C-C_{low} (284.06 eV), graphitic sp2 (284.49 eV), C-C_{high}/Csp2-N (284.61 eV), C-OH/C-O-Csp^3/Csp^3-N/C-N=O (286.67 eV), C=O/O=C-N (288.39 eV), COOH/COOR (289.55 eV), and p-p* transitions (290.74 eV). Likewise, for NVulcan, C-C_{low} (284.24 eV), graphitic sp2 (284.55 eV), C-C_{high}/Csp2-N (285.86 eV), C-OH/C-O-Csp^3/Csp^3-N/C-N=O (287.17 eV), C=O/O=C-N (288.51 eV), COOH/COOR (289.52 eV), and p-p* transitions (290.66 eV).

The peaks at 284.5 eV, that correspond to the sp^2 carbon hybridization state, represent a percentage ratio of 42.3% for NCNOs and 60.1% for NVulcan, see Appendix 3.4. This values that represent the main C1s constituent in both samples, indicating that the non-functionalized carbon state dominates the support matrix configuration. XPS C 1s peaks at 286.5 eV to 289.6 eV are related to carbon-nitrogen interactions, as well as carbon-oxygen bonds within functional groups such as hydroxyl, carboxyl, or carboxylic groups.[84, 89, 153]

The curve fitting of the XPS O 1s spectra shows additional data related to the oxygen-based functionalities present in the samples. Figure 3.5c and 3.5f display the XPS O 1s curve fitting analysis of NCNOS and NVulcan, respectively. The Figure 3.5i and Appendix 3.6 show the percentual contribution of each specie, respectively. Curve fitting, at the XPS O 1s for NCNOs, set the following peaks: C=O/Weak contribution N^{+}–O^{-} (530.98 eV), C-O/O-C=O (532.52 eV), O-C-O (533.93 eV), COOH (535.89 eV), and water (537.20 eV). Whereas, for NVulcan, C=O/Weak contribution N^{+}–O^{-} (530.98 eV), C-O/O-C=O (532.13 eV), O-C-O (532.91 eV), COOH (533.89 eV), and water (535.20 eV).[154, 155]

Previous studies have shown that of nitrogen species and their respective composition change before and after the ORR, suggesting: that the carbon atoms next to N-pyridinic react with -OH species with subsequent change of the N-pyridinic into N-pyridonic, and that the active sites are the carbon atoms next to the pyridinic N rather than pyridinic N themselves.[160] We consider that the percentage of oxygen-based functional groups in our samples affects the oxygen and electrolytes water transport inside of the catalysts carbon supports. We hypothesize that a combination of nitrogen-a and oxygen-based functionalities advantage the ORR as a synergy of chemical/structural interactions in 0.1 M KOH---pyridinic and pyrrolic improve the ORR via 4 electrons, whereas pyridonic works via two-electrons pathway.

3.3.7 *In-situ* H_2O_2 production

Based on the RRDE results, we decided to go a step further testing the NCNOs and NVulcan in the Prototype Generation Unit (PGU) developed by our team. The PGU was designed and built for *in-situ* hydrogen peroxide production under compatibility conditions drinking water resources available in the International Space Station (ISS): 2-3 mS/cm of conductivity, a pH window between 5.5 and 6.7, and total organic carbon (TOC) concentration range <0.18 to 2.5m/L. [141] Furthermore, the PGU was built to support

zero-G environments, which contribute with future secure-cleaned habitats in closed-loop living systems during deep space missions. [3, 11, 13, 141] The PGU is based on a low conductivity water stream, a patented concept of De Nora Technology Inc. (US patent no. 6,254,762 for peroxide).[11] Figures 3.6a) and 3.6b) show a diagram of the PGU and picture of the real reactor, respectively. Figure 3.6c) shows the whole system assembled.

Appendix 3.7 shows polarization plots obtained using NCNOs and NVulcan in the PGU under a single-pass configuration. These output currents, and the H_2O_2 concentration (%w/w), were plotted as a function of the applied potential, and results are shown in Figure 3.6d) and Figure 3.6e), for NCNOs and NVulcan, respectively. Due to the ORR kinetic results, and based on the stability, structure, and physicochemical properties CNOS,[132] our work was aimed to characterize the NCNOs sample by using the PGU. As shown Figure 6d and 6e, curves describe polynomial behaviors regarding H_2O_2 formation, and tendencies suggest that current increase faster in NCNOs than with NVulcan. Data is reported from Appendix 3.8 to 3.11.

Table 3.4 shows that at 2V, the lowest applied voltage, NCNOs produces an output current of 0.05 A and 0.01% of H_2O_2, but current and peroxide values were undetected by using NVulcan as catalyst. At 4 V and 8 V, both materials produce the same concentration of H_2O_2, 0.02% and 0.11%, respectively. These values match with the similar production of hydrogen peroxide previously shown by the RRDE results. At 6 V, the highest concentration of hydrogen peroxide was obtained without bubbles formation, and NCNOs and NVulcan generated 0.06 and 0.07 w/w% H_2O_2, respectively. Similarly, the output currents were 0.40 amps and 0.60 amps for NCNOs and NVulcan, respectively. After 6V, bubbles were formed inside the chamber for NCNOs and NVulcan. As the blue line in Figure 3.6d shows, the tendency of the slope to produce H_2O_2 begins to decrease after 7 V, possibly because the NCNOs promotes H_2O_2 degradation at higher potentials: with the peroxide decomposition rate higher than the formation rate at this potential region. Hence, 6V value was chosen as the reference voltage to compare the efficiency to

produce H_2O_2. Even thought, NCNOs and NVulcan have shown a notable difference in output current, hydrogen peroxide production is slightly higher, 0.07%, on NVulcan, compared with the 0.06 % obtained with NCNOs. Thus, the efficiency increases by 14% for H_2O_2 production in RO water, comparing NVulcan with NCNOs at 6 V. Whereas an increment of 50% in current is earned when NCNOs is compared with NVulcan. NCNOs and NVulcan have equivalent behavior compared to the 0.06 % of H_2O_2 previously generated by the Fe-based catalyst produced by our group, outperforming the 0.03% of H_2O_2 produced by the commercial GDE-MPL.[11]

Based on the total H_2O_2 concentration and the current generated inside the PGU at 6 V, we hypothesize that NCNOs promotes the reactions $O_2 + 2H^+ + 2e^- \rightarrow H_2O_2$ and $O_2 + 4H^+ + 4e^- \rightarrow 2H_2O$, simultaneously. However, an in-dept study with different N-doping proportions is required, to evaluate the influence of nitrogen concentration in the ORR electron pathway, and to achieve a better understanding of the ORR kinetic made by NCNOs and NVulcan. The total products of the ORR mechanism, previously determined by the RRDE technique, could change inside of the PGU. Output products are influenced by the RO water circulating streams, O_2-catalyst interactions, applied voltages, residence time, the reactor inner temperature, interaction with the Nafion-beads electrolyte, and the pH. Also, it is necessary to understand that H_2O_2 could be undetectable in some applied potentials.[128]

Table 3.4 In-situ H_2O_2 generation and output current produced by the NCNOs and the NVulcan catalysts at 2V,4V, 6V, and 8V.

E	**NCNOs**		**NVulcan**	
	H_2O_2	**I**	**H_2O_2**	**I**
(V)	(± 0.01 w/w%)	(± 0.01A)	(± 0.01 w/w%)	(± 0.01A)
2	0.01	0.05	0.00	0.00
4	0.02	0.16	0.02	0.09
6	0.06	0.40	0.07	0.20
8	0.11	0.67	0.11	0.37

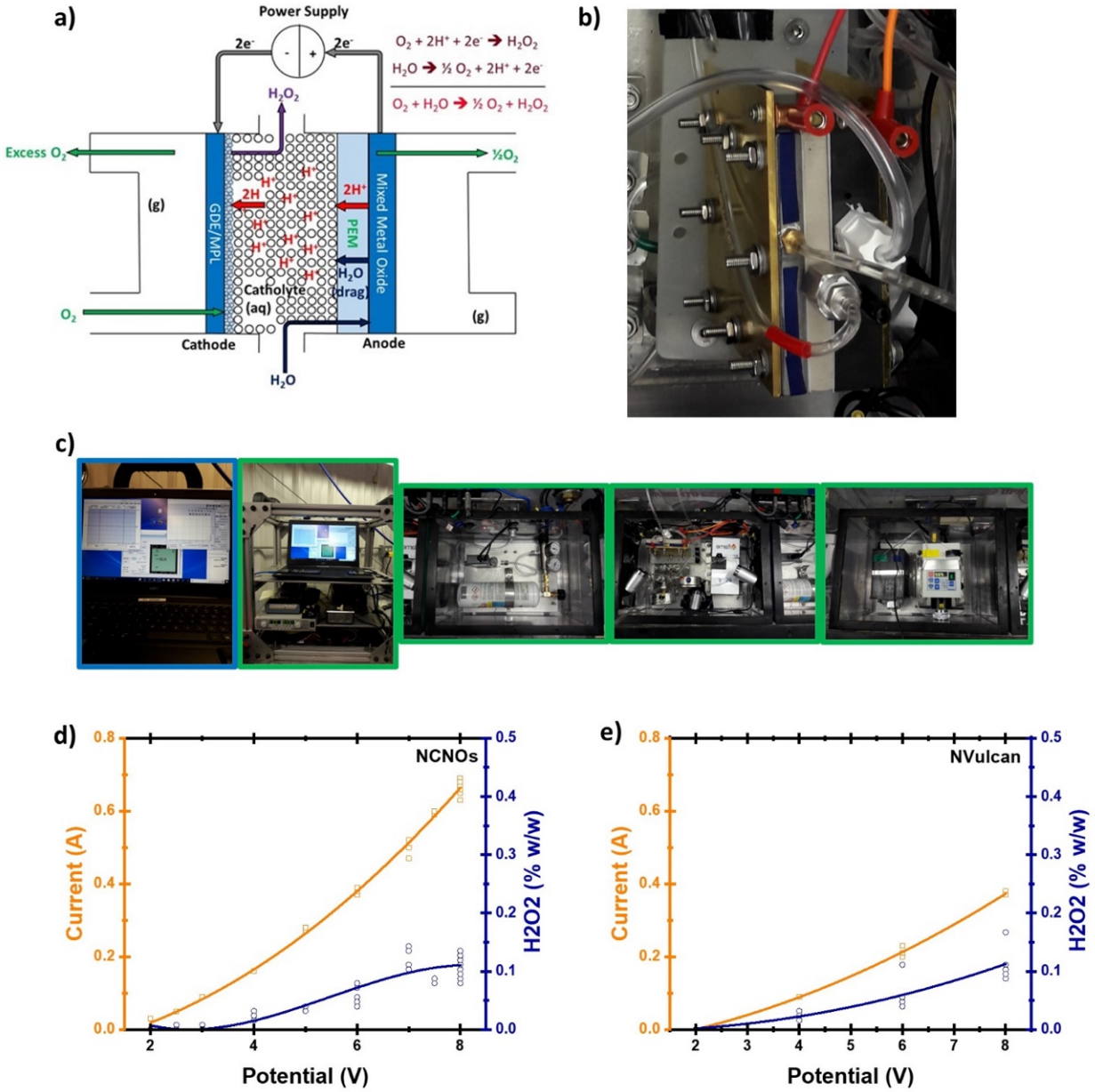

Figure 3.6. *In-situ* H_2O_2 generation: (a) Diagram of the Peroxide Generation Unit (PGU)[11] used for the *in-situ* peroxide generation. (b) Picture of the real reactor. (c) The whole system assembled. Current & H_2O_2 concentration (%w/w) vs. potential plots obtained in the PGU by using (d) the NCNOs, (e) NVulcan.

Concentrations of hydrogen peroxide obtained in this work represent promising results, having in consideration that the RO water conductivity (2-3 mS/cm) used in the PGU is electrochemically unfavorable, in comparison with a strong electrolyte as the 0.1 M KOH solution.[11] Even though NVulcan has shown activity for peroxide production,

NCNOs evidence some features that promote it as a better catalyst: NCNOs is more stable,[132 145] its ORR onset potential in 0.1M KOH appear at more positive values, and the higher values of current obtained with NCNOs facilitate hydrogen peroxide production at lower potentials. All of the above, launches the NCNOs as a promising catalyst for the ORR systems for *in-situ* H_2O_2 generation for Space applications. For future experiments, a recycle-loop orientation[13] is proposed to increase the hydrogen peroxide concentration.

4. Conclusions

Carbonaceous structure of CNOs and Vulcan were doped with nitrogen functionalities using dicyandiamide as N-source. The success of the N-doping method was confirmed by The N 1s XPS curve fitting analysis. Nitrogen leading species at NCNOS are pyridinic and pyrrolic groups, (31.42%) at (398.1-398.9) eV and pyrrolic (31.58%) at (400.1-400.8) eV, respectively. While N-pyridonic (39.21%) at (399.6-399.9) eV is the principal N-based group at NVulcan. The main C1s constituent, with a at peak 284.5 eV in both samples and a percentual ratio of 42.3% for NCNOs and 60.1% for NVulcan, correspond to the sp^2 carbon hybridization state.

The N-doping process added internal modifications at molecular level and partial reduction of sp^3 structures which were confirmed by the increment of the degree of graphitization, I^D/I^G ratio. I^D/I^G changed in 22 % and 3 %, comparing between N-doped and N-undoped species of CNOs and Vulcan, respectively. After thermal treatments both precursors suffered structural changes that were confirmed by TEM.

RDE and RRDE studies of NCNOs and NVulcan evidenced an increased plateau in each limit current density plot, indicating improved diffusion in comparison with their respective precursors. We attribute this increment in current to an improved conductive network that gained nitrogen anchoring sites where ORR occurs. Nitrogen-doping produces N-functional groups that can promote hydrophilic structures, improving

electrolyte and analyte transport during the ORR kinetics. The RRDE analysis reveals the use of NVulcan and NCNOs as metal-free catalysts for the ORR, producing about 50% each, at a window potential between 550 and 600 mV_{RHE}. In terms of the ORR kinetics, the N-doping process improved current density, and shifted E_{onset} and $E_{1/2}$, toward more positive values.

RDE and RRDE results have shown efficient catalysts with controlled ORR process via two- and four-electron pathways. The ORR electron transfer pathway would be controlled and directed through an appropriate modification of the chemical structures on the catalyst surface, adding stable nitrogen and oxygen functional groups, and improving electrical properties of the materials.

NCNOs and NVulcan are promising catalysts to be used under the electrochemically unfavorable RO water conductivity (2-3 mS/cm) in the PGU at low potentials: 2 V for NCNOs and 4 V and 6 V for NCNOS and NVulcan, respectively. A combination of nitrogen- and oxygen-based functionalities, as a synergy of chemical/structural interactions, control the ORR mechanism in 0.1 M KOH, in a rate of four- and two-electrons pathways such as the PGU produces 0.06% for NCNOs and 0.07% for NCNOs at 6V, outperforming by 50% the production of H_2O_2 on the commercial GDL-MPL. Pyridinic and pyrrolic groups improve the ORR via 4 electrons, whereas pyridonic works via 2 electrons. Carbon atoms next to N-pyridinic react with -OH species with subsequent change of the N-pyridinic into N-pyridonic, and the active site is the carbon atom next to the N-pyridinic group instead of the N-pyridinic itself. Likewise, the percentage of oxygen-based functional groups in our samples affects the transport of oxygen, electrolytes, and water inside of the catalysts.

5. Future Works

After thermal treatment both precursors suffer structural changes barely noticeable by TEM, requiring future work to focus on an in-deep characterization through high resolution TEM. Similarly, these catalysts require a pore size and volume distribution and surface area analysis to understand the physical contributions generated on the surface of NCNOs and NVulcan.

6. Acknowledgments

This work was supported by the National Science Foundation NSF-PREM: Center for interfacial Electrochemistry of Energy Materials (CiE^{2}M) grant number DMR-1827622, NSF REU PR-CLIMB Grant No. 1757365, NASA Phase II SBIR Contract NNX16CA43P, and Center for Alkaline Based Energy Solutions (CABES), an Energy Frontier Research Center funded by the U.S. Department of Energy, Office of Science, Basic Energy Sciences under award number DE-SC0019445. The authors acknowledge Dr. Rubén Mendoza Cruz for the TEM images done at the Instituto de Investigación de Materiales of the Universidad Nacional Autónoma de México.

7. References

(1) Vijapur, S. H.; Hall, T. D.; Taylor, E.; Wang, D.; Snyder, S.; Skinn, B.; Peña-Duarte, A.; Cabrera, C. R.; Sweterlitsch, J. *In- Situ* Resource Utilization for Electrochemical Generation of Hydrogen Peroxide for Disinfection. *ICES: International Conference on Environmental Systems* **2019**, *38*, 14 pages.

(2) Nelson, G. J.; Vijapur, S. H.; Hall, T. D.; Brown, B. R.; Peña-Duarte, A.; Cabrera, C. R. Electrochemistry for Space Life Support. *Electrochemical Society Interface* **2020**, *29* (1), 47-52. DOI: 10.1149/2.f06201if.

(3) Peña-Duarte, A.; Vijapur, S. H.; Hall, T. D.; Hayes, K. L.; Larios-Rodríguez, E.; Pilar-Albaladejo, J. D.; Santiago, M. E. B.; Snyder, S.; Taylor, J.; Cabrera, C. R. Iron Quantum Dots Electro-Assembling on Vulcan XC-72R: Hydrogen Peroxide Generation for Space Applications. *ACS Applied Materials & Interfaces* **2021**. DOI: 10.1021/acsami.1c05649.

(4) Kötz, R.; Carlen, M. Principles and applications of electrochemical capacitors. *Electrochimica Acta* **2000**, *45* (15), 2483-2498. DOI: https://doi.org/10.1016/S0013-4686(00)00354-6.

(5) Plonska-Brzezinska, M. E.; Echegoyen, L. Carbon nano-onions for supercapacitor electrodes: recent developments and applications. *Journal of Materials Chemistry A* **2013**, *1* (44), 13703-13714, 10.1039/C3TA12628E. DOI: 10.1039/C3TA12628E.

(6) Plonska-Brzezinska, M. E. Carbon Nano-Onions: A Review of Recent Progress in Synthesis and Applications. *ChemNanoMat* **2019**, *5* (5), 568-580, https://doi.org/10.1002/cnma.201800583. DOI: https://doi.org/10.1002/cnma.201800583 (acccessed 2022/08/28).
(7) Palkar, A.; Melin, F.; Cardona, C. M.; Elliott, B.; Naskar, A. K.; Edie, D. D.; Kumbhar, A.; Echegoyen, L. Reactivity Differences between Carbon Nano Onions (CNOs) Prepared by Different Methods. *Chemistry – An Asian Journal* **2007**, *2* (5), 625-633. DOI: 10.1002/asia.200600426 (acccessed 2020/05/12).
(8) Wang, D.-W.; Su, D. Heterogeneous nanocarbon materials for oxygen reduction reaction. *Energy & Environmental Science* **2014**, *7* (2), 576-591, 10.1039/C3EE43463J. DOI: 10.1039/C3EE43463J.
(9) Rao, C. V.; Cabrera, C. R.; Ishikawa, Y. In Search of the Active Site in Nitrogen-Doped Carbon Nanotube Electrodes for the Oxygen Reduction Reaction. *The Journal of Physical Chemistry Letters* **2010**, *1* (18), 2622-2627. DOI: 10.1021/jz100971v.
(10) Zhang, B.; Wang, C.; Liu, D.; Liu, Y.; Yu, X.; Wang, L. Boosting ORR Electrocatalytic Performance of Metal-Free Mesoporous Biomass Carbon by Synergism of Huge Specific Surface Area and Ultrahigh Pyridinic Nitrogen Doping. *ACS Sustainable Chemistry & Engineering* **2018**, *6* (11), 13807-13812. DOI: 10.1021/acssuschemeng.8b01876.
(11) Zeiger, M.; Jäckel, N.; Mochalin, V. N.; Presser, V. Review: carbon onions for electrochemical energy storage. *Journal of Materials Chemistry A* **2016**, *4* (9), 3172-3196, 10.1039/C5TA08295A. DOI: 10.1039/C5TA08295A.
(12) Thomas, A.; Fischer, A.; Goettmann, F.; Antonietti, M.; Müller, J.-O.; Schlögl, R.; Carlsson, J. M. Graphitic carbon nitride materials: variation of structure and morphology and their use as metal-free catalysts. *Journal of Materials Chemistry* **2008**, *18* (41), 4893-4908, 10.1039/B800274F. DOI: 10.1039/B800274F.
(13) Goettmann, F.; Fischer, A.; Antonietti, M.; Thomas, A. Chemical Synthesis of Mesoporous Carbon Nitrides Using Hard Templates and Their Use as a Metal-Free Catalyst for Friedel–Crafts Reaction of Benzene. *Angewandte Chemie International Edition* **2006**, *45* (27), 4467-4471, https://doi.org/10.1002/anie.200600412. DOI: https://doi.org/10.1002/anie.200600412 (acccessed 2022/08/28).
(14) Zhang, J.-B.; Tan, Z.-C.; Meng, S.-H.; Li, S.-H.; Zhang, L.-M. Heat capacity and thermal decomposition of dicyandiamide. *Thermochimica Acta* **1997**, *307* (1), 11-15. DOI: https://doi.org/10.1016/S0040-6031(97)00323-7.
(15) Ii, J.; Plumlee, D.; Wallace, W.; Gazda, D. *Chemical Characterization and Identification of Organosilicon Contaminants in ISS Potable Water*; 2016.
(16) Koutetskii, Y.; Levich, V. G. The use of a rotating disc electrode for studying kinetic and catalytic processes in electrochemistry. *Dokl. Akad. Nauk SSSR.* **1957**, *117* (3), 441-444.
(17) Schwan, J.; Ulrich, S.; Batori, V.; Ehrhardt, H.; Silva, S. R. P. Raman spectroscopy on amorphous carbon films. *Journal of Applied Physics* **1996**, *80* (1), 440-447. DOI: 10.1063/1.362745 (acccessed 2020/04/19).
(18) Ferrari, A. C.; Basko, D. M. Raman spectroscopy as a versatile tool for studying the properties of graphene. *Nature Nanotechnology* **2013**, *8* (4), 235-246. DOI: 10.1038/nnano.2013.46.
(19) Galiotis, C.; Batchelder, D. N. Strain dependences of the first- and second-order Raman spectra of carbon fibres. *Journal of Materials Science Letters* **1988**, *7* (5), 545-547. DOI: 10.1007/BF01730722.
(20) Hiura, H.; Ebbesen, T. W.; Tanigaki, K.; Takahashi, H. Raman studies of carbon nanotubes. *Chemical Physics Letters* **1993**, *202* (6), 509-512. DOI: https://doi.org/10.1016/0009-2614(93)90040-8.
(21) Mykhailiv, O.; Zubyk, H.; Plonska-Brzezinska, M. E. Carbon nano-onions: Unique carbon nanostructures with fascinating properties and their potential applications. *Inorganica Chimica Acta* **2017**, *468*, 49-66. DOI: https://doi.org/10.1016/j.ica.2017.07.021.
(22) Frumkin, A.; Tedoradse, G. Der Mechanismus der Ionisierung von molekularem Chlor an einer Platinelektrode. *Zeitschrift für Elektrochemie, Berichte der Bunsengesellschaft für physikalische Chemie* **1958**, *62* (3), 251-256. DOI: 10.1002/bbpc.19580620307 (acccessed 2020/04/30).

(23) Frumkin, A.; Nekrasov, L.; Levich, B.; Ivanov, J. Die anwendung der rotierenden scheibenelektrode mit einem ringe zur untersuchung von zwischenprodukten elektrochemischer reaktionen. *Journal of Electroanalytical Chemistry (1959)* **1959**, *1* (1), 84-90. DOI: https://doi.org/10.1016/0022-0728(59)80012-7.
(24) Lozano-Castelló, D.; Cazorla-Amorós, D.; Linares-Solano, A.; Shiraishi, S.; Kurihara, H.; Oya, A. Influence of pore structure and surface chemistry on electric double layer capacitance in non-aqueous electrolyte. *Carbon* **2003**, *41* (9), 1765-1775. DOI: https://doi.org/10.1016/S0008-6223(03)00141-6.
(25) Vélez, C. A.; Corchado-García, J.; Rojas-Pérez, A.; Serrano-Alejandro, E. J.; Santos-Homs, C.; Soto-Pérez, J. J.; Cabrera, C. R. Manufacture of Pd/Carbon Vulcan XC-72R Nanoflakes Catalysts for Ethanol Oxidation Reaction in Alkaline Media by RoDSE Method. *Journal of The Electrochemical Society* **2017**, *164* (14), D1015-D1021. DOI: 10.1149/2.1041714jes.
(26) Garsany, Y.; Ge, J.; St-Pierre, J.; Rocheleau, R.; Swider-Lyons, K. ORR Measurements Reproducibility Using a RRDE. *ECS Transactions* **2013**, *58* (1), 1233-1241. DOI: 10.1149/05801.1233ecst.
(27) Claude, E.; Addou, T.; Latour, J. M.; Aldebert, P. A new method for electrochemical screening basedon the rotating ring disc electrode and its applicationto oxygen reduction catalysts. *Journal of Applied Electrochemistry* **1998**, *28* (1), 57-64. DOI: 10.1023/A:1003297718146.
(28) Paulus, U. A.; Schmidt, T. J.; Gasteiger, H. A.; Behm, R. J. Oxygen reduction on a high-surface area Pt/Vulcan carbon catalyst: a thin-film rotating ring-disk electrode study. *Journal of Electroanalytical Chemistry* **2001**, *495* (2), 134-145. DOI: https://doi.org/10.1016/S0022-0728(00)00407-1.
(29) Sánchez-Sánchez, C. M.; Rodríguez-López, J.; Bard, A. J. Scanning Electrochemical Microscopy. 60. Quantitative Calibration of the SECM Substrate Generation/Tip Collection Mode and Its Use for the Study of the Oxygen Reduction Mechanism. *Analytical Chemistry* **2008**, *80* (9), 3254-3260. DOI: 10.1021/ac702453n.
(30) Hasché, F.; Oezaslan, M.; Strasser, P.; Fellinger, T.-P. Electrocatalytic hydrogen peroxide formation on mesoporous non-metal nitrogen-doped carbon catalyst. *Journal of Energy Chemistry* **2016**, *25* (2), 251-257. DOI: https://doi.org/10.1016/j.jechem.2016.01.024.
(31) Dembinska, B.; Brzozowska, K.; Szwed, A.; Miecznikowski, K.; Negro, E.; Di Noto, V.; Kulesza, P. J. Electrocatalytic Oxygen Reduction in Alkaline Medium at Graphene-Supported Silver-Iron Carbon Nitride Sites Generated During Thermal Decomposition of Silver Hexacyanoferrate. *Electrocatalysis* **2019**, *10* (1), 112-124. DOI: 10.1007/s12678-018-0501-3.
(32) Bleda-Martínez, M. J.; Maciá-Agulló, J. A.; Lozano-Castelló, D.; Morallón, E.; Cazorla-Amorós, D.; Linares-Solano, A. Role of surface chemistry on electric double layer capacitance of carbon materials. *Carbon* **2005**, *43* (13), 2677-2684. DOI: https://doi.org/10.1016/j.carbon.2005.05.027.
(33) Jain, V.; Biesinger, M. C.; Linford, M. R. The Gaussian-Lorentzian Sum, Product, and Convolution (Voigt) functions in the context of peak fitting X-ray photoelectron spectroscopy (XPS) narrow scans. *Applied Surface Science* **2018**, *447*, 548-553. DOI: https://doi.org/10.1016/j.apsusc.2018.03.190.
(34) Blyth, R. I. R.; Buqa, H.; Netzer, F. P.; Ramsey, M. G.; Besenhard, J. O.; Golob, P.; Winter, M. XPS studies of graphite electrode materials for lithium ion batteries. *Applied Surface Science* **2000**, *167* (1), 99-106. DOI: https://doi.org/10.1016/S0169-4332(00)00525-0.
(35) Ayiania, M.; Smith, M.; Hensley, A. J. R.; Scudiero, L.; McEwen, J.-S.; Garcia-Perez, M. Deconvoluting the XPS spectra for nitrogen-doped chars: An analysis from first principles. *Carbon* **2020**, *162*, 528-544. DOI: https://doi.org/10.1016/j.carbon.2020.02.065.
(36) Huang, Z.; Liao, Z.; Yang, W.; Zhou, H.; Fu, C.; Gong, Y.; Chen, L.; Kuang, Y. Different types of nitrogen species in nitrogen-doped carbon material: The formation mechanism and catalytic role on oxygen reduction reaction. *Electrochimica Acta* **2017**, *245*, 957-966. DOI: https://doi.org/10.1016/j.electacta.2017.06.026.
(37) Hu, R.; Li, L.; Jin, W. J. Controlling speciation of nitrogen in nitrogen-doped carbon dots by ferric ion catalysis for enhancing fluorescence. *Carbon* **2017**, *111*, 133-141. DOI: https://doi.org/10.1016/j.carbon.2016.09.038.

(38) Matter, P. H.; Zhang, L.; Ozkan, U. S. The role of nanostructure in nitrogen-containing carbon catalysts for the oxygen reduction reaction. *Journal of Catalysis* **2006**, *239* (1), 83-96. DOI: https://doi.org/10.1016/j.jcat.2006.01.022.
(39) Lai, L.; Potts, J. R.; Zhan, D.; Wang, L.; Poh, C. K.; Tang, C.; Gong, H.; Shen, Z.; Lin, J.; Ruoff, R. S. Exploration of the active center structure of nitrogen-doped graphene-based catalysts for oxygen reduction reaction. *Energy & Environmental Science* **2012**, *5* (7), 7936-7942, 10.1039/C2EE21802J. DOI: 10.1039/C2EE21802J.
(40) Casanovas, J.; Ricart, J. M.; Rubio, J.; Illas, F.; Jiménez-Mateos, J. M. Origin of the Large N 1s Binding Energy in X-ray Photoelectron Spectra of Calcined Carbonaceous Materials. *Journal of the American Chemical Society* **1996**, *118* (34), 8071-8076. DOI: 10.1021/ja960338m.
(41) Betancourt, L. E.; Ortiz-Rodríguez, Á. M.; Corchado-García, J.; Cabrera, C. R. RoDSE Synthesized Fine Tailored Au Nanoparticles from Au(X)4– (X = Cl–, Br–, and OH–) on Unsupported Vulcan XC-72R for Ethanol Oxidation Reaction in Alkaline Media. *ACS Applied Energy Materials* **2019**, *2* (1), 287-297. DOI: 10.1021/acsaem.8b01284.
(42) Guo, D.; Shibuya, R.; Akiba, C.; Saji, S.; Kondo, T.; Nakamura, J. Active sites of nitrogen-doped carbon materials for oxygen reduction reaction clarified using model catalysts. *Science* **2016**, *351* (6271), 361. DOI: 10.1126/science.aad0832.

CHAPTER 4. Uranium onto Boron-Doped Diamond: An Electro-Assembling Method for U-Films Fabrication

4.1 Introduction

4.1.1 The Uranium

Uranium-based technologies under atmospheric environments is scarce and require novel insights and experimental improvements. Uranium composites formation, with homogenous and stable composition is particularly useful for several applications under different atmospheric conditions.[25-28] Stabilization of uranium compounds need solutions against non-inert environments to: (1) improve safety; (2) produce cost-effective processes; and (3) generate environmentally friendly systems for extraction, recycling and recovery, transportation and storage, and fuel development.[29-39] Lately, diverse techniques to control the uranium oxidation have been developed.[40] Uranium oxides are used in catalysts,[41, 42] semiconducting approaches,[43, 44] nuclear technologies,[45] fuel elements in the nuclear core,[6, 51-53] and neutron sensors based on fission-tagging neutron capture for neutron detection.[46-48] This last two applications—fuel elements and fission-tagging capture—can be developed through fissile films formation.

Dimension of fuel elements in the nuclear core are important for space technologies which need: more efficient and transportable systems for transporting fissile materials from Earth to space and safer nuclear-based resources of energy—with fissile materials with well-controlled dimensions within the core fuel elements—.[3, 5, 7, 8, 12] Nasa is looking for new systems based in fission based materials.[14, 15] Likewise, neutron sensors are meaningful for the strategies of deterring nuclear weapons proliferation established by the International Atomic Energy Agency (IAEA).[161] The IAEA recognized the necessity of new technologies and strategies for a new, regenerative, and tunable non-proliferation shield for a safer world.[161, 162] Although IAEA existing efforts for deterring

proliferation, new nuclear treats can proliferate open or clandestinely---this triggers up the necessity of new technologies and strategies for a new, regenerative, and tunable non-proliferation shield for a safer world. Due to deterrence derives from the ability to detect,[162] there is a continuous need create new technologies: such as mobile platforms that will increase deterrence value by adding uncertainty to the possibility of being discovered.[163] Also, uranium monitoring from mines to national laboratories become a compulsory need. The US Department of Energy is addressing protocols for defense of uranium mining and milling sites, in order to protect human health and the environment.[38] For instance, monitoring of nuclear material by using neutron detectors appears as strategy for safeguards and non-proliferation nuclear weapons: at close distances from the nuclear reactor or in a radiation detector network.[164]

4.1.2 Fuel-Fissile Films, Neutrons, and Neutron Detectors

Specifically for space applications, the used of HEU supported in aerogels for core fission fragment rocket engine, as advance propulsion solutions for interplanetary mission, has currently resumed for study.[14, 15] U235 is one of the most practical fissile material due to uranium fission release more than 81% as kinetic energy.[49] The idea is that fission fragments escape from the core of a nuclear reactor.[50] The fuel elements in the core can consist of several parallel fuel (fissile material) films deposited on metallic plates.[6, 51-53] Plate and film thickness affects the core power density generated due to it determine the ratio of fuel-volume to fuel-element surface area accessible for elimination of heat.[5] Variations in film thicknesses produce changes in peak power locations and magnitude increments of the peak power.[54] In this sense, more homogeneous fuel-fissile-based films with well-controlled thickness are needed to improve the efficiency of reactor reactors.

Neutrons are neutral sub-atomic particles. The neutron “neutrality” comes from its quarts content---two valence down quarks and one valence up quark. Neutrons can

decay via the week force into a proton, an electron, and an antielectron neutrino. This behavior allows the study of several interaction inside the Standard Model and beyond--by using more simple interaction-analyses in comparison to entire nuclei performance. An efficient neutron detection with spatial, temporal, and energy resolution is demanded, in order to improve or develop new technologies in research fields focused on non-proliferation of nuclear weapons, neutron scattering, neutron forensics, and dark matter hunting.[165]

Fission detectors are devices used to detect real-time neutron flux. Inside of these detectors, a thin fissile layer situated between parallel anode and cathode that convert incident neutrons into energetic fission fragments, see Figure 4.1.[166] Then, the fission fragments ionize gas within the detector chamber, as a sensing mechanism.[48, 167]

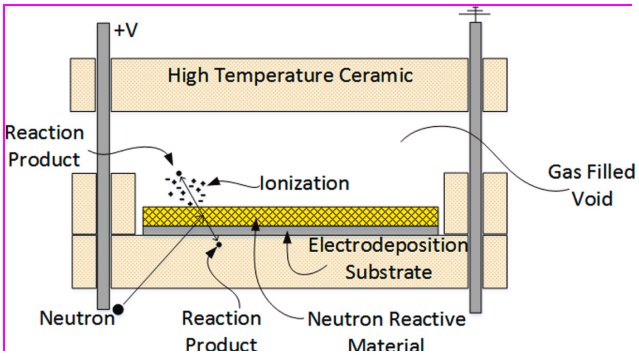

Figure 4.1. Schematic of a Fission Detector[166]

4.1.3 The Problem

Whether for fuel-fissile elements or for fission detectors, we need high quality fission layers. Our strategy was focused on create stable films of fissile materials—as a first approximation of fission layers—that can be used in neutron detectors and extrapolated to fuel elements in nuclear reactors. Fissile electrodes of U and Th have been fabricated through cyclic voltammetry (CV),[168] however this method presented inconsistences such as regions without electrodeposited material and deposition of uranyl-based precursors. Even though on a CV different electrodeposition-stripping

processes can occur to a determined analyte-electrode system, CV represents an inadequate electrochemical technique for electroplating.

Fission detectors demand a precise deposition of fissile material onto varied substrates to evaluate its electrochemical response and chemical physics properties. The fissile material represents the central piece of a detector of neutrons:[46, 168] fissile material quality must be enhanced to achieve its stability and increase the specific activity for neutron detection. Sensitivity and fission response are related to the kind of fissile material fissile and layer dimensions.[168, 169] Taguchi *et al*,[170] have accumulated uranium compounds on diamond electrodes for uranium determination via uranium stripping; however, the electro-assembling process and chemical physics characterization were unspecified. Likewise, uranium onto nickel electrodes has been previously deposited by Saliba *et al*.[171] using a high concentration of uranium precursor instead of using a stable electrolyte that promote processes of nucleation of uranium. Under Saliba *et al* experimental conditions, nitrate can be transformed to a different compound producing a mixture of electrodeposited compounds. Their uranium-based film was fragile after dehydration, showed fractures and crystals formation-accumulation,[171] that can be attributed to precipitation of the precursor material. Even though Saliba *et al* developed an electrode coating process,[171] the experimental conditions that they applied and their yellowish uranium-films, we consider that the major part of the material constitute crystals of uranyl nitrate.

Herein, we proposed an electrodeposition technique of low enriched uranium (LEU) onto boron-doped diamond (BDD) for: uranium oxides electro-assembling, U electrowinning (as U electroextraction alternative), and U-films formation for future applications in neutron detection and fuel elements in nuclear reactors. We hypothesized that the U electrodeposition on BDD would create an electro-assembled uranium-carbon arrangement without crystal growths and regions without uranium compounds. To our understanding, this is the first attempt to create a U- and BDD-based electro-material

through chronoamperometry. This methodology allows the uranium electrowinning from aqueous solution, by forming homogenous U-thin layers that can be used as fissile target material, improving the neutron target efficiency.[166] Our system operates at room temperature and without hazardous compounds. The U-based films obtained consist primarily of uranium oxides that, depending on the application, can be oxidized, or reduced by controlling the atmosphere inside of a furnace. In general, this work contributes with uranium-based technologies---of remarkable need for the uranium-based target formation---through a better understanding of the U electrochemical properties, e.g., formation of uranium oxides, uranium redox systems, and evaluation of uranium compounds stability.

4.2 Electrochemistry of Uranium and the U/BDD Films Fabrication

4.2.1 Materials and Electrochemical Methods

A boron doped diamond (BDD) electrode form Element Six was used as substrate material. The BDD electrode was 10.0x10.0mm, 0.60mm thick Electrochemical Processing Grade Diafilm EP, with a boron concentration between 2 and $6x10^{20}$ atoms/cm^3, and resistivity between 0.20 and $1.8x10^{-3}$ Ohm.m.[172]

The uranium electrochemical properties, such as deposition potential, the onset of hydrogen reduction reaction, and the onset of anodic oxidation, were determined through a linear sweep voltammetry (LSV) and using f uranyl acetate dihydrate as uranium source. The LSVs were done as follows: (1) A new boron doped diamond (BDD) electrode was sonicated during 2 h first in 0.5M H_2SO_4 and then in deionized water (DI). (2) The cleaned BDD was assembled in a plane-electrode electrochemical cell with a reversible hydrogen electrode (RHE) and Pt wire, that were used as refence and counter electrodes, respectively. (3) The electrochemical measurements were done using a SP-200 Potentiate/Galvanostat Electrochemical Workstation from Biologic. (4) The BDD

electrode was tested first in 0.1 M $KClO_4$, and then in a 5 mM uranyl acetate dihydrate ($UO_2(C_2H_3O_2)_2 \cdot 2H_2O$) solution in 0.1 M $KClO_4$. (5) The solutions were bubbled with ultra-high pure N_2 for 15 min. (6) LSV were done in a potential window between 0.85 V and −1.7 V vs RHE and at a potential scan rate of 10 mV/s. These LSVs allowed to study the BDD surface modification and the U nucleation progression. (7) The electrodeposition of uranium on the BDD electrode was controlled by chronoamperometry: BDD electrode was exposed to the 5 mM uranyl acetate in 0.1 M $KClO_4$. After 15 min nitrogen bubbling, the electroplating was done at -1.75 V vs. RHE during 30 min. Finally, samples were rinsed with deionized water, dried, and stored without atmosphere control.

4.2.2 Uranium Electrochemistry: Linear Sweep Voltammetry (LSV) Analysis

Linear Sweep Voltammetry (LSV) was used to study the uranium nucleation on boron-doped diamond (BDD) electrodes. Figure 4.2 shows the LSV of the BBD in 0.1M $KClO_4$ (dashed line) and in 5mM uranyl acetate and 0.1M $KClO_4$ (solid line) at the potential window ranging from: Figure 4.2a) 0.8V to -1.0V vs. RHE; Figure 4.2b) 1.8V to -1.8V vs. RHE. The dashed LSV in Figure 4.2a) shows a broad cathodic peak between 0 to -600 mV, associated with molecular hydrogen formation through protons reduction ($2H^+ + 2e^- \rightarrow H_2$).[173] Cathodic current increases after -700mV with a quasi-vertical tangent steep slope, associate to the kinetically controlled water splitting reaction ($2H_2O + 2e^- \rightarrow H_2 + OH^-$).[174, 175] The solid LSV in Figure 4.2a) shows two cathodic peaks, that appear after adding the uranium precursor. Peak at 200mV can be associate with uranyl (UO_2^+) reduction by transferring one electron and forming either U^{4+} and UO^+ (which is U^{3+}). Subsequently, at -550 mV, U^{4+} is reduced to U^{3+}.[171, 176]

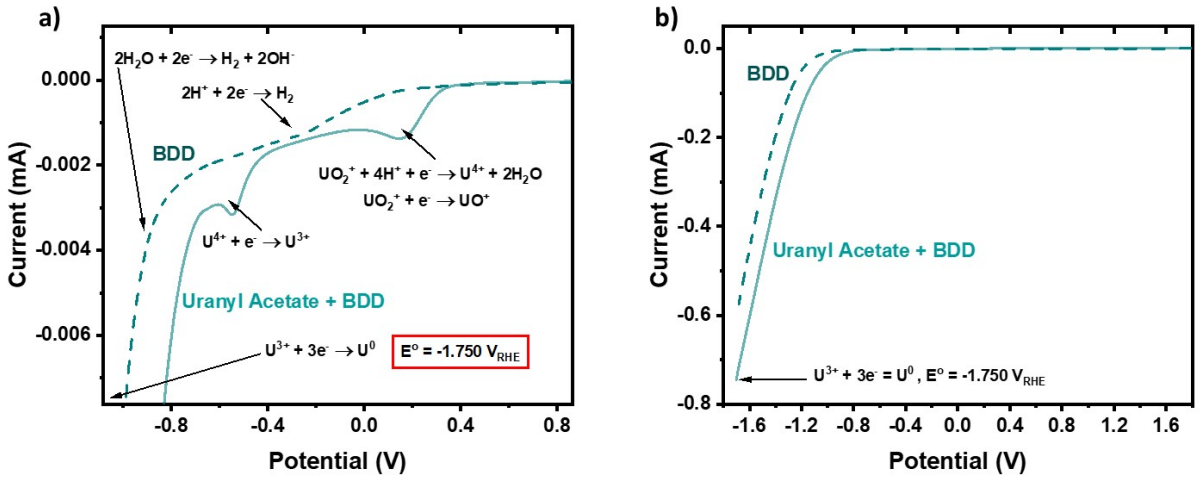

Figure 4.2. Linear Sweep Voltammetry of the boron-doped diamond (BBD) electrode in 0.1M $KClO_4$ (dashed line) and in 5mM uranyl acetate and 0.1M $KClO_4$ (solid line) at the potential window between: a) 0.8V and -1.0V vs. RHE; b) 1.8V and -1.8V vs. RHE.

In presence of uranyl acetate, the hydrogen evolution current is shifted to -650 mV, which can occur due to changes in pH. The standard reduction potential to form metallic uranium is -1.75 V_{RHE}.[171, 176, 177] To reach the uranium electroplating is necessary to work in a potential region with a strong evolution of hydrogen, as shows Figure 4.2b). At this potential region the HER competes with the uranium reduction process. Although HER is a system that must be studied, controlled, and mitigated to reduce its effects in the uranium electrodeposition, HER is out of the scope of this work. We aimed our research to develop an electrodeposition technique to form uranium films for diverse applications.

4.2.3 Uranium Electrodeposition: Electro-Assembling of Uranium onto BDD Electrodes

The uranium onto BDD (U/BDD) electroplating was done through chronoamperometry at -1.750 V vs. RHE for 30 min. Figure 4.3 shows the chronoamperometric analysis of the BBD in 5mM uranyl acetate and 0.1M $KClO_4$. Figure 4.3a) shows the characteristic current profile behavior for electrodeposition systems.[11] Figure 4.3b) shows a dark brown-grayish film, obtained on the BDD electrode after 30 minutes of electrodeposition. The enhanced view in Figure 4.3c), with the first ten

seconds of electrodeposition, evidences a narrow current peak related with the most beginning nucleation[11] of uranium on the BDD electrode. Current spikes associate with the hydrogen evolution,[11, 171] appear in another enhanced view of the chronoamperometric profile between 600 and 1000 seconds, see Figure 4.3d).

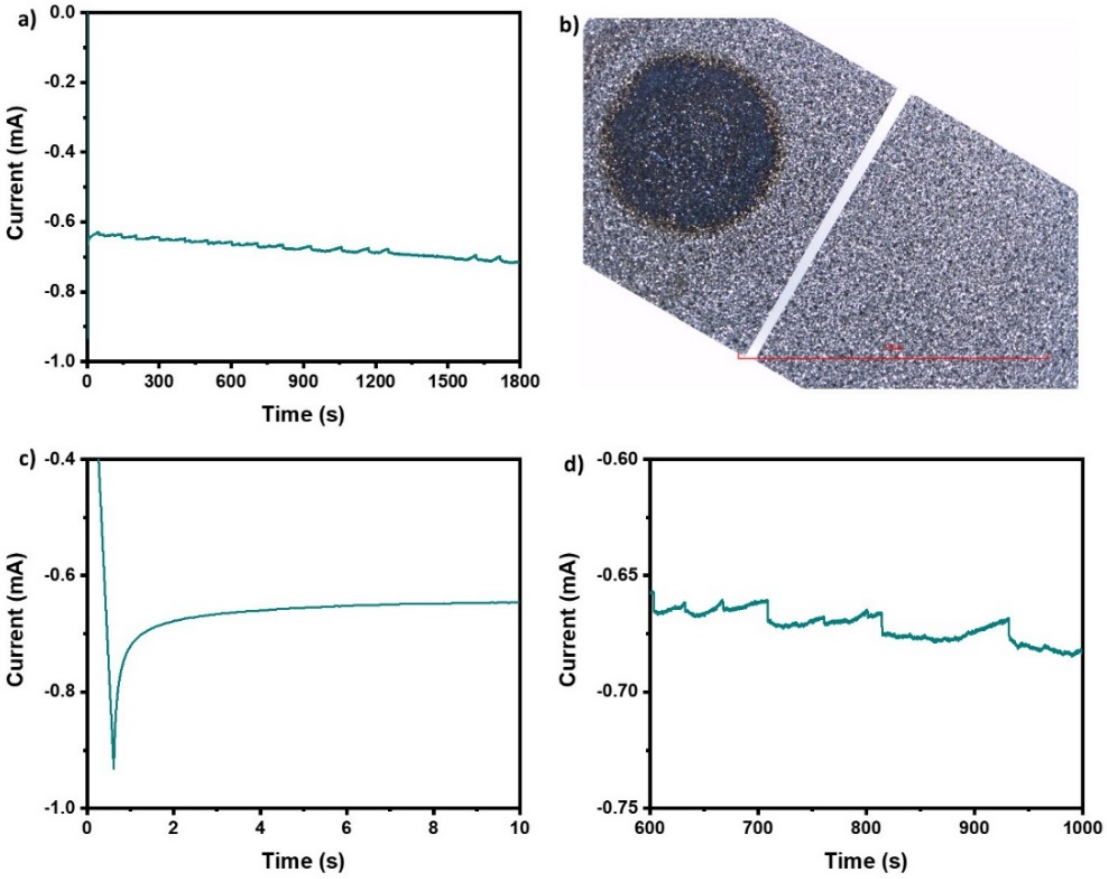

Figure 4.3. Chronoamperometry of the boron-doped diamond (BBD) electrode in 5mM uranyl acetate and 0.1M $KClO_4$ at -1.750 V vs. RHE during 30 min: a) current profile behavior associated with electrodeposition process; b) dark brown-grayish film was obtained on the BDD electrode (figure scale is 10 mm); c) chronoamperometric profile enhanced view of the first ten seconds of electrodeposition, showing a narrow current peak related with the most beginning nucleation of uranium on the BDD electrode; d) enhanced view of the chronoamperometric profile between 600 and 1000 seconds, with current spikes associate with the hydrogen evolution.

Aimed at scaling up this U/BDD electrodeposition system, the contamination with platinum single atoms represents a negligible variable for first a scaled up electrochemical approach forwarded to uranium-films fabrication.[46] This is proved,

having in consideration that previous works reported electrodeposition of uranium species by using CV onto nickel and platinum.[47, 166, 171, 178] Even though the impurities in the fissile material have a negligible effect on fission,[46] a three-electrodes cells with individualized compartments would reduce the probability of contamination with platinum from the counter electrode. For more rigorous studies, we recommend the use of a electrochemical cell with individualized sections for each electrode, linked with conductive bridges, analogous to the cell used in our previously published work.[11]

4.3 Physicochemical Characterization

4.3.1 Experimental Techniques and Setup

The scanning electron microscopy (SEM) with energy-dispersive X-ray fluorescence spectroscopy (EDS) studies were done with an SEM/EDS JEOL JSM-IT500HR. The SEM images were captured by applying an accelerating voltage of 20.0 kV at a working distance (WD) of 10.2mm, and magnifications between x750 and x45,000. The SEM-EDS Mapping study was done with a magnification of x3,500 at 20.0 kV. Sample mapping was obtained in a dwell time of 315 seconds with 64 frames. Chemical functionalities of the pristine BDD support and the U/BDD samples were studied through Raman spectroscopy. Raman spectra were done at room temperature, using a Thermo Scientific DXR Raman Microscope with a laser wavelength of 532 nm. Wavelengths between 100 and 3000 cm^{-1} were measured with an error of ±2 cm^{-1}. The laser power was placed at 5.0 mW to prevent sample changes or decomposition. The dominant composition of functionalities was studied onto the U/BDD surface by using X-ray photoelectron spectroscopy (XPS). The samples were analyzed using a high performance XPS surface analysis system manufactured by Thermo Fisher with an Al Kalfa monochromatic source (1486.68 eV) and with a pass energy of 50.0eV. All binding energies are referenced to C1s at 285.0 eV. Binding energies of the surface species were

identified by using the XPS instrument software. Reproducibility of the electro-assembling technique and stability of the U/BDD system were evaluated by two different specialists preparing three independent coatings of U/BDD in two different laboratories, at the University of Puerto Rico, Río Piedras Campus.

4.3.2 Scanning Electron Microscopy (SEM) & Energy Dispersive Spectroscopy (EDS)

Scanning Electron Microscopy (SEM) & Energy Dispersive Spectroscopy (EDS) results are shown in Appendix 4.4: the pristine BBD electrode, Appendix 4.1a) and 4.1b), and the BDD electrode after the chronoamperometry in 5mM uranyl acetate and 0.1M $KClO_4$, Appendix 4.1c) and 4.1d). SEM-EDS results reveal that the film obtained is essentially uranium-based compounds. The coating obtained covers evenly the BDD surface with small particles below 50 nm, see Appendix 4.2. Some cracks are present on the film which can be produced by influence of the HER. A TEM is suggested for a more accurate size particle analysis.

The U-electroplating technique developed in this work produces uniform and smooth surfaces, free of voids, with homogeneous tiny particles of stable uranium oxides. Contrarily to the chunky particles with uranium compounds mixtures and large fibers of the uranyl-based precursor, previously reported in the literature.[47, 166, 178] This are promising results, taking in consideration that, as was shown in Figure 4.2, the U electrodeposition competes with a strong hydrogen evolution from water splitting.[174, 175] Even though the HER can mitigate the uranium electrodeposition and can remove portions of the electrodeposited film, the SEM/EDS analyses have shown BDD electrodes fully covered with uranium-based films. Although the topography of the U-film is directed influenced by the picks and valleys of the microcrystalline pristine BDD electrode (roughness Ra <30 nm), smooth and uniform uranium coatings are revealed on the plain areas of the electrode.

In Figure 4.4, a SEM-EDS mapping study shows the distribution of uranium, carbon, and oxygen on the BDD surface. Figure 4.4a) shows the SEM micrograph from which the C, U, and O were measured, and described in Figures 4.4b), 4.4c), and 4.4d), respectively. The C-K, U-M, and O-K lines were taken to build the mapped image with the elements' distribution, shown in Figures 4.4e) and 4.4f). Mapping analysis shows that the BDD electrode was uniformly coated with uranium, oxygen, and carbon. Mapping in Figure 4.4 and punctual analysis in Appendix 4.3 show that all the deposited material is uranium, forming a film on the BDD electrode. The oxygen composition obtained by SEM-EDS comes from oxidized uranium species. UO_2 becomes easily oxidized to U_3O_8 in the presence of oxygen when it is present in very fine particles,[36] as shown Appendix 4.1. Carbon originates predominantly from the diamond structure on the electrode; however, a portion of carbon can also come from the acetate contained in the uranium precursor.

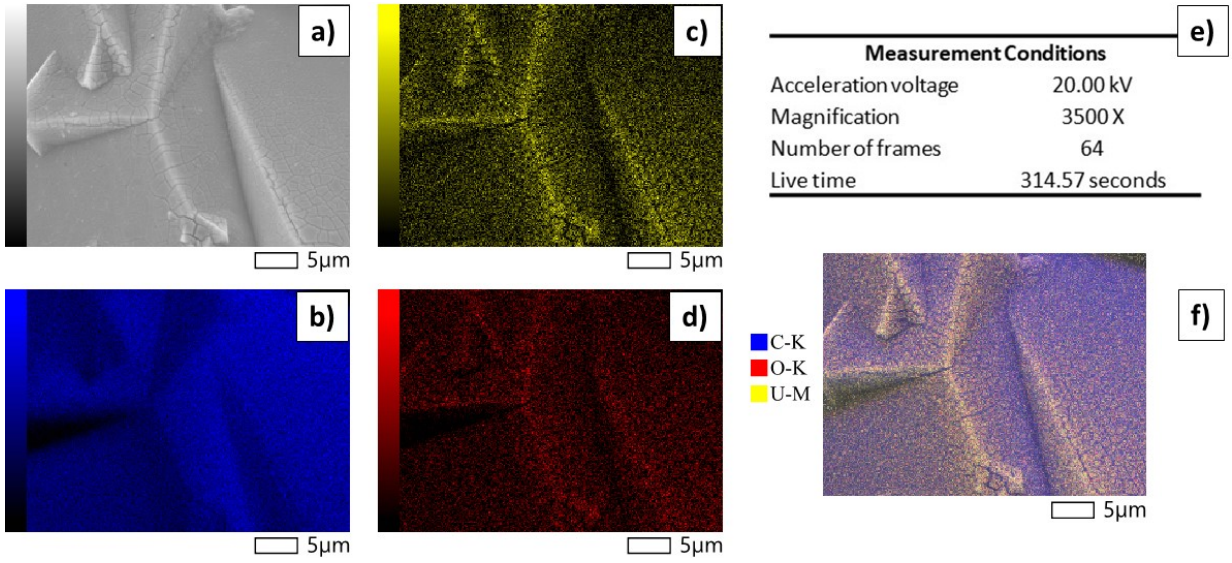

Figure 4.4. SEM mapping with EDS analysis: a) U/BDD SEM micrograph, b) C-K line, c) U-M line, d) O-K, e) measurement conditions, and f) mapped-image with the elements' distribution. SEM micrographs scale is 5 µm.

4.3.3 Raman Spectroscopy

Figure 4.5 shows Raman spectra that evidence the growth of UO_2 and U_3O_8 onto the BDD electrode. Figure 4.5a) shows a peak-free and smooth spectrum for the pristine BDD electrode, at the Raman shift window between 50 to 800 cm^{-1}. Figure 4.5b) reveals Raman peaks at the shifts 625 and 400 cm^{-1} which are associated in the literature with UO_2; the peak at 200 cm^{-1} is related to U_3O_8. The peak at 80-90 cm^{-1} is associated with both uranium oxides, UO_2 and U_3O_8.[179, 180] Nevertheless, Raman spectrum for U_2O_5 has not been yet reported in the literature---conceivably the Raman spectrum shown in Figure 4.5b) belongs to the U_2O_5 specie. The entire Raman spectra of the pristine BBD electrode and the U/BDD sample are presented in Appendixes 4.4a) and 4.4b), respectively. Figure 4.4a) reveals the typical Raman peak for diamond at 1330 cm^{-1} (Fig mode).[181, 182]

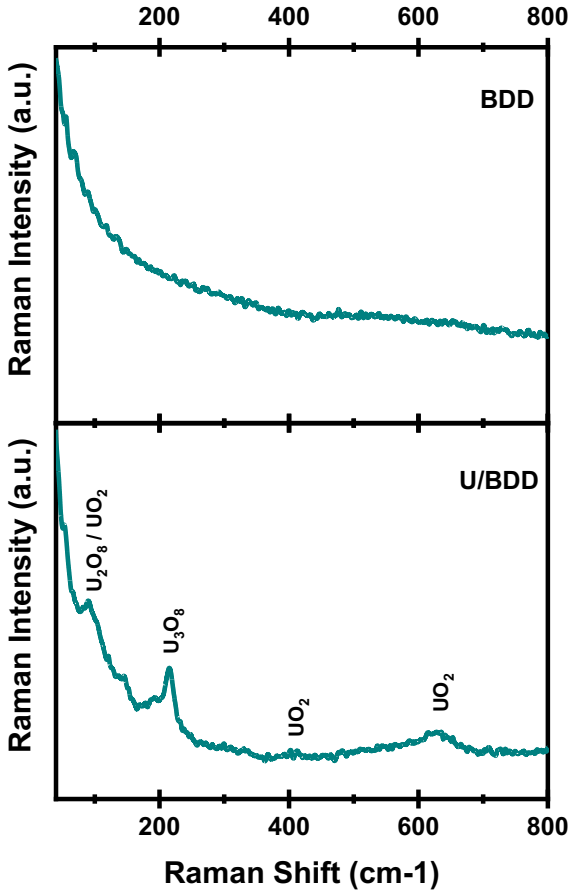

Figure 4.5. Raman Spectra of the pristine BBD electrode in 0.1M $KClO_4$ and the BDD electrode after the chronoamperometric deposition in 5mM uranyl acetate and 0.1M $KClO_4$.

4.3.4 X-ray Photoelectron Spectroscopy (XPS)

Figure 4.6 shows the survey X-ray Photoelectron Spectroscopy (XPS) spectra recorded for three different U/BDD samples. Figure 4.7a) shows the XPS U 4f core-level with the spin orbit split doublet U $4f_{7/2}$ and U $4f_{5/2}$ peaks[28] at 381.9 and 392.8 eV, respectively. The relative energy between peaks is ΔE=10.9 eV. Additionally, the spectrum shows shake-up satellites around the characteristic U 4f doublet, with ΔE of 4.1, and 9.8 eV, with respect to the U $4f_{5/2}$ peak, which can be related to U-O ratios corresponding to stoichiometric proportions of UO_3. Similarly, the ΔE=7.5 eV can be associated with UO_2 and U_2O_5 species.[25, 28] Uranium intermediate oxides can be generated by exposing the U/BDD samples to atmospheric conditions.[28]

Figure 4.7b) shows the O 1s core-level spectrum with three curve fitted peaks at 530.2, 531.1, and 532.2, that are associated with U-O-U, ^{-}O, ^{-}OH bonding, respectively. An additional shoulder related to H_2O emerges at 532.9eV. Figure 4.7c) shows the XPS U $4f_{7/2}$ spectrum curve-fitting with three peaks at 380.0, 380.8, 381.7 eV which can be related to the U^{4+}, U^{5+}, and U^{6+} species, respectively.[183, 184] The U-speciation composition were 37.03, 27.33, and 35.64 % of U^{4+}, U^{5+}, and U^{6+}, respectively. Figure 4.d) shows the XPS C1s binding energy region, with a curve fitting that shows the presence of C-H, C-O, C=O, and COO^{-} functional groups at 284.7, 285.3, 286.3, and 289.1 eV, respectively. The carbon presence, as seen in the XPS survey shown in Figure 4.6 and Table 4.1, come predominantly from the diamond electrode and, probably, from the uranyl acetate solution precursor.

Table 4.1. Element Atomic Composition (%) based on the X-ray Photoelectron Spectroscopy (XPS) survey spectra recorded for the three samples of uranium films electro-assembled onto BDD electrodes, Figure 4.6.

Sample	**Element Atomic Percentage (± 0.01 %)**		
	U 4f7	O 1s	C 1s
U-01	4.52	36.30	59.18
U-02	4.40	35.55	60.06
U-03	5.65	41.90	52.45

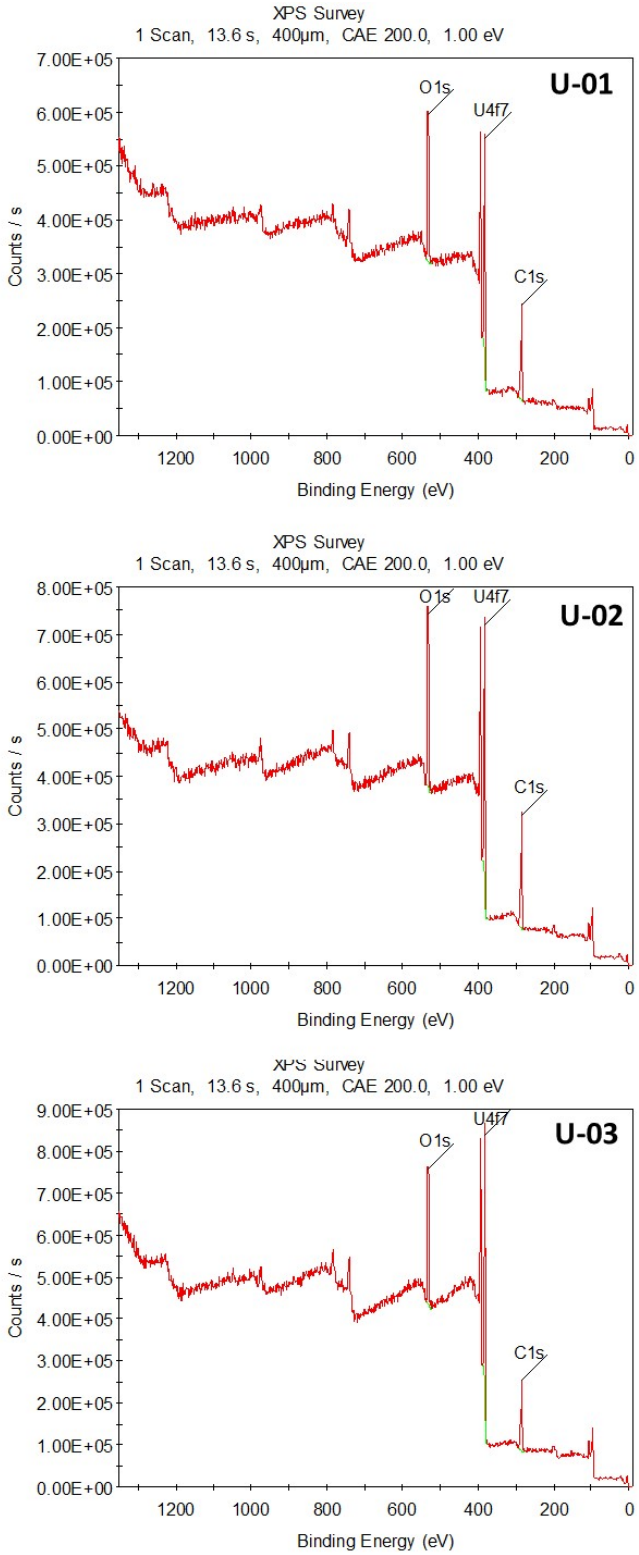

Figure 4.6. X-ray Photoelectron Spectroscopy (XPS) survey spectra recorded for the three samples of uranium films electro-assembled onto BDD electrodes.

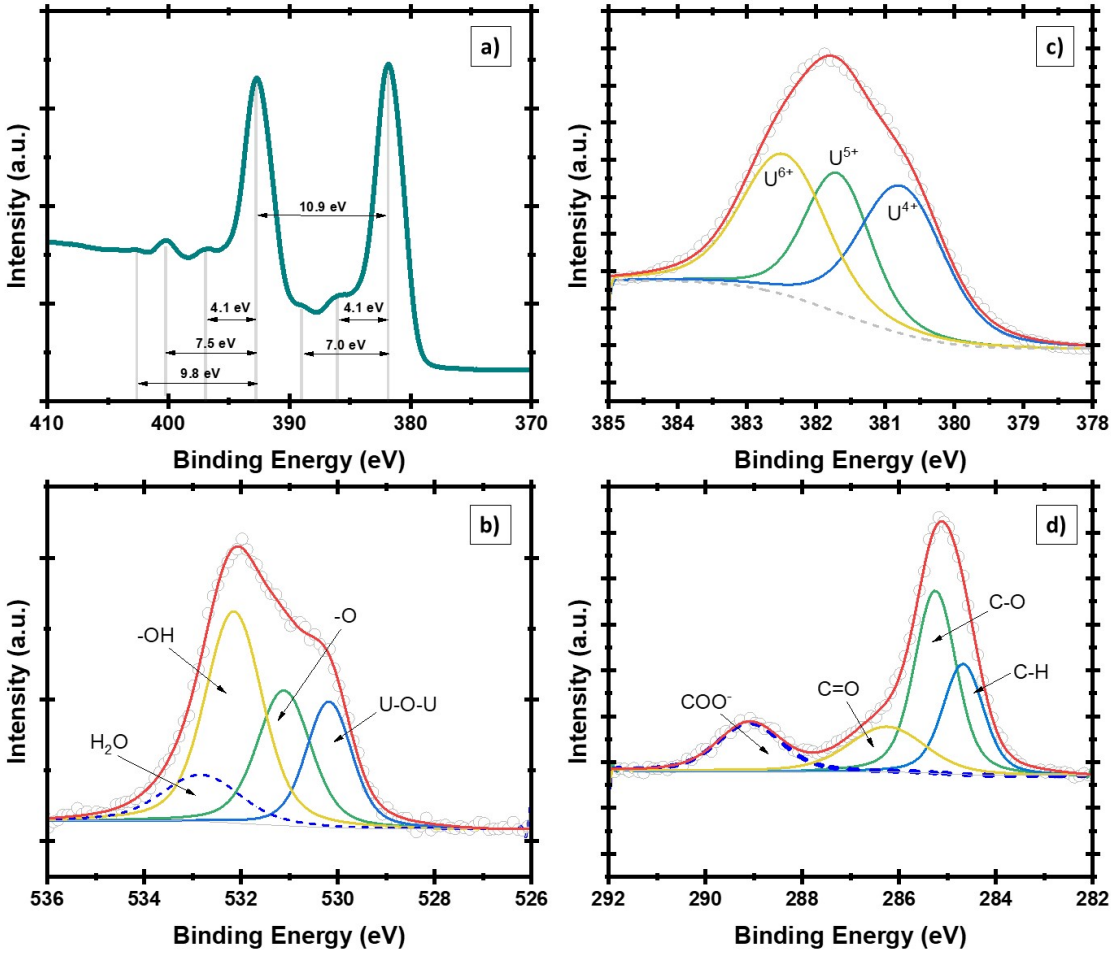

Figure 4.7. X-ray photoelectron spectra recorded for the uranium films electro-assembled onto BDD electrodes: a) U 4f core-level with the relative energy between the U $4f_{5/2}$ and U $4f_{7/2}$ peaks, including the shake-up satellite around the characteristic U 4f doublet; b) O 1s; c) U $4f_{7/2}$ and curve fit; and d) C 1s.

The valence-band XPS binding energy region for U/BDD is shown in Figure 4.8. In the binding energy region between 0 to 15 eV, that correspond to the outer valence molecular orbitals,[29] the XPS spectrum shows a symmetric U5f peak at 1.68 eV, which is consistent with f^1 and f^2 emissions for the configurations U_2O_5 and UO_2, respectively.[25, 28] These results match with the analysis of the U 4f shake up satellite studied in Figure 4.7a). The O 2p transition appears between 2 to 9 eV. Analogously, between 15 to 40 eV, the region of the inner valence molecular orbitals,[29] appear three broadened peaks associated to U $6p_{3/2}$, O 2s, and U $6p_{1/2}$ transitions.

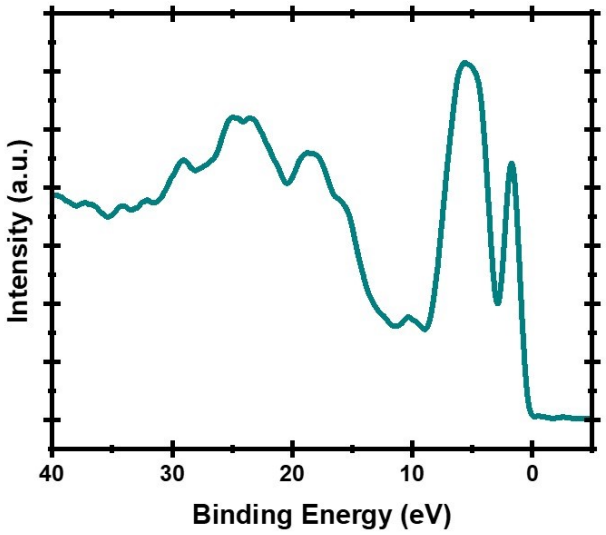

Figure 4.8. X-ray photoelectron spectroscopy's valence band spectra of the U/BDD electrode surface.

4.3.5. A Reproducibility Approach

Appendix 4.5 offers a comparison of the XPS U 4f core-level binding energy region of three different uranium-based samples: U-01, U-02, and U-03. Appendix 4.5 shows imperceptible variations between the all the spectra. As was previously explained in Figure 4.7a), the XPS U 4f region[28] with a ΔE of 10.9 eV between the U $4f_{7/2}$ and U $4f_{5/2}$ peaks, located at 381.9 and 392.8 eV, respectively. For the three samples, the shake-up satellite peaks appear around the characteristic U 4f doublet, with approximately ΔE of 4.1, 7.5, and 9.8 eV, with respect to the U $4f_{5/2}$ main peak. These results evidence reproducibility and stability under atmospheric conditions.

The XPS U $4f_{7/2}$ binding energy region curve fitting is presented in Figure 4.9. Curve-fitting of the spin-orbit pair revealed three peaks at 380.0, 380.8, 381.7 eV associated with the U^{4+}, U^{5+}, and U^{6+} species, respectively.[183, 184] The uranium speciation and composition of each component are presented in Appendix 4.6. Discrepancies in composition can be due to different areas where the samples were irradiated during the

XPS analysis. However, since samples were stored without controlling the atmosphere, the variations reported in Appendix 4.7 are negligible.

The oxidation of uranium stops due to saturation effects between U_3O_8 and UO_3, and this equilibrium was maintained under two different atmospheric conditions in two different laboratories, Molecular Science Research Center and Facundo Bueso Building at the University of Puerto Rico Rio Piedras Campus, with 70-80% of relative humidity. As shown Figure 4.9, the oxidation state IV, V, and IV coexist in all the samples. The presence of U^{5+} avoids corrosion and dissolution,[28] providing stability to the U/BDD system.

Metallic uranium reacts exothermically in water to produce UO_2, releasing -513.2 kcal/mol of U. This high energy indicates high stability of UO_2 in comparison with the metallic uranium electrodeposited, which is oxidized instantly after having contact with water. Analogously, it can be compared to the -285.8 kcal/mol of H released during the formation of water from hydrogen and oxygen.[37]Additionally, UO_2 particles below 0.3 μm are easily oxidized to U_3O_8 in the presence of oxygen gas.[36]

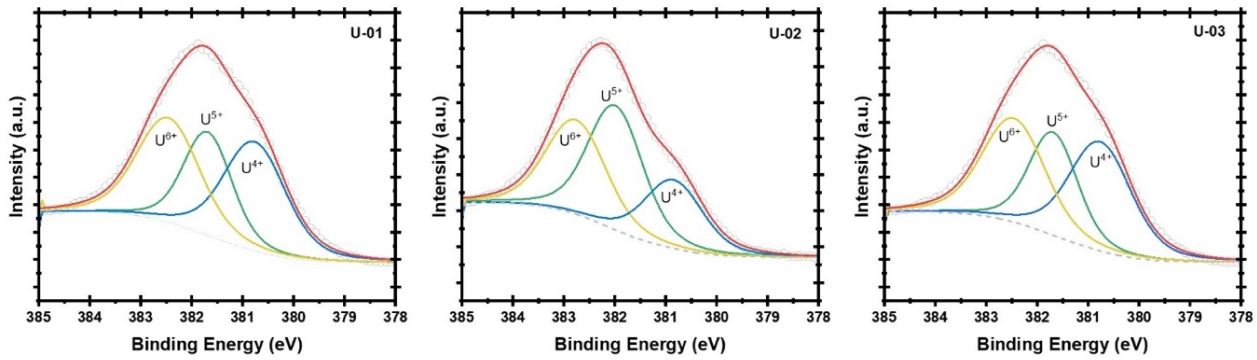

Figure 4.9. X-ray photoelectron spectroscopy of U $4f_{7/2}$ binding energy region comparison recorded for the uranium films U-01, U-02, and U-03 electro-assembled onto BDD electrodes with curve fitting.

Even though BDD electrodes are robust and stable, uranium can react with carbon based materials like graphite forming uranium carbide.[26, 36] In this sense, and to understand what occur in the interface between the uranium film and the diamond electrode, new XPS characterization is proposed. Also, for neutron detection applications, we are planning to evaluate the counting time required to measure neutron sample

activity after U deposition, this will allow to determine the correlation between the chronoamperometric time and the deposited mass and the neutron specific activity. Low-enriched uranium is needed to complete this phase.

4.3.6 X-Ray Diffraction (XRD)

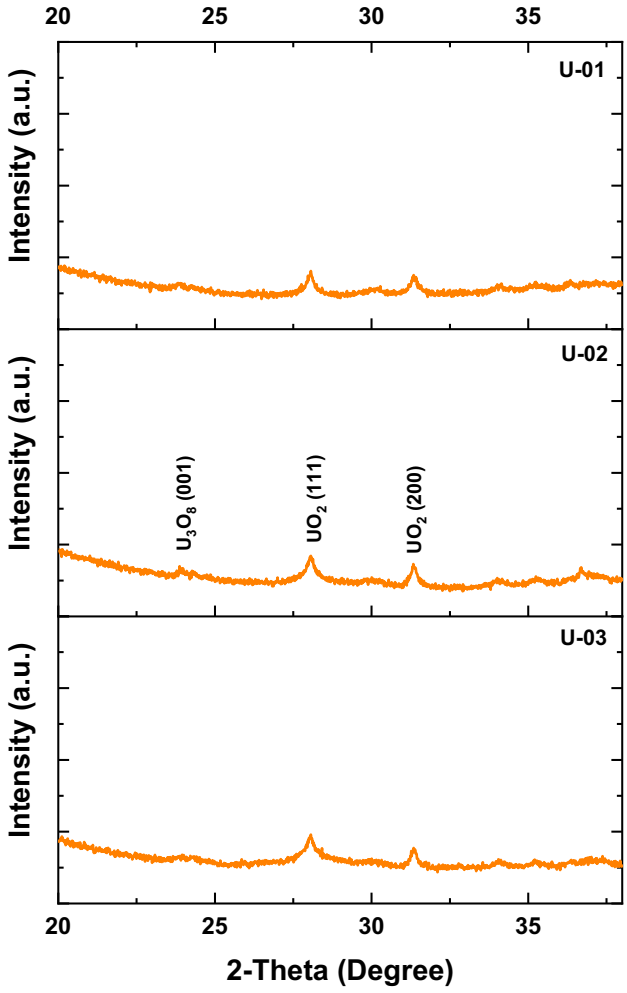

Figure 4.10. An increased area of XRD diffractograms (see Appendix 4.7) between 2 to 38 degrees of the uranium films U-01, U-02, and U-03 electro-assembled onto BDD electrodes.

Based on the scope research for this Chapter, we consider that Raman spectroscopy and x-ray photoelectron spectroscopy (XPS) are two powerful techniques which provide relevant information to determine the oxidation states and what kind of

uranium compounds were electrodeposited. Also, XPS is the technique most used to characterize uranium-based compounds.[25, 28] However, to go a step further, we characterize our U/BDD samples by using XRD. Appendix 4.7 shows XRD diffractograms of the uranium films U-01, U-02, and U-03 electro-assembled onto BDD electrodes. The three samples present an intense pick about 44 degrees corresponding to the diamond (111) diffraction. In Figure 4.10 shows an increased region, between 2 to 38 degrees of diffractograms presented in Appendix 4.7. XRD diffractograms evidence U_3O_8 (001), UO_2 (111), and UO_2 (200).[185-190] All peaks show low intensity, preventing the resolution of other XRD peaks associate to uranium oxides.[185-190] The small thickness of uranium oxide films requires a characterization through grazing-incidence x-ray diffraction (GIXRD). We propose to evaluate the U-based films by using GIXRD, decreasing x-ray penetration depth as decreases the incident angle,[191, 192]to minimize the depth into the sample surface and improve peaks intensity.

4.4 U/BDD Applications: Future Works and Projections

Sensitivity and response in fission detector are determined by the fissile layer mass and to the source of fissile material.[168, 169] In our electrochemical cell the working electrode diameter restricts the film diameter to 0.20 mm, hence the fissile mass can only be modified by the layer thickness. [168, 169] Electrodeposition of uranium films with small thickness could improve homogeneity and evenness on coatings, and also can control oxygen composition.[28] New U/BDD electroplating experiments at different potentials and electrodeposition times are under development. The idea is to determine the optimal control parameters for U deposition onto boron-doped diamond (BDD) electrodes: fission detectors require the accurate deposition and characterization of fissile material. We are evaluating these U-based films through SEM/EDS, Raman spectroscopy, profilometry, and atomic force microscopy (AFM). Also, x-ray photoelectron

spectroscopy (XPS), as the most used characterization technique for uranium-based compounds,[25, 28] is being used to determine the uranium oxidation states. To the best of our knowledge, Raman spectroscopy and XPS are the two most powerful techniques which provide relevant information to determine kind of uranium compounds, and their oxidation states, were electrodeposited.

XRD can be used as complementary characterization technique, however for of uranium oxide films with small thickness, a characterization through grazing-incidence x-ray diffraction (GIXRD) is suggested to minimize the depth into the sample surface and improve peaks intensity: decreasing x-ray penetration depth as decreases the incident angle.[191, 192]

All our experiments were done using U^{238} as a safety way to evaluate and control all parameters required for electrodeposition. Our results obtained with U^{238} can be extrapolated to electrodeposition processes by using Low-Enriched Uranium (LEU): a mixture of U^{235} and U^{238}.[47, 166, 178] In a second phase we are scheduling U electroplating but using LEU, however, this measurements require facilities equipped to work with radioactive materials. The use of LEU reduces the time required to determine the film activity due to U^{235} in the LEU has a higher specific activity compared to natural uranium.[166, 168] Reichenberger *et al*,[166] used LEU to prove the effectiveness of their neutron detectors.

The thickness of our uranium oxides must be controlled to improve the neutron sensitivity applications.[168] In this sense, a study of correlation between chronoamperometric time, thickness of uranium oxide deposited, and the neutron specific activity (NSA) is being planned. The NSA will be evaluated by counting time required to measure the sample activity after deposition LEU films.

4.5 Conclusions

An electroplating method for uranium oxides electro-assembling, electrowinning (as electroextraction alternative), and future neutron detection and fuel-fissile elements applications has been presented. This uranium electrodeposition onto BDD technique creates smooth surfaces, free of voids, with uniform deposition of homogeneous tiny particles of stable uranium oxides. Our U/BDD system suppress U-based chunky particles formation, prevent uranium compounds mixtures, and inhibit crystallization of fibers of the uranyl-base precursor.

The U/BDD electrochemical method operates without high temperatures nor hazardous compounds. U films can be oxidized or reduced inside a hydrogen flow furnace, depending on the application.

The U-based coating on BDD surfaces consists primarily of uranium oxides. Uranium corrosion and oxidation processes occur spontaneously: metallic uranium reacts exothermically with water to produce UO_2.

U^{4+}, U^{5+}, U^{6+} are present and stable under open atmospheric conditions. The small thickness of the films promotes the UO_2 oxidation to U_3O_8 in the presence of oxygen, resulting in a blend of uranium oxides with IV, V, and IV oxidation states.

Our U/BDD electrodeposition method may be used to recover uranium from natural water deposits, using salts dissolved in sea water as electrolyte. Also, it may be used for uranium recycling and recovering from wastewater systems and contaminated waters. Simultaneously, it will co-produce hydrogen during the uranium electrodeposition process on BDD electrodes.

In general, this work contributes with uranium-based technologies, improving them and contributing to a better understanding of their electrochemical properties, e.g., uranium redox processes, uranium oxides formations, and stability studies. The U/BDD electro-assembling method provides a sustainable strategy for uranium electro-recovery from nuclear waste---immobilizing uranium, as storage method, or as U-film fabrication

(U/BDD) for future neutron detection applications. The use of our U/BBD formation as environmental protocol---to recover and immobilize U^{235} and other fissile materials from civil and defense wastes, contaminated systems, and stockpiles---is proposed.

4.6 References

(1) Jamal, G. E.; Gouder, T.; Eloirdi, R.; Jonsson, M. Monitoring the gradual change in oxidation state during surface oxidation or reduction of uranium oxides by photoemission spectroscopy of the 5f states. *Journal of Nuclear Materials* **2022**, *560*, 153504. DOI: https://doi.org/10.1016/j.jnucmat.2021.153504.

(2) Salvato, D.; Vigier, J. F.; Dieste Blanco, O.; Martel, L.; Luzzi, L.; Somers, J.; Tyrpekl, V. Innovative preparation route for uranium carbide using citric acid as a carbon source. *Ceramics International* **2016**, *42* (15), 16710-16717. DOI: https://doi.org/10.1016/j.ceramint.2016.07.138.

(3) Lammers, L. N.; Rasmussen, H.; Adilman, D.; deLemos, J. L.; Zeeb, P.; Larson, D. G.; Quicksall, A. N. Groundwater uranium stabilization by a metastable hydroxyapatite. *Applied Geochemistry* **2017**, *84*, 105-113. DOI: https://doi.org/10.1016/j.apgeochem.2017.06.001.

(4) Gouder, T.; Eloirdi, R.; Caciuffo, R. Direct observation of pure pentavalent uranium in U2O5 thin films by high resolution photoemission spectroscopy. *Scientific Reports* **2018**, *8* (1), 8306. DOI: 10.1038/s41598-018-26594-z.

(5) Maslakov, K. I.; Teterin, Y. A.; Popel, A. J.; Teterin, A. Y.; Ivanov, K. E.; Kalmykov, S. N.; Petrov, V. G.; Springell, R.; Scott, T. B.; Farnan, I. XPS study of the surface chemistry of UO2 (111) single crystal film. *Applied Surface Science* **2018**, *433*, 582-588. DOI: https://doi.org/10.1016/j.apsusc.2017.10.019.

(6) Ulrich, K.-U.; Ilton, E. S.; Veeramani, H.; Sharp, J. O.; Bernier-Latmani, R.; Schofield, E. J.; Bargar, J. R.; Giammar, D. E. Comparative dissolution kinetics of biogenic and chemogenic uraninite under oxidizing conditions in the presence of carbonate. *Geochimica et Cosmochimica Acta* **2009**, *73* (20), 6065-6083. DOI: https://doi.org/10.1016/j.gca.2009.07.012.

(7) Matzke, H. Radiation damage-enhanced dissolution of UO2 in water. *Journal of Nuclear Materials* **1992**, *190*, 101-106. DOI: https://doi.org/10.1016/0022-3115(92)90080-5.

(8) He, H.; Qin, Z.; Shoesmith, D. W. Characterizing the relationship between hyperstoichiometry, defect structure and local corrosion kinetics of uranium dioxide. *Electrochimica Acta* **2010**, *56* (1), 53-60. DOI: https://doi.org/10.1016/j.electacta.2010.09.064.

(9) Smirnov, A. L.; Rychkov, V. N.; Umanskii, A. B.; Galyanina, E. A.; Klyushnikov, A. M. Kinetic features of underground uranium leaching from ores of hydrogenous uranium deposits. *Radiochemistry* **2009**, *51* (1), 61-64. DOI: 10.1134/S1066362209010147.

(10) He, H.; Zhu, R. K.; Qin, Z.; Keech, P.; Ding, Z.; Shoesmith, D. W. Determination of Local Corrosion Kinetics on Hyper-Stoichiometric UO[sub 2+x] by Scanning Electrochemical Microscopy. *Journal of The Electrochemical Society* **2009**, *156* (3), C87. DOI: 10.1149/1.3046112.

(11) Shoesmith, D. W.; Sunder, S. The prediction of nuclear fuel (UO2) dissolution rates under waste disposal conditions. *Journal of Nuclear Materials* **1992**, *190*, 20-35. DOI: https://doi.org/10.1016/0022-3115(92)90072-S.

(12) Glazoff, M.; Van Rooyen, I.; Coryell, B.; Parga, C. *Comparison of Nuclear Fuels for TREAT: UO2 vs U3O8*; 2016.

(13) Delegard, C. H.; Schmidt, A. J. *Uranium Metal Reaction Behavior in Water, Sludge, and Grout Matrices*; PNNL--17815; United States, 2008. http://inis.iaea.org/search/search.aspx?orig_q=RN:40057505.

(14) Energy, U. D. o. *US Department of Energy Strategic Plan, at: https://www.energy.gov/downloads/us-department-energy-strategic-plan-0*. 2020. (accessed.

(15) Harris, W. E.; Kolthoff, I. M. The Polarography of Uranium. III. Polarography in Very Weakly Acid, Neutral or Basic Solution1. *Journal of the American Chemical Society* **1947**, *69* (2), 446-451. DOI: 10.1021/ja01194a073.
(16) Burrell, A. K.; McCleskey, T. M.; Shukla, P.; Wang, H.; Durakiewicz, T.; Moore, D. P.; Olson, C. G.; Joyce, J. J.; Jia, Q. Controlling Oxidation States in Uranium Oxides through Epitaxial Stabilization. *Advanced Materials* **2007**, *19* (21), 3559-3563, https://doi.org/10.1002/adma.200701157. DOI: https://doi.org/10.1002/adma.200701157 (acccessed 2022/04/06).
(17) Walker, G. S.; Lapszewicz, J. A.; Foulds, G. A. Partial oxidation of methane to methanol-comparison of heterogeneous catalyst and homogeneous gas phase reactions. *Catalysis Today* **1994**, *21* (2), 519-526. DOI: https://doi.org/10.1016/0920-5861(94)80175-4.
(18) Lazareva, S.; Ismagilov, Z.; Kuznetsov, V.; Shikina, N.; Kerzhentsev, M. Uranium oxide catalysts: environmental applications for treatment of chlorinated organic waste from nuclear industry. *Environmental Technology* **2019**, *40* (14), 1881-1889. DOI: 10.1080/09593330.2018.1432696.
(19) Craig, A. K.; Sanjoy, M.; David, S.; Thomas, M.; Brandon, S.; Taylor, C.; Jerrad Philip, A. Semiconductor neutron detectors using depleted uranium oxide. In *Proc.SPIE*, 2014; Vol. 9213. DOI: 10.1117/12.2063501.
(20) Young, C.; Petrosky, J.; Mann, J. M.; Hunt, E. M.; Turner, D.; Kelly, T. The work function of hydrothermally synthesized UO2 and the implications for semiconductor device fabrication. *physica status solidi (RRL) – Rapid Research Letters* **2016**, *10* (9), 687-690, https://doi.org/10.1002/pssr.201600203. DOI: https://doi.org/10.1002/pssr.201600203 (acccessed 2022/04/06).
(21) Enriquez, E.; Wang, G.; Sharma, Y.; Sarpkaya, I.; Wang, Q.; Chen, D.; Winner, N.; Guo, X.; Dunwoody, J.; White, J.; et al. Structural and Optical Properties of Phase-Pure UO2, α-U3O8, and α-UO3 Epitaxial Thin Films Grown by Pulsed Laser Deposition. *ACS Applied Materials & Interfaces* **2020**, *12* (31), 35232-35241. DOI: 10.1021/acsami.0c08635.
(22) Technology, M. I. o. *Nuclear Reactor Laboratory, Core Description, https://nrl.mit.edu/reactor/core-description*. 2023. (accessed May 21, 2023).
(23) Newswire, A. N. S.-N. *Inside MIT's Nuclear Reactor - ANS Nuclear Cafe Friday Matinee, https://www.ans.org/news/article-2060/inside-mits-nuclear-reactor-ans-nuclear-cafe-friday-matinee/*. 2018. (accessed May 21, 2023).
(24) Yuan, Q.; Zhao, J.; Mok, D. H.; Zheng, Z.; Ye, Y.; Liang, C.; Zhou, L.; Back, S.; Jiang, K. Electrochemical Hydrogen Peroxide Synthesis from Selective Oxygen Reduction over Metal Selenide Catalysts. *Nano Letters* **2021**. DOI: 10.1021/acs.nanolett.1c04420.
(25) Mark, D. D.; Sebastian, S.; Vincent, M. L. Nuclear Thermal Propulsion. In *Nuclear Reactors*, Chad, L. P. Ed.; IntechOpen, 2022; p Ch. 1.
(26) Bacak, M.; Aïche, M.; Bélier, G.; Berthoumieux, E.; Diakaki, M.; Dupont, E.; Gunsing, F.; Heyse, J.; Kopecky, S.; Laurent, B.; et al. A compact fission detector for fission-tagging neutron capture experiments with radioactive fissile isotopes. *Nuclear Instruments and Methods in Physics Research Section A: Accelerators, Spectrometers, Detectors and Associated Equipment* **2020**, *969*, 163981. DOI: https://doi.org/10.1016/j.nima.2020.163981.
(27) Reichenberger, M. A.; Unruh, T. C.; Ugorowski, P. B.; Ito, T.; Roberts, J. A.; Stevenson, S. R.; Nichols, D. M.; McGregor, D. S. Micro-Pocket Fission Detectors (MPFDs) for in-core neutron detection. *Annals of Nuclear Energy* **2016**, *87*, 318-323. DOI: https://doi.org/10.1016/j.anucene.2015.08.022.
(28) Unruh, T.; Reichenberger, M.; Stevenson, S.; McGregor, D.; Tsai, K. *Enhanced Micro-Pocket Fission Detector for High Temperature Reactors - FY17 FInal Project Report* . U.S. Department of Energy - Office of Scientific and Technical Information, United States, 2017. https://doi.org/10.2172/1468579DOI: doi:10.2172/1468579.
(29) Nelson, G. J.; Vijapur, S. H.; Hall, T. D.; Brown, B. R.; Peña-Duarte, A.; Cabrera, C. R. Electrochemistry for Space Life Support. *Electrochemical Society Interface* **2020**, *29* (1), 47-52. DOI: 10.1149/2.f06201if.

(30) Vogel, S. C.; Monreal, M. J.; Shivprasad, A. P. Materials for Small Nuclear Reactors and Micro Reactors, Including Space Reactors. *JOM* **2021**, *73* (11), 3497-3498. DOI: 10.1007/s11837-021-04897-3.
(31) Harvey, S.; Communication, I. O. o. P. I. a. *Ensuring Safety on Earth from Nuclear Sources in Space*, https://www.iaea.org/newscenter/news/ensuring-safety-on-earth-from-nuclear-sources-in-space. 2020. (accessed May 21, 2023).
(32) Fulton, J.; Laboratories, S. N. *Space Nuclear Launch Safety*, https://energy.sandia.gov/programs/nuclear-energy/launch-safety-for-space-nuclear-missions/. (accessed May 21, 2023).
(33) Lin, C.-S.; Youinou, G. Design and Analysis of a 250 MW Plate-fuel Reactor for Nuclear Thermal Propulsion. *Nuclear and Emerging Technologies for Space* **2020**, 95-99.
(34) Weed, R. *Aerogel Core Fission Fragment Rocket Engine, NIAC 2023 Phase I and Phase II Selections*, https://www.nasa.gov/directorates/spacetech/niac/2023/. 2023. (accessed 2023 May 21).
(35) Weed, R.; Horsley, M.; Chapline, G. Aerogel Supported Fission Fragment Rocket Engine Core. *Nuclear and Emerging Technologies for Space (NETS-2022), Proceedings* **2022**.
(36) IAEA Division of Public Information, Department of Safeguards, *Safeguards: Staying Ahead of the Game*, Vienna, Austria, 2007.
(37) Rosenthal, M.; Stern, W. M. *Deterring Nuclear Proliferation: The Importance of IAEA Safeguards*; 2019.
(38) Cazalas, E. Defending Cities Against Nuclear Terrorism: Analysis of A Radiation Detector Network for Ground Based Traffic. *Homeland Security Affairs* **2018**, *14*.
(39) van der Ende, B. M.; Li, L.; Godin, D.; Sur, B. Stand-off nuclear reactor monitoring with neutron detectors for safeguards and non-proliferation applications. *Nature Communications* **2019**, *10* (1), 1959. DOI: 10.1038/s41467-019-09967-4.
(40) Clark, R.; Sheldon, R. Dusty Plasma Based Fission Fragment Nuclear Reactor. In *41st AIAA/ASME/SAE/ASEE Joint Propulsion Conference & Exhibit*, Joint Propulsion Conferences, American Institute of Aeronautics and Astronautics, 2005.
(41) Chapline, G. Fission fragment rocket concept. *Nuclear Instruments and Methods in Physics Research Section A: Accelerators, Spectrometers, Detectors and Associated Equipment* **1988**, *271* (1), 207-208. DOI: https://doi.org/10.1016/0168-9002(88)91148-5.
(42) DeHart, M. D.; Karriem, Z.; Pope, M. A.; Johnson, M. P. Fuel element design and analysis for potential LEU conversion of the Advanced Test Reactor. *Progress in Nuclear Energy* **2018**, *104*, 117-135. DOI: https://doi.org/10.1016/j.pnucene.2017.09.007.
(43) Caruso, A. N. The physics of solid-state neutron detector materials and geometries. *Journal of Physics: Condensed Matter* **2010**, *22* (44), 443201. DOI: 10.1088/0953-8984/22/44/443201.
(44) Reichenberger, M. A.; Nichols, D. M.; Tsai, K.; Stevenson, S. R.; Swope, T. M.; Hilger, C. W.; Hewitt, J. D.; Kellogg, K. E.; Roberts, J. A.; Chen, C.-H.; et al. Electrodeposition of low-enriched uranium onto small platinum electrodes. *Nuclear Instruments and Methods in Physics Research Section A: Accelerators, Spectrometers, Detectors and Associated Equipment* **2019**, *941*, 162350. DOI: https://doi.org/10.1016/j.nima.2019.162350.
(45) McGregor, D. S.; Ohmes, M. F.; Ortiz, R. E.; Sabbir Ahmed, A. S. M.; Kenneth Shultis, J. Micro-pocket fission detectors (MPFD) for in-core neutron flux monitoring. *Nuclear Instruments and Methods in Physics Research Section A: Accelerators, Spectrometers, Detectors and Associated Equipment* **2005**, *554* (1), 494-499. DOI: https://doi.org/10.1016/j.nima.2005.06.086.
(46) Nichols, D. M.; Reichenberger, M. A.; Maile, A. D.; Holtz, M. R.; McGregor, D. S. Simulated Performance of the Micro-Pocket Fission Detector in the Advanced Test Reactor Critical Facility. *Nuclear Science and Engineering* **2021**, *195* (10), 1098-1106. DOI: 10.1080/00295639.2021.1898922.
(47) de Izarra, G. COSICAF, a fission chamber simulation tool for academic purposes. *EPJ Nuclear Sci. Technol.* **2020**, *6*, 10.1051/epjn/2020011.

(48) Taguchi, S.; Surugaya, N.; Kurosawa, A.; Hiyama, T.; Tanaka, T. Determination of Trace Amounts of Uranium by Stripping Voltammetry Using a Boron-Doped Diamond Electrode. *BUNSEKI KAGAKU* **2010**, *59*, 1035-1041. DOI: 10.2116/bunsekikagaku.59.1035.
(49) Saliba, A.; Oliveira, E. T.; Durazzo, M. Uranium Electrodeposition Using Direct Potential Technique in Less Acidic Aqueous Media. *ECS Transactions* **2014**, *61*, 1-8. DOI: 10.1149/06124.0001ecst.
(50) ElementSix™. Boron Doped Diamond (BDD) Electrode, https://e6cvd.com/us/application/all/pe-10x10-mm-0-6-mm-thick.html. **2023**.
(51) Kahyarian, A.; Schumacher, A.; Nesic, S. Mechanistic Investigation of Hydrogen Evolution Reaction from Multiple Proton Donors: The Case of Mildly Acidic Solutions Containing Weak Acids. *Journal of The Electrochemical Society* **2019**, *166* (8), H320-H330. DOI: 10.1149/2.0411908jes.
(52) Monteiro, M. C. O.; Koper, M. T. M. Alumina contamination through polishing and its effect on hydrogen evolution on gold electrodes. *Electrochimica Acta* **2019**, *325*, 134915. DOI: https://doi.org/10.1016/j.electacta.2019.134915.
(53) Marcandalli, G.; Boterman, K.; Koper, M. T. M. Understanding hydrogen evolution reaction in bicarbonate buffer. *Journal of Catalysis* **2022**, *405*, 346-354. DOI: https://doi.org/10.1016/j.jcat.2021.12.012.
(54) Brown, M. A.; Gelis, A. V.; Fortner, J. A.; Jerden, J. L.; Wiedmeyer, S.; Vandegrift, G. F. A Novel Method for Molybdenum-99/Technetium-99m Recovery via Anodic Carbonate Dissolution of Irradiated Low-Enriched Uranium Metal Foil. *Industrial & Engineering Chemistry Research* **2015**, *54* (2), 712-719. DOI: 10.1021/ie503858j.
(55) Wheeler, V. J.; Dell, R. M.; Wait, E. Uranium trioxide and the UO3 hydrates. *Journal of Inorganic and Nuclear Chemistry* **1964**, *26* (11), 1829-1845. DOI: https://doi.org/10.1016/0022-1902(64)80007-5.
(56) Peña-Duarte, A.; Vijapur, S. H.; Hall, T. D.; Hayes, K. L.; Larios-Rodríguez, E.; Pilar-Albaladejo, J. D.; Santiago, M. E. B.; Snyder, S.; Taylor, J.; Cabrera, C. R. Iron Quantum Dots Electro-Assembling on Vulcan XC-72R: Hydrogen Peroxide Generation for Space Applications. *ACS Applied Materials & Interfaces* **2021**. DOI: 10.1021/acsami.1c05649.
(57) Reichenberger, M. A.; Ito, T.; Ugorowski, P. B.; Montag, B. W.; Stevenson, S. R.; Nichols, D. M.; McGregor, D. S. Electrodeposition of uranium and thorium onto small platinum electrodes. *Nuclear Instruments and Methods in Physics Research Section A: Accelerators, Spectrometers, Detectors and Associated Equipment* **2016**, *812*, 12-16. DOI: https://doi.org/10.1016/j.nima.2015.12.046.
(58) Allen, G. C.; Butler, I. S.; Nguyen Anh, T. Characterisation of uranium oxides by micro-Raman spectroscopy. *Journal of Nuclear Materials* **1987**, *144* (1), 17-19. DOI: https://doi.org/10.1016/0022-3115(87)90274-1.
(59) Ho, D. M. L.; Jones, A. E.; Goulermas, J. Y.; Turner, P.; Varga, Z.; Fongaro, L.; Fanghänel, T.; Mayer, K. Raman spectroscopy of uranium compounds and the use of multivariate analysis for visualization and classification. *Forensic Science International* **2015**, *251*, 61-68. DOI: https://doi.org/10.1016/j.forsciint.2015.03.002.
(60) Elsherif, O. S.; Vernon-Parry, K. D.; Evans-Freeman, J. H.; May, P. W. Effect of doping on electronic states in B-doped polycrystalline CVD diamond films. *Semiconductor Science and Technology* **2012**, *27* (6), 065019. DOI: 10.1088/0268-1242/27/6/065019.
(61) Prawer, S.; Nemanich, R. J. Raman spectroscopy of diamond and doped diamond. *Philosophical Transactions of the Royal Society of London. Series A: Mathematical, Physical and Engineering Sciences* **2004**, *362* (1824), 2537-2565. DOI: 10.1098/rsta.2004.1451 (acccessed 2022/04/04).
(62) Senanayake, S. D.; Waterhouse, G. I. N.; Chan, A. S. Y.; Madey, T. E.; Mullins, D. R.; Idriss, H. The reactions of water vapour on the surfaces of stoichiometric and reduced uranium dioxide: A high resolution XPS study. *Catalysis Today* **2007**, *120* (2), 151-157. DOI: https://doi.org/10.1016/j.cattod.2006.07.040.
(63) Donald, S. B.; Dai, Z. R.; Davisson, M. L.; Jeffries, J. R.; Nelson, A. J. An XPS study on the impact of relative humidity on the aging of UO2 powders. *Journal of Nuclear Materials* **2017**, *487*, 105-112. DOI: https://doi.org/10.1016/j.jnucmat.2017.02.016.

(64) Wang, Q.; Li, G.-D.; Xu, S.; Li, J.-X.; Chen, J.-S. Synthesis of uranium oxide nanoparticles and their catalytic performance for benzyl alcohol conversion to benzaldehyde. *Journal of Materials Chemistry* **2008**, *18* (10), 1146-1152, 10.1039/B716990F. DOI: 10.1039/B716990F.
(65) Amrute, A. P.; Krumeich, F.; Mondelli, C.; Pérez-Ramírez, J. Depleted uranium catalysts for chlorine production. *Chemical Science* **2013**, *4* (5), 2209-2217, 10.1039/C3SC22067B. DOI: 10.1039/C3SC22067B.
(66) Hu, J.; Lu, X.; Foord, J. S.; Wang, Q. Electrochemical deposition of Pt nanoparticles on diamond substrates. *physica status solidi (a)* **2009**, *206* (9), 2057-2062, https://doi.org/10.1002/pssa.200982226. DOI: https://doi.org/10.1002/pssa.200982226 (acccessed 2022/12/11).
(67) Lin, J.; Dahan, I.; Valderrama, B.; Manuel, M. V. Structure and properties of uranium oxide thin films deposited by pulsed dc magnetron sputtering. *Applied Surface Science* **2014**, *301*, 475-480. DOI: https://doi.org/10.1016/j.apsusc.2014.02.106.
(68) Elorrieta, J. M.; Bonales, L. J.; Rodríguez-Villagra, N.; Baonza, V. G.; Cobos, J. A detailed Raman and X-ray study of UO2+x oxides and related structure transitions. *Physical Chemistry Chemical Physics* **2016**, *18* (40), 28209-28216, 10.1039/C6CP03800J. DOI: 10.1039/C6CP03800J.
(69) Murillo, J.; Panda, D.; Chakrabarti, S.; Hattori, A.; Griego, L.; Chava, V. S. N.; Sreenivasan, S. T.; Ramana, C. V.; Fortier, S. Room temperature synthesis of UO2+x nanocrystals and thin films via hydrolysis of uranium(iv) complexes. *Inorganic Chemistry Frontiers* **2022**, *9* (4), 678-685, 10.1039/D1QI01248G. DOI: 10.1039/D1QI01248G.
(70) Tracy, C. L.; Chen, C.-H.; Park, S.; Davisson, M. L.; Ewing, R. C. Measurement of UO2 surface oxidation using grazing-incidence x-ray diffraction: Implications for nuclear forensics. *Journal of Nuclear Materials* **2018**, *502*, 68-75. DOI: https://doi.org/10.1016/j.jnucmat.2018.01.052.
(71) Popel, A. J.; Lebedev, V. A.; Martin, P. G.; Shiryaev, A. A.; Lampronti, G. I.; Springell, R.; Kalmykov, S. N.; Scott, T. B.; Monnet, I.; Grygiel, C.; et al. Structural effects in UO2 thin films irradiated with fission-energy Xe ions. *Journal of Nuclear Materials* **2016**, *482*, 210-217. DOI: https://doi.org/10.1016/j.jnucmat.2016.10.024.

III. General Summary

We were able to design and develop electrochemical strategies for life support system in space missions—producing electrocatalytic developments for *in-situ* H_2O_2 production and fabricating stable U-based films as a first strategic approximation of fissile transportable films.

In Chapter 1 we were able to disassemble, clean, and reform the NASA approved Electrochemical Microgravity Laboratory (*eml*) to redesign, build, and evaluate the new Electrochemical Microgravity Laboratory II (*eml-II*), that was configurated for *in-situ* hydrogen peroxide production under microgravity conditions. The *eml-II* accomplishes the NASA requirements of producing *in-situ* H_2O_2 under the water resource available onboard the ISS—with a conductivity of 2–3 μS/cm, a pH of 5.5–6.7, and a total organic carbon (TOC) content between 0.18 and 2.5 mg/L—using the U.S. patent number 6,254,762, for low conductivity water stream. The parabolic flight was successfully carried out aboard a modified Boeing 727, the G-Force One from Zero-G Corporation, where the *eml-II* achieved 0.08 w/w % of *in-situ* H_2O_2, demonstrating the viability of generating hydrogen peroxide under μ-*g* conditions. The flight test showed that there are no adverse effects of μ-*g* environments on the performance of *eml-II* system in comparison with terrestrial conditions. The successful performance of the *eml-II* during the parabolic flight evidence that the *eml-II* can be used to produce *in-situ* hydrogen peroxide as life support system in future space missions.

In Chapter 2, we designed and controlled the rotating disk slurry electrodeposition technique (RoDSE) to produce iron quantum dots onto a solid carbonaceous support. The structural and physicochemical characterization exposes that our well-dispersed 4nm Fe QDs are an arrangement of different oxidations states of iron: Fe^0, $Fe^{2+/3+}$, and Fe^{3+}, tunable as a function of potential. The RDE and RRDE results revealed that the Fe/Vulcan

catalyzes the ORR via two-electron pathway. Comparing the performance of both catalysts inside the PGU, Fe/Vulcan produced 87% more hydrogen peroxide and 25 % more current than the commercial GDE-MPL. This *in-situ* H_2O_2 production---under compatibility conditions of the drinking water resources available in the ISS---triggered up our Fe/C catalyst for sanitizing solutions in space missions. Additionally, the electrodeposited Fe/Vulcan is a promising material to be used in the PGU at low potentials: 4 and 6 V.

Carbonaceous structure of carbon nano-onions (CNOs) and Vulcan were doped with nitrogen functionalities using dicyandiamide as N-source in Chapter 3. The success of the N-doping method was confirmed by the N 1s XPS curve fitting analysis. The N-doping process added internal modifications at molecular level and partial reduction of sp^3 structures which were confirmed by the increment of the degree of graphitization, I^D/I^G ratio changes in 22 % and 3 %, comparing with the pristine N-undoped CNOs and Vulcan, respectively. NCNOs and NVulcan are promising catalysts to be used under the low-conductivity stream (2-3 mS/cm) in the PGU at low potentials: 2 V for NCNOs and 4 V and 6 V for NCNOS and NVulcan, respectively. A combination of nitrogen- and oxygen-based functionalities, as a synergy of chemical/structural interactions, control the ORR mechanism in 0.1 M KOH, in a combination of four- and two-electrons pathways, such as the PGU produced 0.06% for NCNOs and 0.07% for NCNOs at 6V, outperforming by 50% the production of H_2O_2 on the commercial GDL-MPL.

An electroplating method for uranium oxides electro-assembling, electrowinning (as electroextraction alternative), and fabrication of core-fuel-elements and fissile layers for future neutron detection was presented in Chapter 4. Our U/BDD system forms primarily uranium oxides, suppressing U-based chunky particles formation, preventing uranium compounds mixtures, and inhibiting crystallization of fibers of the uranyl-base precursor. Stable U^{4+}, U^{5+}, U^{6+} oxidation states were confirmed and reproduced under open atmospheric conditions. The small thickness of the films promoted the UO_2

oxidation to U_3O_8 in the presence of oxygen, resulting in a blend of uranium oxides with IV, V, and IV oxidation states. However, these U-films can be oxidized or reduced inside a furnace, with air or hydrogen flow, respectively, to form different uranium-based compounds for diverse applications. In general, the uranium electroplating method developed in this work contributes with uranium-based technologies, improving them and contributing to a better understanding of their electrochemical properties, e.g., uranium redox processes, uranium oxides formations, and stability studies. The U/BDD electro-assembling method, developed in Chapter 4, is proposed as a sustainable strategy for uranium electro-recovery from nuclear waste as environmental protocol—to recover and immobilize U^{235} and other fissile materials from civil and defense wastes, contaminated systems, and stockpiles.

APPENDIX 1

Appendix 1.1. Detailed schematic front view custom-made triple containment configuration was modified for the *μ-g* experiment.

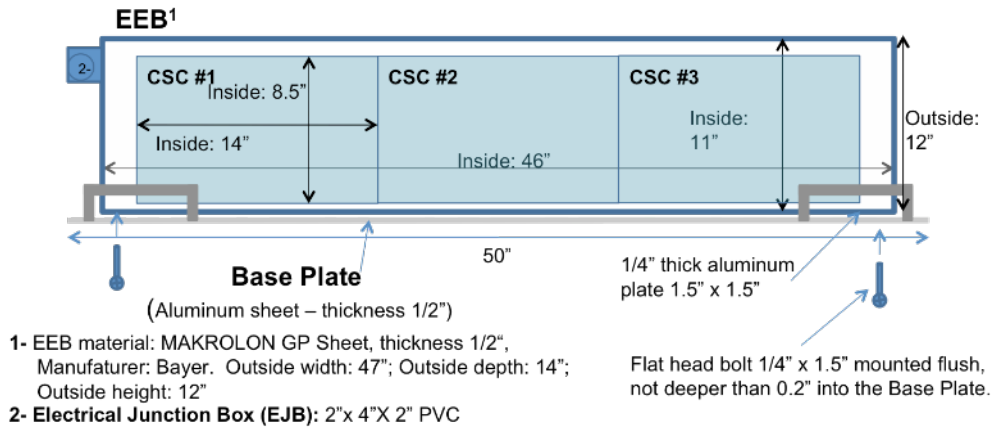

Appendix 1.3. U.S. patent number 6,254,762 De Nora Technology Inc. for low conductivity electrolytes stream.

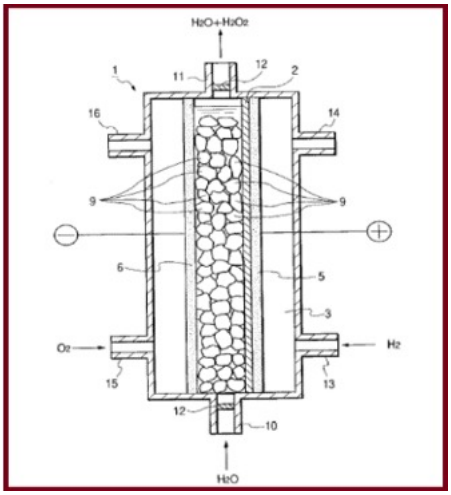

Appendix 1.3. Catalyst evaluation at FTI

We evaluated the catalysts onto GDE and investigated its peroxide generation performance at 4V, 6V, 8V, 10V, 12V, and 14V, the comparison of these catalysts is showed in Table 2.1. The samples were dispersed in an ethanol:isopropanol:water (1:1:2) mixture with a total solution volume of 750μL and 60μL of nafion solution 5% in ethanol. Dispersions were painted and coated onto a new GDE MPL. Differential polarization trial was performed at the following processing conditions:
Pass – Single pass
Electrode – New GDE MPL
Electrolyte – RO water
Flow rate – 2 mL/min
Catholyte plate thickness – 0.37″
Pressure balance – 1 psi
Nafion beads – Nafion NR 50 Beads + POWDion-Insoluble, 40-60 mesh.
Activated Nafion beads:
~80°C in 3% H2O2 for 1 hour
~80°C in deionized water for 2 hours
~80°C in 1 M H2SO4
Stored in deionized water.

A comparative plot of hydrogen peroxide production by different catalysts at 6V is shown in Figure A.1.3.1. Whereas Figures A.1.2 to A.1.16 show single pass polarization trials conducted using GDE MPL coated with catalyst presented in Table 2.1. Significant currents were observed with increasing voltages for almost all catalyst, the highest current being the nitrogen doped CNOs. Although peroxide was generated in slight concentration by NCNOs catalyst, the significant current showed project this catalytic as a promising material in ORR applications. Based on total H_2O_2 concentration and current production, we could infer that Fe-Vulcan and NCNOs promote reactions O2 + 2H+ + 2e- → H2O2 and O2 + 4H+ + 4e- → 2H2O, respectively.

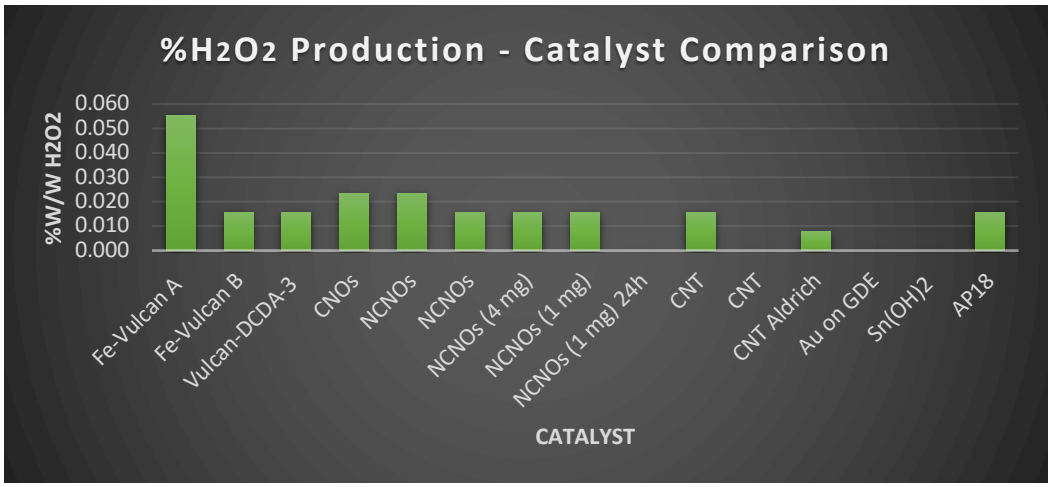

Figure A.1.1. Plot of hydrogen peroxide production by different catalysts at 6V.

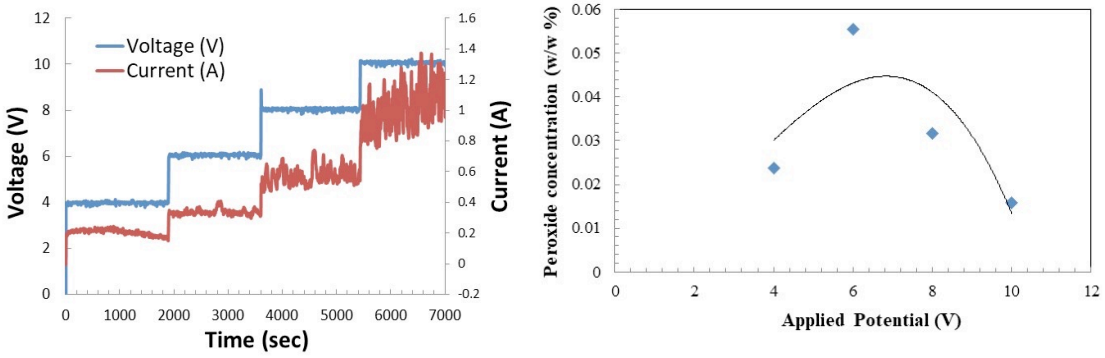

Figure A.1.3.2. Fe-Vulcan-940 on GDE (4.6mg, brush painting technique), non-active beads and powder.

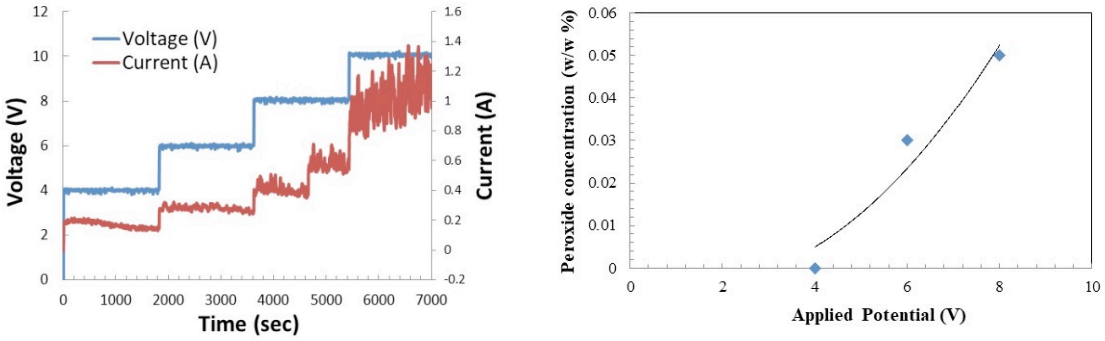

Figure A.1.3.3. Fe-Vulcan-940, (5mg, dropping) non-active beads and powder.

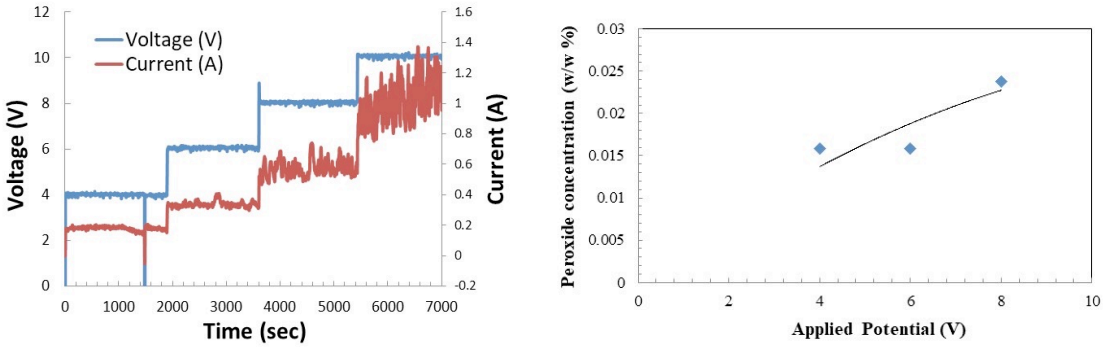

Figure A.1.3.4. Vulcan-DCDA-3 on GDE, non-active beads and powder

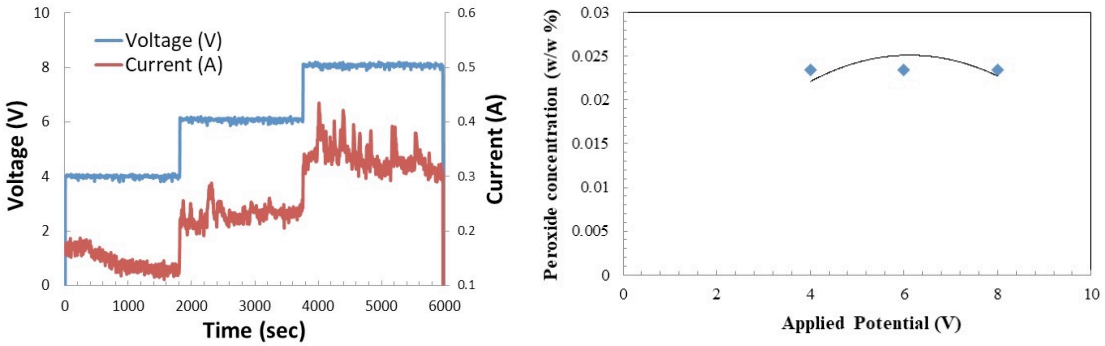

Figure A.1.3.5. CNOs, **active** beads and powder

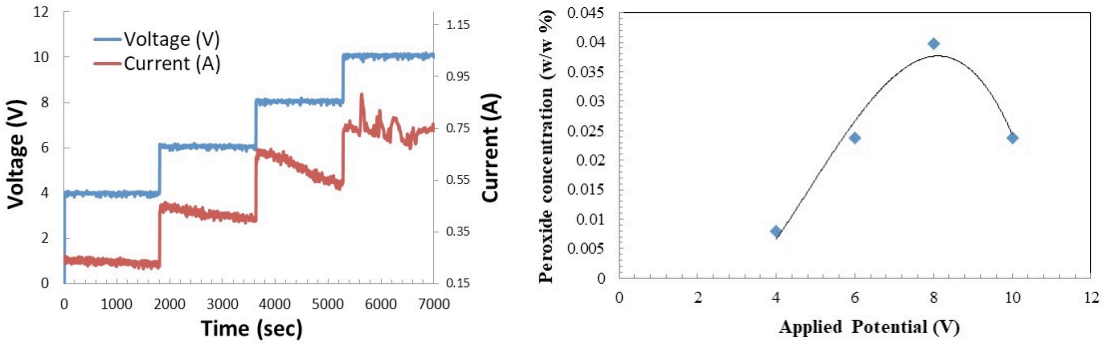

Figure A.1.3.6. NCNOs, **active** beads and powder.

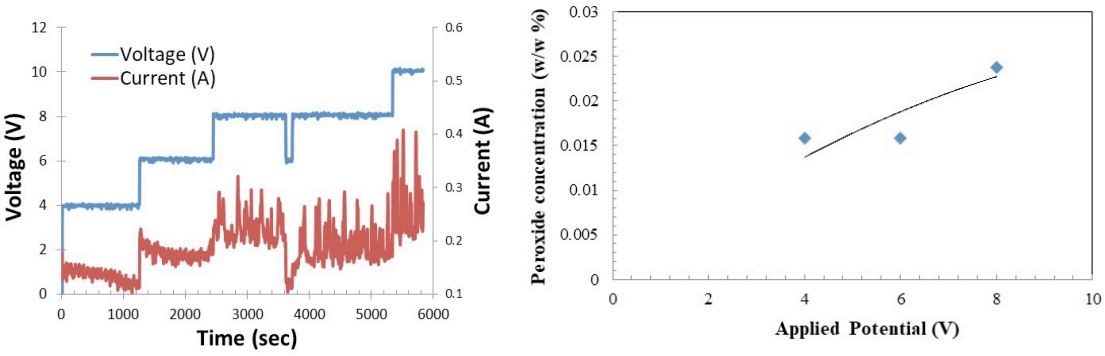

Figure A.1.3.7. NCNOs, on GDE, non-active beats.

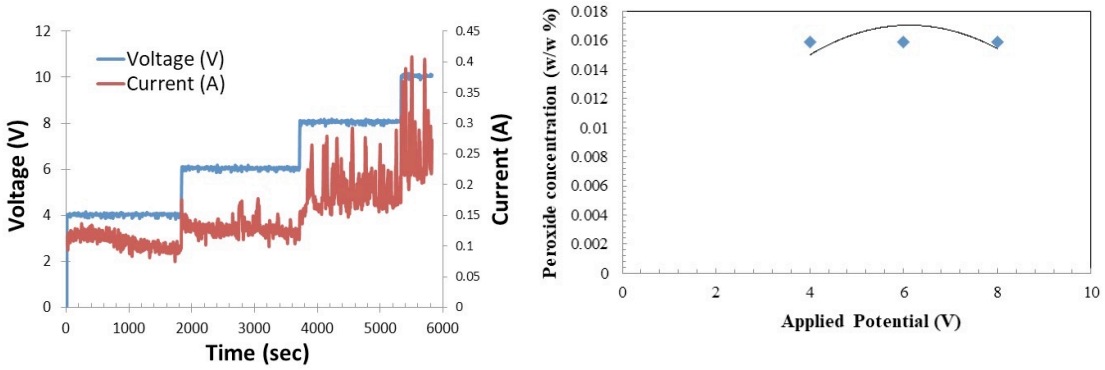

Figure A.1.3.8. NCNOs on GDE (4 mg)), non-active beads and powder.

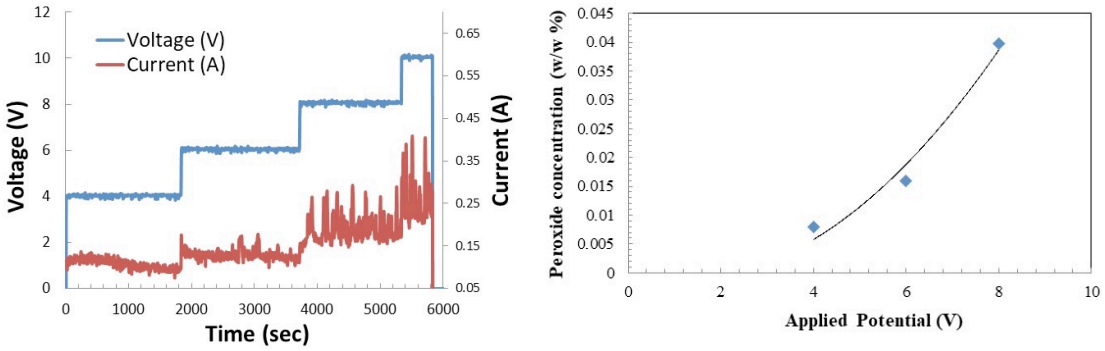

Figure A.1.3.9. NCNOs on GDE (1 mg), non-active beads and powder.

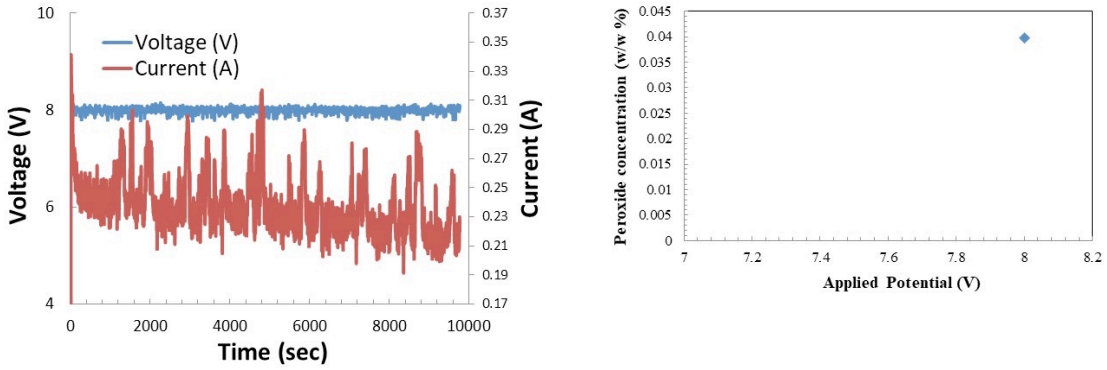

Figure A.1.3.10. NCNOs on GDE (1 mg), non - active beads and powder, 24h.

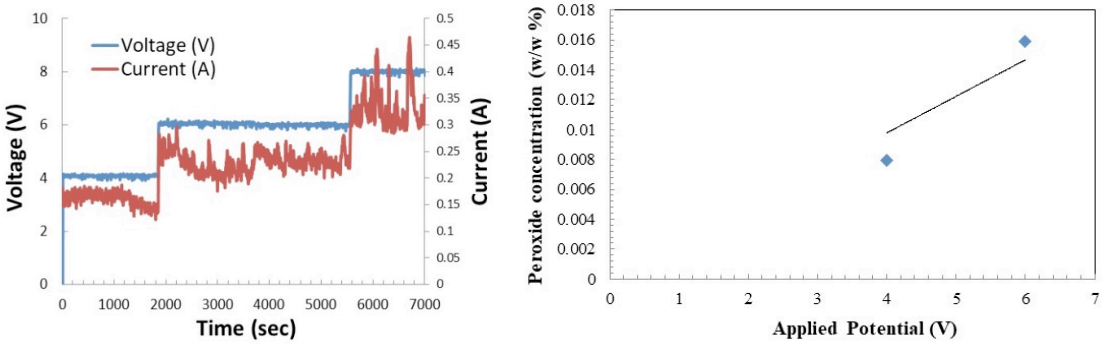

Figure A.1.3.11. CNT on GDE, non-active beads and powder.

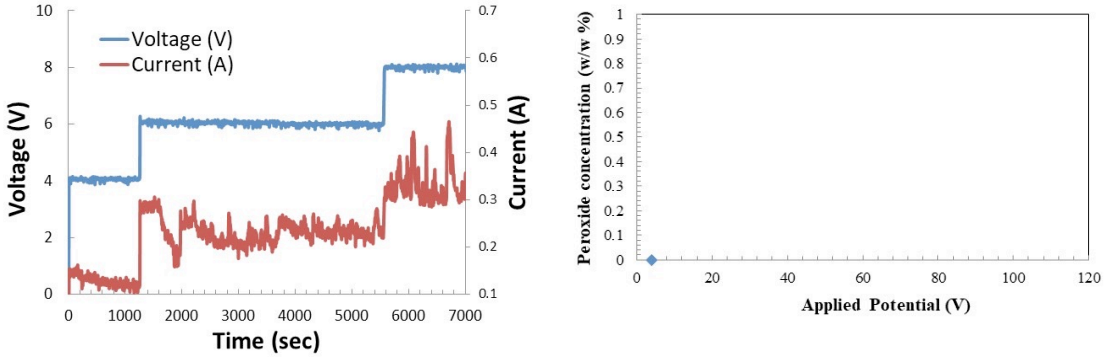

Figure A.1.3.12. CNT on Carbon Paper, non-active beads and powder.

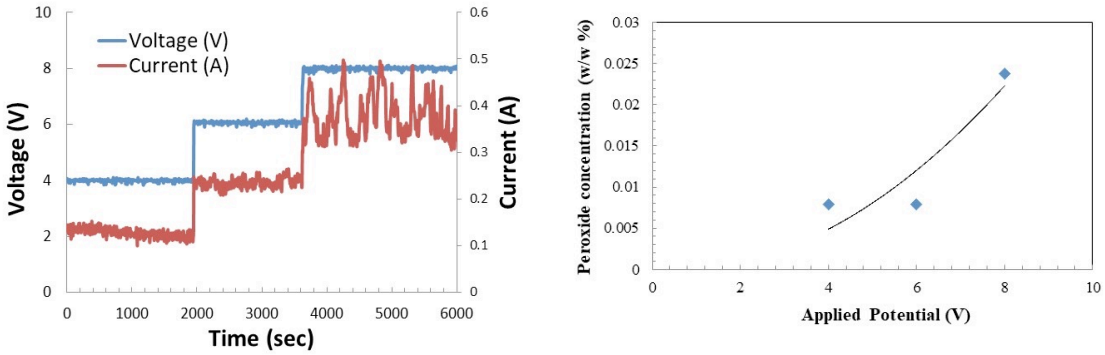

Figure A.1.3.13. CNT Aldrich on GDE, non-active beads and powder.

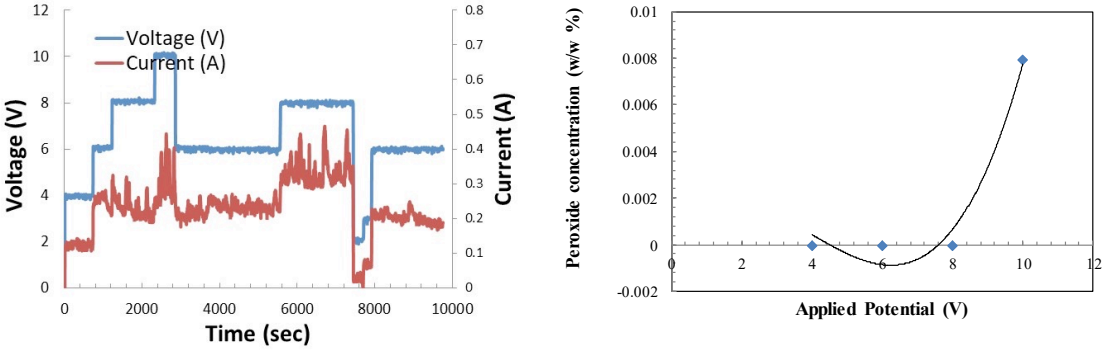

Figure A.1.3.14. Au on GDE, non-active beads and powder.

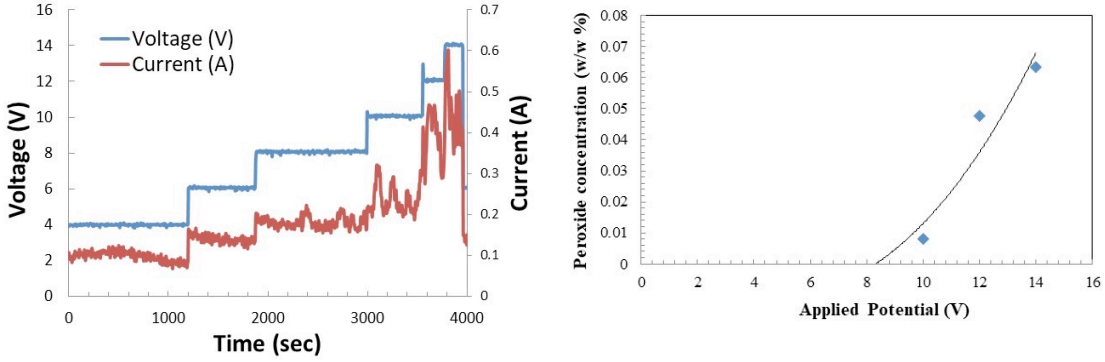

Figure A.1.3.15. Sn(OH)2 on GDE, non - active beads and powder.

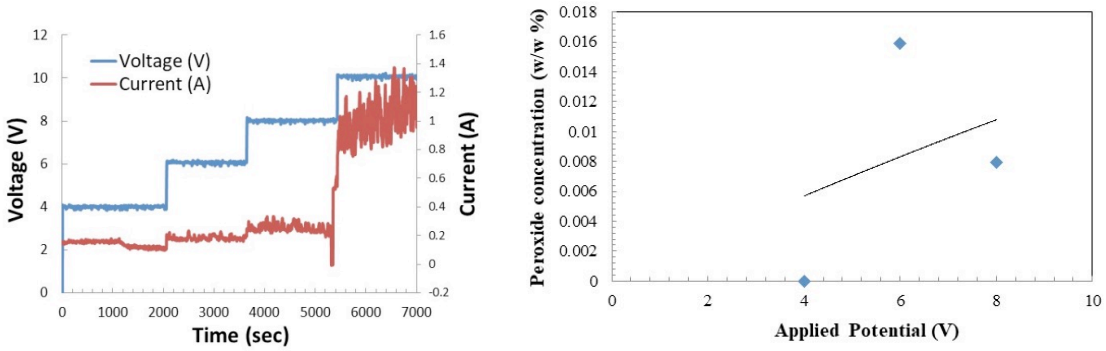

Figure A.1.3.16. AP18, non-active beads and powder.

Appendix 1.4. Parabolic flight accelerometer data with the overall Martian, Lunar and μ-g environments (blue line), and pressure readings (red dots).

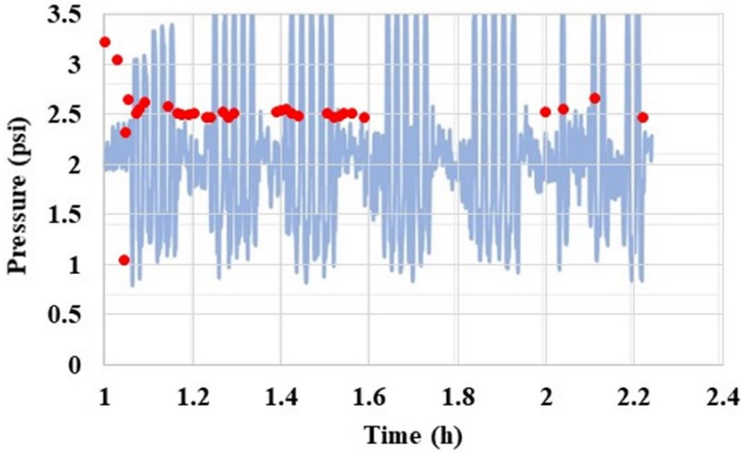

APPENDIX 2

Appendix 2.1. Second cycle of the Fe/Vulcan XC-72R cyclic voltammetry analysis. It was done in a nitrogen-purged 0.1 M KOH solution. Catalyst surface modifications are evidenced through modifications of the cathodic and anodic peaks in comparison with the first cycle.

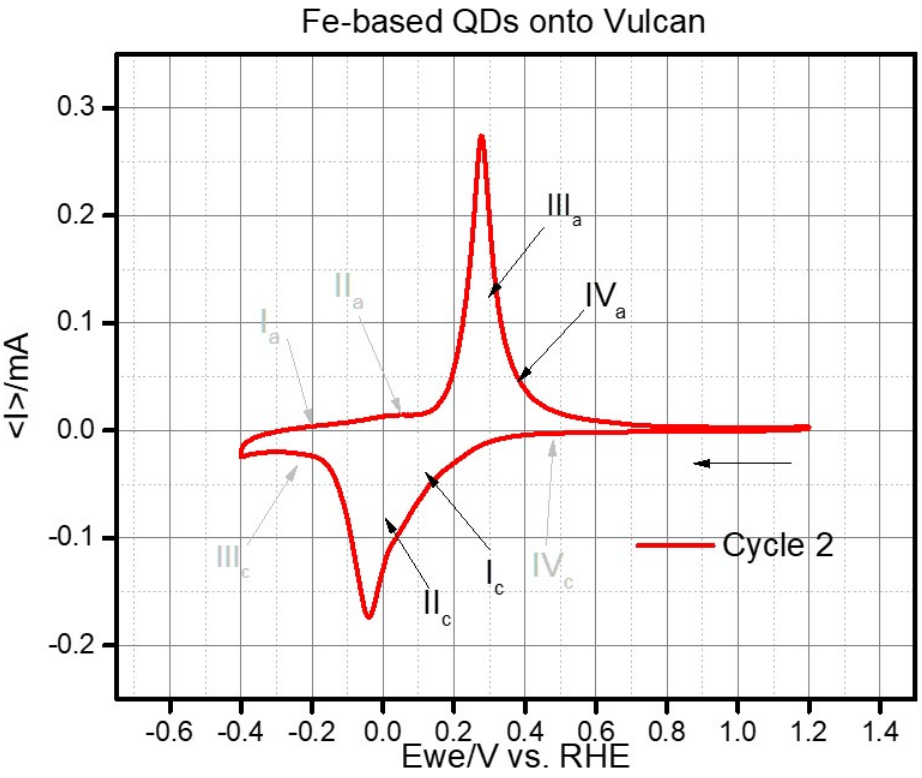

Appendix 2.2. a) Cyclic voltammetry profile vs. RHE, at a scan rate of 10 mV/s and at room temperature, of the Fe/Vulcan XC-72R. The deviation of the first cycle, from the successive second cycle, is observed in both reduction and oxidation peaks. The potential is swept in the cathodic direction starting at 0.5 V and ending at -0.9 V. b) A enlarged view of the IIa oxidation peak at the potential window -200 to 200 mV is shown.

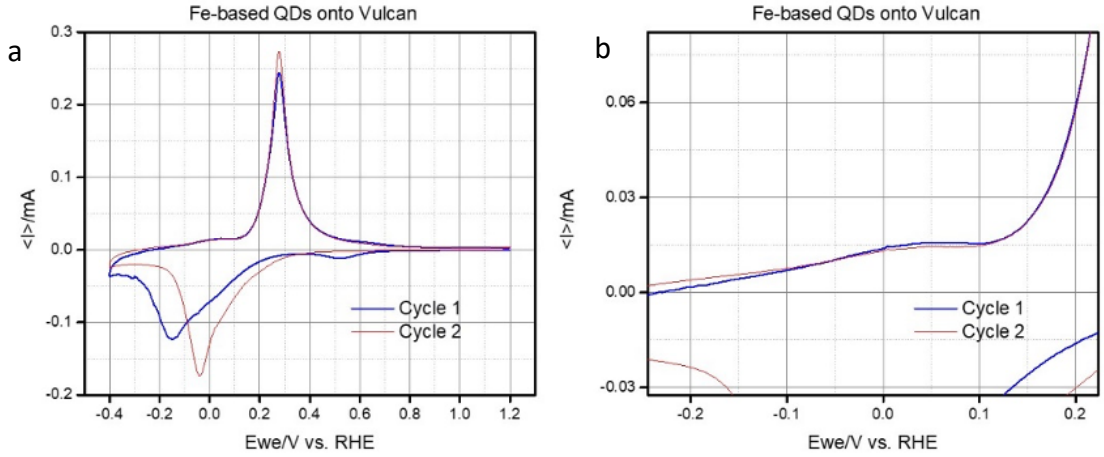

Appendix 2.3 Induced Coupled Plasma-Optical Emission Spectroscopy (ICP-OES) and metal loading: The quantitative determination of the total iron electrodeposited and its percentage ratio loading efficiency by the RoDSE technique were performed through Induced Coupled Plasma-Optical Emission Spectroscopy (ICP-OES).

Spectrometer Perkin Elmer Optima 8000

$\%Fe_{loading}$ = (25.00 ± 0.03) %

$\%Fe_{ICP}$ = (15.54 ± 0.03) %

Electrodeposition Efficiency = 62.16%

Appendix 2.4. The TEM electron diffraction pattern of the Fe/Vulcan catalyst electrodeposited by the RoDSE technique. The diffraction pattern analysis confirms iron-oxide based species.

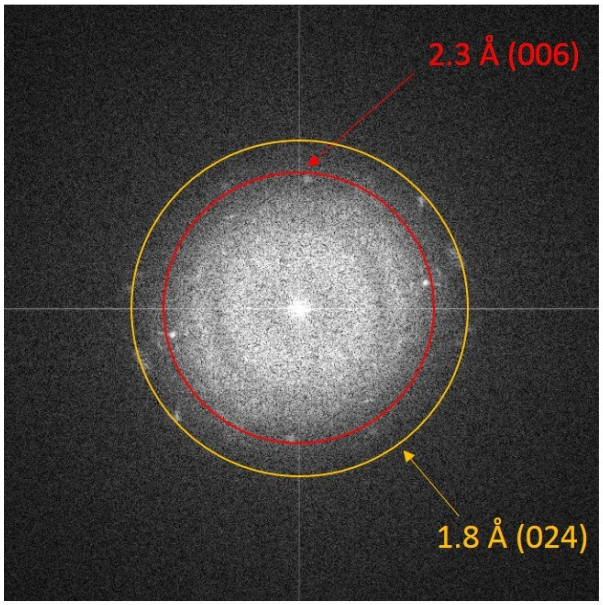

Name and formula

Reference code:	98-002-4791
Mineral name:	Hematite
Compound name:	Hematite
Common name:	Hematite
Chemical formula:	Fe_2O_3

Crystallographic parameters

Crystal system:	Hexagonal
Space group:	R -3 c
Space group number:	167
a (Å):	5.0325
b (Å):	5.0325
c (Å):	13.7404
Alpha (°):	90.0000
Beta (°):	90.0000
Gamma (°):	120.0000

Peak list

No.	h	k	l	d [A]	2Theta[deg]	I [%]
1	0	1	2	3.68022	24.164	33.6
2	1	0	4	2.69785	33.180	100.0
3	1	1	0	2.51625	35.652	75.7
4	0	0	6	2.29007	39.311	2.1
5	1	1	3	2.20535	40.887	20.3
6	2	0	2	2.07715	43.535	1.8
7	0	2	4	1.84011	49.495	39.4
8	1	1	6	1.69365	54.106	47.7
9	2	1	1	1.63556	56.195	0.8
10	1	2	2	1.60187	57.485	2.3

Appendix 2.5. X-ray diffraction (XRD) measurements were performed on fresh iron-based catalyst synthesized by the RoDSE Technique.

XRD analysis evidences the successful deposition of iron on the carbon support. The metallic peak (110) in the characteristic 2q about 46º support the presence of the zero valent iron specie in a fresh catalytic sample. The broadness and ill-definition of diffractogram peaks are characteristic very small nanostructures. Oxidation of iron is evidenced by the presence of other peaks associated with pattern of iron oxidizes species.

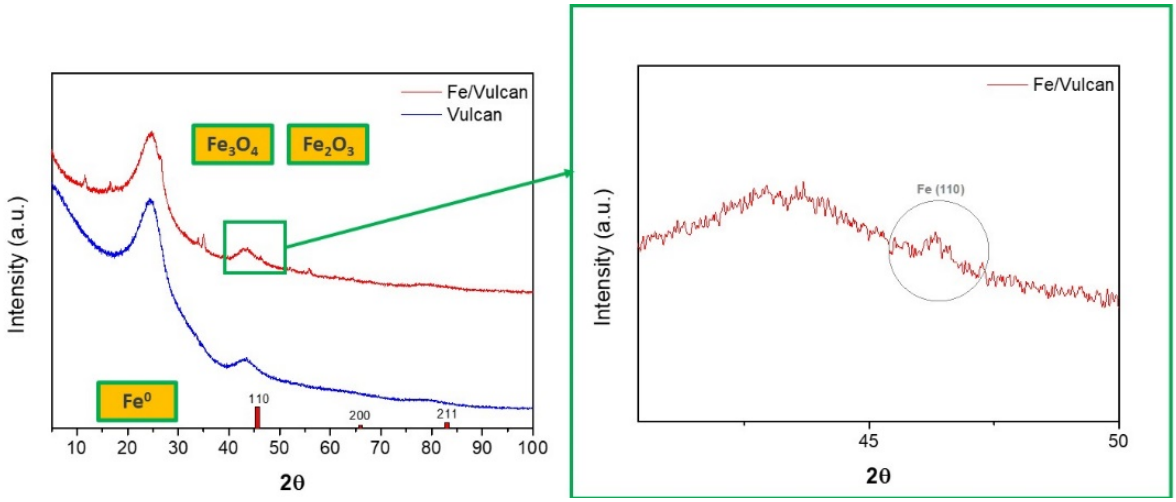

Appendix 2.6. X-ray photoelectron spectroscopy (XPS) Fe 2p binding energy region scan with the Fe $2p_{1/2}$ and Fe $2p_{3/2}$ duplet (top), and the Voigt deconvolution analysis of the Fe $2p_{3/2}$ binding energy region (bottom) for the iron-based QDs onto Vulcan XC-72R electrodeposited by the RoDSE technique.

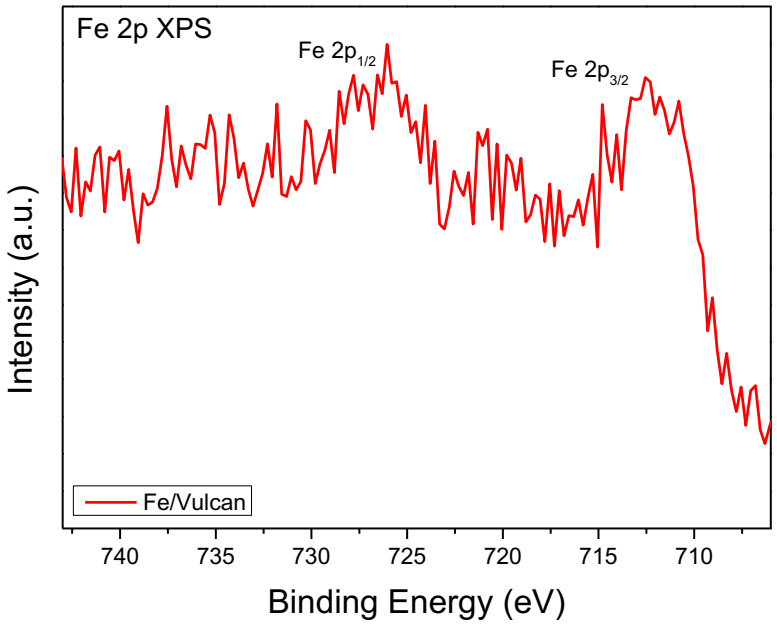

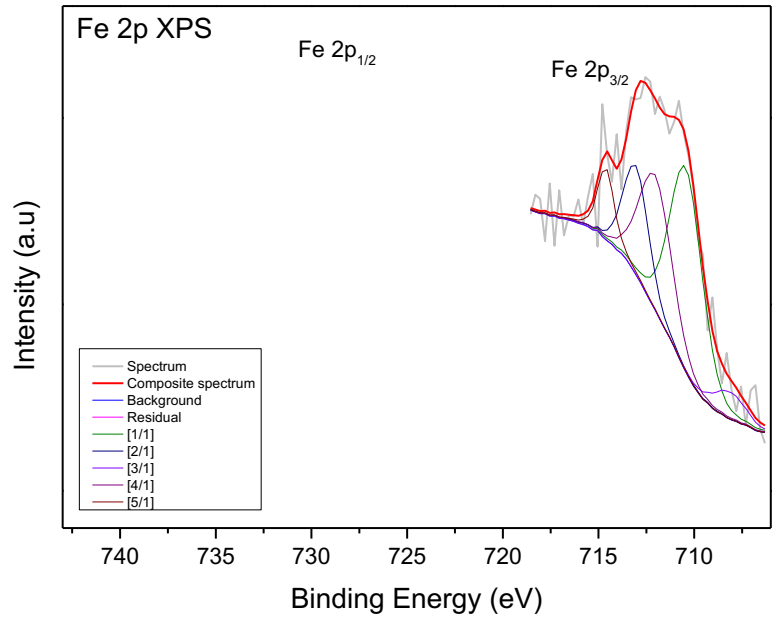

Appendix 2.7. XPS Peaks Assignments for the C 1s Components

C 1s Components	Binding Energy (eV)
Graphite (sp^2)	284.5
C-H (sp^3)	285.0
C-OH/C-O-C (sp^3)	286.1–286.3
C=O	287.6–287.7
COOH/COOR	288.6–289.1
π-π^*	290.5–290.8

Appendix 2.8. XAFS data at the Fe edge for Fe/Vulcan catalyst and the Fe foil.

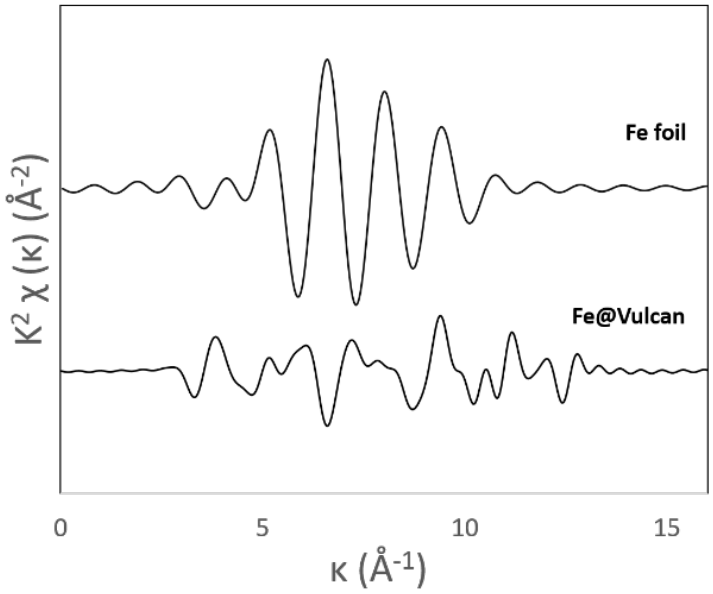

Appendix 2.9. Quantitative ORR kinetics parameters calculated for the ORR in 0.1M KOH

Catalyst	E_{onset} (V vs RHE)	$E_{1/2}$ (V vs RHE)	# of electrons
Fe/Vulcan	0.566	0.467	2.6
Vulcan	0.642	0.573	1.6
Pt(20%)/GC	0.876	0.785	4.0

Appendix 2.10. Rotating-disk electrode polarization curves for the Vulcan XC-72R (a) and Fe/Vulcan (b) catalyst, electrodeposited by the RoDSE technique. The Koutechy-Levich (K-L) analysis was done in O_2-saturated 0.1 M KOH solution at a scan ratio of 10 mV/s. at different rotation speeds between 400 and 2400 rpm. The linear sweep voltammetry was done form 1.0 V to -0.3 V vs RHE.

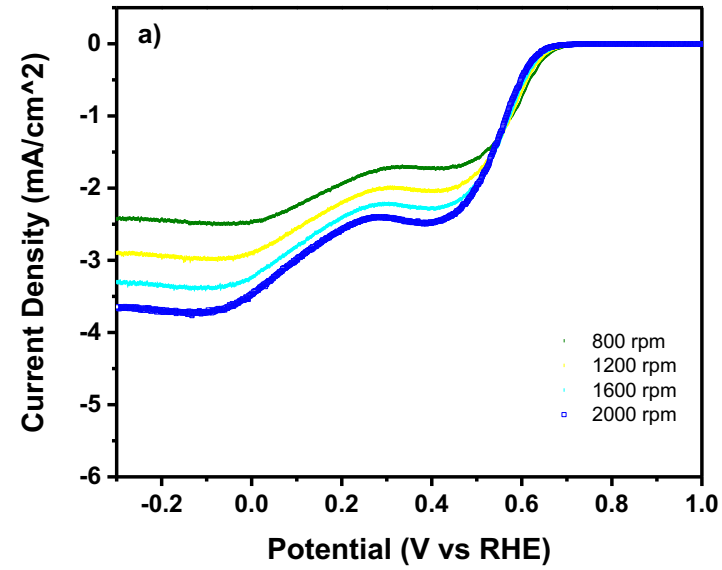

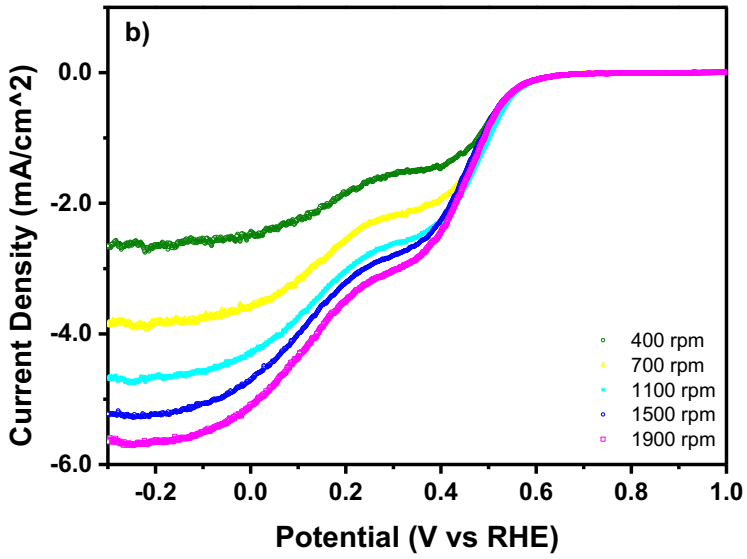

Appendix 2.11. Normalization and tuning-treatment before the ORR studies. The cathodic peak vanishes after the 1st CV, showing that iron was reduced to Fe^0.

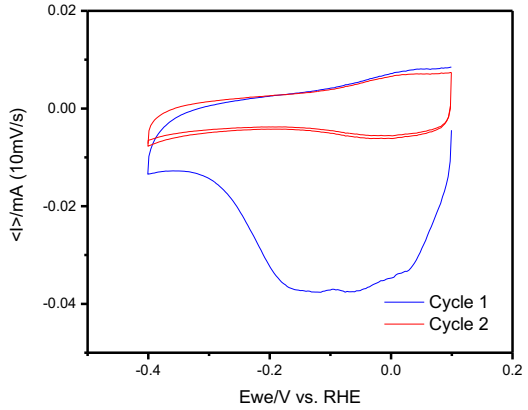

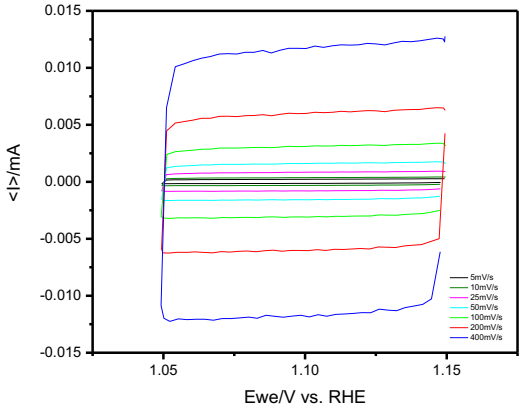

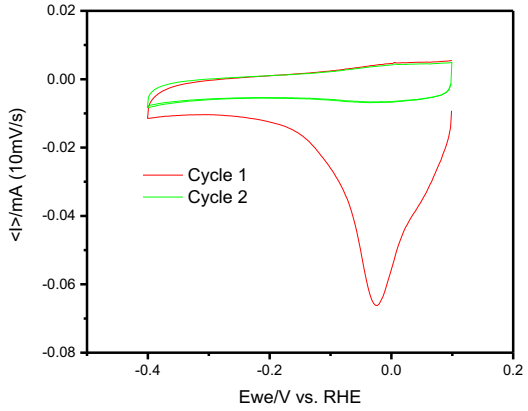

Appendix 2.12. Comparison of hydrogen peroxide production and the output current by Fe/Vulcan and GDE-MPL at 6V, using RO water in the peroxide generation unit (PGU) for space applications. Experiments were done at room temperature under terrestrial conditions.

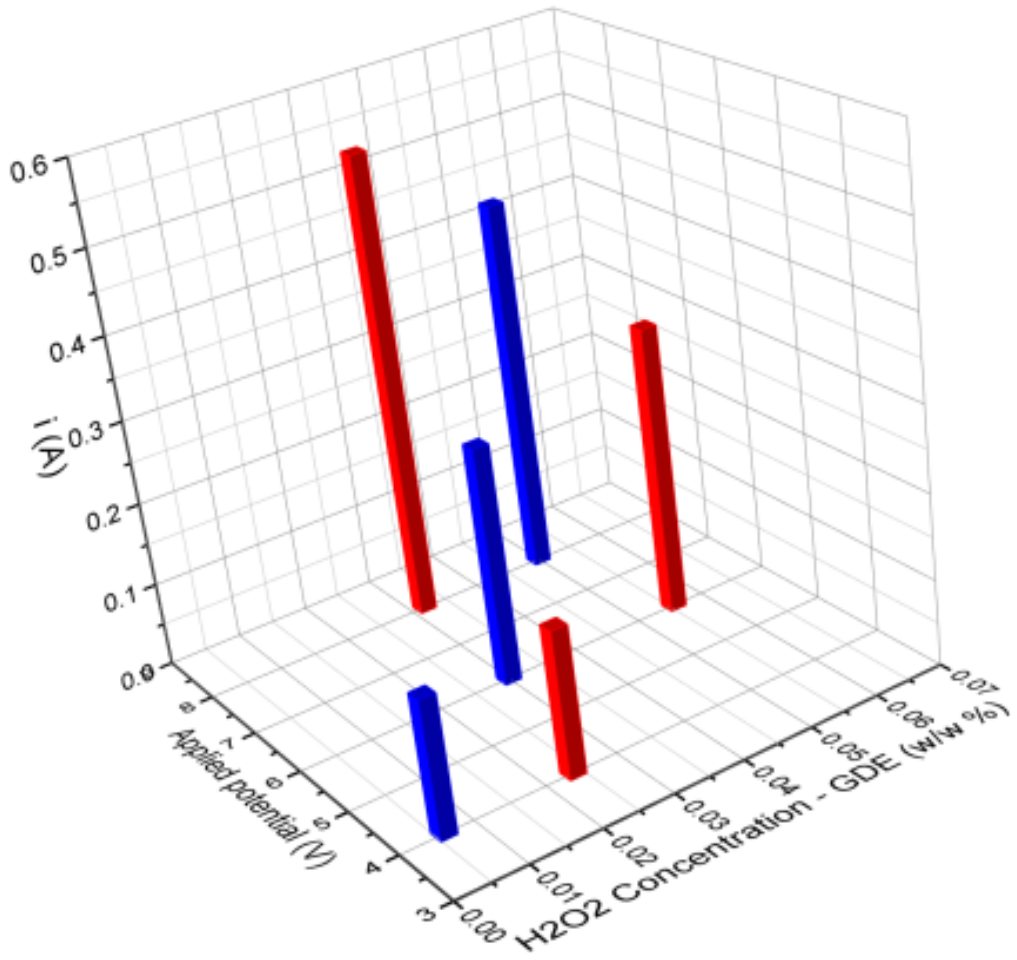

Appendix 2.13. Polarization curve for the *in-situ* hydrogen peroxide generation on the GDE-MPL at 6 V. Blue line shows the output current of the GDE-MPL decreases significantly as time goes by. Its exponential decay behavior indicates a possible decomposition of the carbon in the surface GDE, and a consequently penetration of water in the cathode---after opening the PGU, we observe water presence in the cathodic side. In fact, the GDE trial current decrease exponentially in seconds from (3120sec, 0.315 amps) to (3840sec, 0.281amps), with (time, current) as (x, y) coordinates. Red line shows a comparative behavior of the output currents for the Fe/Vulcan and the GDE-MPL at 6 V.

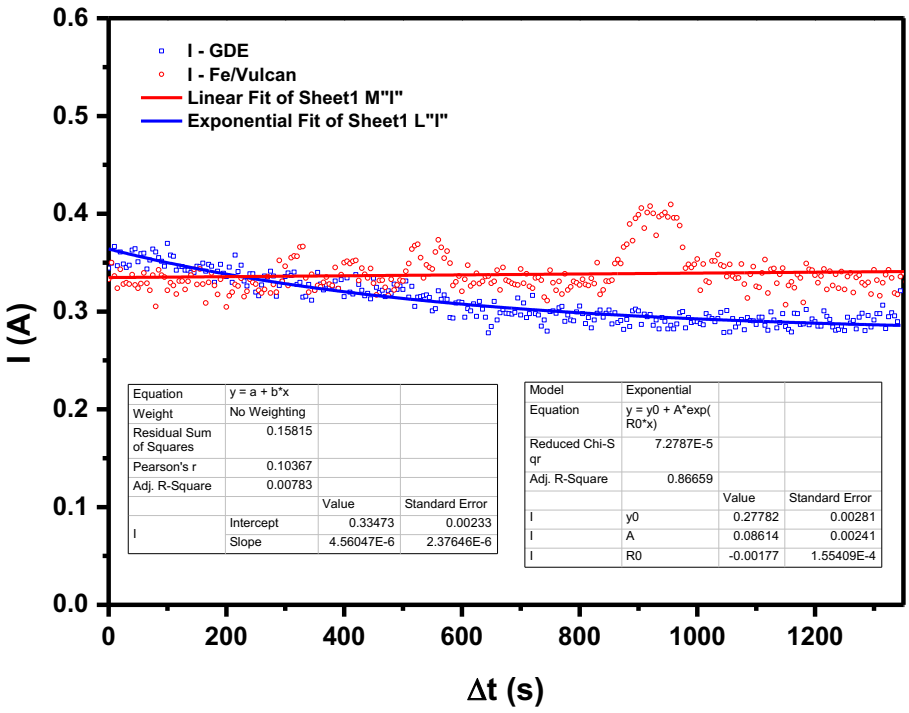

Equation	y = a + b*x		
Weight	No Weighting		
Residual Sum of Squares	0.15815		
Pearson's r	0.10367		
Adj. R-Square	0.00783		
		Value	Standard Error
I	Intercept	0.33473	0.00233
I	Slope	4.56047E-6	2.37646E-6

Model	Exponential		
Equation	y = y0 + A*exp(R0*x)		
Reduced Chi-Sqr	7.2787E-5		
Adj. R-Square	0.86659		
		Value	Standard Error
I	y0	0.27782	0.00281
I	A	0.08614	0.00241
I	R0	-0.00177	1.55409E-4

APPENDIX 3

Appendix 3.1a. Induced Coupled Plasma-Optical Emission Spectroscopy (ICP-OES) metal concentration by catalyst.

Metal	Concentration (%wt.) in Vulcan	Concentration (%wt.) in CNOs
Fe	< 0.009 ± 0.001	< 0.003 ± 0.001
Co	< 0.0006 ± 0.0002	< 0.0004 ± 0.0001
Mn	BQL	BDL
Pd	BDL	BDL
Pt	BDL	BDL

BQL: Below quantification limit, BDL: Below detection limit

The Induced Coupled Plasma-Optical Emission Spectroscopy (ICP-OES) analysis was done as follow: Vulcan and CNOs metal content (Fe, Co, Mn, Pd and Pt) were determined using an Optima 8000 Perkin Elmer ICP – OES with standard plasma parameters as shown in Table SI1b). Digestion procedures to extract the selected metals were performed as follow: 10 mg of each sample were digested with a 10 mL aqua regia solution and refluxed until approximately 1 mL remained. An additional 5 mL aqua regia aliquot was added to all samples and heated to simmering until a paste was formed. The solutions passed through Whatman glass microfiber filters (GF / F grade) and reconstituted to 25 mL with 2% HNO_3 solution.

Appendix 3.1b. Induced Coupled Plasma-Optical Emission Spectroscopy (ICP-OES) plasma parameters.

	Gas Flows (L/min)		RF Power (Watts)	Pump Flow Rate (mL/min)
Plasma	Auxiliary	Nebulizer		
1.5	0.2	0.55	1300	1.5

Calibration curves for the selected metals were built starting to their quantification limits as calculated from the instrument manual. Appendix 3.1c) contains the selected ranges for metal.

Appendix 3.1c. Induced Coupled Plasma-Optical Emission Spectroscopy (ICP-OES) calibration curve range per metal.

Metal	Instrument Quantification Limit (μg/L)	Upper limit (μg/L)
Fe	0.63	5
Co		
Mn		
Pd	5.0	40
Pt	7.5	60

Appendix 3.2. Rotating Disk Electrode Analysis – The Koutechy-Levich (K-L) Study.

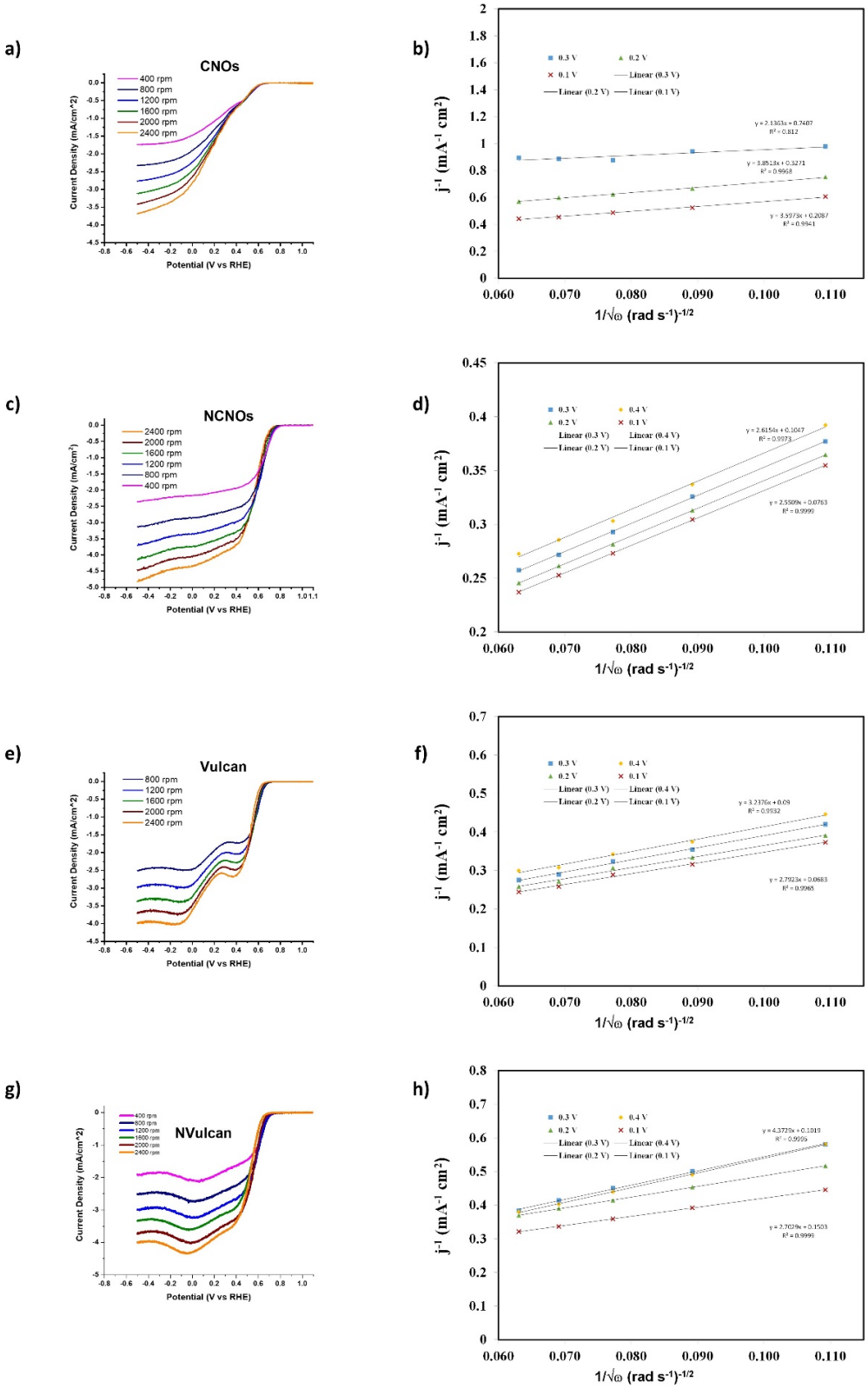

Appendix 3.3. XPS characteristic binding energies for the principal nitrogen groups in N-doped nanocarbons.

Groups: Pyridinic, pyridonic,[154] pyrrolic, graphitic, and oxidized species.[134, 155-158, 193, 194]

Binding energy region	Interaction assignments	Binding energy (eV)
N 1s	N-pyridinic	398.1-398.9
	N-pyridonic	399.6-399.9
	N-pyrrolic	400.1-400.8
	N-quaternary	401.0-401.6
	N-oxides	402.0-405.0
C 1s	C-C low defect Defective carbons in five-member rings	283.2-284.1
	C-C primary graphitic sp2	284.3-284.8
	C-C high/ /Csp2-N Carbon in more than six-member ring/Carbon bonded to N in pyridinic, pyrrolic in both defect and defect free regions	284.8-285.5
	C-OH/C-O-C sp^3 /Csp3-N/C-N=O Ether ground found in esters and lactone/Graphitic Nitrogen in aromatics/Nitrogen Oxides	285.9-286.5
	carbonyl species/O=C-N Pyridone, amide/Carbonyl groups	286.5-287.6
	COOH/COOR groups Carboxyl, esters, lactone and other related carbons bonded to 2 and 3 heteroatoms	288.4-288.9
	p-p*	290.5–290.8
O 1s	A weak contribution of the Oy of the pyridine Oxide N^+–O^- [193]	531.0-531.5
	C=O	531.0-532.0
	C-O/O-C=O	531.8-533.0
	O-C-O	532.8-534.0
	COOH	533.8-536.0
	H_2O	536.0-537.5

Appendix 3.4. XPS characteristic binding energies for the principal carbon groups in N-doped nanocarbons.

N-doped nanocarbons[84, 89, 153]

Sample	C 1s Interaction assignments	Binding energy (eV)	Ratio contribution (%)
NCNOs	C-C low	284.06	6.07
	Graphitic sp^2	284.49	42.26
	C-C high / Csp^2-N	284.61	13.94
	C-OH / C-O-Csp^3 / Csp^3-N / C-N=O	286.67	15.07
	Carbonyl species / O=C-N	288.39	11.14
	COOH / COOR	289.55	3.59
	p-p*	290.74	7.93
NVulcan	C-C low	284.24	9.42
	Graphitic sp^2	284.55	60.14
	C-C high / Csp^2-N	285.86	17.50
	C-OH / C-O-Csp^3 / Csp^3-N / C-N=O	287.17	7.32
	Carbonyl species / O=C-N	288.51	1.45
	COOH / COOR	289.52	3.21
	p-p*	290.66	0.96

Appendix 3.5. X-ray photoelectron spectroscopy (XPS) of the N 1s binding energy region of pristine carbon supports: (a) CNOs and (b) Vulcan.

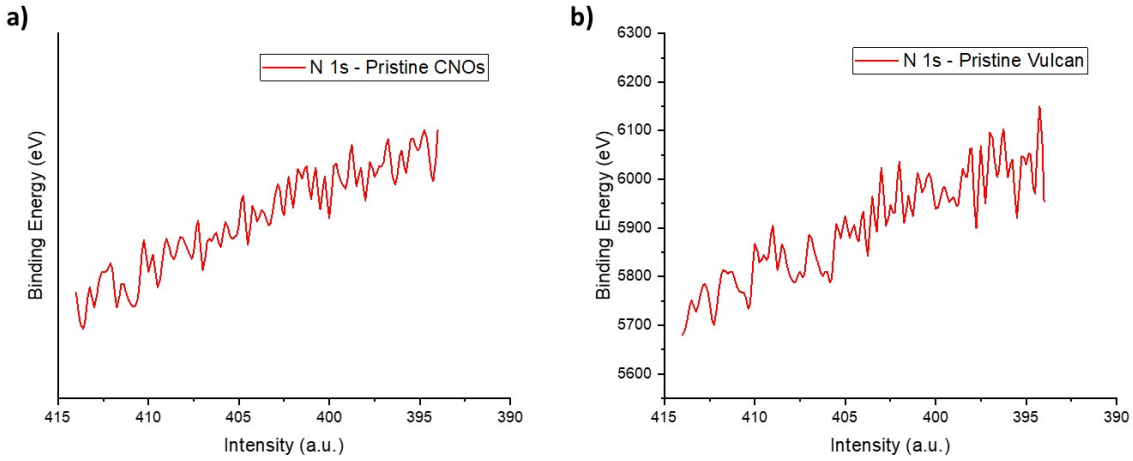

Appendix 3.6. XPS characteristic binding energies for the principal oxygen groups in N-doped nanocarbons.

Oxygen groups in N-doped nanocarbons[154, 155]

Sample	O 1s Interaction assignments	Binding energy (eV)	Ratio contribution (%)
NCNOs	C=O / Weak Contribution N^+–O^-	530.98	22.09
	C-O/O-C=O	532.52	28.10
	O-C-O	533.93	24.37
	COOH	535.89	13.32
	H_2O	537.20	12.13
NVulcan	C=O / Weak Contribution N^+–O^-	530.98	24.41
	C-O/O-C=O	532.13	39.21
	O-C-O	532.91	12.57
	COOH	233.89	21.43
	H_2O	535.02	2.38

Appendix 3.7. Polarization curves for the in-situ hydrogen peroxide generation on NCNOs (a) and NVulcan (b). Polarization curves were done in RO water at different potentials between 2 V to 10 V.

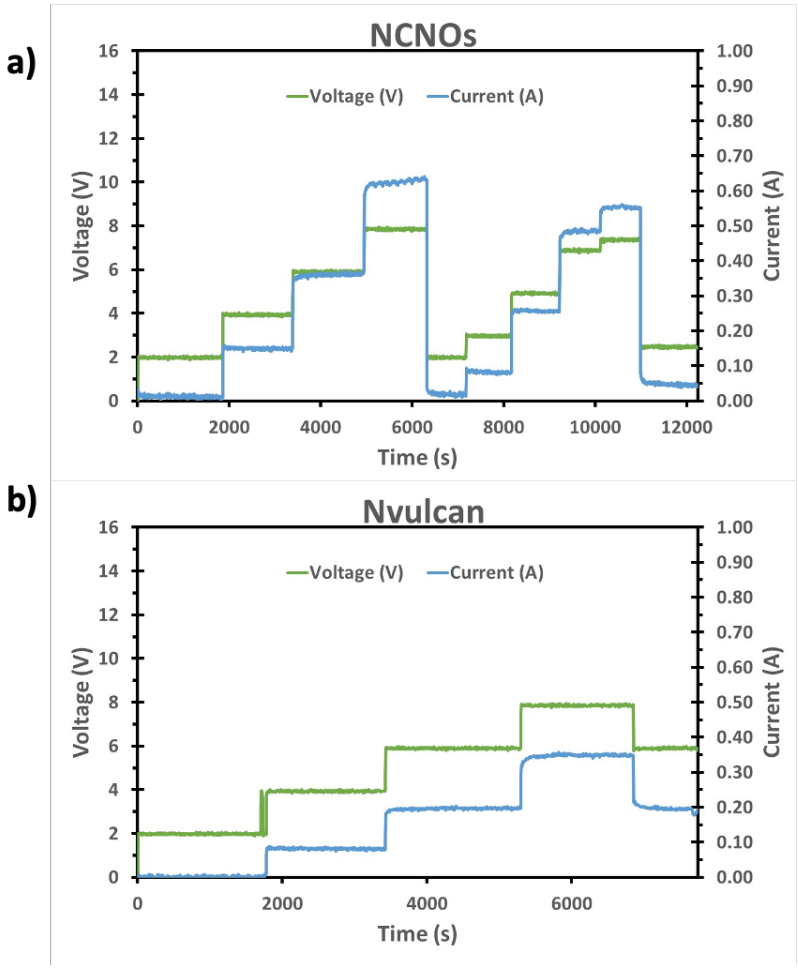

Appendix 3.8. Curve fitting parameters for the current (A) vs. potential (V) plot obtained on NCNOS.

EQUATION	Y = INTERCEPT + B1*X^1 + B2*X^2
PLOT	Current
WEIGHT	No Weighting
INTERCEPT	-0.05847 ± 0.02762
B1	0.02145 ± 0.01192
B2	0.0086 ± 0.00113
RESIDUAL SUM OF SQUARES	0.00594
R-SQUARE (COD)	0.99503
ADJ. R-SQUARE	0.9945

Appendix 3.9. Curve fitting parameters for the H_2O_2 concentration (%w/w) vs. potential (V) plot obtained on NCNOS.

EQUATION	Y = INTERCEPT + B1*X^1 + B2*X^2 + B3*X^3
PLOT	H2O2
WEIGHT	No Weighting
INTERCEPT	0.11424 ± 0.07336
B1	-0.09354 ± 0.0499
B2	0.02274 ± 0.0102
B3	-0.00139 ± 6.46263E-4
RESIDUAL SUM OF SQUARES	0.01294
R-SQUARE (COD)	0.8261

Appendix 3.10. Curve fitting parameters for the current (A) vs. potential (V) plot obtained on NVulcan.

EQUATION	Y = INTERCEPT + B1*X^1 + B2*X^2
PLOT	Current
WEIGHT	No Weighting
INTERCEPT	-0.05159 ± 0.02199
B1	0.017 ± 0.0088
B2	0.00451 ± 8.22166E-4
RESIDUAL SUM OF SQUARES	5.44371E-4
R-SQUARE (COD)	0.99599
ADJ. R-SQUARE	0.99466

Appendix 3.11. Curve fitting parameters for the H_2O_2 concentration (%w/w) vs. potential (V) plot obtained on NVulcan.

EQUATION	Y = INTERCEPT + B1*X^1 + B2*X^2
PLOT	H2O2
WEIGHT	No Weighting
INTERCEPT	-0.00217 ± 0.05306
B1	-0.00205 ± 0.02015
B2	0.00205 ± 0.0018
RESIDUAL SUM OF SQUARES	0.00772
R-SQUARE (COD)	0.74545
ADJ. R-SQUARE	0.70628

APPENDIX 4

Appendix 4.1. Scanning Electron Microscopy (SEM) micrographs at X20,000 and Energy Dispersive Spectroscopy (EDS) Spectra.

At the pristine BBD electrode (a and b) and the BDD electrode after the chronoamperometry in 5mM uranyl acetate and 0.1M $KClO_4$ (c and d). SEM micrographs scale is 1 μm.

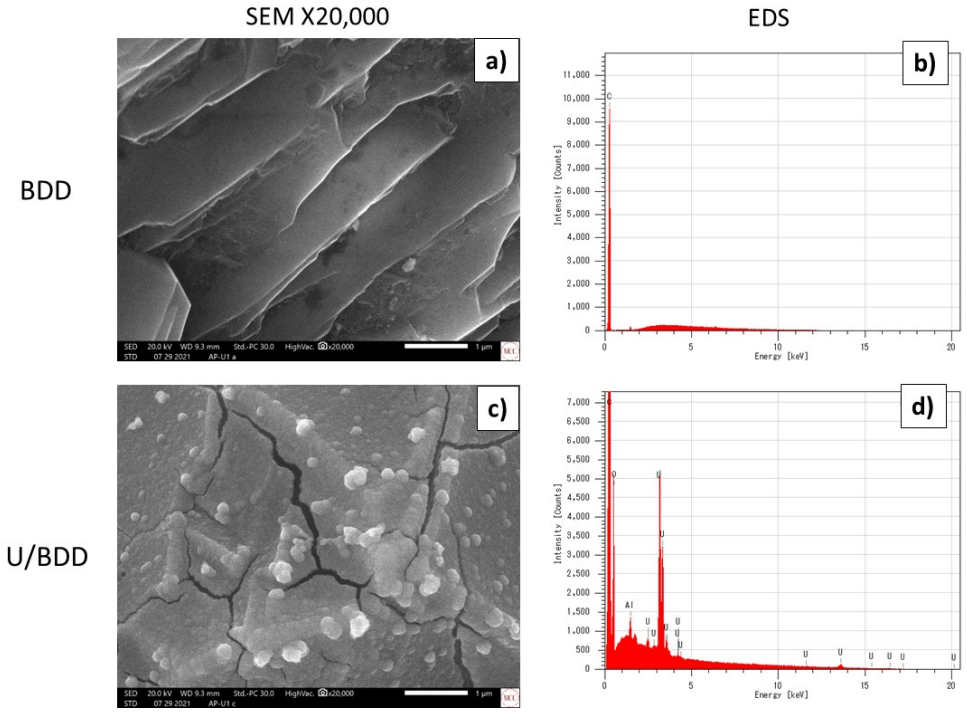

Appendix 4.2. Scanning Electron Microscopy (SEM)micrographs of the BDD electrode after the chronoamperometry in 5mM uranyl acetate and 0.1M $KClO_4$ at different magnifications: X5,000 (a), X45,000(b), and X110,000 (c).

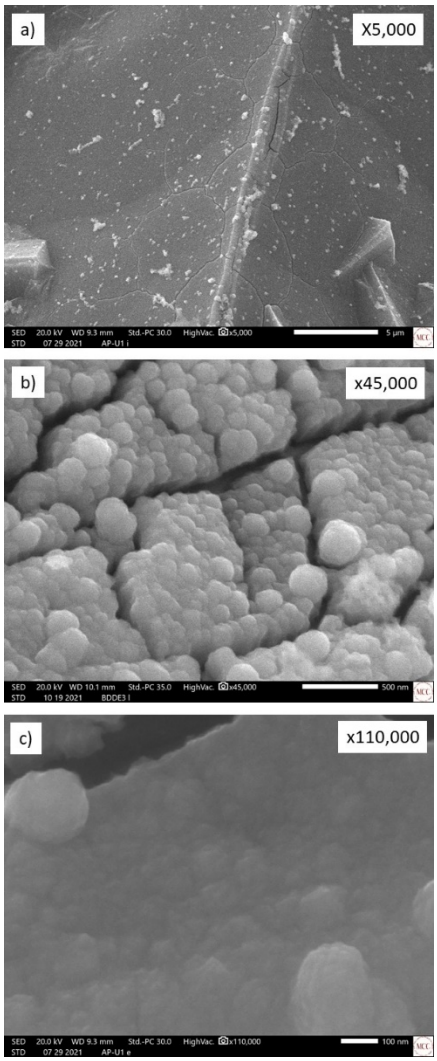

Appendix 4.3. Scanning Electron Microscopy (SEM)micrographs of the BDD electrode after the chronoamperometry in 5mM uranyl acetate and 0.1M $KClO_4$ - A punctual analysis for the uranium-based film onto BDD electrodes.

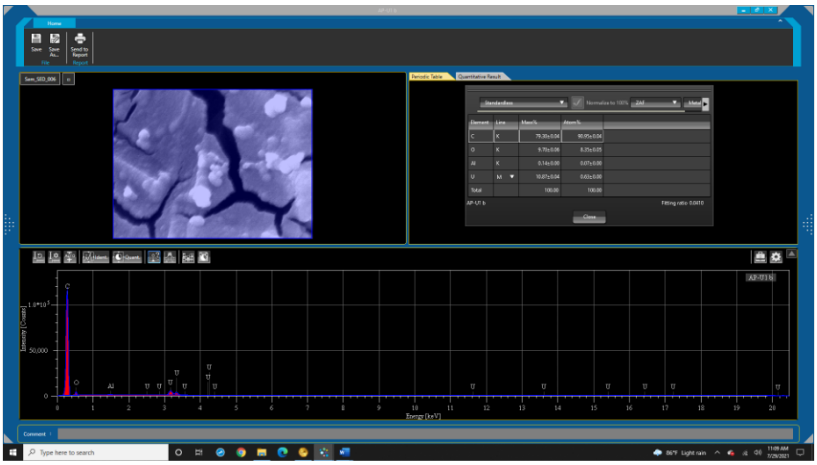

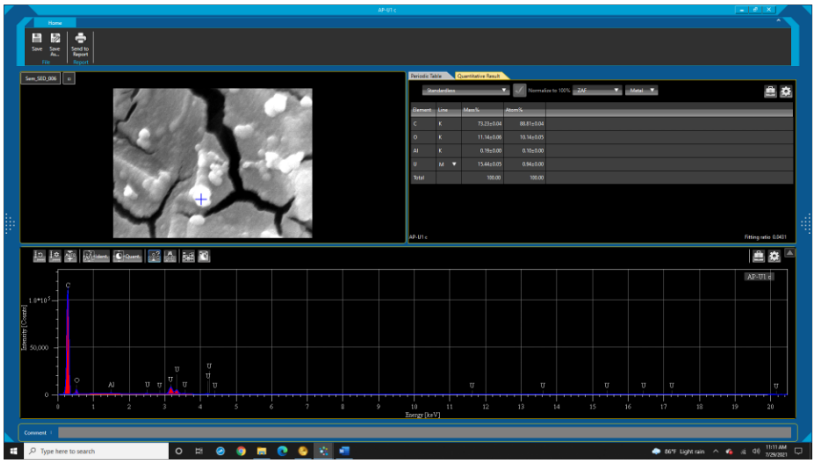

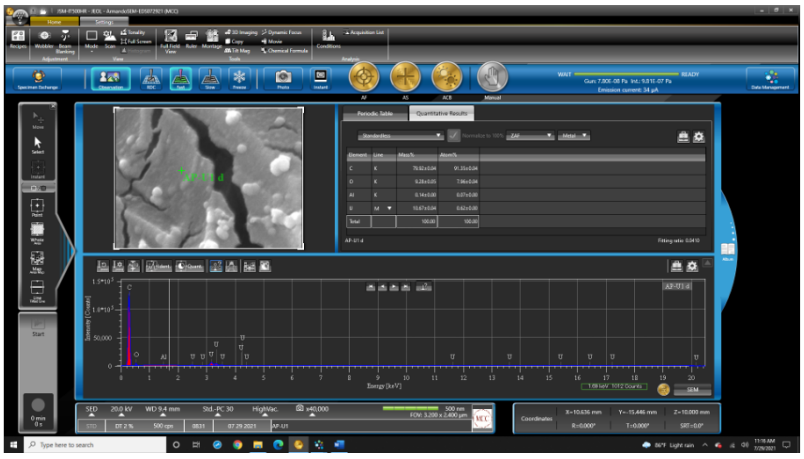

Appendix 4.4. Raman Spectra of the pristine BBD electrode in 0.1M KClO4 (a) and the BDD electrode after the chronoamperometric deposition in 5mM uranyl acetate and 0.1M $KClO_4$ (b).

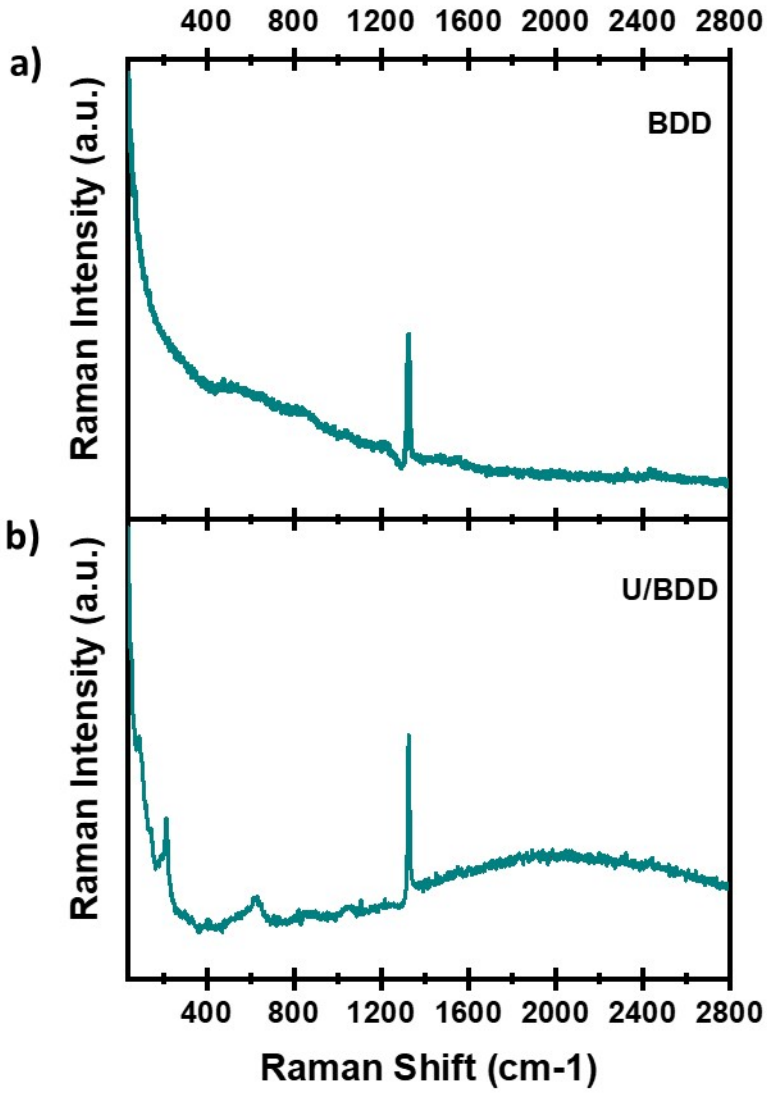

Appendix 4.5. Comparison of the X-ray photoelectron spectroscopy U 4f core-level binding energy region recorded for the U-01, U-02, U-03 uranium films electro-assembled on boron doped diamond electrodes. The relative binding energy between the U $4f_{5/2}$ and U $4f_{7/2}$ peaks, including the shake-up satellite around the characteristic U 4f doublet is reported for each sample.

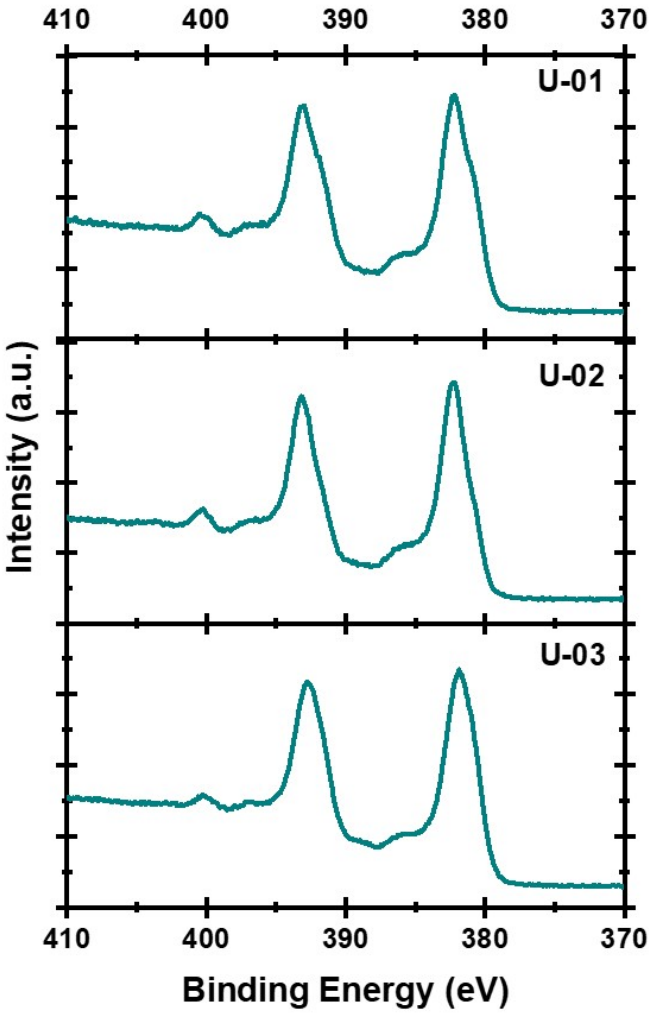

Appendix 4.6. Variation of uranium speciation and the composition of U^{4+}, U^{5+}, and U^{6+} components were obtained from the XPS U $4f_{7/2}$ binding energy region curve fitting presented in Figure 5.

Sample	**Uranium Specie (± 0.01 %)**			
	U^{4+}	U^{5+}	$U^{4+} + U^{5+}$	U^{6+}
U-01	31.79	33.60	65.39	34.61
U-02	24.17	41.60	65.77	34.23
U-03	37.03	27.33	64.36	35.64

APPENDIX 5

Appendix 5.1. List of publications

1. **Armando Peña-Duarte**, Aminda Cheney-Irgens, Timothy D. Hall, Santosh H. Vijapur, Arnulfo Rojas, Jennings Taylor, Luis Echegoyen, and Carlos R Cabrera. Nitrogen-Doped Nanocarbons for In-Situ Hydrogen Peroxide Production - A Sustainable Electrochemical System for Life-Support Environments. *ACS Sustainable Chemistry and Engineering*, **2023** (Under Review).
2. **Armando Peña-Duarte**, Alexis Acevedo, Richard M Lagle, Mebougna L Drabo, Stephen U. Egarievwe, and Carlos R Cabrera. Stable Uranium Oxide Under Atmospheric Conditions: An Electroplating Technique for U Film Fabrication at Boron Doped Diamond Electrodes. *ACS Materials Au*, **2023** (Aceppted).
3. Subhajit Bhunia, **Armando Peña-Duarte**, Huifang Li, Hong Li, Mohamed Fathi Sanad, Pranay Saha, Matthew A. Addicoat, Carlos R Cabrera, Miguel José Yacamán, Ram Seshadri, Santanu Bhattacharya, Jean-Luc Brédas, Luis Echegoyen. [2,1,3] Benzothiadiazole-Spaced Active-Site Engineering of CoPorphyrin-based Covalent Organic Frameworks for Remarkable O2 Reduction. *ACS Nano*, 17, 4, 3492-3505, **2023**.
4. Camila Morales-Navas, Roberto A. Martínez-Rodríguez, Francisco J. Vidal-Iglesias, **Armando Peña-Duarte**, Joesene J. Soto-Pérez, Pedro Trinidad1, José Solla-Gullón, Toshko Tzvetkov, Jonathan Doan, Eugene S. Smotkin, Eduardo Nicolau, Juan M. Feliu, and Carlos R. Cabrera. Autonomous Electrochemical System for Ammonia Oxidation Reaction: Measurements at the International Space Station. *npj Microgravity* **9**, 20, **2023**.
5. Joesene Soto-Pérez, **Armando Peña-Duarte**, Pedro Trinidad, Gerardo Quintana, Xueru Zhao, Kotaro Sasaki, Miguel José Yacamán, Rubén Mendoza Cruz, and Carlos R. Cabrera. Combined Rotating Disk Slurry Electrodeposition (RoDSE)-Spontaneous Galvanic Displacement (SGD) for Pt-M (M=Co, Ni and Cu) Catalysts Synthesis for Oxygen Reduction Reaction in Alkaline Media. *ACS Apply Energy Materials*, 5, 12, 15175-15187, **2022**.
6. Del Pilar Albadalejo, Joselyn; Alonso-Sevilla, Suheily; Cintrón, Nicohl; Feng, Xinran; García, Angel; Martinez-Torres, Dinorah; Rodríguez, Astrid; Román-Montalvo, Natalia; Torres, José; Yang, Yao; **Pena-Duarte, Armando**; Singhal, Rahul; Debefve, Louise; Pollock, Christopher; Cabrera, Carlos; Abruña, Héctor; Santiago-Berríos, Mitk'El. Ex situ and In situ Analysis of the Mechanism of Electrocatalytic Hydrogen Peroxide Production by $Co_xZn_{1-x}O$ ($0 < x < 0.018$) Materials in Alkaline Media. *ACS Appl. Energy Mater.* 5, 6, 6597–6605, 2022.
7. **Armando Peña-Duarte**, S.H. Vijapur, T.D. Hall, Kathleen L. Hayes, Eduardo Larios-Rodríguez, Joselyn del Pilar Aldabalejo, Stephen Snyder, E. Jennings Taylor, and

Carlos R. Cabrera. Iron Quantum Dots Electro-Assembling on Vulcan XC-72R: Hydrogen Peroxide Generation for Space Applications. *ACS Appl. Mater. Interfaces,* 13, 25, 29585–29601, **2021**.

8. Vijapur, S. H.; Hall, T. D.; Taylor, E.; Wang, D.; Snyder, S.; Skinn, B.; **Peña-Duarte, A**.; Cabrera, C. R. *In- Situ* Resource Utilization for Electrochemical Generation of Hydrogen Peroxide for Disinfection. *ICES: International Conference on Environmental Systems*, 12 pages, **2021**.
9. Melissa Vega-Cartagena, Arnulfo Rojas-Pérez, Guillermo S. Colón-Quintana, Daniel A. Blasini Pérez, **Armando Peña-Duarte**, Eduardo Larios-Rodríguez, Marco A. De Jesús, Carlos R. Cabrera, Potential dependent Ag nanoparticle electrodeposition on Vulcan XC-72R carbon support for alkaline oxygen reduction reaction. *Journal of Electroanalytical Chemistry*, Volume 891, 115242, **2021**.
10. Nelson, G. J.; Vijapur, S. H.; Hall, T. D.; Brown, B. R.; **Peña-Duarte, A**.; Cabrera, C. R., Electrochemistry for Space Life Support. *Electrochemical Society Interface***,** 29 (1), 47-52, **2020**.
11. Vijapur, S. H.; Hall, T. D.; Taylor, E.; Wang, D.; Snyder, S.; Skinn, B.; **Peña-Duarte, A**.; Cabrera, C. R.; Sweterlitsch, J., *In- Situ* Resource Utilization for Electrochemical Generation of Hydrogen Peroxide for Disinfection. *ICES: International Conference on Environmental* Systems, 38, 14 pp, **2019**.
12. **Armando Peña-Duarte** and Carlos R Cabrera. The Oxygen Reduction Reaction onto an Iron/Nitrogen/Carbon Composite. *Journal of The Electrochemical Society* (In Progress).
13. **Armando Peña-Duarte**, Aminda Cheney-Irgens, Joesene Soto-Pérez, Louise Debefve,, Christopher Pollock, and Carlos R Cabrera. Iron Oxidation States of the RoDSE Iron/Nanocarbons: Determining the Influence of Carbon Structure via XANES. *ACS Appl. Mater. Interfaces* (In Progress).
14. **Armando Peña-Duarte**, Kathleen L. Hayes, and Carlos R Cabrera. Oxygen Reduction Reaction Controlled by The Iron-Carbon-Nanoonion Composite (Fe/CNOs). *Journal of The Electrochemical Society* (In Progress).
15. **Armando Peña-Duarte**, Joesene Soto-Pérez, and Carlos R Cabrera. Platinum onto Carbon via RoDSE: Determining the Influence of Carbon Structure. *Journal of The Electrochemical Society* (In Progress).
16. **Armando Peña-Duarte**, Joesene Soto-Pérez, and Carlos R Cabrera. Chalcogenides and electrocatalysis. *Catalysts* (Ready to be submited).

Vita

Armando Manuel Peña-Duarte is a Venezuelan—from ***Caracas***—passionate for science, space, and architecture. After getting his Bachelor of Science in Chemistry from the Simon Bolivar University in Caracas, he moved to Puerto Rico where he got his Master of Science in Physics from the University of Puerto Rico at Mayaguez, mentored by Dr. Maharaj Tomar. Then, Armando decided to continue his graduated studies in the Chemical Physics PhD program at the University of Puerto Rico at Rio Piedras, where he started his career in electrochemical for space in the Dr. Carlos R Cabrera group. When Dr. Cabrera invited him to move to The University of Texas at El Paso (UTEP), he decided to undertake this new scientific adventure, transferring his graduated records to UTEP. In El Paso, TX, Armando has found a huge spectrum of novel academic and scientific opportunities, friends, and certainly singular challenges. Currently, Armando is at Los Alamos National Laboratory working as a Graduate Researcher in fuel cells applications, looking forward to new journeys as he moves into postdoctoral and job positions.